Aquifer properties from Earth and barometric tides analysis : application to the Gallo-Roman archaeological site of Genainville (French Vexin)

Elijah Edet Nkitnam

Aquifer properties from Earth and barometric tides analysis: application to the Gallo-Roman archaeological site of Genainville (French Vexin)

Thèse de Doctorat de Sorbonne Université

École doctorale ED398, Géosciences ressources naturelles et environnement

Présentée par

Elijah Edet NKITNAM

Pour obtenir le grade de

DOCTEUR de SORBONNE UNIVERSITÉ

devant le jury composé de:

Mme Béatrice LEDÉSERT	GEC, CY Cergy Paris Université	Rapporteure
M. Frédéric DELAY	ITES, Université de Strasbourg	Rapporteur
Mme Valérie PLAGNES	METIS, Sorbonne Université	Examinatrice
Mme Audrey BONNELYE	MinesNancy, Université de Lorraine	Examinatrice
M. Pascal SAILHAC	GEOPS, Université Paris-Saclay	Président
M. Vivien BARRIÈRE	Héritages, CY Cergy Paris Université	Invité
M. Jérôme WASSERMANN	L2MGC, CY Cergy Paris Université	Encadrant de Thèse
M. Alexis MAINEULT	METIS, Sorbonne Université	Directeur de Thèse

Tuesday, 28 May, 2024

Abstract

The well-being of human societies requires knowledge of the reciprocal impacts between anthropogenic activities and ecosystem services. In order to mitigate global, regional and local climate change, methods and techniques must be developed to maintain valuable interactions between human societies and ecosystems. In the continental context, floods are often brutal and catastrophic events, altering the well-being of human societies for more or less long periods and also threatening cultural heritage.

Gallo-Roman society developed hydraulic knowledge and drainage techniques in order to take advantage of the natural environment and develop its activities. However, these techniques have not always been sufficient to mitigate climatic events such as flooding, which may have resulted in the abandonment of the occupied environment. Nowadays, flood risk management remains a difficult task, in particular concerning the prediction of flooding by groundwater, which then saturates the vadose zone, leading to significant consequences on buildings, present or past.

The study of the dynamics of the water table and the saturation of the vadose zone is classically carried out by hydrological measurements in piezometers. Geophysical methods make it possible to explore a larger area, but with a resolution that depends on the density of the sensor network.

This thesis work tests and combines different geophysical methods on a pilot site located in the French Vexin, in Genainville, a site which has been anthropized for thousands of years. The sustainability of this Gallo-Roman archaeological site, where remains and artefacts dating from the 2^{nd} century AD were excavated, is threatened by the presence of a shallow water table. The materi-

als and structures of the built heritage, including a two-cell temple and a limestone amphitheatre, are in fact subject to fluctuations in the water table. As part of a multidisciplinary effort to support archaeological research and conserve site structures, we report geophysical imaging results (electrical resistivity sections) combined with hydrological groundwater monitoring. The analysis of temporal hydrological chronicles made it possible to quantitatively evaluate the hydraulic and geo-mechanical characteristics of the subsurface using a non-destructive approach. Groundwater levels in three piezometers and barometric pressure data were acquired at 60-second intervals. These continuous data were decomposed using signal processing techniques.

Using the regression deconvolution method, the barometric pressure response was decoupled from the measured water levels. Theoretical parameters of Earth tides were calculated using the PyGtide code, based on the ETERNA PREDICT program. Harmonic analysis of raw and filtered data, using classical fast Fourier transform and singular spectrum analysis, identifies the M_2, S_2 and K_1 components of the tidal wave as the dominant components of the signal. The harmonic constituents K_1 and S_2 are present in the filtered and raw data sets with different amplitudes. The amplitude response method was used to calculate the poroelastic properties of the aquifer and characterize the heterogeneity of the subsurface. The model identified a semi-confined aquifer as the primary groundwater storage system at the site. The developed methodology appears to be a promising tool for monitoring saturation variations during seasonal periods, in order to prevent the risk of flooding of shallow water tables.

Le bien-être des sociétés humaines nécessite la connaissance des impacts réciproques entre les activités anthropiques et les services écosystémiques. Afin d'atténuer les changements climatiques globaux, régionaux et locaux, il faut développer des méthodes et des techniques pour maintenir des interactions précieuses entre sociétés humaines et écosystèmes. Dans le contexte continental, les inondations sont souvent des événements brutaux et catastrophiques, altérant le bien-être des sociétés humaines pendant des périodes plus ou moins longues et menaçant également le patrimoine culturel.

La société gallo-romaine a développé des connaissances hydrauliques et des techniques de drainage,

afin de tirer profit de l'environnement naturel et de développer ses activités. Néanmoins, ces techniques n'ont pas toujours été suffisantes pour atténuer les événements climatiques comme les inondations, ce qui a pu entraîner l'abandon de l'environnement occupé. De nos jours, la gestion des risques d'inondation reste une tâche difficile, en particulier concernant la prévision des inondations par les eaux souterraines, qui saturent ensuite les zones vadoses, entraînant des conséquences importantes sur les bâtis, présents ou passés.

L'étude de la dynamique de la nappe phréatique et de la saturation de la zone vadose est classiquement réalisée par des mesures hydrologiques dans des piézomètres. Les méthodes géophysiques permettent d'explorer une plus grande surface, mais avec une résolution qui dépend de la densité du réseau de capteurs.

Ce travail de thèse teste et combine différentes méthodes géophysiques sur un site pilote situé dans le Vexin français, à Genainville, site qui a été anthropisé pendant des milliers d'années. La durabilité de ce site archéologique gallo-romain, où des vestiges et des artefacts datés du 2ème siècle de notre ère ont été excavés, est menacée par la présence d'une nappe phréatique peu profonde. Les matériaux et les structures du patrimoine bâti, comprenant un temple à deux. Deux chambres et un amphithéâtre faits de maçonneries calcaires, mortiers et briques sont en effet soumis aux fluctuations du niveau de la nappe. Dans le cadre d'un effort multidisciplinaire visant à soutenir les recherches archéologiques et à conserver les structures du site, nous rapportons ici des résultats d'imagerie géophysique (sections de résistivité électrique) combinés au suivi hydrologique des eaux souterraines. L'analyse des chroniques hydrologiques temporelles a permis d'évaluer quantitativement les caractéristiques hydrauliques et géo-mécaniques de la subsurface selon une approche non destructive. Les niveaux des eaux souterraines dans trois piézomètres et les données de pression barométrique ont été acquis à des intervalles de 60 secondes. Ces données continues ont été décomposées selon des techniques de traitement du signal.

En utilisant la méthode de déconvolution par régression, la réponse à la pression barométrique a été dissociée des niveaux d'eau mesurés. Les paramètres théoriques des marées terrestres ont été calculés à l'aide du code PyGtide, basé sur le programme ETERNA PREDICT. L'analyse harmonique des données brutes et filtrées, à l'aide de la transformée de Fourier rapide classique et de l'analyse spectrale singulière, identifie les composantes M_2,S_2 et K_1 de l'onde de marée comme étant les composantes dominantes du signal. Les constituants harmoniques K_1 et S_2 sont présents dans les ensembles de données filtrées et brutes avec des amplitudes différentes.

L'analyse basée sur un modèle poro-élastique a permis de caractériser les propriétés de l'aquifère. Celui-ci apparaît semi-confiné. La méthodologie développée semble être un outil prometteur pour surveiller les variations de saturation pendant les périodes saisonnières, afin de prévenir les risques d'inondation des nappes phréatiques peu profondes.

Acknowledgment

I am deeply grateful to my thesis advisors, Dr. Maineult and Dr. Wassermann, for agreeing to supervise my research and secondly, for their rich intellectual acumen and friendly disposition which electrified the working atmosphere.

Thank you, Dr. Maineult, for agreeing to guide me through this rigorous doctoral training. The training has yielded the anticipated outcomes. You took three initial steps to place the research on a pedestal of success. Firstly, you contacted Dr. Wassermann to secure the site for this thesis. Secondly, you eased the inscription burden that could have arisen due to the global pandemic by availing of all possible communication channels, including calls and posts, to facilitate the procedures. Lastly, you allowed me to develop my competence in Python programming. Through your collaborations, METIS-UMR 7619 (Sorbonne Université, SU) approved the MURGALLO convention that funded my visits to the site and the research itineraries. I am grateful for the time you spent to ensure the success of the research and the energy put into the field experiments to acquire the spontaneous potential, pumping test, and two-dimensional (2-D) electrical resistivity tomography (ERT) data sets. I saw how you paid attention to details as we worked in the field. I learned from you many things that spurred the research to be accomplished e.g., a conducive environment, constant communication, and experience. You also deployed your bilingual asset.

Thank you, Dr. Wassermann, for your diligence in retrieving the data. Your regular visits to the site, and ensure that all tools, instruments, and materials are functional. You have continuously availed yourself to ensure the data processing meets the standard anticipated for each dataset. You are vocal in expressing your expectations of the research. I truly thank you for your interest

and continuous guidance. Your car became the field vehicle. It was always ready and driven by you throughout the data acquisition periods. Thank you for the time we spent collecting data. I learned from you the motivation for the work and the importance of writing in detail and structuring my report.

I truly appreciate your collaborative efforts through which the sensors and instruments used to acquire water pressure, spontaneous potential, and thermal tracing data were obtained from the PREVENT (Le PatRimoine dans son EnVironnemENT) project. The PREVENT project was supported by a state grant from the French National Research Agency (Agence Nationale de la Recherche) under the Investment for the Future programme integrated in France 2030, with the reference ANR-17-EURE-0021 Ecole Universitaire de Recherche Paris Seine - Foundation for Cultural Heritage Sciences.

I am grateful to Dr. Fernando Lopez (formerly of the Institut de Physique du Globe de Paris (IPGP)) for granting access to his Singular Spectrum Analysis (SSA) code, written in the Matlab programming language. Thank you, Dr. Lopez and Dr. Maineult, for the various updates to the SSA codes used in my thesis.

I received valuable support from Dr. Vivien Barrière, an archaeologist and associate professor at Laboratoire Héritages UMR 9022, CY Cergy Paris Université (CYU), and Director of Archaeological Fieldwork and Project Manager for the "Archaeological Site of Genainville" project. Thank you for the opportunity to acquire my data sets alongside the ongoing archaeological programs. The summer of 2022 was particularly eventful, with archaeologists, students, and other researchers on-site for their excavations. I stayed with them, performing the geophysical and thermal experiments and collecting water pressure data. I appreciate your participation in the follow-up committee and this research.

My gratitude goes to Roger Guérin, hydrogeophysicist and professor at the METIS laboratory (SU). I greatly appreciate your quality guidance when acquiring 2-D ERT and field training on using the Syscal Pro Resistivity meter and accessories. I am grateful for access to RES2DINV software, Surfer 13, and the in-house PanneauGrd and mklvlviridis packages for gridding the data and generation of Viridis-colored inverted resistivity models. Thank you for your time and careful disposition to field procedures and post-acquisition detailing of the processing steps. Your guidance and participation in my thesis committee meetings are happily appreciated. Thank you once again, Pr. Guérin.

To Mr. Didier Vermeersch, archaeologist and researcher, thank you for the warm welcome and the invaluable legacy you and your colleagues have left at the Genainville site.

Mr. Jonhattan Vidal, research engineer at the Regional Archaeology Service within the Heritage and Architecture Division of the Regional Directorate of Cultural Affairs (DRAC), Bourgogne-Franche-Comté Region, provided the Digital Elevation Model (DEM) used for the watershed and streamflow models. Thank you, Mr. Vidal, for the data and the support you offered me in the field.

Topography data used in the inversion of the two-dimensional resistivity values were courtesy of Thomas Terrace. He also provided Theodolite survey information on features at the site.

I truly appreciate the hospitality and camaraderie of the archaeology students (L' AEVA - Association Etudiante Valdoisienne d'Archéologie) from CYU and other institutions during the 2022 Summer School and my visits to the site.

All used Open-Source materials, software, and works are duly acknowledged. They include but are not limited to the barometric and earth tides correction (BETCO) program, PyGTide-ν0.7.1, Latex, VirtualBox, Ubuntu, and QGIS. Python libraries, packages, and codes.

I am grateful to the Nigerian government's Tertiary Education Trust Fund (TETFund) for sponsoring my doctorate programme through the award of the Overseas Scholarship Programme following my nomination by the Alex Ekwueme Federal University.

My nomination was a sequel to the collaboration between the French government and Alex Ekwueme Federal University for a joint scholarship programme (Franco-Funai Joint Scholarship Programme) initiated by the then Vice-Chancellor, Pr. Chinedum Nwajuba, and co-ordinated by Pr. (Mrs) Nnenna Nwosu-Nworuh. I truly appreciate the administration and guidance I received from Campus France Nigeria and the Embassy of France in Nigeria. I thank Pr. Sunday O. Elom, the current Vice-Chancellor, Mrs. Odisa Okeke, the former Registrar, and Dr. Chinwe Okolo, former coordinator of Franco-Funai, for their support.

I appreciate the facilitation and support of Professor Emeritus Mosto Onuoha.

To my colleagues at Alex Ekwueme Federal University: Mr. Sowechi E. Ebi, Dr. E. M. Abraham, Dr. G.-B. Azuoko, Dr. T. O. Daniel, Dr. Ifeoma Agbi, Dr. K. I. Chima, Dr. O. V. Omonona, Dr. O. P. Aghamelu, and Pr. A. C. Ekwe, thank you for inspiring me and providing support at all times. Pr. Sylvie Leroy and Dr. Ekeabino Momoh are the gateways to my path at ISTeP, which transited to METIS. Thank you, Gbenga E. OMONIYI, Folorunso D. JAYEOLA, George A. AGWU, and Mon-

day N. IGWE, we journeyed together and crowned it with success. Thanks to the men and women of goodwill who supported my stay and studies including Opeyemi and Olufunmilola Davies and children: Precious, Peace and Praise; Paul and Jennifer Ohonbamu and children; Paul and Sharon Aimuan and children; Joseph and Sophia Peter and children, Mme Lila Ugochi Ugboaja and family, James and Esther Jumbo and family, M. Osaro Osundu and family, M. Cyrille Janssen, Mme Claudia Nardini and Mme Veronique Dirain. I thank Chibuike Nnamani, Joshua Avidime, Bisan Yabuwat, Japhet Soni, Ibrahim Yakubu, Ada Manga, and Friday Omorejie and their families for their support.

Thank you, Mrs. Naomi Ibrahim and family, especially for your unfailing confidence and years of support. Thank you to my good sisters, Mrs. Miriam Adeyemi, Mrs. Amina Jika, and Mrs. Alda Joshua, and their spouses and children, for your consistent care and support.

Thank you, my good brothers and sisters, for your support: Atim, Charity, Victor, Late James, Mary, Friday, and your spouses and children.

Thanks to all the scientists, technical, and administrative staff at UMR 7619 METIS and SU, including the professors, researchers, and students, for the warm and cordial atmosphere and positive attitude. Thank you, Pr. Jean-Marie Mouchel, Mme Bénédicte Sabbatier, Mme Valérie Girard, the doctoral students, and post-doctoral researchers. Thank you, SU, for providing facilities for my research. Thank you, professors, engineers, researchers, and students of L2MGC (Laboratoire de Mécanique et Matériaux du Génie Civil), CYU, for the warm and peaceful environment that marked my visits and also for the collaboration and facilities provided for the thesis through the conventions with METIS and SU.

Ecole Doctorale (ED) 398 - Géosciences, ressources naturelles et environnement (GRNE) yielded unwavering support and facilitated my academic and career pursuits. Thank you, Pr. Loïc Labrousse, for the administration and the confidence in your students. Thank you, Mme Lawrence Pastor, for the prompt administrative work.

I appreciate Pr. Valérie Plagnes and Pr. Pascal Sailhac for their participation and useful advice during the thesis committee meetings. I thank Pr. Demian Jougnot for his support during the thesis meeting. I am grateful to the rapporteurs and examiners for their thoughtful comments.

To my father, thank you for showing me the way to success: discipline, devotion, and diligence. I have taken your dream and made it a reality. To my mother, thank you for your silence and support in the background. To my lady and my generations, with love and gratitude, thank you.

Dedication

This work is dedicated to the loving memory of

my younger brother,

James Edet,

my father,

Effiong Elijah (baptized John and fondly called Edet),

and my grand father,

Chief Elijah Nkitnam

Contents

List of Figures

List of Tables

Listings

CHAPTER 1

General introduction

1.1 Conservation of cultural sites and heritage materials

Heritage buildings, sites, and materials are movable properties, and immovable remains of archaeological, historical, natural, cultural, or artistic significance. They include collections of artworks, sculptures, paintings, masonry, architectural works, features, and objects depicting traces of human activities erected or buried in soils, or buildings of historical or cultural relevance (Cao et al., 2021; Mekonnen et al., 2022). They represent assets and materials for connecting the evolution of civilization with the past. Embedded in them are creative ideas and prowess displayed in portraits, carvings, coinages, paintings, and writings showcasing deities, royalty, heroism, nobility, literacy, masonry, and natural phenomena inscribed on walls and buildings for memorial, aesthetic, educational, or religious purposes (UNESCO, 2023). Historical, archaeological, or heritage buildings and sites include monuments, structures, and landscape endowments passed to us by nature or its ancient inhabitants. They provide aesthetic and cultural links to the past and present.

The conservation of heritage properties are measures taken to retain the form, stability, and appearance of monuments, sites, and structures, in addition to cultural, historical, and natural interest properties. It considers all measures and actions that involve protection, detection of anomalies, restoration, and preservation of the sites, properties, and the immediate environment to ensure its sustainability. Enforceable guidelines and laws to protect heritage properties from theft or

deliberate destruction are now enshrined in government legislation and international conventions among nations (Mekonnen et al., 2022). Notably is the United Nations Educational, Scientific and Cultural Organization (UNESCO) 1954 convention that supports the protection of movable and immovable heritage properties from being destructed, pillaged, looted, or illicitly trafficked (UNESCO, 2023). Movable heritage items, including artworks, metallic objects, sculptures, and other materials from the past, are traditionally preserved in museums, designated halls, and galleries. These ensure they are safe and readily available or accessible to tourists, researchers, and the general public.

In-situ archaeological, cultural, and natural heritage sites and structures are exposed to various field situations that threaten their perpetuity (Chen et al., 2017). These threats include dust cover, the effects of climate change, groundwater ingress, pilfering, injuries, and destruction by intruders, tourists, and armed individuals. Neglect by governments, institutions, and the host communities has allowed patrimonial sites and structures to suffer natural, willful, or deliberate destruction to the chagrin of archaeologists, curators, conservationists, researchers, and the public.

Groundwater ingress, and incursions are a major environmental threat to the sustainability and eternity of cultural heritage properties and sites (Amin, 2017; Cao et al., 2021; Carruthers, 2023; Coppola et al., 2020). A classic example is the Temple of the Rising Sun also known as the Nubian Monuments, which is located in Egypt. The temple of Ramses II at Abu Simbel and the sanctuary of Isis at Philae were threatened by the incursions of rising waters from the Nile following the construction of the Aswan Dam (Figure 1.1) (see also Carruthers, 2023; Hassan, 2007; UNESCO, 2023).

These outstanding archaeological features were rescued from the imminent deterioration and obliteration following the global campaign effort led by UNESCO that resulted in their relocation to a safer site (UNESCO, 2003). While irrigation-induced heightened groundwater levels in the Abu Mena region (located south of Alexandria, Egypt) have accelerated the deterioration of notable early Christian buildings and sites including the church, basilicas, baptistery, monasteries, houses, and the tomb of the holy city's martyr Mena (Amin, 2017; Vincent, 2007).

A larger portion of the heritage properties in the important town has either collapsed or threatened to collapse (Figure 1.2). As a result, the Abu Mena site was enlisted into UNESCO's World Heritage in Danger List in 2001, following its earlier placement in UNESCO's World Heritage List in 1979 due to the threat of rising groundwater levels.

Figure 1.1: The Temple of the Rising Sun in Egypt was moved to higher ground following the impact caused by rising groundwater. Source: Rolls Press / Popperfoto via Getty Images

Wooden heritage structures are also suffering a similar fate from groundwater intrusion. The Xianyang Shahe Wooden Bridge in Xi'an China, is a cultural ruin built during the Qin Dynasty (221 – 206 BC). The wooden bridge's destruction is accelerated by groundwater fluctuations (Cao et al., 2021). The movement of water and salt is reported to have altered the heritage artifact and its subsurface environment, allowing weathering and biogeochemical activities to lead to the gradual deterioration of the cultural ruin.

Conventionally, the extent of moisture content or groundwater ingression in historic walls, monuments, and cultural heritage properties and sites are detected with nondestructive testing (NDT) which has gained significant usage in archaeological prospecting (Chen et al., 2017; Deiana et al., 2022). The sensitivity of nondestructive geophysical measurements such as ground penetrating radar and electromagnetic techniques, to moisture content in soils and structural materials, is a response characteristic that has been extended to caution investigations for the protection of heritage (Barone and Ferrara, 2018).

Electrical resistivity tomography (ERT) and total magnetic field methods are geophysical techniques that have also enhanced the detection of archaeological objects and anomalies buried within the Earth as well as the mapping of portions infected by moisture (Clark, 1990; Deiana et al., 2018; Epov and Chemyakina, 2009; Mol and Preston, 2010; Moník et al., 2018). Modified ERT techniques are now components of the conservation strategy for heritage structures and monuments.

Figure 1.2: St Mena area (Abu Mena town) showing the ruins of the religious complex impacted by neglect and rising groundwater levels. *Source: Ko Hon Chiu Vincent (Vincent, 2007).*

Sass and Viles (2006), adapted a novel approach employing ERT to assess the moisture distribution in the stone structure of Byland Abbey. The modified ERT method effectively resolved the spatial and temporal moisture content structure of the ruined monument wall (Sass and Viles, 2006). The results of this investigation rely on the response of the geophysical signal to the contrast in the physical properties of the feature to delineate for example area ingress by water. However, the factors that drive fluctuations and rise in groundwater or control flow within the soils and rock sequences on which lay the cultural heritage buildings have not been identified. The drivers of hydrological processes in an in-situ archaeological or cultural heritage site, the properties of the subsurface sequence, and the response of the groundwater systems are vital information for a holistic approach to a standardized heritage site protection scheme.

Conceptually, the groundwater systems in archaeological, historical, or cultural sites like any other natural or physical environment respond to different influences, stress, or drivers that result in changes in groundwater levels in time and space (Rasmussen and Crawford, 1997; Rau et al., 2022; Toll and Rasmussen, 2007) (see also Figure 1.3). Groundwater levels are known to respond to anthropogenic and natural inducements including barometric pressure, infiltration triggered recharge, evapotranspiration, temperature differentials, and earth tides to ensure rise and changes

in water levels (Doan et al., 2006; Jia et al., 2021; McMillan et al., 2019; Rasmussen and Mote, 2007; Spane, 2002; Wilkinson and Brassington, 1991).

Figure 1.3: The Angkor Temple impacted by groundwater. Photo by F. Chen (2017).

1.2 Climate and environmental variability

Temperature, relative humidity, and precipitation are among the climatic and environmental variables whose impact influences both natural and anthropogenic activities on Earth. These parameters have a profound effect on natural resources and infrastructures. They regulate and maintain different processes emplaced by nature and humans. Extreme conditions have severe effects on the optimum level and function of the resource and infrastructure (e.g. Bonazza and Sardella, 2023; Sardella et al., 2020; Sesana et al., 2021).

Groundwater is a natural resource distributed on the Earth. It is the water found in pores, voids, and fractures in soils, sediments, and rock sequences in the subsurface (Figure 1.4). Water flows through the interconnected pores to fill other voids and spaces, when these pore spaces are saturated, the water rises to a level in the subsurface known as the phreatic surface or the water table (Domenico and Schwartz, 1998; Fetter, 2001). Below the phreatic surface is the saturated zone or the permeable water-bearing rock layer called the aquifer (Figure 1.4).

Above the groundwater level or the phreatic surface is the unsaturated zone also known as the

vadose zone. The phreatic level in the subsurface is balanced by the upward thrust of the water level and by the weight of atmospheric gases. The unsaturated zone extends to the Earth's surface and houses infrastructures including buildings, walls, foundations, and drainage systems (Bresciani et al., 2020; Das and Sobhan, 2014). Climatic change and changing environmental pa-

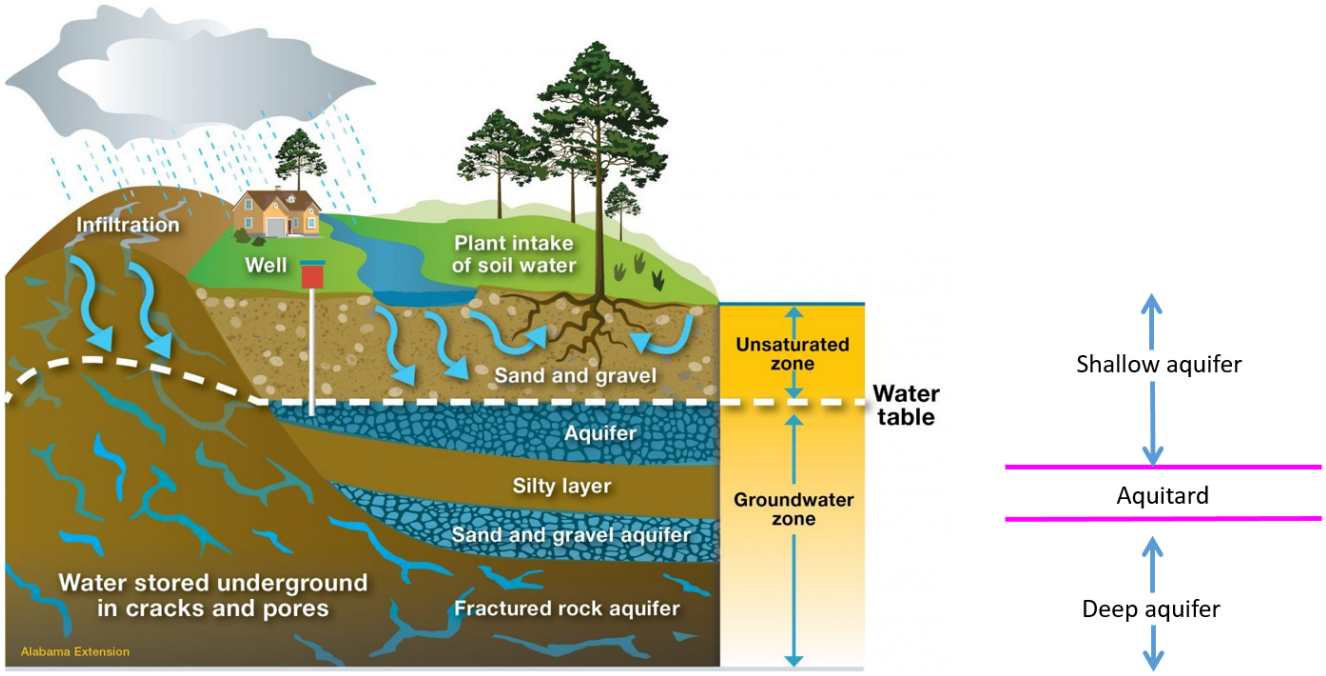

Figure 1.4: Groundwater and shallow aquifer. (Source: https://www.aces.edu/blog/topics/fish-water/what-is-an-aquifer/)

rameters can affect both the groundwater in the subsurface and infrastructures on the surface and unsaturated zones (Figure 1.5). Extreme climate events such as torrential rainfall have resulted in more runoff, and overfilled drainage channels leading to surface water flood and damage to infrastructure. In the event of rapid infiltration, the groundwater levels are known to increase and rise to cause subsurface flooding. Building foundations, walls, and buried infrastructures flooded by groundwater are exposed to environmental variability that affects their stability and sustainability. When groundwater rises, it carries dissolved salts which it deposits on the surfaces of the building foundations, walls, and buried infrastructures on receding (ACIA, 2004; Araújo et al., 2021; Dunleavy, 2021). The fluctuations in groundwater levels also perturbed the existing geochemical relationships in the subsurface. This facilitates the decay of the foundations and walls. In the same manner, rising global temperatures, accompanied by rapid evapotranspiration, severe heat waves, decreasing groundwater levels, and changes in the spatiotemporal distribution of groundwater for abstraction affect aquifer levels (Beer and Seither, 2015; Dunleavy, 2021; Holman et al., 2012; Sesana et al., 2018; Taylor et al., 2013). Groundwater fluctuates in response to the impact

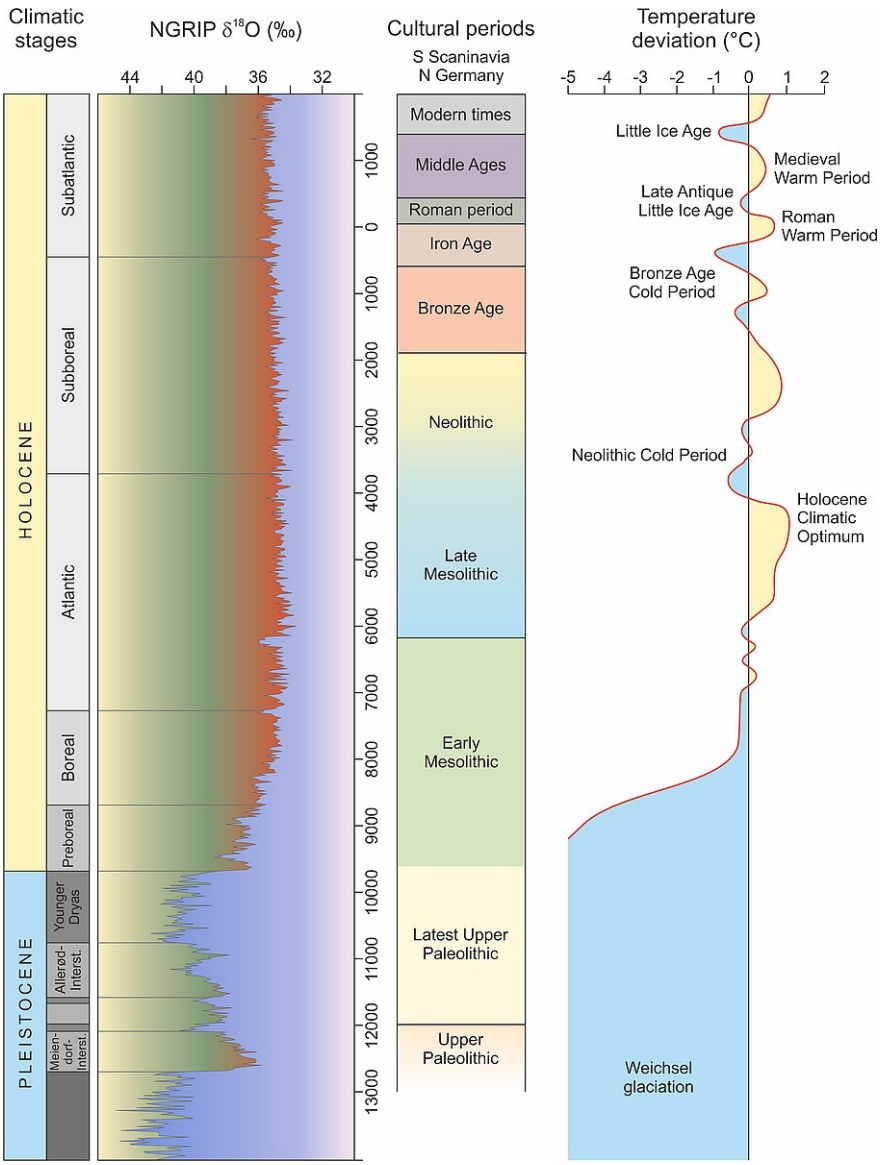

Figure 1.5: Post-glacial development of the climate and prominent climatic extremes in the western hemisphere (Hepp and Terberger, 2023).

caused by physical, environmental, and human behavioral changes. These variations in its levels over time and space have a pattern that can be graphed. The representation would display variants including trends, rise, declines, and seasonality (Box et al., 2015; Lee et al., 2018; Neto et al., 2016; Rosenquist et al., 2010). Conceptually, groundwater levels are registered periodic and aperiodic changes which can be analyzed to derive information on the hydraulic and physical properties of the aquifer and rock sequence (Kottegoda, 1980; Rosenquist et al., 2010; Xie et al., 2021).

A periodic pattern represents a phenomenon that repeats at a specific time interval. They have amplitude, frequency, and phase behaviors. They repeatedly influence aquifer levels at different periods from sub-daily to higher periods. The boundary between short and long-term groundwater events may be subjective, however, it is common to classify annual events (occur once a

year) with a period of 365 days and a frequency of 0.00274 cycles per day as long-period events while sub-diel events as short period events (Neto et al., 2016). Groundwater levels are spatiotemporal indicators of the state of the aquifer systems. They provide information on the changes in the aquifer water levels (Larocque et al., 1998; Neto et al., 2016).Groundwater response to climate change and environmental variability poses a major threat to the sustainability of heritage buildings and sites (Figure 1.5). Heritage buildings and structures are now faced with the menace of groundwater ingress due to increasing variability in the conditions that predate their construction and emplacement. For example, in the Saint Mena area of Egypt, rising groundwater levels attributed to irrigation have led to reported subsurface flooding of heritage buildings and the decay of foundations and walls. This scenario has resulted in the eventual collapse and loss of valuable historical buildings.

Mitigation measures deployed such pumping were temporal and not cost-effective as many boreholes and wells would be required to be installed with pumps and powered. The fate of the building rests on an anticipated adequate protection measure. However, the Temple of the Rising Sun was saved from total obliteration by the destructive effect of groundwater by a global campaign spearheaded by UNESCO. The Abu Simbel temples were relocated to higher ground to escape the ingression at a heavy cost (Carruthers, 2023; Hassan, 2007). The Angkor temples (figure 1.3) in Cambodia (Chen et al., 2017), the Taj Mahal in India (Atwood, 2002; Lal, 2018), the Wooden Bridge in China (Cao et al., 2021), and the Bryggen archaeological site in Norway are renounced heritage sites facing one environmental challenge or the other.

The report of rising and fluctuating groundwater levels and its deterioration of historical, cultural, and archaeological sites, buildings, and monuments calls for cost-effective protective measures to be put in place. For example, a mitigation measure can be implemented through dewatering programs via traditional pumping to lower the water levels. However, it implies wells will eventually have to be drilled and powered with solar energy or electricity, which seems inefficient and unsustainable. On the other hand, if human activities are halted, groundwater will continue to flow and respond to natural fluctuations cycles such as seasonal recharge, changes in barometric pressure, strain by Earth tides, and other inducements.

Hence, a method for monitoring and characterization, that is both passive and respects the principle of minimum intervention is proposed for evaluating hydraulic properties of the subsurface sequence beneath the heritage structures and sites towards its protection from groundwater inva-

sion. The resulting parameters will be viable as input in the implementation of heritage buildings and site restoration projects and the design of heritage sustenance devices. First, it requires an understanding of the prevailing hydrological process in the area and the response of the groundwater systems, leading to the fluctuations. The passive characterization of the hydraulic and mechanical properties of the subsurface sequence to evaluate its permeability and transmissivity. The aquifer evaluation test is a classic approach to estimating hydraulic properties of transmissivity and specific storage. It is widely used following the formulation of mathematical methods (Domenico and Schwartz, 1998; Fetter, 2001). The approach tends to be invasive and works well in low to moderately permeable geological settings. In high permeability formations where the drawdown is small, and occurs for a few minutes, recovering almost to its initial level, immediately after the pumping stop. In such settings, pumping tests to assess aquifer properties are difficult to execute (e.g. Cutillo and Bredehoeft, 2011; Kuang et al., 2020; Sun et al., 2019).

1.2.1 Groundwater levels and warming scenarios in Europe

The long-term inducement of the climate or global climate change (GCC), has a wide range of impacts on economic and socio-cultural activities, among its many effects on life and resources. Built heritage structures and materials as components of the physical environment are equally exposed to these variabilities in climatic conditions. Rising temperatures and fluctuations in precipitation are some of the physical changes affecting the natural systems (ACIA, 2004) and causing physical and chemical damage to archaeological sites and materials (Hollesen et al., 2018).

Groundwater is a global resource whose availability affects many domestic, industrial, agricultural, and cultural activities. The effects of changes in climatic and environmental conditions affect its availability and cause spatial and temporal variations in its quantity.

Jing et al. (2020), assessed the impact of climate change on terrestrial groundwater cycles using the Groundwater Quantity and Travels Time Distribution (TTD) method. They evaluated the response of groundwater to different levels of warming. The models produced with temperatures of 1.5, 2.0, and 3.0 °C indicated a general increase in water levels with increasing temperatures, hence, they asserted that the global warming effect relates to the rising water levels in the subsurface in the European German territory.

Their results were consistent with the reconstructed groundwater warming models of Tegel et al. (2020), using proxy palaeoclimate data, the tree-ring chronology. The reconstructed ground-

water warming models by Tegel *et al.* concerned the Roman, Medieval, and Modern warming periods, with the first two warming events being natural and the most recent event being human-induced. The models by Tegel *et al.* were the converse for cold period reconstructed groundwater levels for the Little Antique Ice Age and Little Ice Age period. The variability of groundwater in the site in response to climate and environmental conditions is discussed in section 2.4.4.

1.3 Challenges, objectives, and proposed methodology

Field-based heritage properties and sites are not immune to the impact of climatic and environmental changes. These changes in the prevailing climatic and environmental conditions are caused by both natural and anthropogenic factors or inducements that influence the dynamics of temperature, pressure, precipitation, and groundwater, among others (Beer and Seither, 2015; Bonazza and Sardella, 2023; Harper, 2016; Hollesen et al., 2016; Sabbioni et al., 2007; Sardella et al., 2020; Sesana et al., 2018, 2021; Spane, 2002; Taylor et al., 2013).

In light of the current global climate change events referred to as global warming with its associated extreme events such as torrential rainfall, heat waves, surface water, and groundwater flooding which have a variety of impacts on the safety, stability, and sustainability of the built heritage and archaeological materials, structures and sites as it affects all physical environments (e.g. Bonazza and Sardella, 2023; Hollesen et al., 2016, 2018; Sabbioni et al., 2007; Sesana et al., 2018).

The Gallo-Roman archaeological site at Genainville (see e.g. Cholet and Delestre, 1992; Cholet et al., 1996; Mitard, 1983, 1984; Mitard et al., 1993; Orième, 1937; Vermeersch and Chupin, 2012), is a site with 2^{rd} century CE historic buildings that are deteriorating due to the effects of rising groundwater levels (Liu et al., 2016). The phenomena of rising and fluctuating groundwater levels and their intermittent intrusion into heritage buildings and sites, at various scales with a reported record of flooding events, has been hypothesized as an accelerator of site abandonment by the Gallo-Romans (see e.g. BURGEAP, 1992). These phenomena are currently challenging archaeological investigations, conservation drive, and the sustainability of the structures exposed to groundwater. The impact is the gradual weakening of the cohesion of the masonry at the archaeological site, resulting in its deterioration (Liu et al., 2016). The archaeological and historical development of the site is discussed in chapter 2.

The threat posed by the influx of groundwater into heritage sites, buildings, and structures has led to the deterioration and eventual loss of buildings and structures on the site. Some heritage struc-

tures have been relocated at a huge financial and material cost, to the detriment of the structure-site relationship and historical affinity (e.g. UNESCO report on the Nubian temples or monuments).

The destruction caused by groundwater is traditionally mitigated by dewatering schemes. Traditional methods of monitoring changes in groundwater levels are both invasive and expensive to deploy and maintain. They do not address the immediate and long-term changes and causes of groundwater level variations. Rather, they help to detect changes in water levels and could lead to interventions that result in dewatering, traditionally by pumping. The dewatering schemes do not take into account the temporal and spatial influences caused by natural and anthropogenic events triggered by climatic and environmental variability.

The Genainville site, therefore represents a pilot site for testing methods and models for non-destructive use and environmental substainability. It presents an on-site laboratory for the application of hydrogeological and geophysical ideas and concepts in an archaeological setting for the temporal and spatial characterization of the subsurface properties and groundwater dynamics.

This study presents a cost-effective method for assessing groundwater response to natural and anthropogenic phenomena, which can be used to monitor fluctuations and rises. The method also assesses aquifer properties from the response of the water levels to the stimuli.

Figures 1.6 and 1.7 detail the data-model relationship from the active and passive measurements, the end-point objectives of which are to investigate the drivers of the changes in the water levels and to constrain the influences or forcings in time and frequency as well as to confirm or not the presence of artifacts in the subsurface at the site. The investigation will also focus on understanding the saturation state of the subsurface sequences at the site.

The proposed methodology begins by obtaining a finer image of the subsurface for a higher resolution of structures or features, which will serve as a guide for prospecting for cultural and historical artefacts and anomalies, in addition to groundwater aquifers. With the finer models of the subsurface, the natural electric field monitoring and thermal experiments will be followed to assess the saturation characteristics. This will involve assessing the flow structures and responses of the sequences to natural electrical and thermal fields for the characteristics of fluid and lithological properties. Afterward, classic and harmonic pumping tests will be performed for aquifer

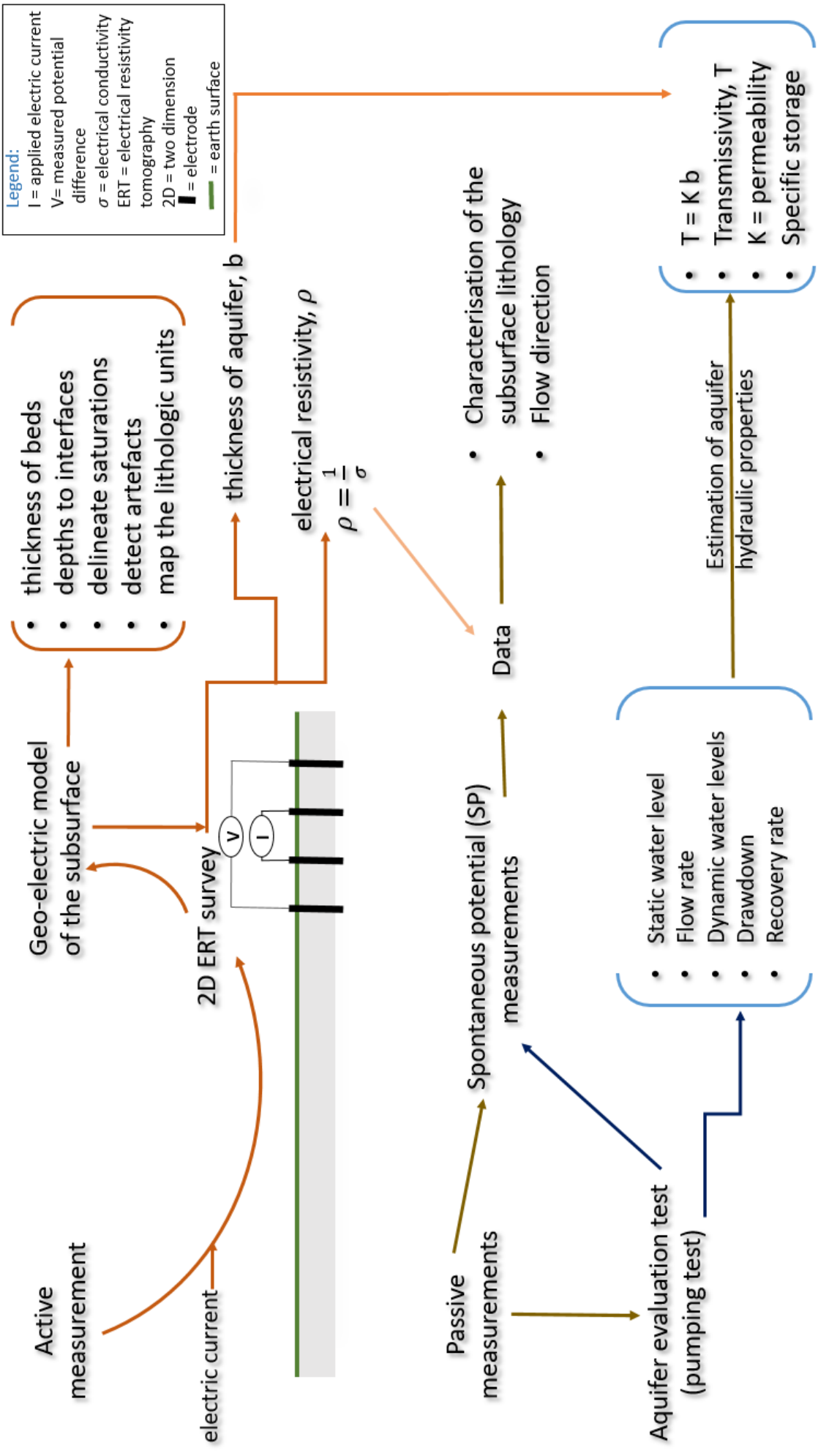

Figure 1.6: The method proposed for the investigation comprises active and passive data measurements. The representation shows the link of information and field procedure to model inputs and anticipated outcomes.

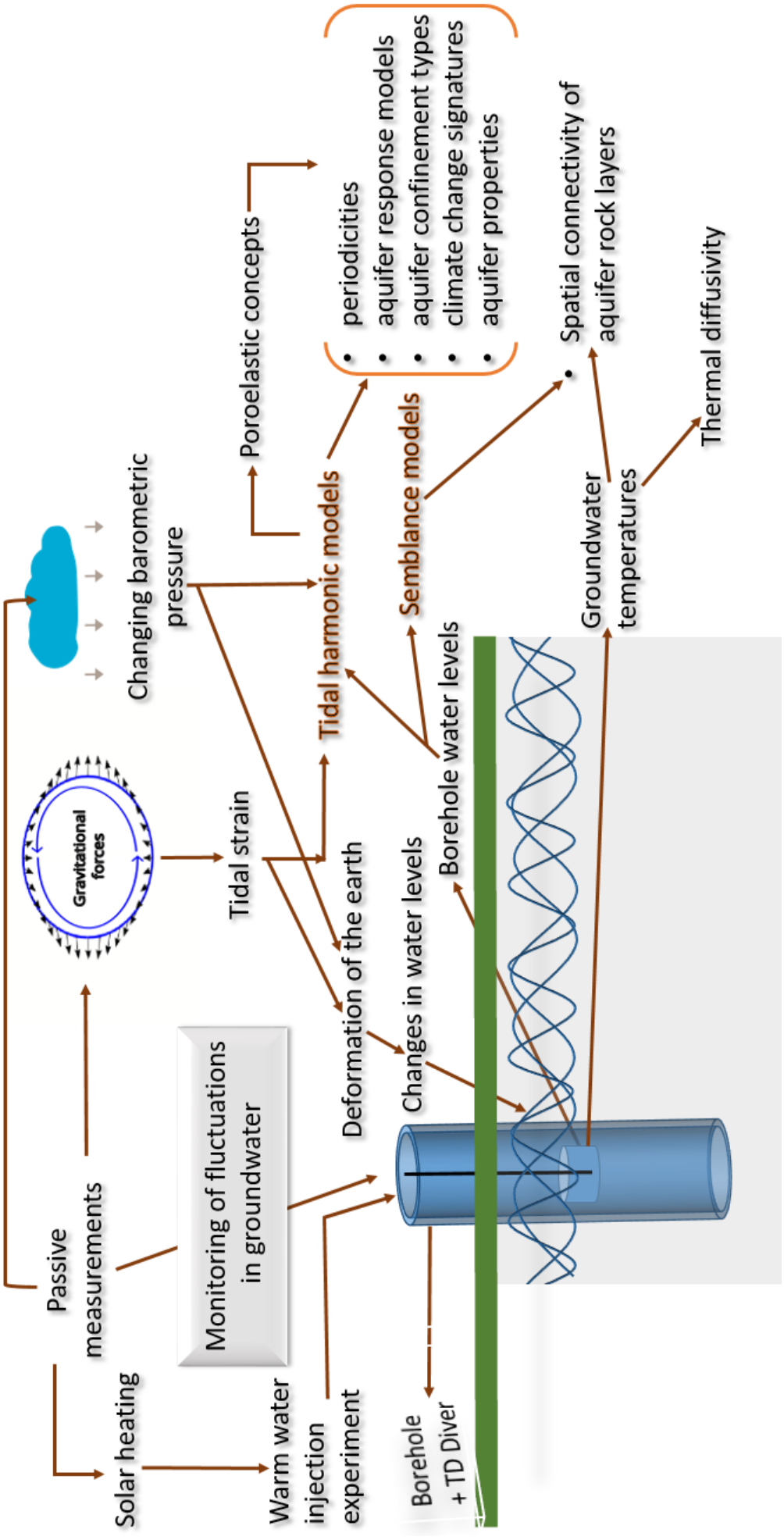

Figure 1.7: This representation of the proposed method of investigation details the second phase of the passive measurements with information on the data-model relations to the outcome.

hydraulic properties to resolve the question regarding the permeability of the subsurface materials.

Traditional Discrete Fourier Transform (DFT) is then performed on the time series data including the water pressure, modeled Earth tides, and barometric pressure to extract the periodic signals (signature of inducements) at established or specified frequencies. The mechanical and hydraulic properties of the subsurface are then computed from the amplitude response method. Each time series data is then decomposed with SSA into components and analyzed based on its period and amplitude response. The advantage of introducing, incorporating, or using the SSA method (in this research) is the ability to separate the composite signal into individual components, which allows the identification of specific inducements and their examination. To achieve the outlined objectives of this research. The thesis is structured into seven chapters.

The introductory chapter outlines the contextual essence of the research. The impact of environmental and climatic variability on heritage properties and sites as well as the objectives of this research.

The second chapter contains the description of the pilot site derived from the compilation of relevant and accessible historical and archaeological information as well as field data acquired at the site. Details of the geometry and archaeological prospection of the remains of the sanctuary, theatre (or amphitheater), secondary buildings, and the site are included. Geological, hydrological, and hydrogeological information is reported from the available literature and the analysis of a digital elevation model covering the study area and its surroundings.

The third chapter focuses on the search for cultural and geological anomalies using finer images of the subsurface provided by electrical resistivity tomography. The survey was conducted along three profile lines. A background information explaining the essence and motivation precedes the description and investigation of each profile. An inverted electrical resistivity model of the subsurface beneath each survey line was produced from the observed data. The robust inversion method and cell-based discretization of the subsurface essentially discriminate beds and features for ready identifications of geological, hydrogeological, and archaeological materials.

The fourth chapter presents the analysis and results of the field experiments carried out on the site: natural electric field, thermal tracing, and classical and harmonic aquifer evaluation tests. The field procedure deployed to acquire each data set is carefully explained. This is followed by

a qualitative description of each data set with plots to highlight observed patterns and behaviors and a discussion of preliminary results and field situations encountered.

Chapter five contains analyses of the measured water pressure, barometric pressure, and theoretically computed Earth tides using various signal analysis methods combined to a poroelasticity approach to determine aquifer characteristics. In the sixth chapter, the main findings are discussed and corroborated with literature to substantiate the results. Each point is mentioned and reviewed with relevant references.

The seventh chapter contains a general discussion that recapitulates the main findings of the research. The perspectives and recommendations suggested areas where further investigations can be carried out to strengthen or complement the obtained outcome.

The appendix contains information and tables of results produced and cited in the chapters. Some of the computer programs used during the data analysis are also included. A bibliography of the cited works of literature preceded the appendix.

CHAPTER 2

Description of the pilot site

2.1 Introduction

The Genainville archaeological site is herein considered a pilot site due to certain important aspects. First, the site is a historic location with rich collections of historical materials that motivated the government to grant it the status of a national monument of interest.

Secondly, groundwater springs into the built structures: the temple building, the baths, and the basins, to provide naturally sourced water for different uses including religious cleansing, conceived healing powers, and thermal therapy. Conceptually, a shallow aquifer medium is conceived due to the continuous presence of water reaching near the Earth's surface as observed in the baths.

Thirdly, there is the presence of buried artifacts at this site with a shallow aquifer medium. Fourthly, the interaction of water with artifacts and the standing historic ruins caused by rising water levels threatens the conservation drive and the need to protect the site and materials for posterity.

Hence, the site is chosen as it will allow testing of new and existing methods and models in geophysics, hydrogeology, hydrology, and other related science and engineering concepts to solve the deterioration of the site and built structures.

In this chapter, the details of the geographical description of the site chosen for testing the proposed methods are provided in section 2.2 with historical information that covered its discovery

and cultural significance in section 2.3; and tables A.1, A.2 and A.3 of appendix A.1. The major remains at the site are described in subsections 2.3.1, 2.3.2 and 2.3.3. The hydrological and geological information is contained in section 2.4. The age-long relationship of the site with water is highlighted in subsections 2.3.2, 2.4.1, 2.4.2 and 2.4.3. The global effect of climate and environmental variability on the groundwater at the site is discussed in the literature in subsection 2.4.3.

2.2 The study area

The Gallo-roman sanctuary site is an archaeological site located at Genainville near Paris in France (Figure 2.1 and 2.2). Genainville is a village in the French Vexin territory of northwestern France. The Vexin or French Vexin area (as it is called today) was inhabited by the Gaulish tribe before its conquest between 58 - 50 BC by Julius Cesar, of the now defunct Roman Empire. Gaul was the name given to Western Europe which included the area known today as France, when it was a province of Rome. Gaul was partitioned for administrative convenience into three parts: *Aquitania*, *Belgica* and *Gallia Celtia*. The name Vexin originated from Veliocasses, the Celtic inhabitants of the Seine River valley, on the border between the ancient Celtic Gaul and Belgium Gaul territories (e.g. Barrière, 2020). The archaeological site in Genainville is situated between Paris, the ancient capital of the Gaul tribe, and Rouen, the former capital of Veliocasses.

The post-conquest period was followed by the Romanisation of the Gaulish communities, which included the adoption of the Roman language and culture and the intermarriages that ensued from the mixing. The Gallo-Romans are persons born in the period succeeding the conquest and the ensuing civilization. They are offsprings of a mixture of cultures and religious practices that included the worship of Roman and Celtic deities. The Gallo-Roman civilization flourished between the first and fourth centuries and left behind rich collections of heritage materials and structures, great arenas, and edifices. The Romanized culture had bequeathed to modern civilization characteristic architectural works, buildings, walls, and surfaces embellished with awesome mosaics, paintings, and artworks. Typical settlement patterns and building styles portray unique attributes such as royalty, fortification, cultural aesthetics, treasures, polytheism, and resourcefulness of the ancient inhabitants.

The archaeological site is an area bound by longitude 1.70 - 1.90°E and latitude 49.09 - 49.14°N (Figures 2.1 and 2.2). It is located in a natural horse-shoe-shaped valley found below the Vexin plateau (Figure 2.3). The valley has an approximate width of 130 meters at its base and a

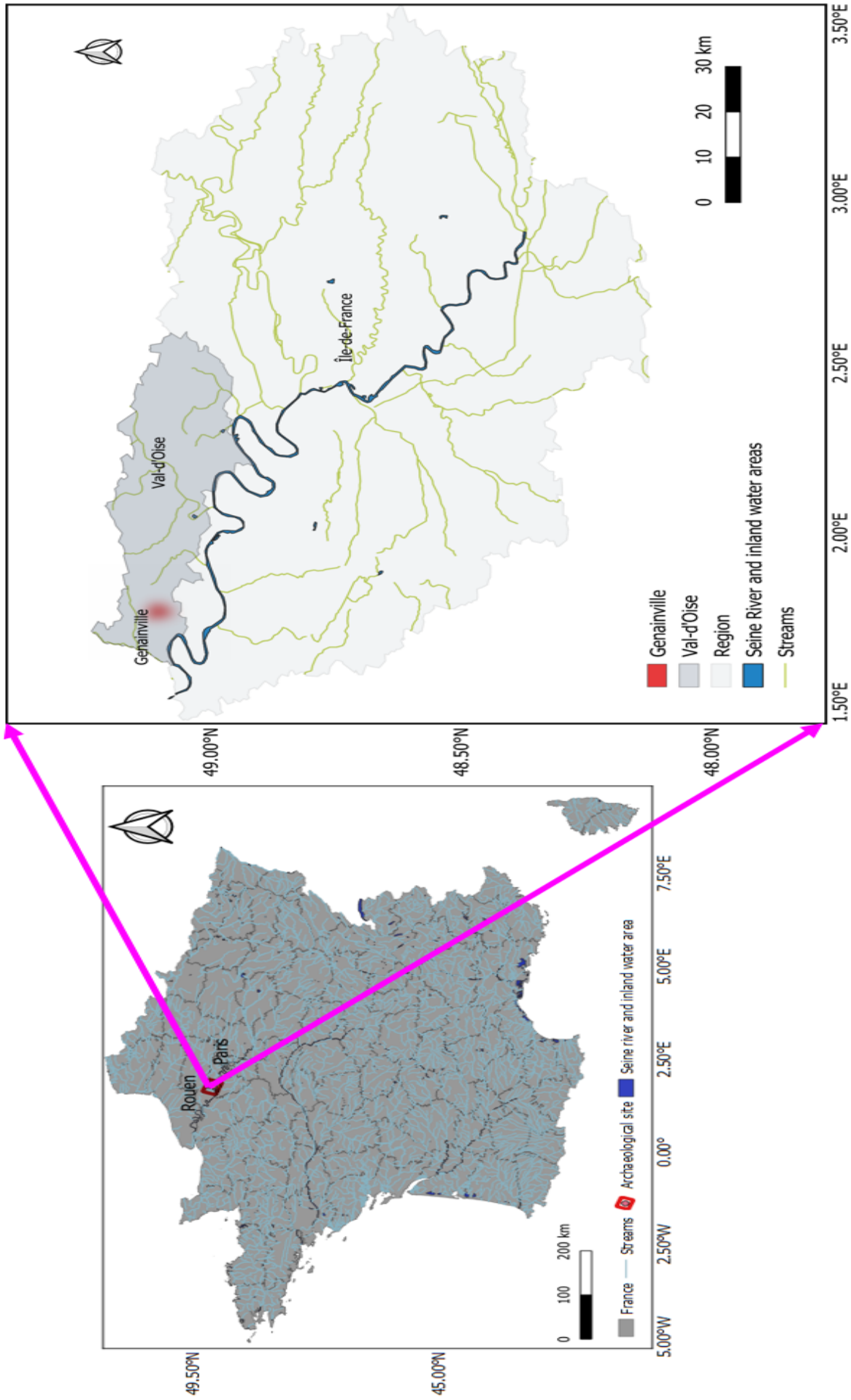

Figure 2.1: The location of Genainville in Val d'Oise Community.

minimum surface length of 400 meters. The site is 1500 meters east of Genainville city. It was a sanctuary site used by the Gallo-Romans for worship and habitation before it was abandoned in the 5^{th} century AD (Mitard et al., 1993). The ancient settlement now consists of vestiges and relics of a sacred temple area, an amphitheater, a nymphaeum (consisting of a main basin and two annex basins) located south of the temple, secondary buildings for lodging and areas for religious, aesthetic, and social activities. The temple area is more conveniently called the Sacred Area. Lit-

Figure 2.2: The Gallo-roman sanctuary site, *Les Vaux de la Celle*, Genainville

.

erature also contained reports of mining activities in the site mainly as an in-situ source of Lutetian Limestone and Bartonian clay for building and fabrication of earthen materials in the era ensuing the occupation by the romanized Gauls (Garnier and Dessevre, 2004; Garnier, 2004). It may not be convenient to suggest that the shoe-shaped valley could have been fashioned solely by nature without human interference. As it is likely that the weak zones or fracture lines were exploited for readily available clay and limestone products, and mined before and or after the abandonment that preceded the discovery.

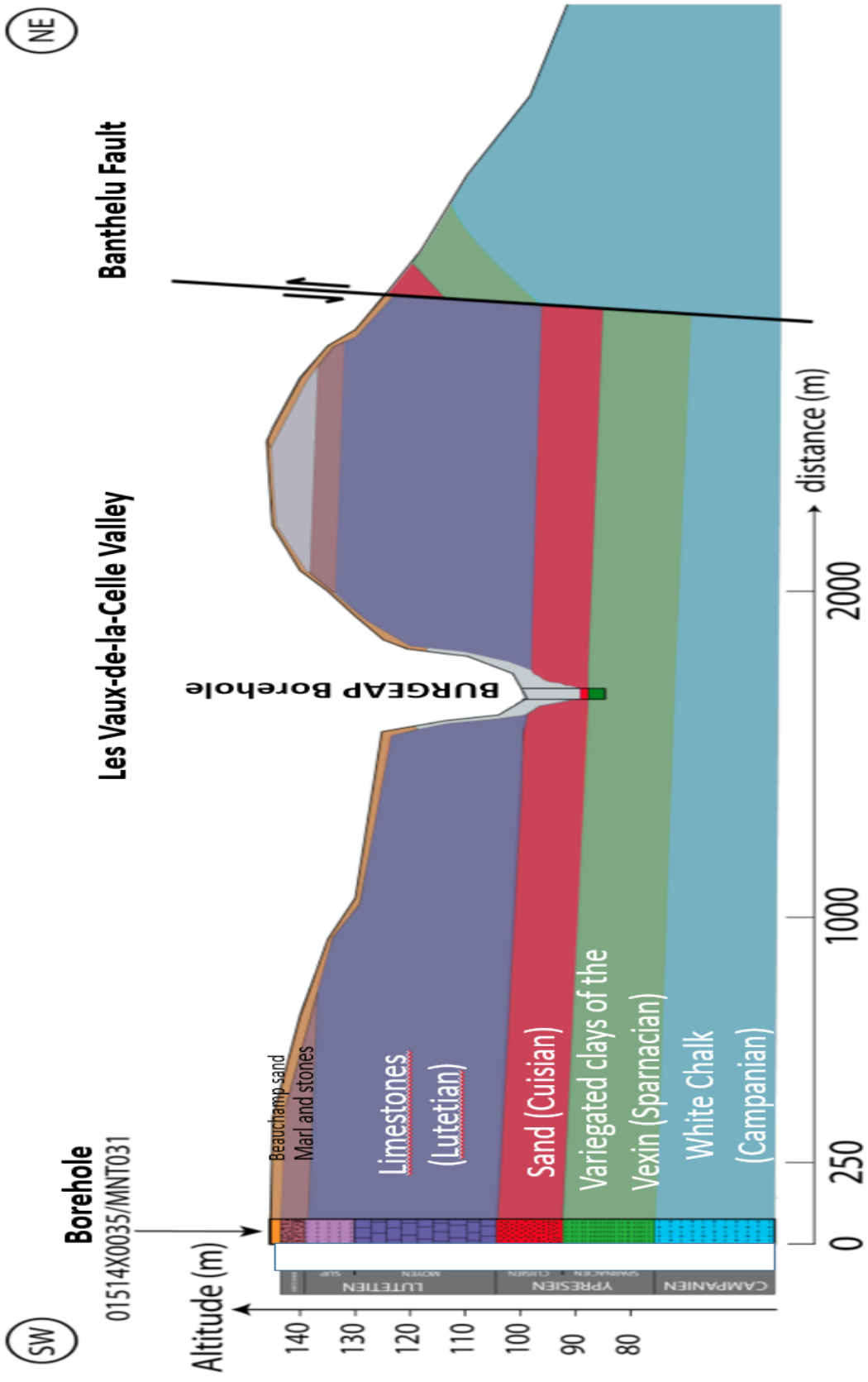

Figure 2.3: The geological section of the site and the surrounding areas, after BURGEAP (1992) and Fores (2013).

2.3 The discovery and archaeological excavations

The valley with its form of a horse-shoe was locally thought to contain the remains of a castle-like building, *Château Bicêtre*, partially immersed in its rubble. The idea persisted until it was overturned by the view expressed by a scholar, Victor Le Ronne, around 1900 as the relics of an *Ancient Arena* buried in the rubble.

An architect called Pierre Orième is credited with unearthing the ruins of a structure, buried in rubbles in a valley near Genainville. The structure was later identified as the remains of a theater following the first series of excavations he led between 1935 and 1936 (Brunet-Gaston, 2011). Orième named the structure *Le Pavillon* (Orième, 1937). Following the excavations from the rubble of artifacts such as sculptures, coinages, and tools used by the former residents of the site by Architect Orième and his team. Ceramics and metallic objects dated to the Bronze Age were also recovered (e.g. Barrière et al., 2019; Mille, 2019; Mitard, 1982; Mitard et al., 1993).

Three built sites were identified though still partially buried in the rubble: a residential building site, an arena for spectacles and events, and a building near the water source in the lower section of the valley (Orième, 1937). The team observed that the lower part of the valley was covered with thick colluvium largely consisting of rubble of mortar, marbles, and bricks from the destroyed materials, built structures, and weathering of the carbonate rocks in the Vexin plateau, mainly from the Lutetian limestone (Figure 2.4). The search was short-lived as it was abandoned in 1948 as

Figure 2.4: The sacred area at the commencement of excavations in 1967 (the picture shows the remains of the temple filled with rubble). The photograph was extracted from Barrière (2020).

the team became discouraged at the sight of the thick colluvium and other Earth materials that covered the buildings. The recoveries from initial excavations turned out to be impressive and promising, therefore, it attracted the government's attention.

The government through its Department of Antiquities exercises control over the site and regulates research, learning, and tourism with legislative frameworks, monitoring, and curative services. Three laws are significant to the continuity and promotion of archaeological, geoscientific, and other activities at the site. First, the French government law of *9 August 1941* that classified the site as "*monument historique*" and the second law, allowed the subsequent *acquisition of a land mass of about 5.5 hectares* to secure the archaeological materials and the vicinity of the valley was effected on 23 June 1981 (Barrière, 2020). About 5.0 hectares of the site is fenced off with barbed wire to prevent intrusion or trespassing, and restricted to the public. The secured area enclosed the ruins and the valley morphology from its base to the pediments, scalp or slope, and parts of the surrounding plateau. Access is granted to researchers and students with approved authorization, while the site is open to the public for events or special days such as *Journées Européennes du Patrimoine*, *Journées Nationales de l'Archéologie* and *Semaine de l'Histoire et de l'Archéologie*. Thirdly, the 5 January 1983 law raised the status of the site to a *major national location* of interest for enhancement.

The subsequent law in 1988 handed the management of the site and the supervision of archaeological and educational activities to the region (il-de-France). The enactment in 1988 recognized the site as a *rural sanctuary* and from 1989, the department of culture for the region directed the day-to-day workings at the site. The recovered movable artifacts and vestiges are now preserved in the city museum for archaeology known as *Musée Archéologique Départemental du Val-d'Oise* (MADVO) located in Guiry-en-Vexin. It is important to note that the proprietorship of the vestiges and ruins was fully taken over by the State in 1946 after over ten years of its management by Architect Orième, who acquired the land and directed archaeological operations in the land. Additional vestiges and relics were unearthed in two archaeological campaigns that took place in 1947 and 1948. Afterward, there was a momentarily halt to prospections, until Pierre-Henri Mitard and his team restarted in year 1960 the archaeological search for buried artifacts and recovery of the ruins (Figures 2.4 and 2.5). Mitard led the team from the Ancient Archaeology Group of the Touring Club of France to carry out the archaeological investigations and contributed to the establishment of the city Museum where the movable artifacts are kept (Figure 2.6).

Figure 2.5: Southeast view of the temple ruins taken in 1973 (Mitard et al., 1993)

.

Pierre-Henri Mitard, an archaeologist and a researcher with the National Centre for Scientific Research was responsible for organizing annual archaeological activities including classic trenching, digging, and drilling to uncover buried cultural and historical artifacts. An engagement, he undertook from 1960 to 1991 with a rich collection of artifacts excavated, identified, documented, and archived.

A temple with two *cellae* dedicated to two Roman deities, Mercury and Rosmerta was unearthed at the lower section of the valley (Figure 2.7). The temple is associated with a *nymphaeum* and baths. The temple site comprising the sanctuary building and its facade, the *numphaeum*, baths, and supporting buildings is called the *Sacred Area*. It had been reported that the temple completed in 2^{nd} Century was built on a natural water source that springs to feed the *nymphaeum* and baths to fountain the altars built for the deities (Cholet and Delestre, 1992; Cholet et al., 1996; Mitard, 1984; Mitard et al., 1993). The historical and archaeological events at the site are briefly summarized in tables A.1, A.2 and A.3 on pages 221, 222 and 223 in appendix A.1. The details of the structures and hydrological considerations are reviewed in subsections 2.3.1, 2.3.2, 2.3.3, 2.4.1, and 2.4.2.

Figure 2.6: Some recovered historic artifacts kept at the city museum (*Musée Archéologique Départemental du Val-d'Oise*) situated at Guiry-en-Vexin

.

Figure 2.7: Some recovered Gallo-roman sculptures

.

2.3.1 The temple building

At the sacred area, a *fanum* type of temple, typical of Celtic temples of the Roman Empire was unearthed (Mitard, 1983). About 5 m of the temple ruin is still standing after periods of excavations and curative works by Mitard and his team (Figure 2.4). The temple was built with bricks, mortar, and limestone (of *Lutetian* age) on a foundation constructed with stones and rubbles in the 2^{nd} Century AD. The square-shaped temple measures 28 m on each side.

It consists of two *cellae* measuring 27.20 m x 27.60 m (Figure 2.8). The *Cellae* is recognized as Northern *Celle* and the Southern *Celle*. Each *celle* housed an altar with an effigy of a deity. One *celle* was dedicated to *Mercury*, the Roman god of good fortune and luck, fertility, wealth, and thievery. The other *celle* to a consort, *Rosmerta*, the goddess of fertility and abundance. The temple is associated with a *nymphaeum* (a main basin and two annex baths) to its south (Figure 2.8).

The temple building is enclosed by a 111 m x 77 m rectangular *peribolus* and accessible through a facade or more likely a portico to the east via a 35 meters long and 8 meters wide paved walkway that connects the temple with the cultural zone (Mitard, 1984; Mitard et al., 1993; Vermeersch and Chupin, 2012).

A temple with two *cellae* is reported a rare structure in romanized Gaulish territories (Brunet-Gaston, 2011). It is also a model building built on a spring (natural water source). The temple walls were colorful and decorated with *horror vacui* type of art with inscriptions and images showcasing theistic, heroic, or nobility as well as the literary output of the inhabitants. The decor is an art in concordance with the Aristotelian postulate “nature abhors a vacuum”. Also of interest are the adorable collections of lapidary recovered which point to the verse nature of the religious architecture in place. The lapidary collections included finely cut, carved stones, rocks, and precious materials (see e.g. Barrière et al., 2019).

The temple walls were erected with mortar and carbonate rubbles in a layered sequence, with bricks near the surface and at intervals within the layers. The bricks, a seemingly impervious material, alternate the layered rubbles sequences used for the building. Conceptually, the layered mortar-bricks arrangement is a protective measure to preserve the integrity of the structure (e.g. Li et al., 2018). The essence of the alternation as deduced from engineering and masonry viewpoints includes inhibiting groundwater access into the wall structures. The emergence of the water table currently near the Earth’s surface within the sacred area has deflated the envisaged protection

Figure 2.8: The remains of the Temple masonry in petit appareil (rubbles, mortar and bricks), showing what is left of the *Cellae*: the northern *Cella* and the southern *Cella*, as well as the baths located south of the ruins and paved ancient road that leads to the cultural zone.

against groundwater ingress (Liu et al., 2016). Classical archeological investigations and historical reconstruction are also threatened by the rising groundwater levels owning to weakening wall structures and vestiges (Liu et al., 2016).

2.3.2 Nympheaum

At the Southern end of the sanctuary building, the Gallo-Roman craftsmen constructed three basins that served as baths. The three basins consist of a main basin and two annex basins with one basin located to the west and the other to the east of the main basin herein referred to as the *nymphaeum* (Cholet and Delestre, 1992; Cholet et al., 1996; Mitard, 1984; Mitard et al., 1993). The basins are lined at the base with a *Corroi* (a mixture of clay and silica (from sand)), to function as an impervious surface to impede the water from being drained. The basin walls were cordoned with meter-thick clay to enhance its stability and to serve as an impediment to water inflow. A wooden pipe built into the walls connects the third basin to the central basin, equally, a similar insertion connects the eastern basin to the main basin. The *Nympheaum* (the main basin) is accessed with stairs from the surface to its base, and two basins annex to the main basin (Figures 2.2 and 2.8).

The nymphaeum is a rectangular basin measuring 5 m x 3 m x 2.35 m, flanked to the east by a smaller basin (2 m x 1.70 m). This second basin located east of the nymphaeum is accessible by stairs and was furnished with a bench. It seems that it was built to intercept the water table and

receive horizontal inflow. The 3^{rd} basin is situated west of the Numpheiaum, measures 7.50 m x 3.30 m x 2.65 m.

The 4^{th} basin, is located 15 m west of the temple. The basins are naturally filled with water all year. The borehole located west of the 3^{rd} basin and south of the 4^{th} basin was drilled at the sacred area to assess the hydraulic and geotechnical properties of the aquifer beds and rock sequence by the BURGEAP group following a commissioned hydrogeological study carried out in 1991 (Figure 2.9). The Gallo-roman baths in Genainville were built to gain from the natural spring for continued wa-

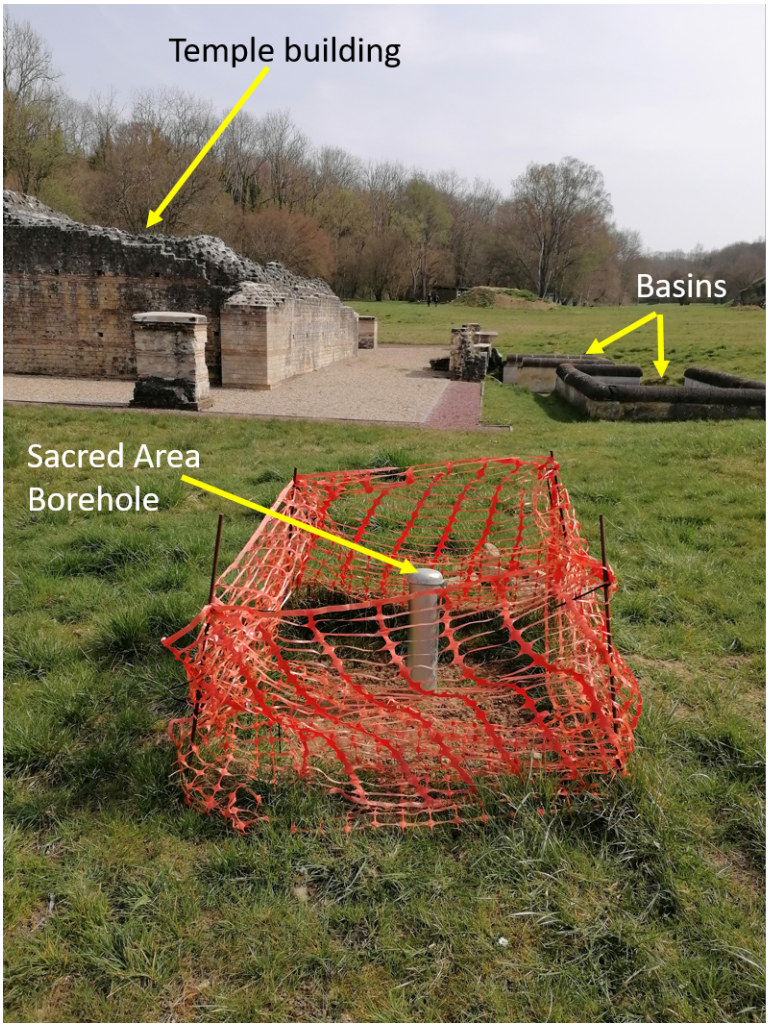

Figure 2.9: Eastern view of the Borehole at the Sacred Area and Gallo-Roman basins

.

ter supply for rituals. They are naturally fed by groundwater from the multilayered aquifer made of sand beds overlaid by coarse limestone sequence followed by the colluvium and the alluvium (Figure 2.10). The weathered units of the Lutetian limestone and Bartonian clay including marl and calcite constitute the near-surface beds and flow all year round.

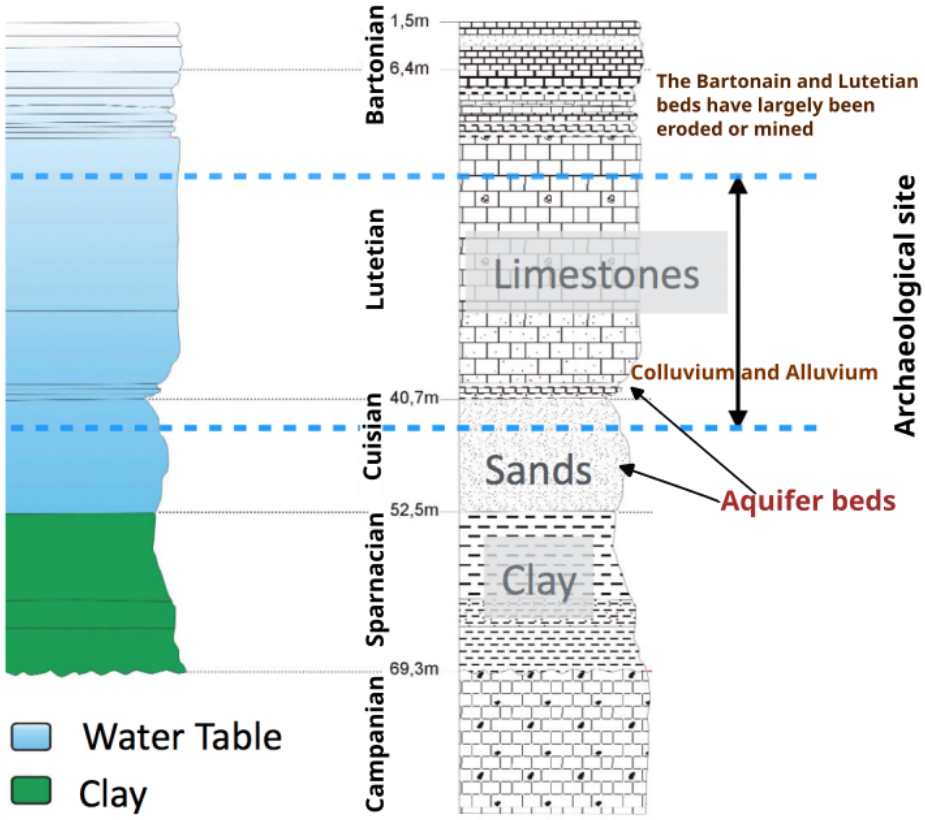

Figure 2.10: The geological log at the site showing the main rock units after Garnier (2004).

2.3.3 The remains of the amphitheater

The site of the ruins initially called the *monument of spectacles* or Arena of Events was first investigated by Orième and his team leading to the unearthing of a theater-like structure (Mitard et al., 1993; Orième, 1937). The structure located southwest of the temple building was unearthed after excavation and found to be semicircular with its southern end built into the hillside. The semicircular ruin was then identified as an *amphitheater* and may be called the theatre in this documentation and thesis (Figure 2.11). It has a diameter of 110 meters and the capacity to receive 4000 -u 8000 spectators, many authors have reported that 5000 - 10000 persons can be accommodated in the unearthed theatre during an event (e.g. Barrière et al., 2019; Barrière, 2020; Brunet-Gaston, 2011).

Theaters and amphitheaters are part of the Gallo-Roman cultural identity. Historically, the theaters and amphitheaters were public viewing places for exhibitions and assemblies. They consist of the concentric seating area (*cevea*), exhibition area (*arena*), and the arched entrances (*vomitorium*). They are communal centers for exhibitions, festivities, and other designated gatherings. It

Figure 2.11: Ongoing archaeological investigations at the entrance of the remains of the Gallo-roman amphitheater.

also serves as a meeting point for information dissemination. In the religious context, theaters, amphitheaters, and arenas are grounds for meetings, congregational worship, and renditions of spiritual songs.

The site amphitheater is envisaged to have functioned as a point for information, devotion, and relaxation for the faithful and visitors and other large gatherings such as pilgrimages. Brunet-Gaston (2011) assessed the motive for the localization of the amphitheater and the temple using the dimensions and patterns of features in the ruins to infer that neither visual nor topography constrained the location of the monuments but proximity to the source. The two monuments, the temple and theatre, are separated or connected by an esplanade, the cultural area.

2.4 Hydrology, water and hydrogeology

This section assesses the water distribution in the area from a watershed viewpoint or perspective and hydrogeological concepts. The variability in the water levels is discussed with a focus on climatic and environmental conditions. Afterward, the flooding events experienced at the site are reported.

2.4.1 Watershed

The watershed for the Gallo-Roman archaeological site and its surroundings is delineated using a digital elevation model (Figure 2.12). A digital elevation model (DEM) is a raster form of the spatial data of elevation, longitude, and latitude values. The data was acquired with survey instruments

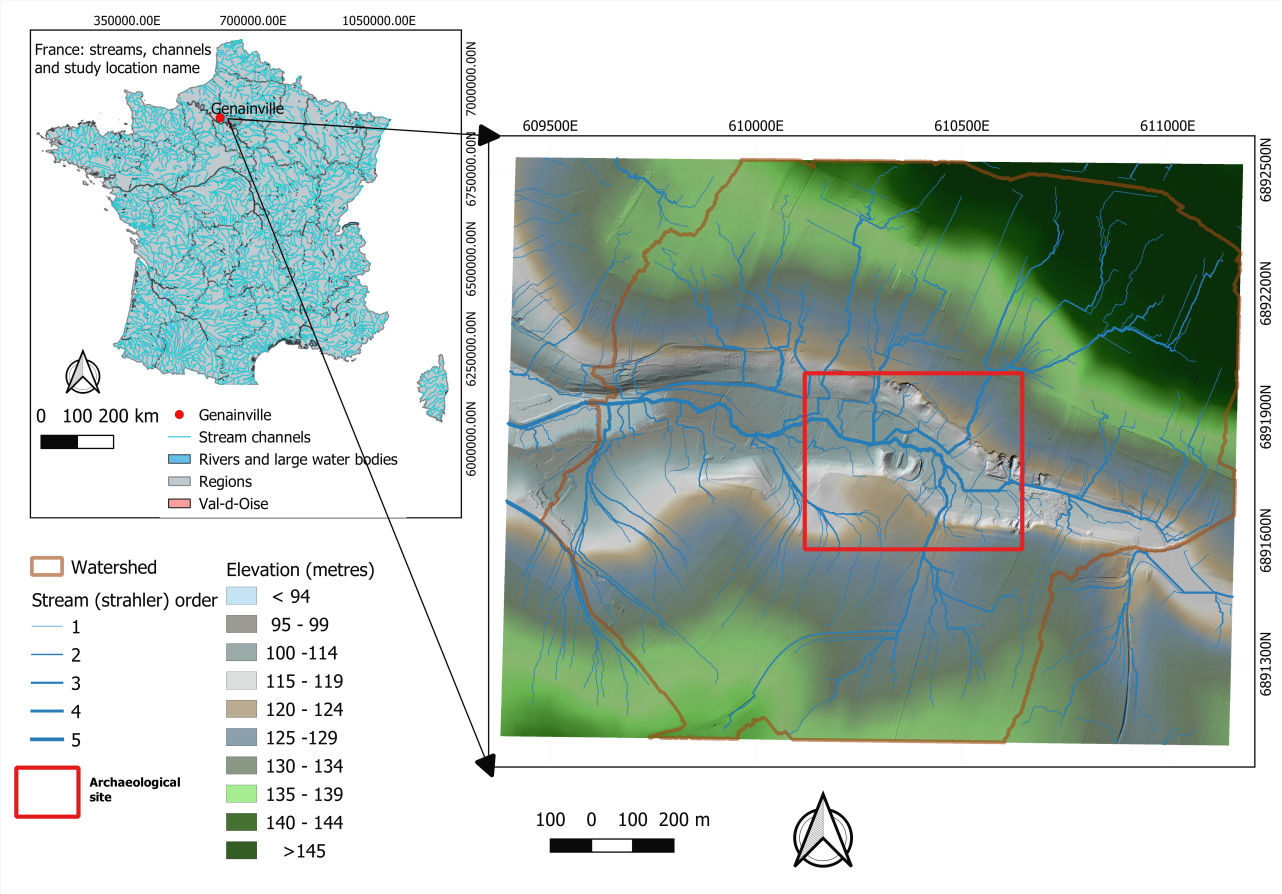

Figure 2.12: The watershed and stream networks in the archaeological site in Genainville and its surroundings.

including a Theodolite and processed from vector to raster data. The raw digital terrain model was provided by Jonhattan Vidal, personnel at the French Ministry of Culture, Paris, and the laboratory UMR 7401 - Archéologies et Sciences de l'Antiquité (ArScAn). The models in figures 2.12 and 2.13 were produced using the open-source QGIS software.

A watershed is an area of land which, because of its topography, receives all incoming precipitation (Edwards et al., 2015). The term incoming precipitations includes runoff following rainfall, snow melt, etc. Watersheds are also called catchment zones or river basins as they are indicators of the direction of flow of runoffs into the main river (stream with highest order) in an area. In other words, a catchment or watershed provides runoff for a stream or river (Edwards et al., 2015;

Healy et al., 2007; Strahler, 1952).

The delineated watershed in figure 2.12 has an area of 1815681.488 m^2. The stream network computed using the method of ordering streams by Strahler (1952) are shown in figure 2.12. From figure 2.12, numerous first, second, and third-order flows originate from the plateau surrounding the site into fourth and fifth-order streams that traverse the site. In practical terms, a watershed determines where water will accumulate and flow. It also provides information about the existence of the differences in elevation.

The precipitation in the Genainville area is rain-dominated. Rainfall is the principal input in the watershed. The precipitation provides the water from which the headwaters begin to flow and give form to other components of the hydrologic cycle. The direction of flow in the watershed ensuing a runoff event is modeled in figure 2.13. The watershed is used to describe the interaction between the landscape and water. From the delineated watershed, the amount of water that flows annually

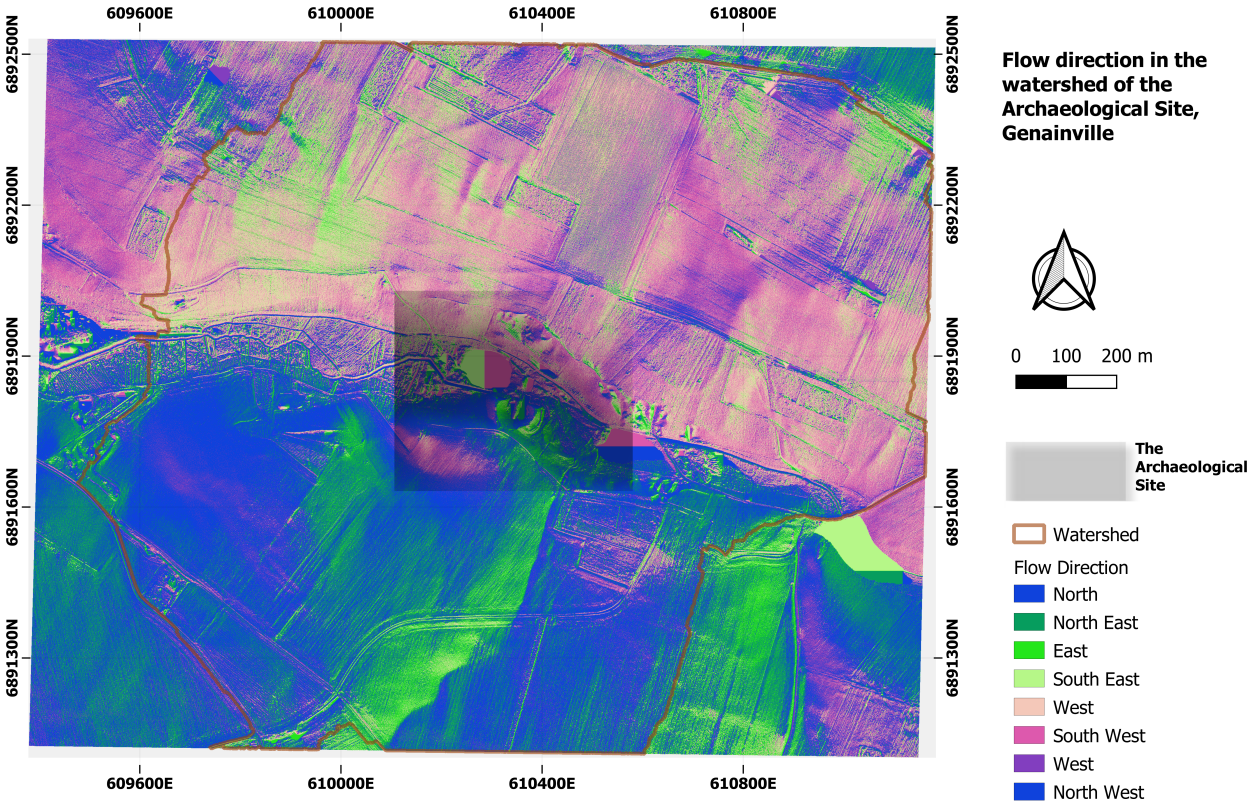

Figure 2.13: A map showing the flow direction of streams in the watershed of the archaeological site in Genainville and its surroundings.

can be estimated using the parameters of the area of the watershed and the annual precipitation.

In 2022, the annual precipitation (rainfall) was 456.00 mm as deduced (computed) from the data of figure 2.14. Thus, the volume of water (rainwater) in the area for the same year is 827 951 m^3. This value is lower than the amount for the previous year 2021, which had an annual rainfall of 816.4 mm and 1, 482, 322 m^3 of water.

The precipitation inputs in the watershed are met by hydrological processes such that rainfall events experience runoff, evapotranspiration, and percolation into the subsurface. Evaporation and transpiration are two processes that reduce water from the total flow and also return moisture to the atmosphere. Some of the water percolating into the subsurface is absorbed by plants, shrubs, and trees and a portion infiltrates to recharge the groundwater.

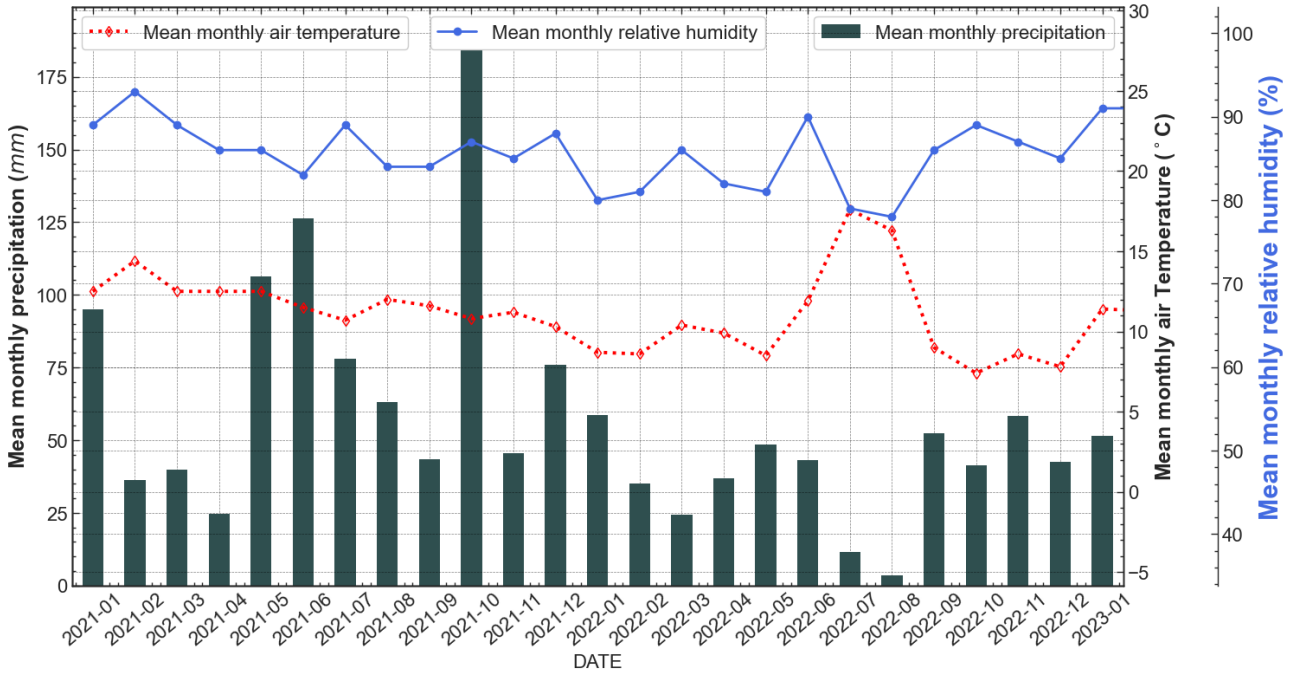

Figure 2.14: Monthly mean precipitation, relative humidity, and air temperature data courtesy of MeteoFrance from it *Wy-dit-Joli-Village* Meteorology Station

The stream channels originate from the headwaters and flow to join other streams at a confluence (junction) to form the next higher order stream (Figure 2.12). Each next higher-order stream is modeled with an increase in size to reflect its role of receiving more flows. Different sub-basins exist within the watershed due to differences in topographic surfaces.

The main direction of water flow from the upland area located north of the archaeological site is southwestwards and pours into the valley, meanwhile the flow from the plateaus south of the valley is directed mainly northeastwards into the valley (Figure 2.13). The lowlands of the valley which houses the buried artifacts and the built heritage structures are faced with receiving run-off

from the upland areas.

The parameters of the hydrological cycle for a watershed can be described using the water budget relation (equation 2.1). The water budget equation is a mathematical expression of the input (precipitation), loss (evapotranspiration), stream flow (runoff), and infiltration in a watershed (Edwards et al., 2015).

$$Q = P - ET \pm \Delta SM \pm \Delta GW - BS \tag{2.1}$$

where Q = stream flow or discharge, P = precipitation, ET = evapotranspiration (sum of evaporation and transpiration from soils, surface-water bodies, and plants), ΔSM = change in soil moisture (that is, water present in all types of soil pores), ΔGW = change in groundwater aquifer storage and BS = groundwater discharge to streams.

$$Q = P - ET \pm \Delta S \tag{2.2}$$

where ΔS = changes in storage = $\Delta SM + \Delta GW$. The components ΔS and ΔGW in equation 2.1 are described as the "change terms" in the water budget equation. They influence the stream flow depending on the period, as they may increase or decrease with time. The influence also depends on how much they change and the direction of change in time (Edwards et al., 2015). The stream flows when the input components exceed the use or output components.

The water budget equation (equation 2.2), expresses three components for water storage in the hydrologic cycle: the atmosphere (precipitation), surface water (stored in streams, ponds, and snow-packs), and subsurface storage (the root zone, the unsaturated zone, and the saturated zone or different geologic units) (Healy et al., 2007). Water stored in the subsurface is commonly extracted through wells, boreholes, and other natural manifestations such as springs.

As shown in the water budget equation, a change in water storage (ΔS), or any component of the water budget equation affects the hydrological cycle.

The changes in water storage, ΔS, as a function of precipitation input, P, and the loss (ET, BS, and Q) or water export term, ΔR, was expressed by Rasmussen and Mote (2007) using equation 2.3.

$$\Delta S = P - \Delta R \tag{2.3}$$

Rasmussen and Mote (2007) presented the expression in equation 2.3 after developing equations 2.4 and 2.5 building it from equation 2.6.

$$\Delta R = P + \Delta B - \frac{\Delta W + \Delta B}{\beta} \tag{2.4}$$

$$\Delta S = \frac{\Delta W + \Delta B}{\beta} - \Delta B \tag{2.5}$$

$$\alpha = -\frac{\Delta W}{\Delta B} \tag{2.6}$$

where α is the barometric efficiency of the aquifer, ΔB is the change in barometric pressure and ΔW is the change in the borehole water level. From equation 2.6, Rasmussen and Mote (2007) showed that barometric pressure influences water stored in the subsurface reservoir (commonly referred to as aquifer). Barometric pressure exerts a loading effect on the aquifer. A change in barometric pressure is proportional to a change in the (aquifer) water level observed (recorded) in the borehole water levels. Studies have shown that natural and anthropogenic factors including barometric pressure and Earth tides influence groundwater levels and the response properties of the aquifer can be derived from changes in the water levels when analyzed (e.g. see Rau et al. (2022); Toll and Rasmussen (2007) and the discussion in chapter 5).

2.4.2 Hydrogeology: aquifers

Hydrogeological studies have indicated that the Temple building and by extension the site rest on a geological sequence made of the *Cuisian* sand and *Lutetian* limestone and regoliths that comprise colluvial and alluvial materials (BURGEAP, 1992; de Lamotte et al., 2022; Garnier, 2004). The main aquifer body comprises the coarse-grained *Lutetian* Limestone and the *Cuisian* sands which are recharge from infiltration and regional flow through the subsurface and fractures considered as offsprings of the regional Banthelu fault zone (see e.g. Figures 2.3 and 2.10).

Hydrological boreholes drilled at different periods in line with the principle of minimum intervention were equipped with piezometers at the Sacred Area, West of the Theatre and the Frontage of the field Store House (built for onsite storage of excavated artifacts, rock cuttings, survey equipment, and materials). The boreholes and other wells are shown in figure 2.15). The Boreholes were drilled by organizations such as the BURGEAP and IGAS groups for hydrological and geological studies (BURGEAP, 1992; Garnier and Dessevre, 2004). Three water boreholes drilled within the site are equipped with probe sensors to simultaneously acquire time-varying water levels and temperature data for this study. The spatial separation, location morphology, and exposure to surface conditions were considered for choosing borehole locations. The objectives include studying aquifer response to forcings (anthropic, natural, Earth and barometric tides). To investigate hydraulic relationships, and structural controls of flow patterns and hydrogeological regimes. The first borehole, designated

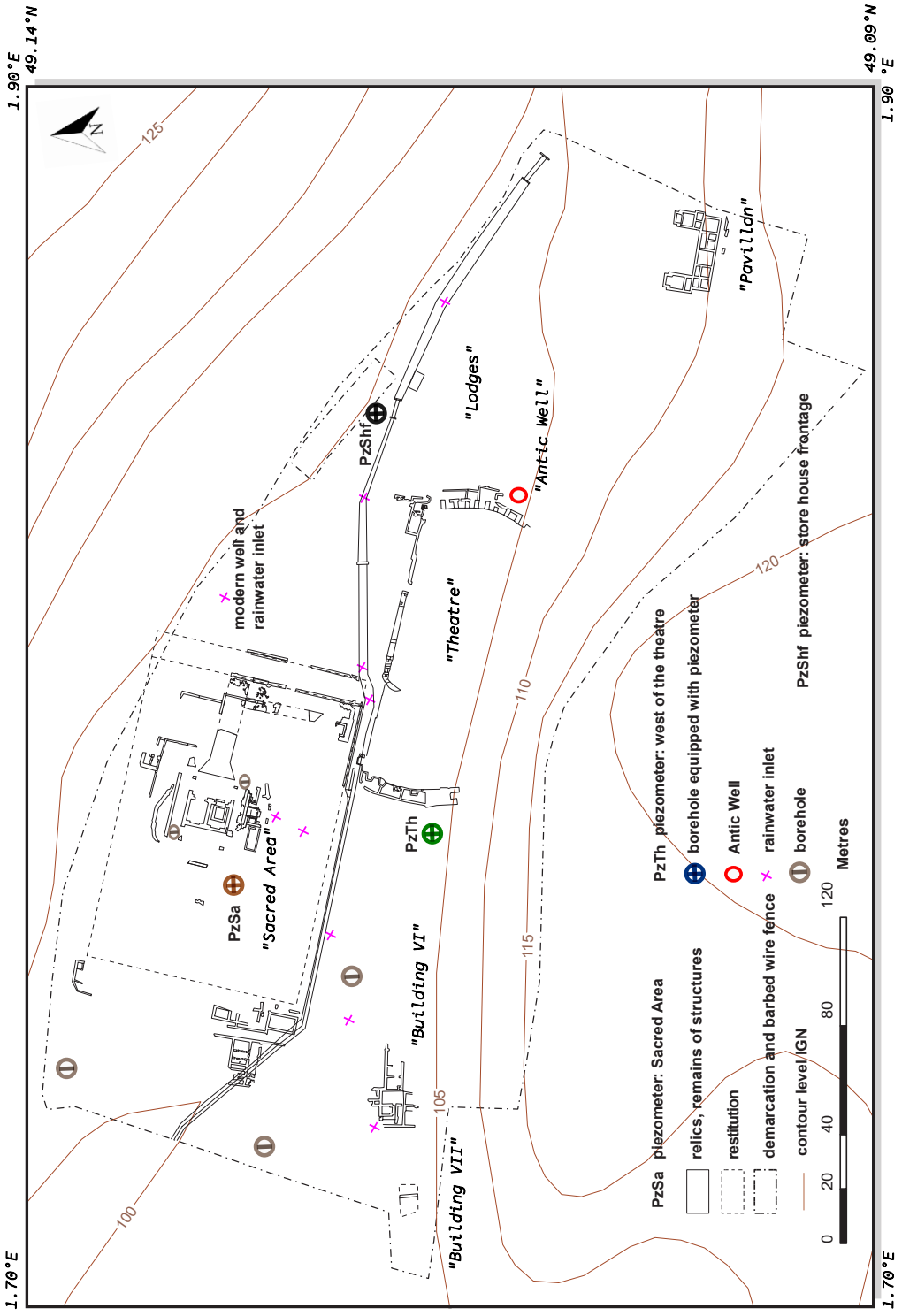

Figure 2.15: Location of boreholes equipped with piezometers at the Sacred Area, Store House Frontage (field building for keeping of survey tools, equipment and storage of excavated relics and artifacts), and West of the Theater respectively designated as *PzSa*, *PzShf* and *PzTh* with other bores and water inlets. The positions of the ruins of the temple, amphitheater and other buildings are shown.

store house borehole (PzShf), is located at the frontage of the Storage building, for excavated relics of rocks, mortars, bricks, and recovered archaeological materials. The PzShf penetrated the elevated area of the site into the Cuisian aquifer beds through the overlying Sparnacian clays, Lutetian limestone and colluvium. The static water levels measured up to 3.16 m. Situated west of the amphitheater is the second borehole, named PzTh. The vertical section of PzTh derived from the lithology log, progressed from the regolith units of recent deposits through the clay intercalations to the Cuisian beds (Garnier, 2004; Garnier and Lemaire, 2006).

The third borehole used in this study was drilled as part of a commissioned hydrogeological study carried out by the BURGEAP group in 1991 (BURGEAP, 1992). The borehole is located west of the sacred area *PzSa*, behind the temple building (Figures 2.9 and 2.15).

The borehole log through the alluvium and colluvium deposits of the valley into the Cuisian aquifer units (Figure 2.16). Its completion parameters are summarized in table 2.1. Time series of ground-

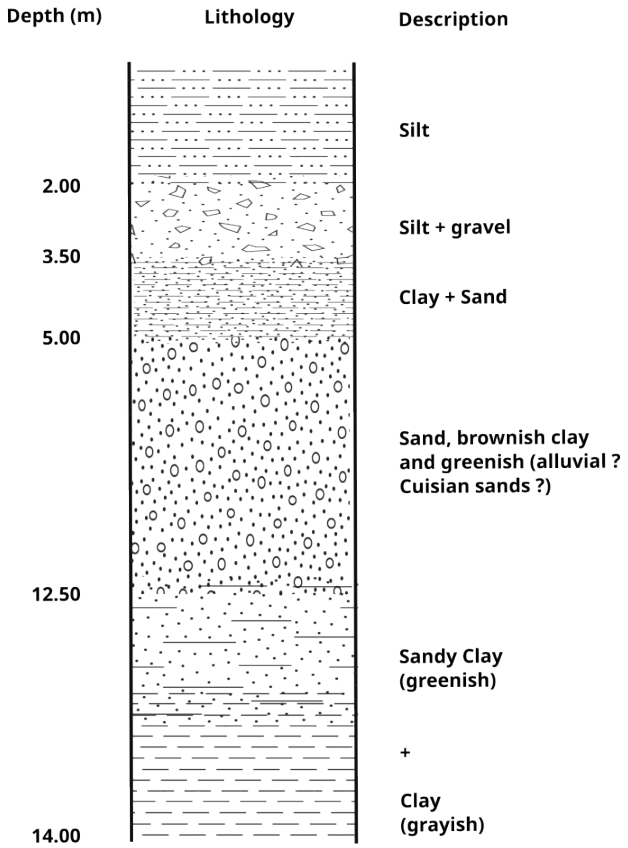

Figure 2.16: The geological beds of lithology from core drill analysis coming from the Sacred Area Borehole with depths after BURGEAP (1992).

water levels and groundwater temperatures with sensors immerse below the static water levels in

the boreholes to measure the variations (Table 2.1). Field or air temperature and barometric temperature variants were recorded near the surface with the Baro-Divers. Mean daily meteorological data were acquired courtesy of Meteo-France from the neighboring *Wy-dit-Joli village* station. Precipitation, relative humidity, air temperature, and wind speed were accessed (e.g. Figure 2.14).

Table 2.1: Observation well

	Obervation well	
		PzSa
Date drilled		$20-22\ October$, 1991
Aquifer, permeable bed		$alluvium, colluvium, silt$
Drilled depth		14.00 m
Cased depth		13.25 m
Casing type		PVC
Length of screen		7.00 m
Length of blind casing		6.25 m
Well radius W_r	62.5 mm	
Well diameter ⊘		125.00 mm
Size of screen		0.50 mm

2.4.3 Variability in water levels

The archaeological site in Genainville inherited three basins built by its former inhabitants, the Gallo-Romans (Figure 2.17); the fourth basin is located west of the temple. The three basins were constructed alongside the two-*cellea fanum* type temple completed in the 2^{rd} century AD for the Gallo-roman worship.

At present, the level of water in the basins has risen to near the surface of the Earth (Figure 2.17b). The ingression or infiltration of water into the temple foundation was not a practice that occurred conceptually at the time of the occupation.It is rather conceived as a later happening caused by changes in the parameters that influence the climate and environment.

From the period pre-dating the completion of the temple at Genainville up to the current times, variations in the environmental and climatic conditions have been reported to have both spatial and temporal effects on the planet. The initial changes in the conditions were caused by solar ra-

diation and geological events, meanwhile, the later changes known as global warming, unlike the earlier ones are caused by human activity that favors the release of greenhouse gases (e.g. Tegel et al., 2020). In other words, the earlier changes were caused by natural events such as the series of volcanic eruptions recorded in 536 AD, meanwhile, the recent inducement of the environment is anthropogenic (Harper, 2016, 2018).

The water levels are rising and posing a threat to the eternity of the historic buildings (Figure 2.18). The ingression by groundwater into the building signals a danger to the site and buildings. Groundwater inclusion into heritage sites and buildings has had a destructive effect on the materials. It gradually deteriorates the fabric and matrix of the cement and blocks leading to the eventual collapse of the building. The case of the early Christian buildings in the St. Mena area of Egypt is a

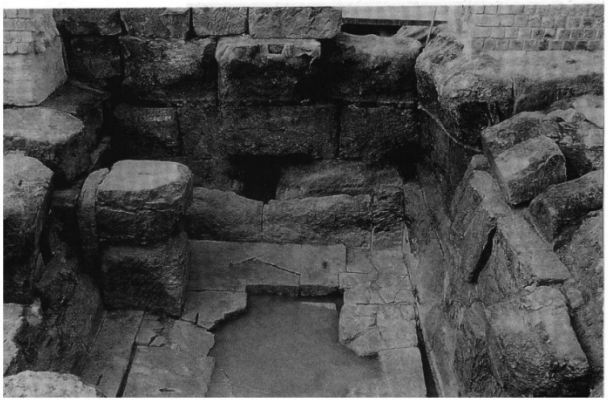

(a) Photograph of the Numphaeum showing it structure during the time of the initial excavations (Mitard et al., 1993).

(b) Aerial photograph of the first three basins showing where the groundwater has risen to near the surface. The stairs were the accessways to the basins' bottom.

Figure 2.17: The first picture (Figure 2.17a) shows an empty basin implying the water levels were either below the basins or had just been exhausted. The first view aligned with recent thinking of the impact of climate change and changing environmental conditions as responsible for the rise of the water levels as shown in the second picture was taken in 2013 (Figure 2.17b).

classic example where rising water levels have resulted in the loss of portions of the heritage structures and buildings (Amin, 2017). A larger portion of the heritage properties in the important town have either collapsed or threatened to collapse. The Abu Mena site was inscribed on UNESCO‘s World Heritage *Danger List* in 2001 following its earlier placement in UNESCO's World Heritage List in 1979 due to the menace of rising groundwater levels.

Wooden heritage structures also suffer a similar fate from groundwater ingression. The Xianyang Shahe wooden bridge in Xi'an, China, is a cultural ruin built during the Qin dynasty (221 – 206 BC). The destruction of the wooden bridge is being accelerated by groundwater level fluctuations (Cao

et al., 2021). T

Figure 2.18: Basement of the temple in contact with groundwater (Barrière, 2015).

From the reports of the excavations notably by Orième (1937), Pierre-Henri Mitard and his team of archaeologists from the Ancient Archaeology Group of the Touring-Club of France and other researchers from the Archaeological Research Center of the French Vexin and the Departmental Archaeological Museum of Val-d'Oise (Mitard et al., 1993) as wells as Didier Vermeersch (Vermeersch and Chupin, 2012) and ongoing archaeological activities.

The water level in the basins has changed. It is rising. It has risen from below the bottom of the basins at the time of the excavations to the surface (Figure 2.17a). Hence, the heritage buildings of the sanctuary are deteriorating due to rising and changing groundwater levels (Liu et al., 2016).

It has been documented that fluctuating groundwater introduces salt into the structure of the walls and foundations of buildings with destructive influence on the masonry materials (Cao et al., 2021; Chmielewski and Muzolf, 2018). The area ingress by the water and deposited salt becomes prone to chemical reactions thereby distorting the existing cohesion and destroying the internal structures of the building masonry. The rise and decline of groundwater, result in the crystallization of deposited salt as the moisture evaporates. The growing crystals exert pressure within the containing pores leading to the breakdown of the matrix masonry surrounding each crystal. As the process repeats, the masonries lose cohesion, decay, and spall off (Chmielewski and Muzolf, 2018).

The site's conservation is critical to sustaining the plethora of recovered cultural assets, teaching, learning, archaeological prospection, and the cultural identity of the Gallo-Roman cult.

To account for the changes in the water levels from the period of the constructions and habitation to its absence during the initial excavations and its continuous rise which is evident in this period. Variability in climatic and environmental conditions is also reported to have a range of impacts on the planet including its groundwater levels (see discussion in section 1.2.1). This variability in climate and environment has led to changes in the climate over time, known as climate change (Figure 1.5). UNESCO asserted that climate change is the principal threat to built heritage sites and materials. The water levels in the site of this research can be compared, perhaps visually for onsite changes in levels (Figure 2.17 versus Figure 2.19).

(a) Southeastern view of the second and third basins, showing the water levels as they have risen to the surface.

(b) Eastern view of the first and the second basins showing groundwater has overflowed to the surface. To the right of the basins are the walls of the Temple building.

Figure 2.19: Groundwater levels in the Gallo-roman basins have risen to the surface in spite of the changing climatic and environmental conditions since the basins were constructed. To the right of each photo are the deteriorating walls of the temple ruins. (The pictures were taken on the 26 July 2023 by Jérôme Wassermann).

2.4.4 Water levels in the nympheaum

The double *cellea fanum* type temple was completed during the first and second century (Mitard et al., 1993; Orième, 1937). The basins were constructed and skilled hydraulically to tap the groundwater. Using the setting in the second basin, a working hypothesis suffices thus. The basins were accessed through the stairs at the southern end of the second basin. The stairs are the access to the bottom of the partially filled basins. The wooden couch is compared to modern seats. It

means the people could sit in the basin and perform the rituals: cleansing and worship of the deity. It is practical, or cultural to have water level in baths maintained at near chest elevation (while seating) in the Romanised civilization. The big boulder with inscriptions represents an altar with a deity positioned on it. The water self-regulates its levels periodically at half depths. This partly half-filled bath hypothesis aligns with the idea that the temple was constructed over a natural water source. Using hydrogeological concepts, two views can be expressed to explain the workings of the water source. First, the source is artesian, water flows upward or spring to fill the basins. Second, which is the most realistic, the basins penetrated the Lutetian limestone sequence and partly rested on the Cuisian sand beds. Hence, a low-pressure zone was created below the water table and the inflow is such that the hydraulic equilibrium is balanced. In this way, inflow ensures the basins have water all-year-around.

2.4.5 Flooding events

Incessant (surface water) flooding events following periods of intense or prolonged rainfall and subsurface flooding caused by rising water levels with the latter being periodic and non-periodic events that spring up or fluctuate. Two types of flooding events are reported to have disturbed the continued occupation of the site and are also threatening the conservation program at the site (BURGEAP, 1992). Flooding events are commonly reported as the impetus for the site abandonment. It is a challenge that periodically disturbs archaeological investigations and poses threats to the conservation and reconstruction of the rich culture of the ancient occupants.

Following the site abandonment in the 5^{th} century AD, about 2 - 3 m column of silt (and clay) had covered the ancient ground level walked on by the cult group and guests before the excavations of the vestiges and remains at the site commenced (Mitard et al., 1993; Orième, 1937). The presence of alluvial materials (e.g. silt and fine-grained clay) in the valley is an indication of a slowly drained condition occasioned by the weathering and transportation of weathered rock particles and regoliths by water from upstream and runoff from within the valley and its slope.

The proneness of the valley to flood was the cause of a commissioned hydrogeological study by the BURGEAP group in 1992 at the instance of the region's department of antiquities (BURGEAP, 1992). The group had the mandate to assess the capacity of the infrastructures at the archaeological site and proffer mitigation steps to forestall the reoccurrence of the flooding events the affected buried artifacts and compromised conservation procedures. The BURGEAP group also

recommends a suitable procedure for lowering the water table to eliminate flooding risks. This is also a sequel to the severe flood recorded in July 1982 and June 1983 where the ancient drainage channel constructed by the Gallo-Romans and reworked in 1978 proved insufficient to accommodate the runoff.

An assessment of the response of the subsurface to natural and anthropogenic influences on the groundwater levels and the properties of the subsurface sequences to derive information on the hydraulic behavior of the subsurface and also noting inputs from monthly mean precipitation and other meteorological data (Figure 2.14).

2.5 Conclusion

The temple building is unique with a rare *fanum* type of architecture. It was built with carbonate rubbles, bricks and mortar sourced from the valley and the Vexin vicinity. From a qualitative viewpoint, the masonry of the ruins suggests the deliberate use of low-permeability materials at the base. Firstly, the building walls were laid on a foundation of stone for stability. Afterward, the layers of rubbles were erected with mortar and alternated with bricks.

At present, the ingress of groundwater into the relics of the Gallo-roman buildings at Genainville now threatens the continued location of the sanctuary believed to be erected at a sacred water source that has both thermal and curative significance (BURGEAP, 1992; Liu et al., 2016). Unlike the Nubian monuments (e.g. see Hassan, 2007) and General Zhang Fei's Temple (e.g. see Zhu and Li, 2022) that had to be relocated for conservation due to threatening environmental and climatic variability including groundwater incursions.

The Genainville vestiges include a sanctuary site associated with water idealized as a natural spring. It is a unique meeting of heritage and hydrogeology. It is an onsite archaeological site with rich cultural and historical relevance, It provides an opportunity to test classical and new concepts, methods, and tools in hydrogeology, geophysics, and related disciplines for its in situ conservation and sustainability.

To decipher the drivers and factors that influence the groundwater levels in the archaeological site where natural, climatic, and environmental variables conceptually dominate anthropogenic activities. This study is being carried out as part of a scientific effort to conserve heritage buildings and sites.

CHAPTER 3

Structure of the subsurface: the search for cultural and geological anomalies using electrical resistivity

3.1 Introduction

Electrical resistivity tomography (ERT) is a method for simultaneously measuring the lateral changes and the vertical variations with depth of resistivity values. It is an imaging technique that has the capacity for a high definition of features.

In this study, the ERT method was applied to search for buried artifacts and cultural materials and provide a planning tool for guided archaeological excavations, thereby limiting invasiveness and also preventing the destruction of traces of historic relevance that can result from unscientific digging or trenching.

The ERT method is sensitive to wetness or saturation in soils, sediments, and rocks and other factors such as porosity (Keary et al., 2002; Telford et al., 1992). Therefore, ERT is used to leverage its electrical resistivity response structure to detect and delineate the saturated porous media in the subsurface, that is, the aquifer. It will help us to ascertain the presence, if any, of the conceived shallow aquifer body, and also determine its depth, and spatial extent and localized it in the geological sequences.

To obtain a refined result for an enhanced, clearer image of the subsurface, a finer electrode spac-

ing of 0.4 - 1.0 m is deployed in this study for the acquisition of two-dimensional (2-D) ERT data. The IRIS Syscal Pro multi-electrode imaging system is used with an array of 96 steel electrodes for the data acquisition with a Wenner-Schlumberger electrode array. The acquired 2D data is processed with state-of-art, RES2DINV inversion software.

In this chapter, the theoretical information is contain in subsection 3.2.2, while the survey concept and field procedure is describe in subsection 3.2.3 and section 3.7, and the instruments in section 3.3. The information detailing the objective of siting each profile is reported in subsections 3.6.1, 3.6.2 and 3.6.3. The results obtained in section 3.9 are discussed in section 3.10.

3.2 Electrical resistivity tomography

3.2.1 Introduction

Electrical resistivity (ER) method is a geophysical survey technique that is based on the electrical properties of Earth materials including rocks and minerals, and those of cultural and archaeological objects. It is a method that is widely used for groundwater prospecting, geological mapping, geothermal investigation, and archaeological search (Clark, 1990; Keary et al., 2002; Telford et al., 1992).

The electrical resistivity of a material is affected by some factors such as porosity, permeability, moisture content, salinity (dissolved salts), the type of mineral constituent, and pressure (Keary et al., 2002; Telford et al., 1992). These properties influence the matrix structure, morphology, physical and geochemical properties of the material and hence its response to applied electric current (Keary et al., 2002; Telford et al., 1992).

For archaeological investigations and built heritage conservation, two forms of surface ER approach are known: classic and non-classic techniques. In the classic approach, metal stakes serve as electrodes for transmitting electric current into the Earth and receiving the resulting changes in the subsurface electric potential. The non-classic approach uses non-invasive EKG electrodes for the ER measurements on buildings (López-González et al., 2022). The approach has been reported effective in delineating moisture content in built structures while preserving the frame and surface decoration on the buildings (Mol and Preston, 2010; Sass and Viles, 2006).

The classic ER approach has evolved from the traditional four electrode arrangement to multi-electrode surveys for 2D or 3D imaging of the subsurface known as Electrical Resistivity Tomog-

raphy, *ERT* (Loke, 1994, 1999). For archaeological investigations, the ERT methods have aided the search for buried materials by defining the geometry of the subsurface (Deiana et al., 2018, 2022), delineating the geological beds and structures (Clark, 1990; Epov and Chemyakina, 2009) and geoelectrical mapping of water-bearing-beds (Clark, 1990; Hermawan and Putra, 2016). ERT can resolve with higher resolution the location and dimension of historical and archaeological materials (Deiana et al., 2018, 2022; Moník et al., 2018).

3.2.2 Theoretical formulation

The electrical resistivity ρ of a material is defined by the relation between the electric field $\vec{E}$ inside the material, and the density of the electric current $\vec{J}$ flowing through it is given by equation 3.1, where ρ is express in ohms-meter (Ω-m), $\vec{E}$ in volts per meter (Vm^{-1}) and $\vec{J}$ in amperes per square meter (Am^{-2}) (Keary et al., 2002; Telford et al., 1992).

$$\vec{E} = \rho\vec{J} \tag{3.1}$$

The relation is derived from Ohm's law. The law gives the relationship between the applied electric current I (in amperes, A), the measured potential V (in volts, V) and the resistance R (express in Ω) of a conductive material (equation 3.2).

$$R = \frac{V}{I} \tag{3.2}$$

By definition, $\vec{J}$ is the amount of electric current I flowing through a unit area A (in square metre, m^2) as shown in equation 3.3. The electric field $\vec{E}$ is the potential field gradient (equation 3.4).

$$\vec{J} = \frac{I}{A} \tag{3.3}$$

$$\vec{E} = \frac{dV}{dr} \tag{3.4}$$

Mathematically, electrical resistivity is inversely related to electrical conductivity σ (equation 3.5). The SI unit of electrical conductivity is Siemens per metre (Sm^{-1}).

$$\rho = \frac{1}{\sigma} \tag{3.5}$$

Using the model relation in equation 3.6, the resistance of a conductive material relates proportionally to its length L and inversely to its unit cross-sectional area A, where the area, A = πr^2 and r = radius of the material.

$$R = \rho\frac{L}{A} \tag{3.6}$$

By inputting the model relations in equations 3.2, 3.3 and 3.4 into equation 3.6, and rearranging to obtain equation 3.7. It can be integrated (see equation 3.8) within the appropriate limit to equation 3.9, for a point source electrode. Equation 3.9, is valid for a point current source on the Earth's surface considered as a half-space model. Here, the Earth's surface or the ground is defined as a semi-infinite space of a hemisphere (Keary et al., 2002; Telford et al., 1992).

$$\frac{dV}{dr} = \frac{I\rho}{\pi r^2} \tag{3.7}$$

$$dV = \frac{I\rho}{\pi} \int \frac{1}{r^2}\, dr \tag{3.8}$$

$$V = \frac{I\rho}{2\pi r} \tag{3.9}$$

3.2.3 Field and survey concepts

ER survey is conventionally carried out with a pair of electrodes assigned as current (or A and B) electrodes and a pair of electrodes designated potential (M and N) electrodes. The four electrodes are arranged in an equal or variable distance manner. The distance or separation between the electrodes is called the electrode spacing. An array is defined by the type of arrangement and spacing between electrodes. In classic ER surveys, four types of electrode arrays or spread are commonly used, namely, the Wenner, Schlumberger, Dipole-Dipole, and Pole-Dipole arrays.

Each array type has some advantages that suit specific types of surveys or environmental conditions. Table 3.1 summarizes the silent features of some electrode arrays. ER data acquired from

Table 3.1: Characteristics of classic electrode arrays

Electrode arrays	Depth / line length	Signal strength	Lateral resolution	Field set-up
Wenner – Schlumberger	20 %	*regular*	*regular*	*regular*
Dipole Dipole	20 %	*weak*	*best*	*regular*
Pole Dipole	35 %	*medium*	*good*	*medium*
Pole Pole	90 %	*best*	*weak*	*weak*

surface measurements with any of the four electrodes array is processed and interpreted in terms of the geology of the area to obtain information about the beds and structures. The interpretation of the nature of the subsurface relies on certain concepts used to estimate the resistivity values

and parameters of features. First, the Earth's subsurface is considered to be a half-space medium. Second, the Earth's subsurface is conceptualized as heterogeneous and layered space. Each layer is homogeneous, isotropic, and infinitely horizontal. The bed homogeneity implies a defined range of resistivity values. Changes in resistivity values with depth or along a bed are used to indicate the presence of a natural or anthropogenic feature.

Equation 3.9, can be rearranged to obtain an expression for ρ (equation 3.10). The measured electrical resistivity is called the apparent electrical resistivity ρ_a. The apparent resistivity ρ_a is by definition the measured resistivity normalized by the geometric factor. In field expressions, r represents the separation between two electrodes.

$$\rho_a = \rho = \frac{\Delta V}{I} 2\pi r \tag{3.10}$$

In practice four electrodes are traditionally used for the measurements and the general expression of the ρ_a for the four electrodes array is given by equation 3.11:

$$\rho_a = \frac{\Delta V}{I} 2\pi \left[\left(\frac{1}{r_1} - \frac{1}{r_2} \right) - \left(\frac{1}{r_3} - \frac{1}{r_4} \right) \right] \tag{3.11}$$

where, $r_1 = C_1P_1$ = distance between current electrode C_1 and potential electrode P_1

$r_2 = C_1P_2$ = distance between current electrode C_1 and potential electrode P_2

$r_3 = C_2P_1$ = distance between current electrode C_2 and potential electrode P_1

$r_4 = C_2P_2$ = distance between current electrode C_2 and potential electrode P_2

The geometric factor K (equations 3.12) is a coefficient that depends on the separations between the C_1, C_2, P_1 and P_2 electrodes.

$$K = 2\pi \left[\left(\frac{1}{r_1} - \frac{1}{r_2} \right) - \left(\frac{1}{r_3} - \frac{1}{r_4} \right) \right], \tag{3.12}$$

$$\rho_a = \frac{\Delta V}{I} K \tag{3.13}$$

3.3 Instrumentation

The instruments and acquisition software use for the two-dimension (2D) electrical resistivity survey include the *Syscal Pro* Resistivity meter and accessories (Figure 3.4), *Electre Pro* and *Prosys* II (Figures 3.1, 3.4 and 3.5).

The *Syscal Pro* Resistivity meter (manufactured by IRIS instruments, France) is an automated multichannel system equipped with an inbuilt multi-electrode selector, data collection and storage

system configured for two and three-dimensional surveys (Figures 3.1, 3.4 and 3.5).

To establish electric contact between the resistivity meter and the ground; metal stakes made with steel were used as electrodes. The electrodes have the form of a needle and a length of 18 cm. The stakes have a diameter of 6.5 mm at the top. Each electrode had a flattened top and a pointed base for ease of hammering into the ground.

The resistivity meter was connected to the steel electrodes through a network of thinly shaped, adequately insulated copper cables in a set consisting of 24 electrodes system. Each cable end is fastened to the stake with a clip for firmness and to ensure it is not stripped off during the survey.

The electrodes were equidistant and partially buried along a collinear array in the Earth (Figures 3.4 and 3.5). A direct current source from a 12 V battery powered the survey.

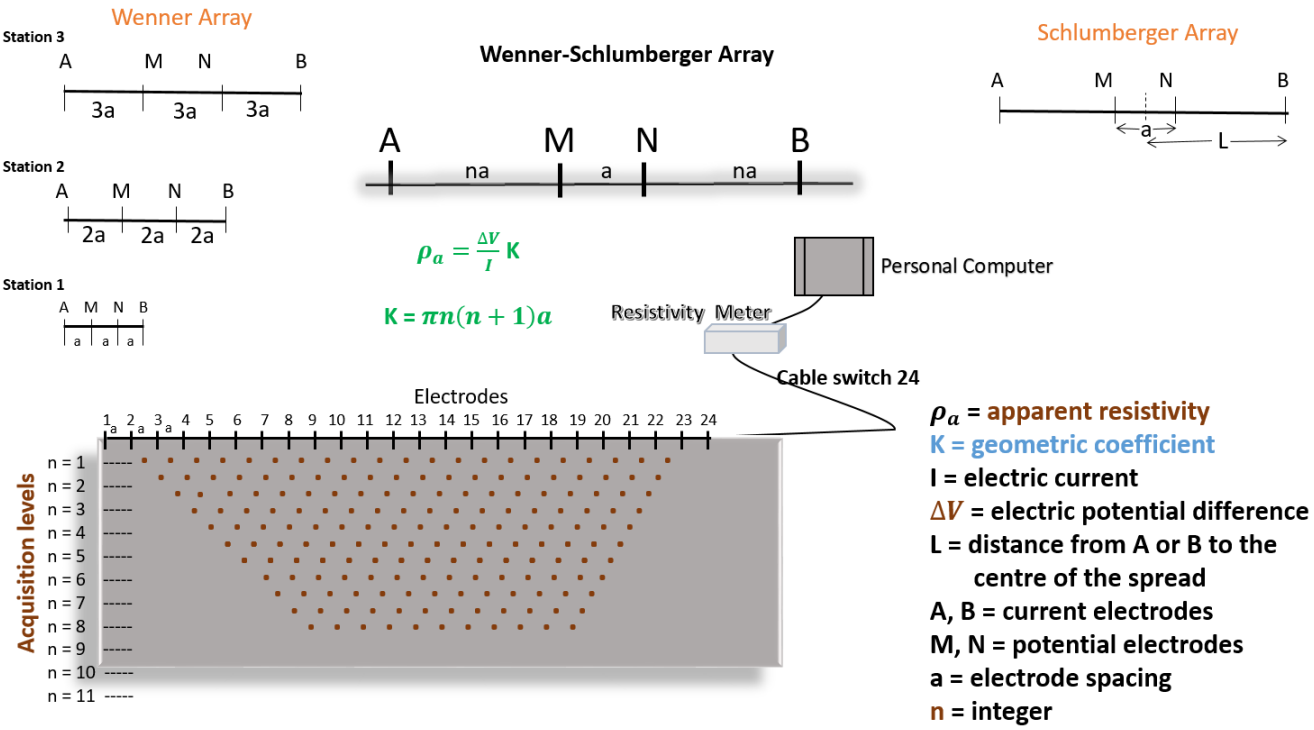

Figure 3.1: Schematic of the Wenner-Schlumberger array and a typical multi-electrode acquisition set-up showing the sampling levels with increasing electrode separation. At the upper right and left corners of the schematic are the models of the Schlumberger array and the Wenner array, respectively.

3.4 Survey sequence and acquisition set-up

3.4.1 Electrode sequence

The ERT data pre-acquisition was done in three steps. First, the survey instruments were assembled as mentioned in section 3.3, after the initial visit to the site for reconnaissance and outlining

the profiles' location and dimension.

In 2D or 3D ERT surveys with the *Syscal Pro* Resistivity meter, the sequence for the multi-electrode survey is built in the *Electre Pro* and transferred into the meter.

The second step involves the definition of the electrode sequence using the *Electre Pro* software. Four tasks were performed in the software: creation of the sequence, configuration set-up, visualization of the depth and subsurface levels expected to be investigated and lastly, the resulting data points were viewed or inspected. The four tasks were accomplished using the creation, configuration, view graph, and view sheet menu of the *Electre Pro* package (Figure 3.2).

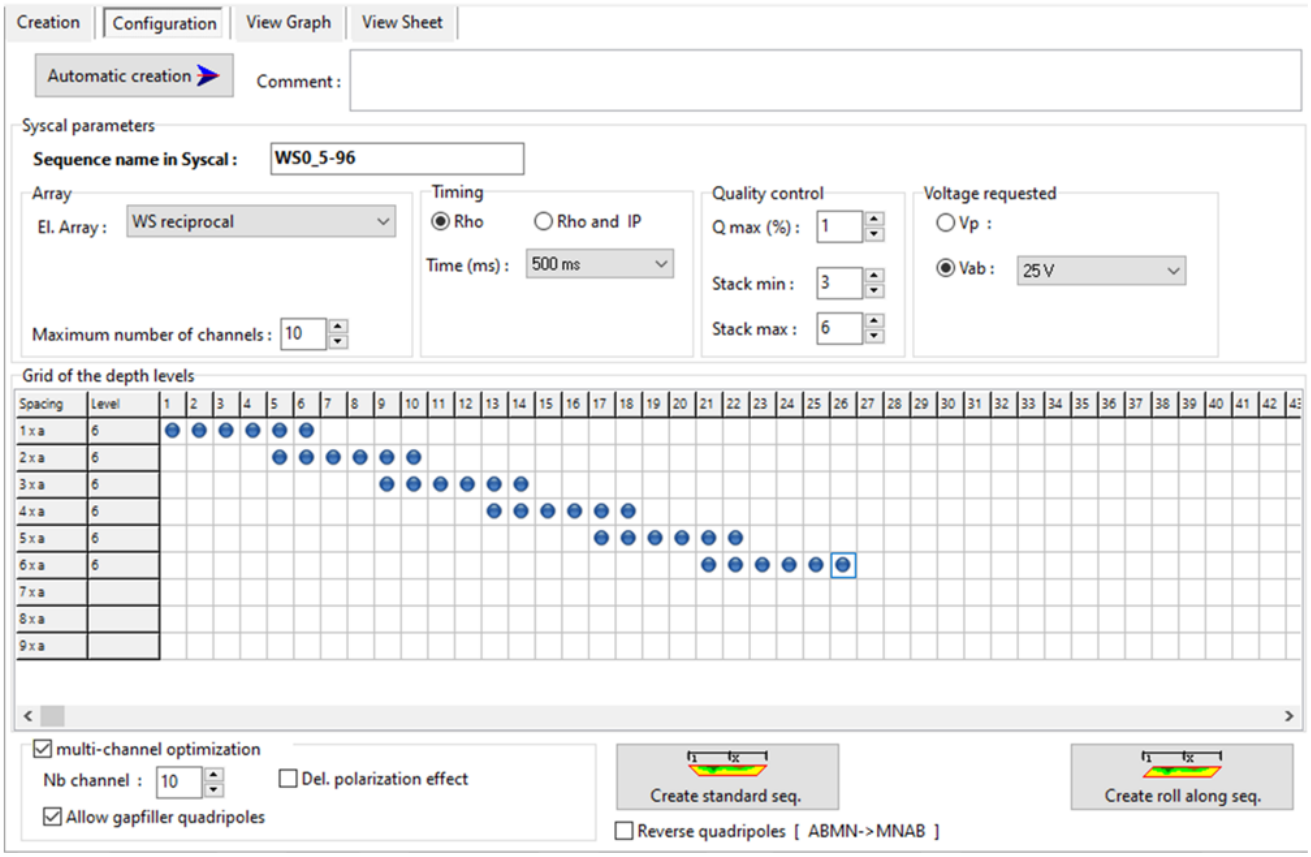

Figure 3.2: The configuration interface of the Electre Pro module shows the acquisition parameters and predicted electrode sequences.

3.4.1.1 Creation Menu

The sequence creation menu has options to indicate the type of measurement, the X-grid spacing, the X-grid size (the number of electrodes), and the X-grid offset. The creation menu items also include an option for indicating *automatic* or *manual* type of grid.

Begin the creation of a new sequence by selecting a file on the menu bar and then new. Thereafter,

the icons on the Creation Task Menu are selected, filled, or marked as appropriate to your survey.

For this survey, the line option was chosen as the type of measurement to indicate a 2D survey. The parameters inputted for x-grid spacing were 40 cm (or 0.4 m) for profiles P_1 and P_3, and 100 cm (or 1 m) for profile P_2. The X-grid option is the position of the first electrode, hence zero was indicated for this survey.

Ninety-six (96) electrodes were used for the survey. They were arranged in a set of 24 (twenty-four) electrodes: $1^{st} - 24^{th}$, $48^{th} - 25^{th}$, $72^{th} - 49^{th}$, and $73^{th} - 96^{th}$.

To complete this task, the automatic grid was chosen and the create grid icon was clicked. The built sequence is stored (saved) in an *Electre Pro* file that contains other accomplished tasks and transferred to the *Syscal Pro* before the survey.

3.4.1.2 Configuration Menu

In this menu, a file name was inputted into the File name option to allow for retrieval of the built sequence and the implementation last phase of the pre-acquisition steps. The Wenner-Schlumberger array was selected as the electrode array type, while *rho* and 500 ms were the respective injection mode and time mode chosen to indicate resistivity and the amount of voltage for the survey (Figure 3.2).

Ten (10) channels were reserved for the *Syscal Pro*. Six (6) survey levels represented the expected spatial density of measurements. The quality control parameters were set at 1 % for maximum Quality (Q max), 3 for minimum stack (Stack min), and 6 for maximum stack (Stack max). It means if the factor for the standard deviation is better than 1, the number of stacks will be 3, if not the number of stacks will be 6. Stacking is a procedure for improving the signal-to-noise for weak or noisy signals. It is an inbuilt capability in the *Syscal Pro* Resistivity System.

For the depth of investigation, six levels of sampling were chosen. Each new levels begin at the last two sample levels, the 5^{th} and 6^{th} points. This menu is executed by clicking the Create standard sequence option. A window appears displaying original and optimized statistics of the built sequence which include the estimated acquisition time. The OK is clicked and a save file name window opens, a file name that will be stored in the computer is entered which should be the same as the file name for *Syscal Pro* and saved.

3.4.1.3 View Graph Menu

In this menu, the model of the subsurface is displayed. The different colors correspond to the different electrode spacing defined in the sequence (1a, 2a, 3a, etc). Each color band shows the spatial density of measurements expected in the field. The investigated depth and spatial extent of the levels are shown in the model. A typical model has the form of an inverted pyramid. The spatial coverage thins downward with increasing spacing. The estimate of the survey period, the number of quadruples formed during the different levels in the survey, and the number of measurements are also shown.

3.4.1.4 View Sheet Menu

The view sheet contain information in two sections. The first section which is on the right contain information on the electrodes' positions. X (m) is the position of the electrodes for the 2D survey, Y (m) had the default zero values and Z (m) is the topography. The topographic can be entered after data is downloaded into the software. This was captured in a separate survey with a *theodolite* and inputted accordingly.

In the second section, the position of each pair current and potential electrodes for each spacing, the geometric factor, and depth are digitally displayed. Lastly, to accomplish the third step of the pre-acquisition, upload the built sequences into the *Syscal Pro* Resistivity meter. First, validate the sequence by clicking on the icon beside the saved filename. Open the file menu, click on communication port, then USB, and next, select upload. A window opens and a message requesting an appropriate connection to the Laptop with a USB is displayed. Installed the USB and connected the Laptop to the Syscal Pro unit, click OK to complete the process.

3.5 The Prosys Package

The next procedure following the acquisition, is the transfer of the data from the *Syscal Pro* to the *Prosys* II software for pre-processing. The *Prosys* II is the interface between the acquisition instrument, *Syscal Pro* and the inversion software, e.g. *RES2DIV* or *RES3DINV*, or export to a file, e.g *ASCII* File. The *Prosys* II is a computer package developed by Iris instruments for the visualization and pre-processing of acquired data, ER or Induced Polarization, before inversion. In the program, the data can be analyzed, interrogated, and edited. The ER data was downloaded with *Prosys* II from the *Syscal Pro* and visualized for detection and edition of outliers. The download

was accomplished by connecting the meter with a compatible external serial device. The section had good data points with neither spikes nor distortions. The program was installed on a Personal Computer (PC) with a Windows operating system.

3.6 Profile Layout

The electrical resistivity ρ data acquisition procedure involved three steps.

i. Field visit and assessment of available archaeological, hydrogeological and geological information as well as previous geophysical reports and lithology logs of the drilled boreholes were carried out to have a view of the subsurface geology and improve survey input. The objective of the ERT survey was at this stage defined and articulated to accommodate the background information provided for each profile.

ii. The profile positions were established to achieve the spell-out objectives. Thereafter the survey equipment and materials were assembled (section 3.3).

iii. The third procedure was implemented in two phases.

   (a) First, the electrode sequence for each profile was built and stored in the meter before the survey by the laid down procedure by the Manufacturer (section 3.4.1).

   (b) Second, after each profile surveyed, the data was downloaded into the *Prosys package* (section 3.5) and pre-processed before it transferred into the inversion software.

In this study, results of three ERT profile lines (P_1, P_2 and P_3) acquired, 13 - 15 July 2021, with an electrode spacing of 40 cm (or 0.4 m) and 100 cm (or 1 m) are presented (Table 3.2). The electrode spacing was 40 cm (or 0.4 m) for P_1 and P_3 and 100 cm (or 1m) for P_2. The profile lines are perpendicular to the facade of the Amphitheatre and parallel to the frontage of the Sanctuary building (Figure 3.3).

Table 3.2: Acquisition data indicating whether or not roll-along technique was implemented

Profile lines	Profile length	Electrode spacing	Roll-along sequence	Orientation
P_1	57.20 m	40.00 cm	R	$N44°E$
P_2	97.20 m	100.00 cm	-	$N42°E$
P_3	57.20 m	40.00 cm	R	$N37°E$

The profiles were laid north-south but numbered east-west ward at 15 - 25 m intervals. Each profile had 96 steel electrodes collinearly implanted in the ground. Profiles P_1 and P_3 were `roll along` to cover the profile length following the 40 cm electrode separation used. The northern segments of the three profiles extend through the motorable, unsurfaced road of varying width.

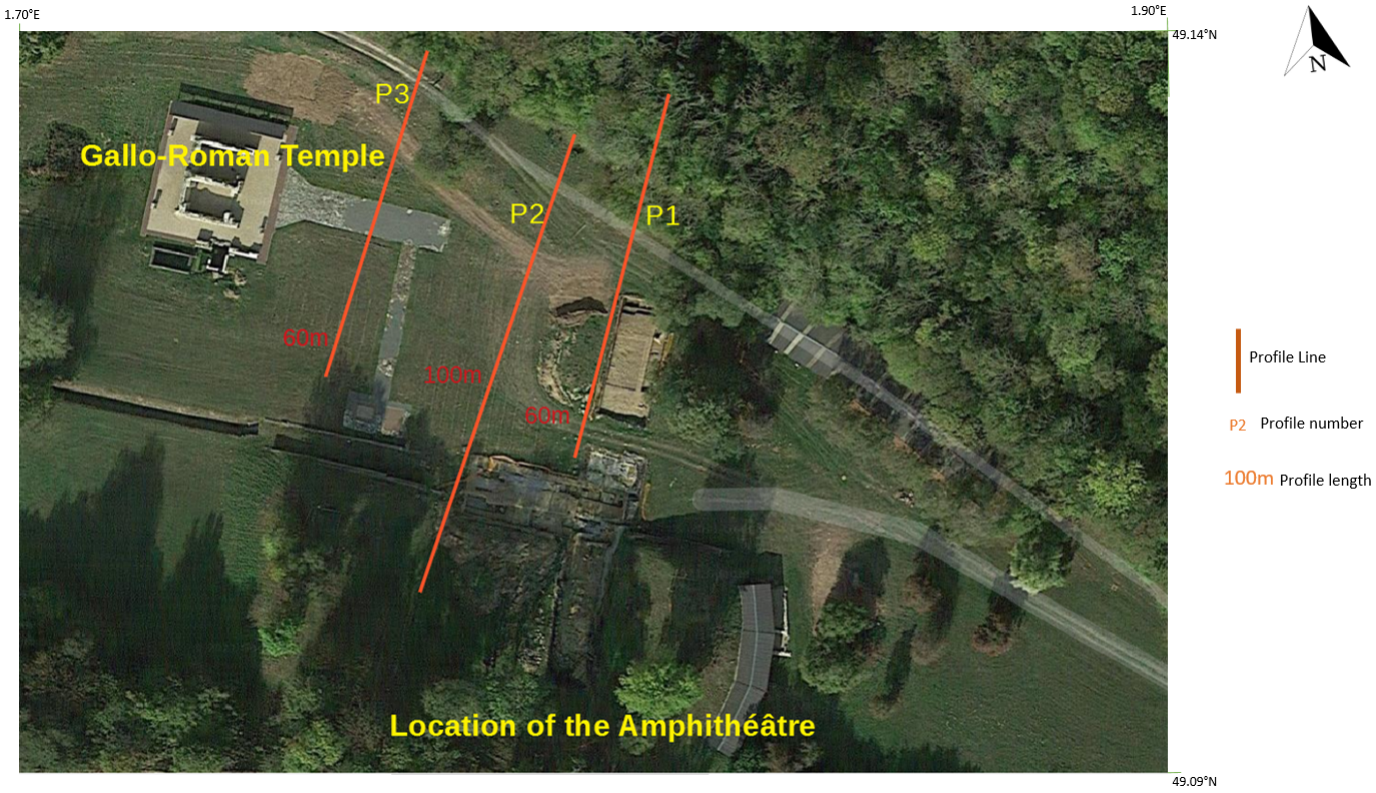

Figure 3.3: Electrical resistivity tomography profiles at the Gallo-Roman Sanctuary Site *des Vaux de la Celle* (the background map was modified from Googles maps: 15 November, 2021).

3.6.1 *Profile* 1 (P_1)

The first profile (P_1) is 57 m long and oriented $N44^{\circ}E$ (Figure 3.4). It is perpendicular to the on-going archaeological excavation at the entrance of the Amphitheatre. Beside P_1 is an excavation site where the remains of an ancient building have been unearthed at a depth of < 2 m. A surface distance of 1 - 3 m separates the excavation site from the profile line. The profile is conspicuously located between the excavation site which is about 25 m in length and a heap of Earth materials chunked out from the excavated trench. The heap covers 6 m of surface length. Excavation campaigns in the cultural area led to the unearthing of two building walls: The first section of the wall was in 2010 while the second wall was in 2016.

The section of the wall discovered in 2016, consists of a layer of blocks resting on a small foundation consisting of a continuous band of pebbles and rubble of limestone. It runs parallel to an

earlier section discovered in 2010. The archaeologists have hypothesized a third section of the wall such that the three walls are perpendicular to one another. To form a square or quadrangular structure as a typical enclosure or dimension of building they argued further for a fourth wall. Therefore, the first profile (P_1) was set up to provide a picture of the subsurface in the cultural area

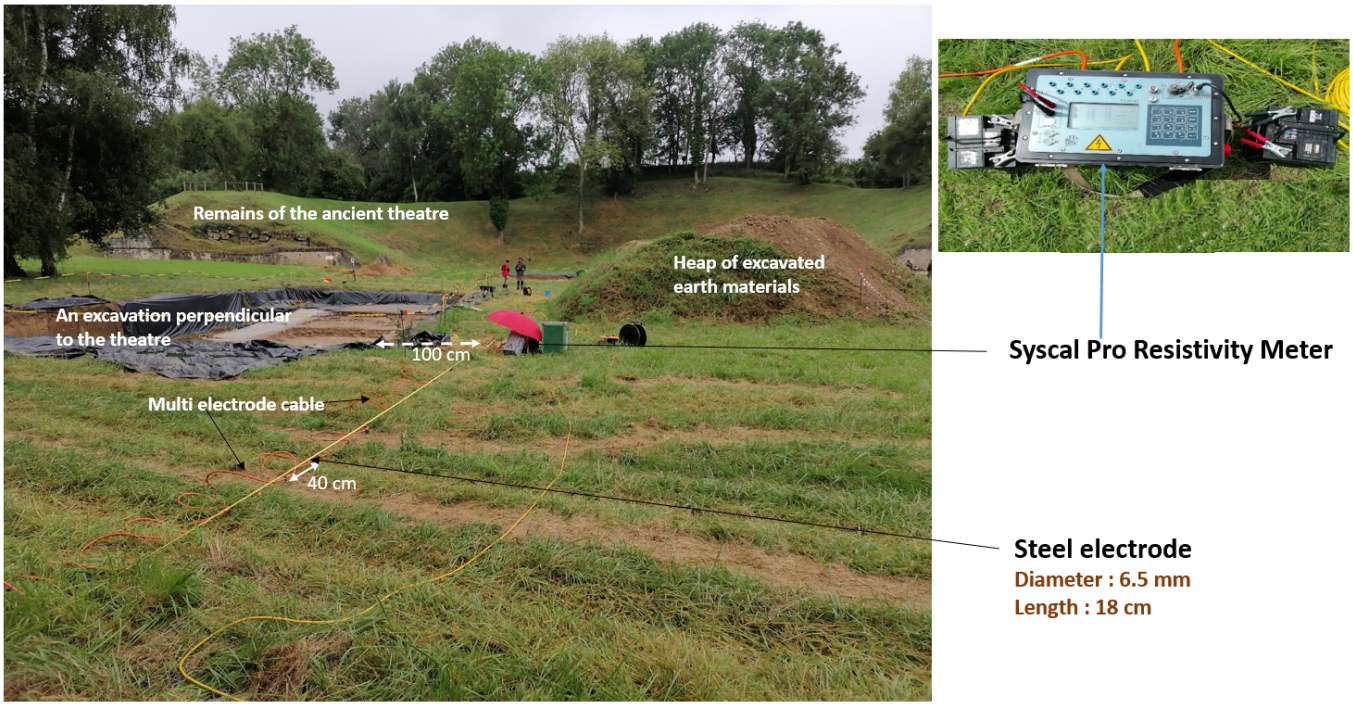

Figure 3.4: The electrode layout of profile 1 showing the distance between electrodes, the Syscal Pro Resistivity Meter and its accessories.

to resolve some questions raised by the archaeologists following the excavations of a wall in the area. First, the enigma by the archaeologist related to the spatial connection of the foundation walls revealed by the excavations close to the *Facade* of the amphitheater and opposite the portico of the sanctuary (e.g. Barrière, 2021).

Hence, to ascertain the boundary or continuity of the revealed wall structure. The survey line was laid to obtain a detailed image of the subsurface and precise the area covered by the wall structure by determining the spatial limits of the foundations and walls using a non-destructive method such as ERT. Second, details of the subsurface structure are important for the mapping of the subsurface geology and determining the physical dimension of the subsurface layers for the hydrogeological disposition of the valley.

3.6.2 $Profile\,2\,(P_2)$

The second profile line (P_2) extends into the western part of the *cavea* (seating area) traversing an ancient drainage channel covered by superficial deposits. Ground width of 50 cm to 2.5 m separates portions of the profile southern section from the about 8 m width excavation site at the theatre entrance. The electrode spacing for profile P_2 was equidistant at 100 cm. The profile is oriented $N42°E$ (Figures 3.3 and 3.5; Table 3.2).

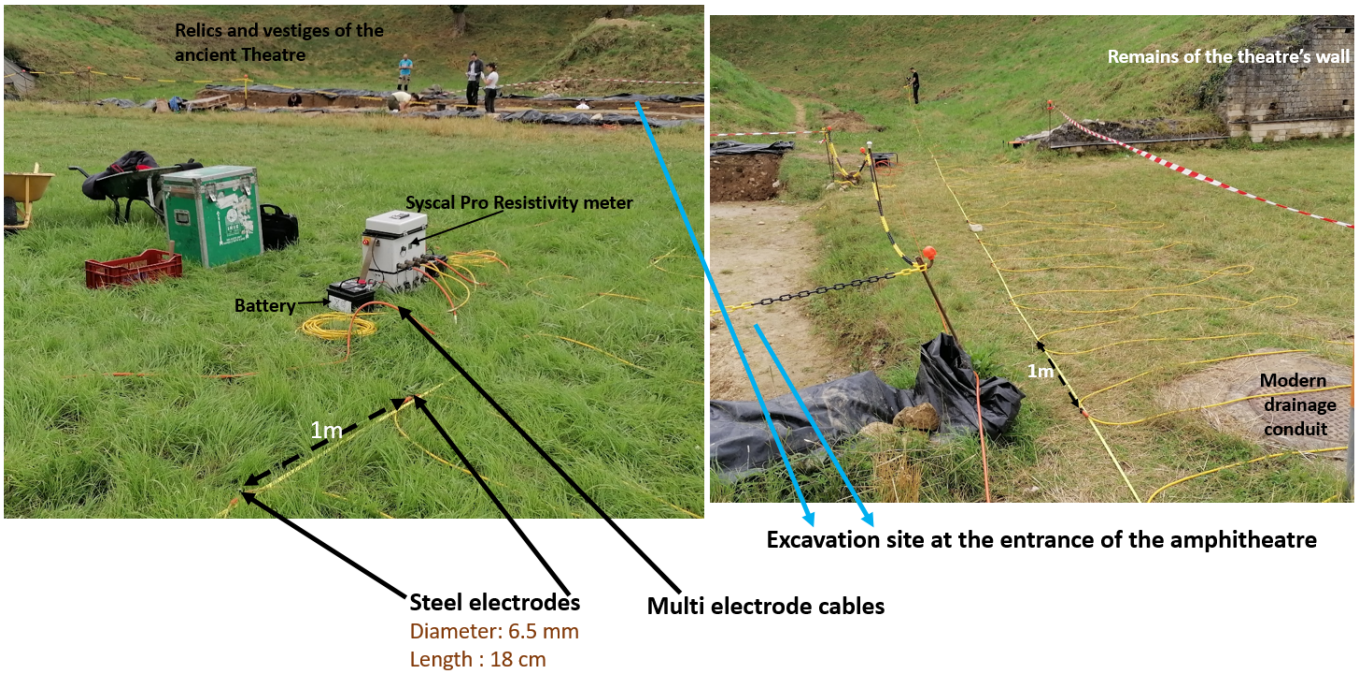

Figure 3.5: The position and electrode layout of profile 2 showing the distance between electrodes, the Syscal Pro Resistivity Meter and it accessories. The picture to the right is the first part of the profile while the second picture to the left is showing the continuation of the profile through frontage, *podium* and seating area.

The second profile, P_2 (Figure 3.5), originates at the western part of the theatre, stretching from a section of the *cevea* through the axis of the podium to the *facade* area, traversing beside a western extension of an excavation site (that was operated by Mitard and his team over half a century ago) to the cultural area. The profile also runs parallel to the 500 m^2 *Aire Ouverte* (Open Air) excavation site located opposite the theatre (Barrière, 2018). Substructures of the theatre covered by the profile line include the *cevea*, *gradins*, *podium*, and *facade*.

The ERT section on the profile is intended to provide details of the geometry of the substructures and a buried sub-drainage channel at the access to the theatre. The image of the subsurface is required to resolve the puzzle as to the actual depth of the geological sequence to differentiate it from the layers of built structures encountered during the 2018 archaeological expeditions (e.g.

Barrière, 2021).

3.6.3 *Profile* 3 (P_3)

The third profile (P_3) was oriented $N44^{\circ}E$ and laid parallel to the frontage of the temple building (Figures 3.6; Table 3.2).

The southern end of profile P_3 did not extend beyond the fringes of the constructed drainage channels which extend in an east-west direction through the facade of the Amphitheatre. However, the northern section of P_3 traverses the Gallo-Roman main road of the site: a paved ground surface measuring about 7.60 m. Electric contact could not be established with the electrodes at points 31, 34, 42, and 45 and the ground due to the paved nature of the area. The third profile, P_3 (Figure 3.3

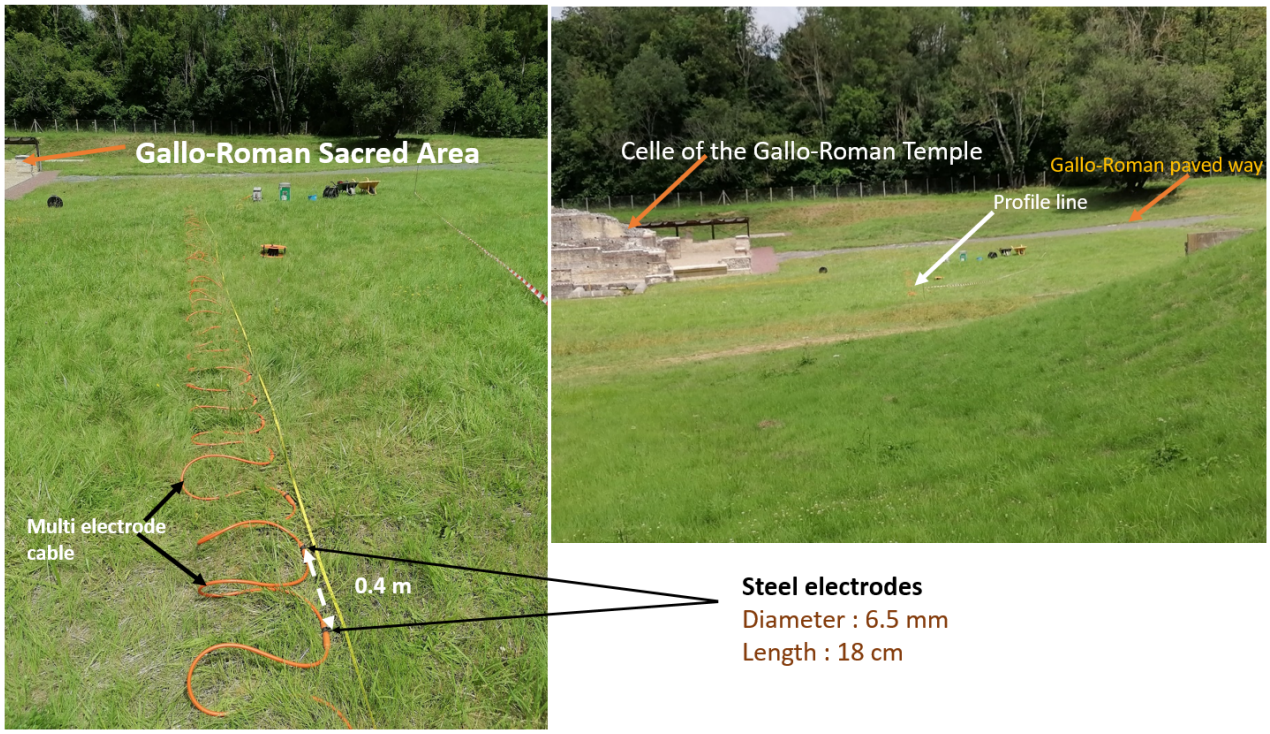

Figure 3.6: The position and electrode layout of profile 3 showing the distance between electrodes. The first picture details the electrode spacing of the profile while the second picture shows the position of the profile relative to the temple ruin and paved road.

and 3.6), begins from the edge of the ancient drainage channel at the vicinity southeast of the remains of the amphitheater; it stretches into the sacred area and traverses the paved road towards the northern end of the valley. It essentially runs parallel to the eastern section of the temple (Figure 3.3).

The profile is located within the same vicinity as profiles T13, T14 and T15 mentioned in Fores

(2013). They are both North-South oriented lines and crossed profiles T10 and T11 (Figure 3.7). In this study, the dimension of Profile 3 extends beyond the limits of T13, T14, and T15 and traverses the Gallo-Roman road towards the northern end of the site width.

The T13, T14, and T15 premises earlier surveyed by Fores were revisited in this study with a finer electrode spacing for refined and more detailed information on the subsurface structures. Fores used a Dipole-Dipole electrode configuration with 0.5 m electrode spacing to investigate the subsurface beneath profiles T13, T14, and T15 (3.7). To obtain a finer image of the subsurface structures and investigate deeper depths, 0.4 m electrode spacing was used and the profile length was extended.

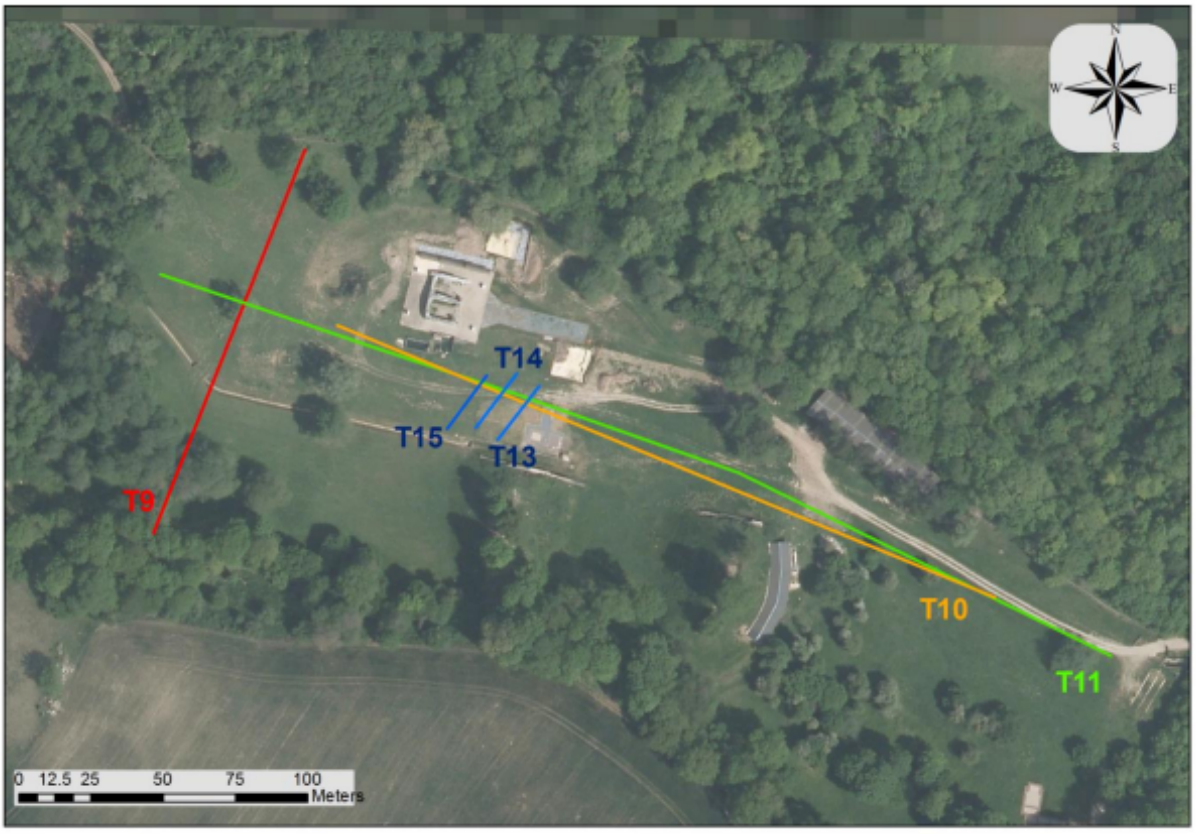

Figure 3.7: Map of the site showing the location of profiles erected for electrical resistivity survey by Fores (2013).

3.7 Field procedure

The electrode spacing factor (n) is varied while maintaining the distance between the two potential electrodes (M and N) for successive measurements with the same electrode spacing (a) along a profile line. To increase the depth of investigation, the spacing between M and N electrodes is increased to 2a and the measurements repeated for n are equal to 1, 2, 3, 4, 5, and 6. Subsequently, the M-N spacing is increased to 3a, 4a, 5a, and 6a, and made on the same sequence of measure-

ments for each spacing.

The electrode sequence was designed using the *Electre Pro* software and transferred into the *Syscal Pro* Resistivity meter using a compatible external serial bus interface (Universal Serial Bus, USB). The graphical mode of the *Electre Pro* was activated to visualize the model of the expected horizontal coverage and the depth extent expected to be investigated on which premise the electrode spacing and electrode sequence.

An overlap in the data measurement sequence was done for adequate sampling of the subsurface structure. The inversion scheme is such that it has the flexibility to accept such data.

3.8 Data treatment

Each acquired data was transferred from the Syscal Pro Resistivity meter to the Prosys software for editing. Formatting was readily accomplished with a compatible external serial device. The Prosys module enables editing of the resistivity measurements and viewing of the 2D sections after acquisitions.

Standard and robust constrain inversion methods were applied to model the 2D electrical resistivity tomography data using RES2DINV software (Loke and Barker, 1996) The file format for inputting the data in the inversion software is described in appendix D.4. The subsurface was discretized into cells with a width half the unit electrode spacing to accommodate the heterogeneities and the variations of the near-surface features.

The measure apparent resistivity data were optimized using the Newton-Gaussian method. The models of measured apparent resistivity data of each profile are shown in Figures 3.8A, 3.9A and 3.10A while models of the inverted resistivity data are shown in Figures 3.8B, 3.9B and 3.10B. The standard smoothness-constrained, least squares method of inversion minimizes the square of the changes in the model resistivity values (de Groot-Hedlin and Constable, 1990).

The robust inversion was chosen over the smooth scheme of the least-square inversion method to obtain sharp layers with clearly defined boundaries. The inversion scheme was preceded by manual examination of the acquired data for anomalies in the data distributions such as high or low values that could indicate bad electrode contact, measurement errors, or noise. The inversion procedure begins with a starting model which is usually a homogeneous Earth model obtained by computing the average of the logarithm of the measured apparent resistivity data. From this

resistivity model, a set of apparent resistivity values that is representative of the real or observed field data is calculated to replicate the resistivity distribution.

The robust inversion-constrained method gives a distinct, sharp contrast compared to the smooth resistivity variations obtained with the standard method. It also reduces the influence of outliers in the inversion model and minimizes absolute changes in the resistivity values (Claerbout and Muir, 1973). In this investigation, the robust constrained inverted models provide an enhanced definition of features. For example, in figure 3.10B, the aquifer was better defined in the robust model.

3.9 Results

Inverted resistivity models (RMS $\neq$ 2 %) were produced from the ERT survey of the three selected profiles and interpreted in terms of the subsurface geology with a guide from the lithology log by the BURGEAP group for *PzSa* (Figure 2.16) and the subsurface geology of the area (Figure 2.10).

Saturated silt and sands beds (12 - 24 Ω m) and other near-surface materials are readily identified at 1 - 2 m depths, whereas delineated resistive features (90 - 124 Ω m) between 10 - 18 m positions of the profile were identified as a paved surface way at <1 m depths.

At the southern end of profile 2 (Figure 3.9), the resistive feature (98 - 138 Ω m) is interpreted as part of the theater's foundation. It extends from the surface to about 2.5 - 4.0 m deep.

An extensive moderately resistive bed (48 - 57 Ω m) interpreted as marls and clays underlain the near-surface heterogeneities. The low permeability bed overlain the thick, 3.5 - 12.5 m, Lutetian limestone sequence (70 - 110 Ω m). The limestone bed is underlain by a conductive bed (12 - 24 Ω m) interpreted as the aquifer at 14 - 16 m depths.

The ERT data acquired at 40 cm (or 0.4 m) spatial resolution allows for dense sampling of the subsurface and detailed definition of subtle geological structures and interfaces, vestiges and other man-made features hitherto not detected in the previous surveys (e.g. Fores, 2013). This electrode spacing has the advantage of higher contrast enhancement compared to the 100 cm (or 1 m) electrode separation readily employed in archaeological search with ERT or classical four-electrode electrical resistivity investigations (e.g. Clark, 1990).

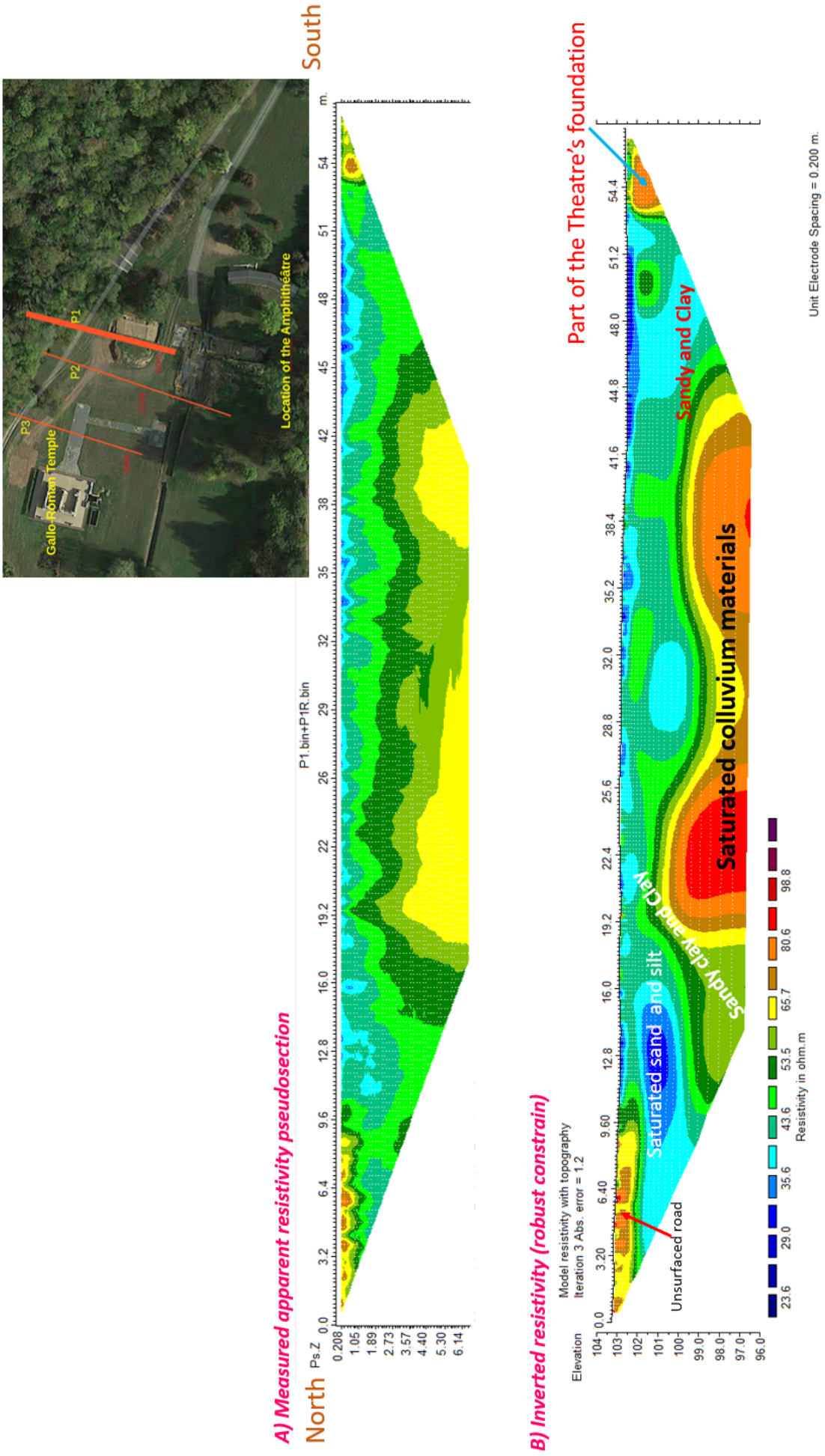

Figure 3.8: Resistivity models of the measured and inverted data showing the inferred geological and hydrogeological units beneath P_1

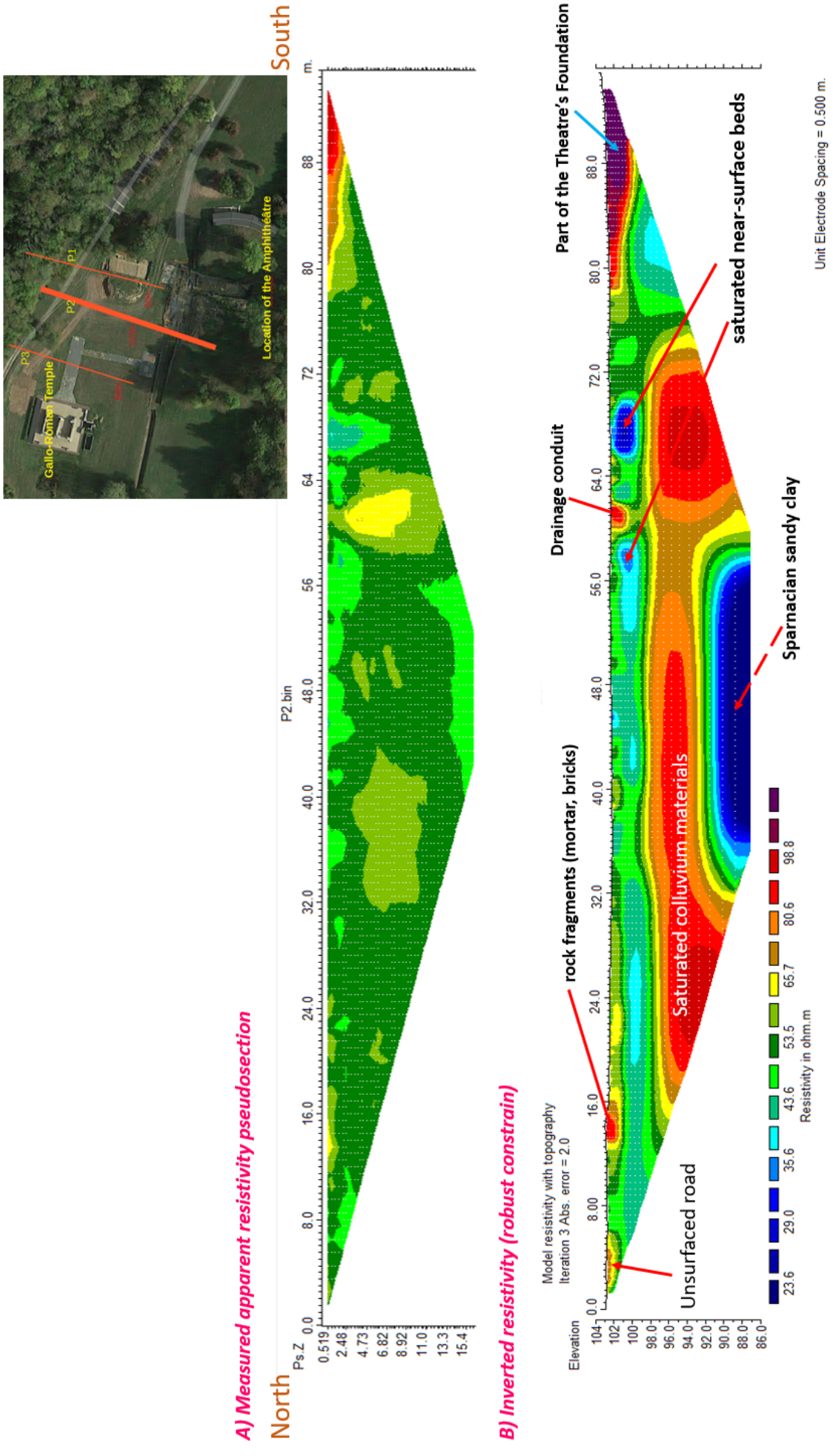

Figure 3.9: Measured apparent resistivity and inverted models showing the inferred geological and hydrogeological units beneath P_2. At the right corner, above the models is a map which the location of the profile line at site

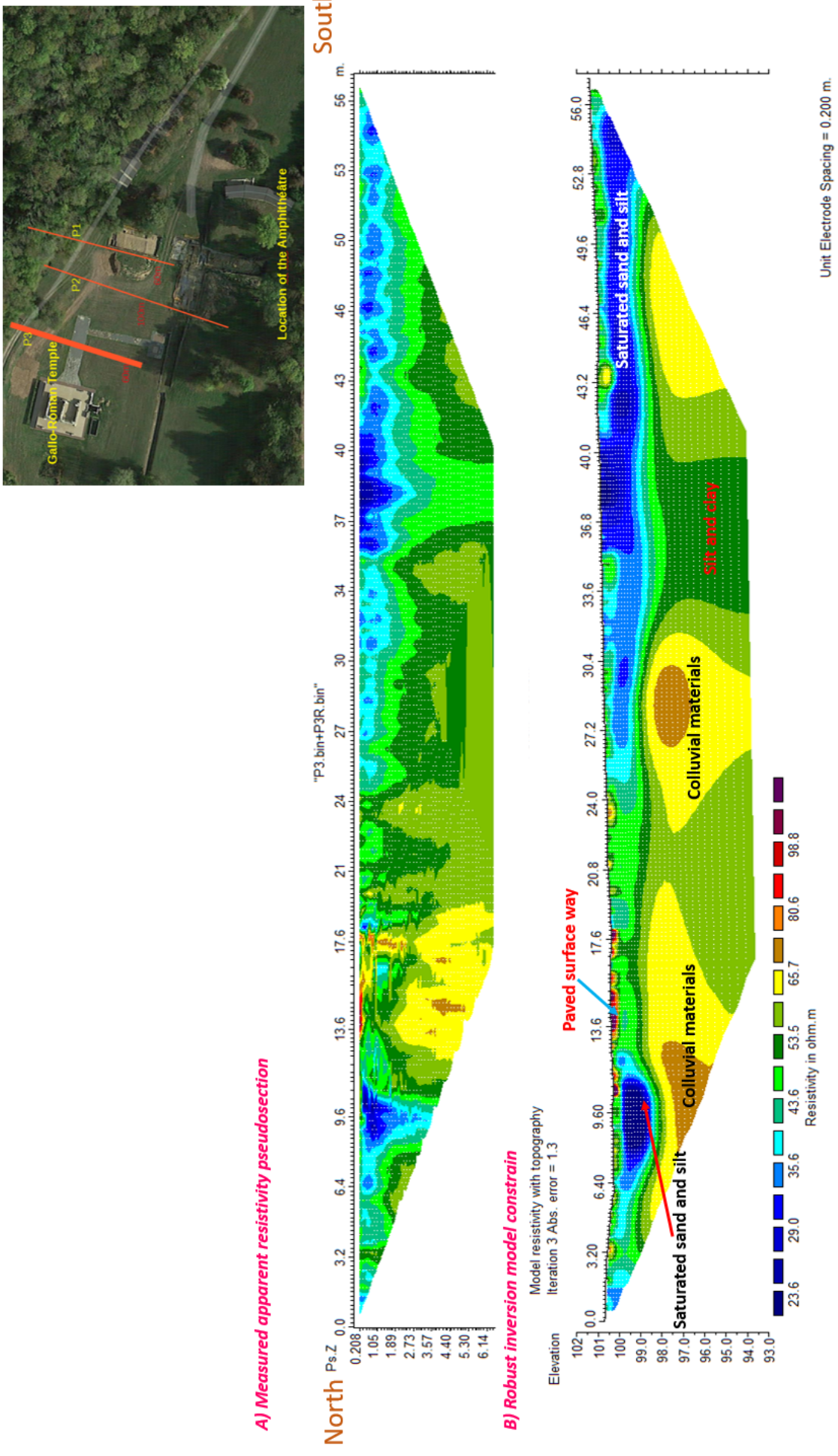

Figure 3.10: Measured apparent resistivity and inverted models showing the inferred geological and hydrogeological units beneath P_3. At the right corner, above the models is a map which the location of the profile line at site

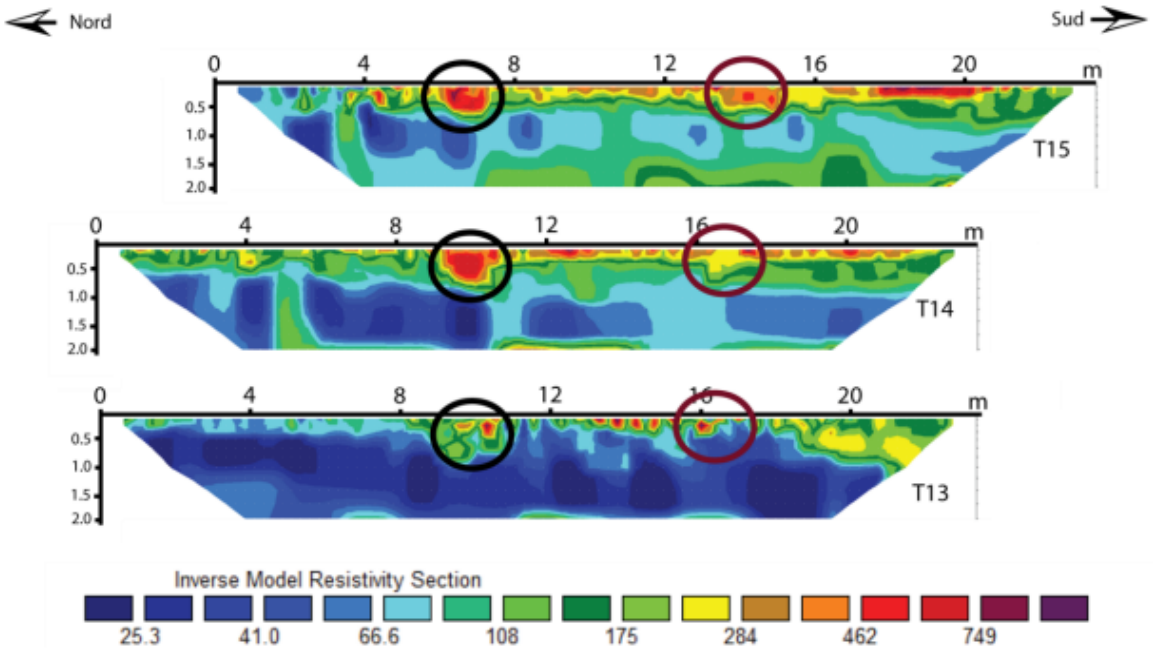

Figure 3.11: Inverted resistivity models of profiles T13, T14 and T15 by Fores (2013). Two anomalies are indicated with a black circle and a red circle at the northern and southern of the profiles.

It thus infers, in the events of prolonged or intense rainfall, the thin sequence of sands and silts overlying the low permeability strata of marls, clays, and limestones readily get saturated leading to the emergence of groundwater at the surface. The surface flow is thus expected to increase in the light of the extreme events. The imaged paved way and theatre foundation give credence to historical and cultural deposits and objects dating to the period of the site occupation.

3.10 Discussion

The ERT survey was carried out with two broad objectives. The first goal was to search for buried historical and cultural anomalies to aid archaeological studies and conservation drives. Hence, for each profile line, a piece of background information was provided in subsections 3.6.1, 3.6.2 and 3.6.3, to highlight the peculiarities that motivated its siting and the spatial question that needs to be resolved. The second goal is mainly to map the geological and hydrogeological response of the beds and structures for a refined definition of the subsurface and to improve the existing information on the knowledge of the geology of the site.

To further aid the visualization of the investigated subsurface, images of sections earlier produced with the classic rainbow colors are reproduced with viridis color scheme for easy comparison for changes in lithology and structures (e.g. Profile P_1 shown in Figures 3.8 and 3.12). Using the

Wenner-Schlumberger electrode array with a finer electrode spacing, the subsurface electrical resistivity distribution obtained with a robust inversion scheme has provided an improved image of the Cultural and Open Air areas (Barrière, 2018). It has laid to rest the idea of a building foundation or a wall structure buried west of the Open Air area extending towards the Temple building (Figure 3.12). No structure was imaged in P_1 and P_2 with a geometric size (or rather, range of resistivity values and corresponding geometry) that can be interpreted as a foundation or wall structure. Hence, no man-made feature elongates from the Open Air area to the Temple site as conceived by the archaeologists (e.g. see Barrière, 2021).

From the ERT sections of P_2 and P_3, the near-surface saturated layer is separated from the lower saturated bed by a less conductive bed. The near-surface bed has variable saturated beds with thicknesses extending from 5 to 7 m.

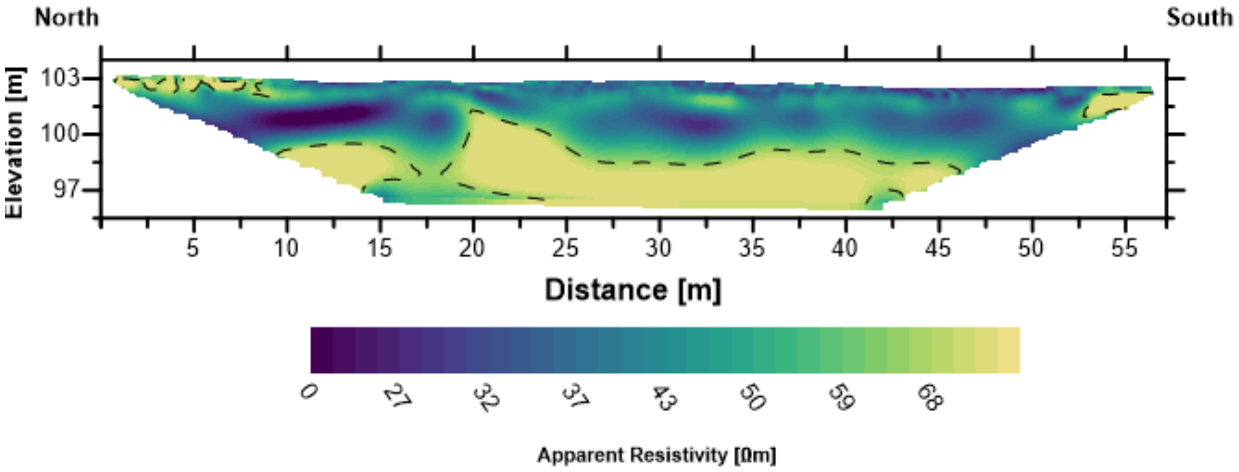

Figure 3.12: Electrical resistivity section beneath profile one (P_1) display with a viridis colour scheme

.

The near surface layer consists of variably saturated materials with resistivity values in the range of 23.6 - 43.5 Ωm and is interpreted to consist of sand, silt, and the remains of the pre-existing *Lutetian* Limestone rocks which now form the alluvial and colluvial soils (e.g. see BURGEAP, 1992). The colluvial soils or colluvium are weathered, transported, and deposited parts of the carbonate rocks; their roles include serving as reservoir rocks (e.g. Zádorová and Pení žek, 2018).

Below the identified near-surface bed is a moderately conductive bed with electrical resistivity values between 65.7 and 98.5 Ωm. This bed has a thickness of 4 - 6 m. From the geology of the site (Figure 2.10), the bed consists of colluvial and alluvial materials from weathered *Lutetian* Limestone and other deposited rock units such as clays.

The next visible bed is a very conductive layer. The layer can be observed in P_2 (Figures 3.9

and 3.13).

From a geo-electric point of view, the three layers in the ERT sections correspond to the responses of the geological beds, which have been accordingly interpreted as mentioned above. The materials in these beds are silts, sands, and clays (Figure 2.10 and 2.16). It is known that silts, sands, and clays are materials with high porosity values (Domenico and Schwartz, 1998, p. 14). These geological materials have the capacity to store and transmit water at different rates (Fetter, 2001, p. 84–89).

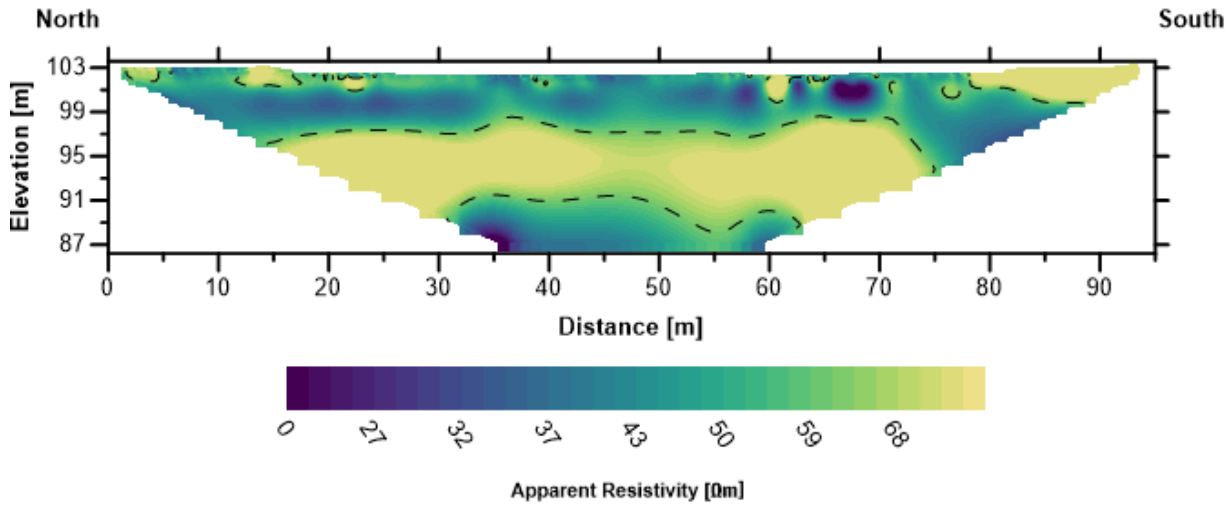

Figure 3.13: Electrical resistivity section beneath profile two (P_2) display with a viridis colour scheme

.

From the subsurface geology of the site, the *Lutetian* limestone and the *Cuisian* sands are the permable rock units. However, the sand units are also found in all the layers described, together with silt. Therefore, in terms of the onsite hydrogeology, the aquifer extends up to near the surface. The top of the aquifer is in contact with the artifacts, while the bottom of the aquifer corresponds to the top of the Sparnacian clay beds (Figures 2.10 and 3.9).

The tomo model of the subsurface beneath the second profile line gives a clearer picture of the presence of the artifacts related to the structure of the amphitheater (Figure 3.9). The foundation of the amphitheater reaches about 4 - 6 m depth, thinning from the seats towards the *podium* and *facade*. It provides an insight into the geometry and construction style employed by the Gallo-Romans. It suggests more materials were used to concretize the seats built in concentric forms, hence the depths in these parts of the theatre. Another insight into the material structure is its non-porous nature as can be deduced from the resistive bed in the tomo section. Therefore, guided archaeological expeditions can conducted to unearth the foundation materials at depths estimated

at 4 - 6 m.

The temple vicinity was revisited with a finer electrode spacing of 0.4 m using the Wenner - Schlumberger spread on a much greater profile length to compare with the outcome of 0.5 m electrode interval used by Fores (2013) with Dipole-Dipole array. The clear advantage of better resolution of features and vertical accuracy provided by the Wenner-Schlumberger spread over other arrays motivated its use in this survey (Hermawan and Putra, 2016; Kneisel and Hauck, 2008; Okpoli, 2013); and also for its wide usage in many terrains (Limestone, Permafrost, crystalline, archaeological, etc) to resolve heterogeneity and discontinuities for contrast as well as mapping of groundwater beds and structures (Clark, 1990; Keary et al., 2002; Kneisel and Hauck, 2008; Loke, 1994; Telford et al., 1992).

The section obtained with the Schlumberger-Wenner array also penetrated more depths compared to the earlier section which did not exceed 4 m and provides a broader view of the geological succession and the buried cultural materials. The section beneath profile P_3 (Figure 3.10 see also Figure 3.14) presence a finer image of the subsurface compare to sections in the same area (see T13, T14 and T15 in Figure 3.7) by Fores (2013). At the northern section of the profile P_3 (Figure 3.6), a resistive bed with a thickness not exceeding 1 m was interpreted as part of the relics of the paved Gallo-Roman road. The position of the imaged bed correlated with the ground expression of a partly surfaced road traversed by the profile (Figure 3.10). The road or the esplanade culturally served as a connection between the temple, the theatre, and the Open-Air zone. The imaged section supports the human activities reported in herein cited references.

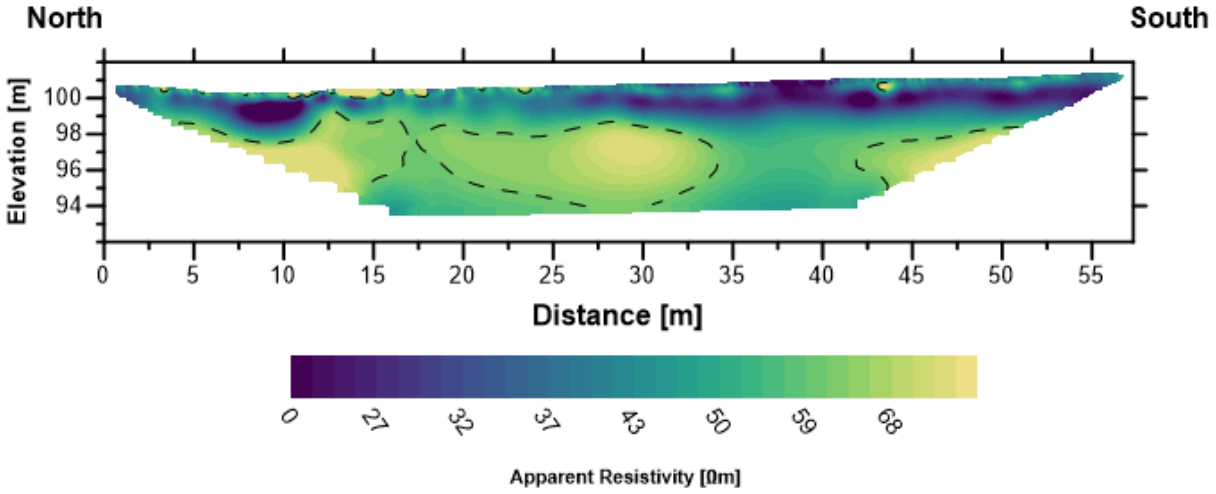

Figure 3.14: Electrical resistivity section beneath profile three (P_3) display with a viridis colour scheme

.

3.11 Conclusion

The finer models of the subsurface from the ERT surveys permit the refining of the archaeological and geological information and the hitherto conceived nature of the subsurface.

The geometry defined in terms of the depth of the amphitheater was determined and other guides to human activities were identified. The curiosity about the spatial continuity of the foundation and walls in the Open Aire has become obsolete.

From the tomographic sections, a three-layer model is proposed for the site based on the distribution of the electrical resistivity values for the subsurface beneath the three mapped profiles: P_1, P_2, and P_3. The first layer consists of alluvium and colluvium including clay and silts, as well as historic and cultural materials and artifacts. It has a depth range of 5 - 7 m. The depth of the ruins extends up to 4 m, especially at the southern end of profile P_2. This layer constitutes the near-surface bed. It has intermittent spatial beds with low resistivity values which correspond to saturated points and sections in the sequence.

The second layer consists of the weathered limestone beds, and its products: silts, clays, and colluviums. The layer thickness is estimated to be 4 - 6 m. It is marked by the near-homogenous resistivity values in the sequence. It covers from the northern to the southern section of both profiles. The resistivity values are greater than 68 Ωm. This bed is clearly delineated in figures 3.13 and 3.14, mainly beneath profiles P_2 and P_3.

The third layer is about 10 - 12 m deep from the Earth's surface. It is a sequence of conductive bed with low resistivity values of below 43 Ωm. The characteristics of the bed inferred from the geology, consist of those of rock units of the weathered *Lutetian* limestone and the *Cuisian* sands overlaid on the *Sparnacian* clay bed. The limestone and the sand beds are the aquifers in the area. The conductive bed from the ERT model is interpreted as the aquifer, hence, consist of the sands with clays as deduced from the site geology and drilled borehole log (Figures 2.3, 2.10 and 2.16).

It can therefore be concluded that the aquifer body extends from the clay-sand unit at the top of the Sparnacian clay bed to the silt, sand, and clay materials at the near surface (Figures 2.10, 3.9, and 3.13). This explains the continuous saturation of the subsurface at the site and therefore confirms the conductive layers at the bottom of the ERT model in profile P_2 and at the near surface in profile P_1. The bottom of the aquifer is therefore at the top of the Sparnacian clay bed, and its top is near the surface and in contact with the artifacts.

CHAPTER 4

Natural field monitoring with active and passive experiments

4.1 Introduction

Natural fields include forces and signals exerted on the Earth by nature and processes that occur naturally in the Earth. Their effects can be measured and utilized passively without deploying any form of energy (Keary et al., 2002; Telford et al., 1992).

By this definition, a wide range of natural phenomena including temperatures and a natural electric field may be included. Natural fields, signals, and processes permit us to investigate the geophysical, hydrological, and geological responses of this historic site and its aquifer.

The natural Earth fields of spontaneous potential, solar heating, barometric pressure, Earth tides, and climatic variables are measured and investigated for the impact of their variations on the aquifer water levels and groundwater flow characteristics. Variations in these fields or signals are known to have an effect and impact on physical processes and physical properties of the Earth (Acworth et al., 2016; Cutillo and Bredehoeft, 2011; Schweizer et al., 2021; Toll and Rasmussen, 2007).

Perturbations in these fields indicate changes in the source or response structure of the signal which can be investigated for its impact on groundwater, aquifer properties, subsurface structures, buried materials, and the environment.

For instance, naturally occurring electric potentials in the subsurface can be measured and ana-

lyzed to provide information on the groundwater flow characteristics and delineation of the subsurface lithology (Maineult et al., 2008; Suski et al., 2006; Titov et al., 2015).

4.2 Meteorological variables and climatic aspects

4.2.1 Introduction

Temperature, precipitation, relative humidity (atmospheric moisture), wind direction, and pressure are among the parameters that define the weather conditions of a location. They influence human activities and the environment, including heritage sites and materials (Bonazza and Sardella, 2023; Sardella et al., 2020).

They provide information on the weather conditions derived from measurements taken over days, weeks, and months. The weather pattern over a long-term period is known as the climate. It spans years and decades.

In the context of global climate change (GCC), exposure to changes in temperature, precipitation, and relative humidity have been identified as among the chief threats to cultural heritage and archaeological materials survival (Sabbioni et al., 2007; Sardella et al., 2020; Sesana et al., 2018, 2021).

Temperature variations in Genainville for the year 2022 - 2023 (Figure 4.1), indicated higher temperatures were recorded in the summer of the year 2022 compared to the same period of year 2023 (e.g. see Lindsey and Dahlman, 2023). The implications include the exposure of the site and materials to climatic and environmental variability which have been reported to cause deterioration of heritage and archaeological materials (Bonazza and Sardella, 2023; Karl et al., 1995; Sabbioni et al., 2007; Sardella et al., 2020; Sesana et al., 2018, 2021).

4.2.2 Materials and methods

Meteorological data including daily mean precipitations (mm), temperature (°C), relative humidity (%) and wind speed (ms^{-1}) from *Wy-dit-joli-Village* meteorological station, situated 6.58 km southeast of the site, were acquired courtesy of the MeteoFrance. These parameters that define weather and climate are classically acquired with different instruments e.g. temperature with a thermometer and relative humidity with a hygrometer. It is important to note that temperature can be measured directly with the thermometer while a parameter like relative humidity can also be defined with an expression. For example, relative humidity is mathematically defined in the

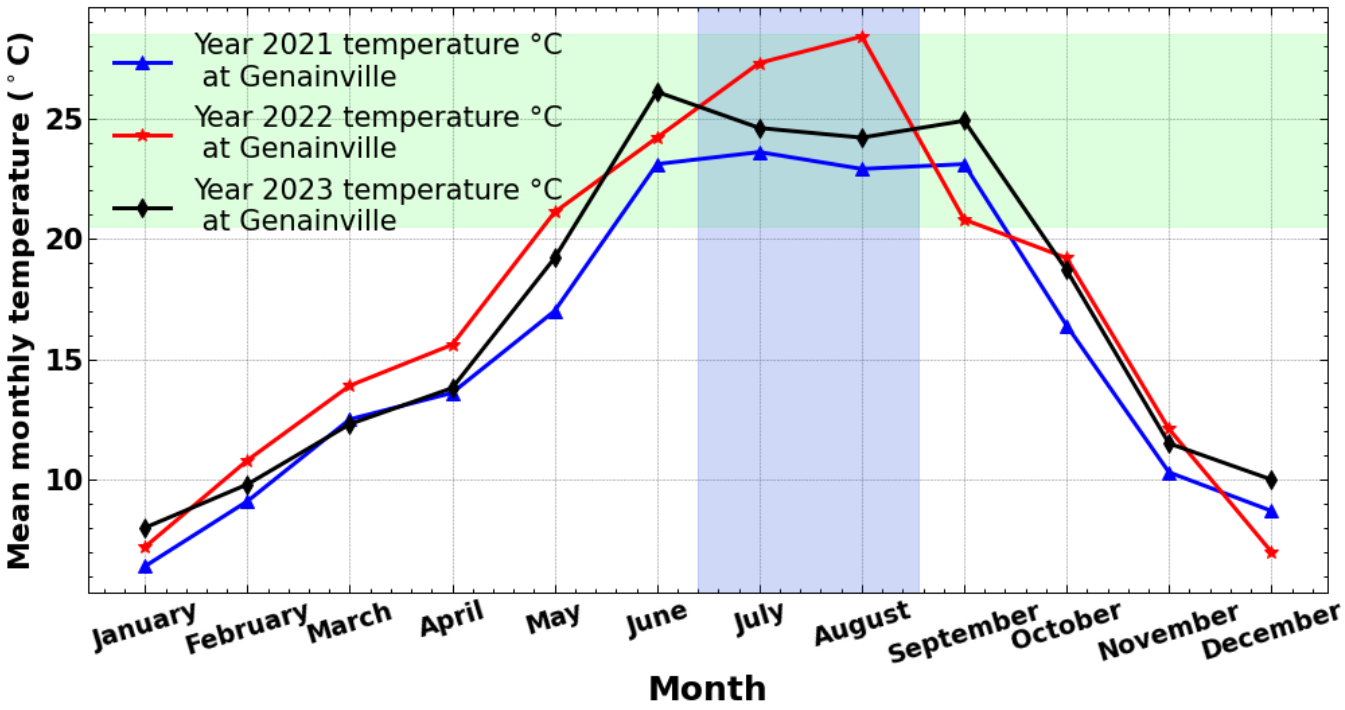

Figure 4.1: Year 2021 and Year 2023 maximum temperatures in Genainville compare with year 2022 maximum temperatures. The data was sourced from MeteoFrance.

relation in equation 4.1.

$$\text{Relative humidity} = \left[\frac{h_t}{H_T}\right] \times 100\% \tag{4.1}$$

where h_t = Amount of moisture in unit volume of air,

H_T = Amount of moisture required to saturate the same volume of air at the same temperature.

For this study, the data are daily mean values of the parameters measured over 24 hours as recorded by the measuring instruments. The monthly changes in temperature, relative humidity, and precipitation are shown in figures 4.2 and 4.3.

4.2.3 Data presentation

The temporal variations of the precipitations, relative humidity, and air temperatures are visualized in figure 4.2. Trends and events in the temperatures display seasonality with visible highs and lows. The hydrological and hydrogeological relations in the site are also discussed in subsection 2.3.2. The Vexin terrain is humid with respective mean and minimum relative humidity values 80% and 37%. The low temperatures of the order of −5°C are recorded. Higher temperature values, sometimes exceeding 40 °C occurs in the months of June, July and August (and some days in September) during the summer period. The mean season value of 11.4 °C can be observe (Fig-

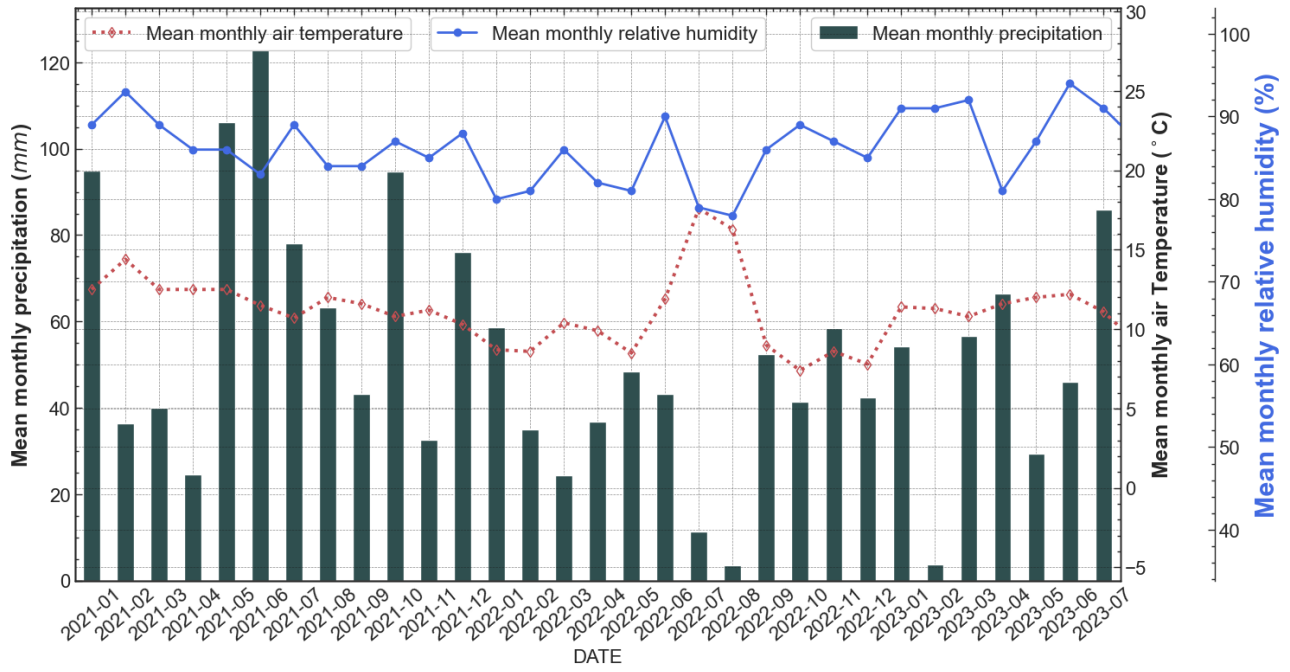

Figure 4.2: Monthly mean precipitation, relative humidity and air temperature data courtesy of MeteoFrance from it *Wy-dit-joli-Village* Meteorology Station

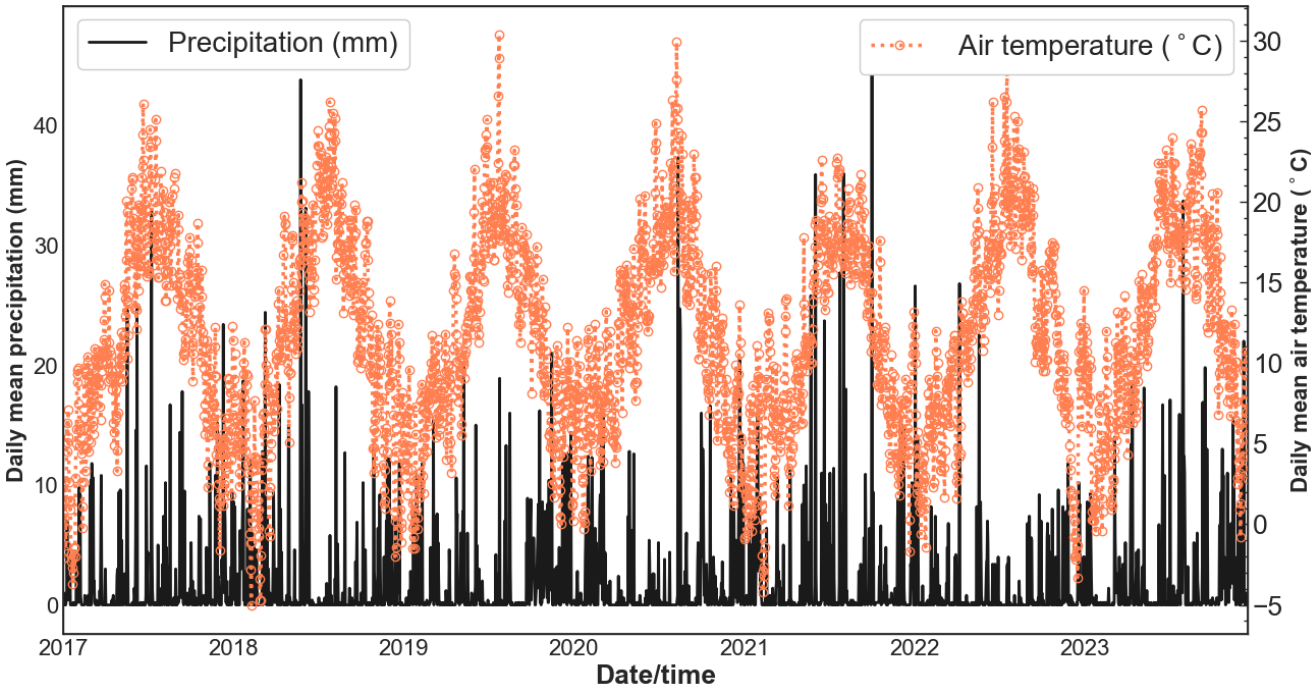

Figure 4.3: Daily mean precipitation and air temperature data courtesy of MeteoFrance from it *Wy-dit-joli-Village* Meteorology Station

ure 4.3).

With a daily mean precipitation of about 47.8 mm and a minimum of 1.84 mm, the site experience continuous wetting of the land and buildings. The intensity and frequency of rain events is expected to increase with GCC (e.g. see ACIA, 2004; Hollesen et al., 2016; Sabbioni et al., 2007;

Sardella et al., 2020). The heritage materials and structures are exposed to this changes in the environmental conditions (see e.g Araújo et al., 2021; Bonazza and Sardella, 2023; Dunleavy, 2021; Hollesen et al., 2018; Karegar et al., 2017; Save et al., 2012; Sesana et al., 2018, 2021; Smith and Zeder, 2013).

4.3 Groundwater monitoring

4.3.1 Acquisition set-up

In line with the principle of minimum intervention, a number of boreholes were previously drilled, at different times for hydrological and geotechnical studies at the site. For this study, three water boreholes were equipped with piezometers (Figures 4.4 and 4.5). The water boreholes are located at the Store House Frontage, West of the amphitheater, Sacred area (southwest of the temple building), and designated PzShf, PzTh and PzSa in this study (Figure 4.4; Table 4.1).

4.3.2 Diver sensors

The barometric pressure sensor known as the Baro-Diver, has ± 0.5 cm accuracy for pressure readings; ± 0.1 $^{\circ}C$ accuracy and 0.01 $^{\circ}C$ resolution for temperature recordings. The TD-Diver is an autonomous submersible sensor for measuring water levels or water pressure in boreholes (e.g. see Figure 4.5), it has ± 0.5 cm accuracy and ± 0.2 cm resolution for water pressure data, while it has ± 0.1 $^{\circ}C$ accuracy and ± 0.01 $^{\circ}C$ resolution for temperature data. Variations in the water levels are visible features in the three hydrographs in figure 5.6. The trends and patterns are similar with different response amplitudes to the fluctuations. An exception can be observed in *PzSa* from July where the water levels is rising compare to decrease in the other two borehole *PzTh* and *PzShf*.

Table 4.1: Location of Boreholes

Borehole Location	Coordinates	Elevation	Depth	Diameter of casing
PzSa (Sacred Area)	49.12027° N, 1.77083° E	99.00 m	9.78 m	80 mm
PzShf (Store House Frontage)	49.12000° N, 1.77333° E	100.56 m	11.06 m	70 mm
PzTh (West of the Theater)	49.11972° N, 1.77083° E	102.66 m	7.35 m	52 mm

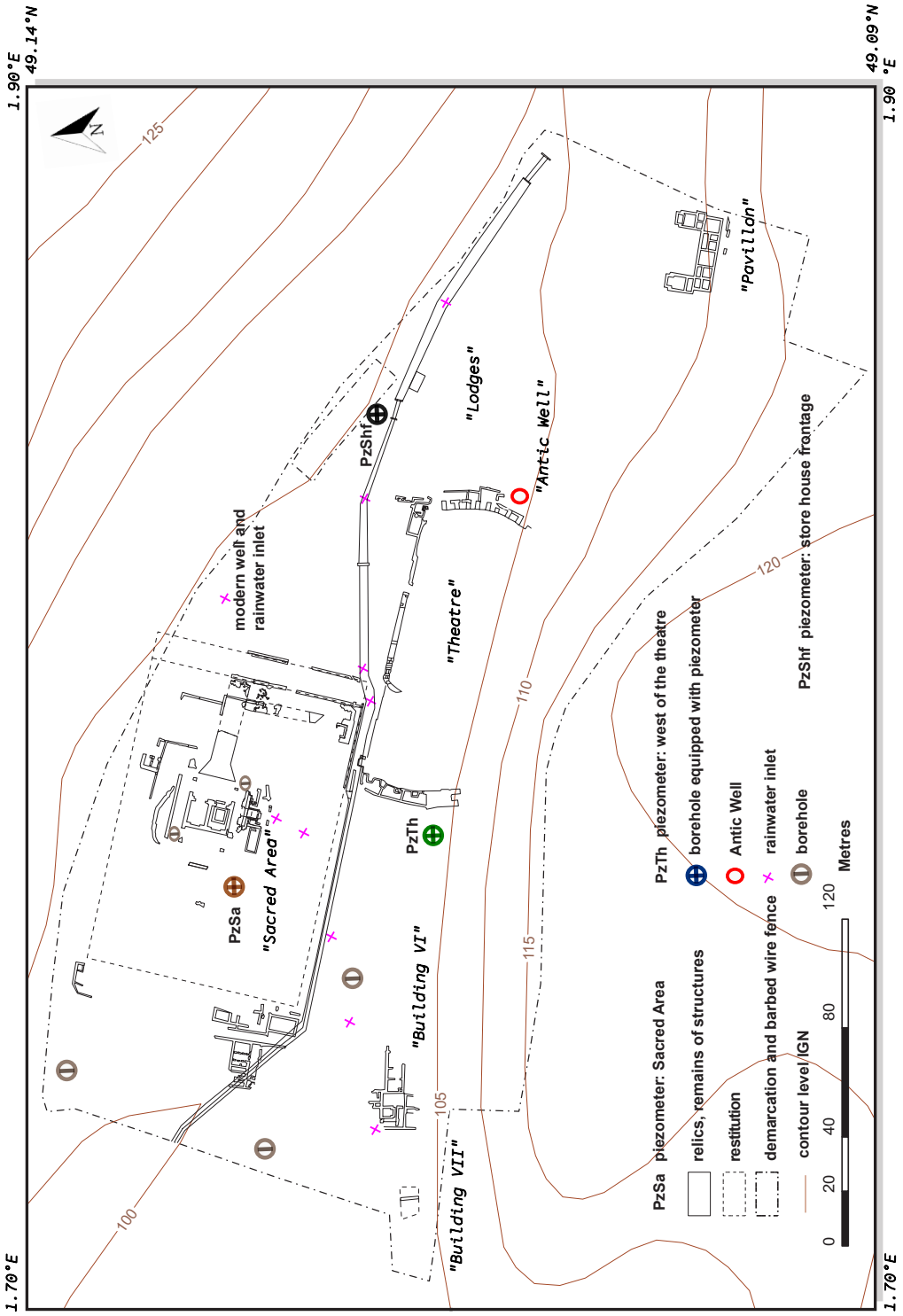

Figure 4.4: Location of boreholes equipped with piezometers at the Sacred Area, Store House Frontage (field building for keeping of survey tools, equipment and storage of excavated relics and artifacts), and West of the Theater respectively designated as *PzSa*, *PzShf* and *PzTh* with other bores and water inlets. The positions of the ruins of the temple and amphitheater and building are shown.

4.3.3 Groundwater data description

A chronicle of borehole water pressure (water column above the sensor) (BL) and groundwater temperature (WT), barometric pressure (BP) and air (surface) temperature (AT) and date time datasets were acquired simultaneously at `60 seconds sampling intervals` with autonomous sensor probes submerged in the water borehole for the BL and WT datasets or installed near at the surface level (on the wellhead) for BP and AT data (Table 4.2). The data was retrieved at intervals from the piezometers; pre-processed and concatenated to produce long series datasets covering years 2017, 2018 and 2019 for the first set of data; and 2020 – 2023 for a continuum of the subsequent datasets.

The *first set* of dataset were collected from *PzShf* while the *second set* of Piezometer data were acquired simultaneously at *PzShf* and *PzTh* from year 2020.

PzSa was included in 2022, to allow for comparative analysis of the time series for localised to site scale, spatial hydraulic relationships. A model plot of the continuous water pressure measured in the three boreholes from 2022 - 2023 is shown in figure 5.6.

The data was accessed and visualised using a computer program written in python programming language (appendix C.3.1).

Figure 4.5: The TD-Diver installed at PzSa

4.4 Barometric pressure data: materials and method

Barometric pressure is among the natural forces that cause aquifer water levels to fluctuate (Rasmussen and Mote, 2007; Rasmussen and Crawford, 1997; Toll and Rasmussen, 2007). Continuous measurement of barometric pressure at 1 minute interval was carried for long term assessment of it effect (Table 4.2). The variations in barometric pressure and air temperatures is shown in figure 4.7.

Table 4.2: Data sets and acquisition tools

Description	Data type	Instrument/Code	Sampling interval
	Hydraulic response		
Subsurface	Water pressure (kPa) Groundwater temperature (°C)	TD-Diver	60 seconds
Surface	Barometric pressure (kPa) Air temperature (°C)	Baro-Diver	
Tides	Solid Earth tides (nm/s^2)	$PyGTide$*	

*Rau (2018)

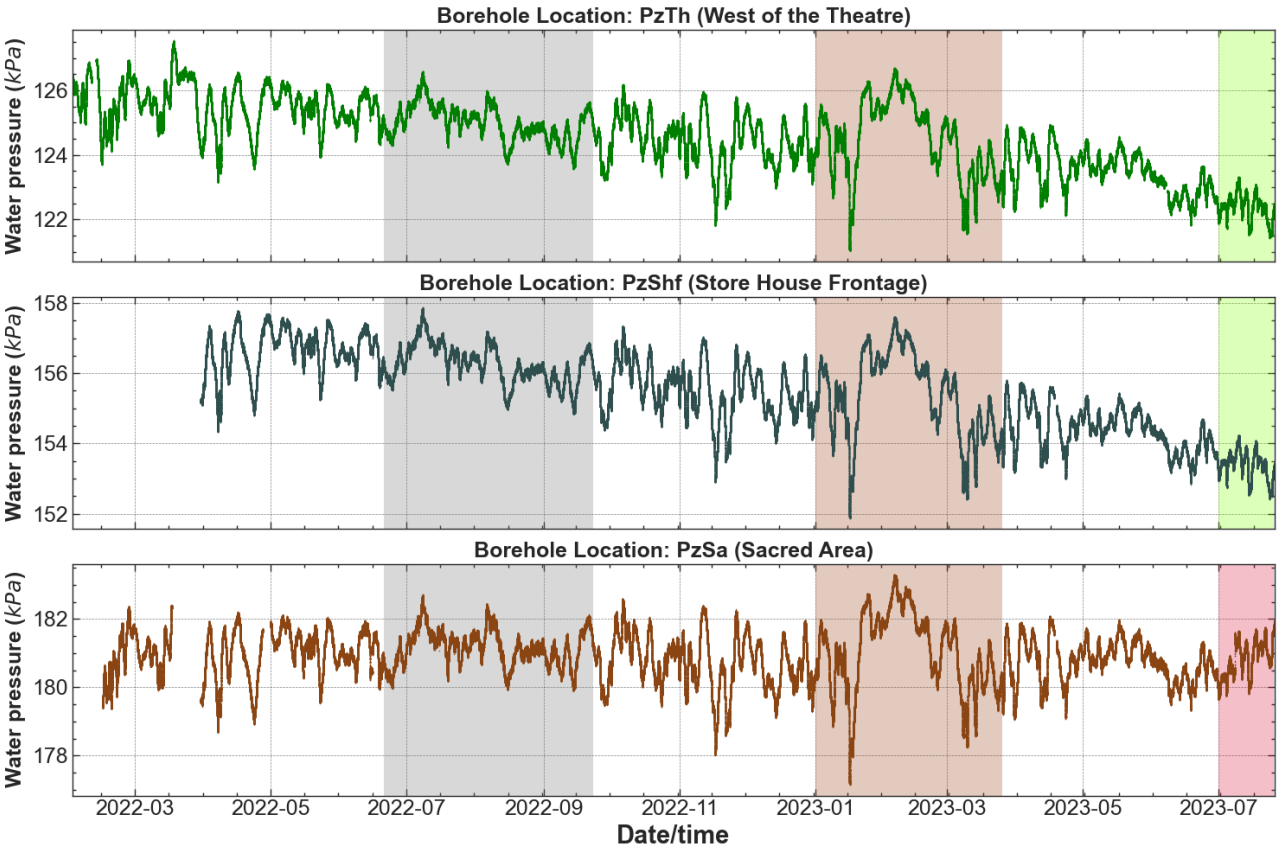

Figure 4.6: Borehole water pressure in the three boreholes acquired at the same period from January, 2022 to July, 2023. Minor gaps in the data due to retrieval and re-installation procedures were between 10 - 15 minutes while major gaps were caused by instruments failure and or disruptions in the acquisition sequence by non-anthropogenic influences.

4.5 Earth tides model

Theoretical Earth tides parameters were computed using the *PyGTide* code by Rau (2018), based on the *ETERNA PREDICT* program by Wenzel (1996), at intervals of *1 minute* (Table 4.2). The synthetic tides were calculated for the three water borehole locations. The input variables use for

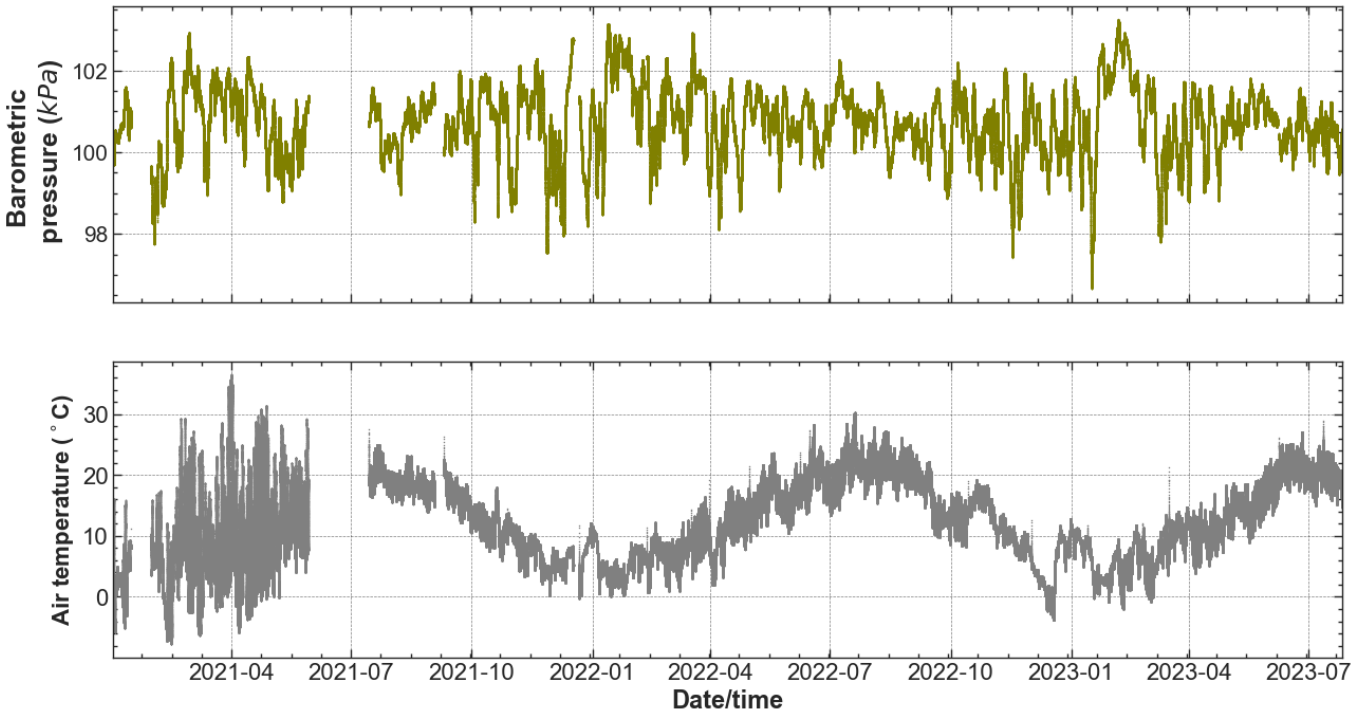

Figure 4.7: Barometric pressure and air temperature variations sample at the interval of 60 seconds.

the computation include the geo-parameter of the location, the sampling rate of the solid Earth tides, the start date and the duration (Table 4.1). The duration defines the calendar period or the date of interest whist the geo-parameter of the location provide the longitude, latitude and elevation data. PyGTide is *ETERNA PREDICT* wrapped in python language. It is based on the latest tidal catalogue which included the *PREDICT* by Kudryavtse (2004). *PyGTide* has the advantages of the input of the updated tidal catalogue and comparative accuracy over similar software use for Earth tides computation e.g. TSoft (Van Camp and Vauterin, 2005).

The output of *PyGTide* incorporating the effects of pole wobble and length of day influences in the computation of the combined Earth tides effect (Rau, 2018; Rau et al., 2020). The computed combined tides were use in this analysis and referred to as Earth tides in this thesis. Figure 4.8 is a computed theoretical earth tides model for `PzSa`.

4.6 Temperature monitoring and thermal tracing experiments

4.6.1 Introduction

Herein is reported the detail experimental procedure deployed to study the thermal response of the subsurface fluid and materials in this site. The idea came from the observation of thermal signatures in time with raining events in PzTh.

Thermal experiments were performed following the response recorded of the groundwater and air temperatures in the site. The two temperatures showed seasonal alternation with variations in amplitudes (Figure 4.9). The investigation was complemented with additional temperature sensors installed in *PzSa*. The studies was preceded by continuous monitoring of the background electrical potential field (see section 4.8) and aquifer evaluation experiments to perturb the natural electric field. The data sets acquired for the analysis are shown in table 4.4. Groundwater temper-

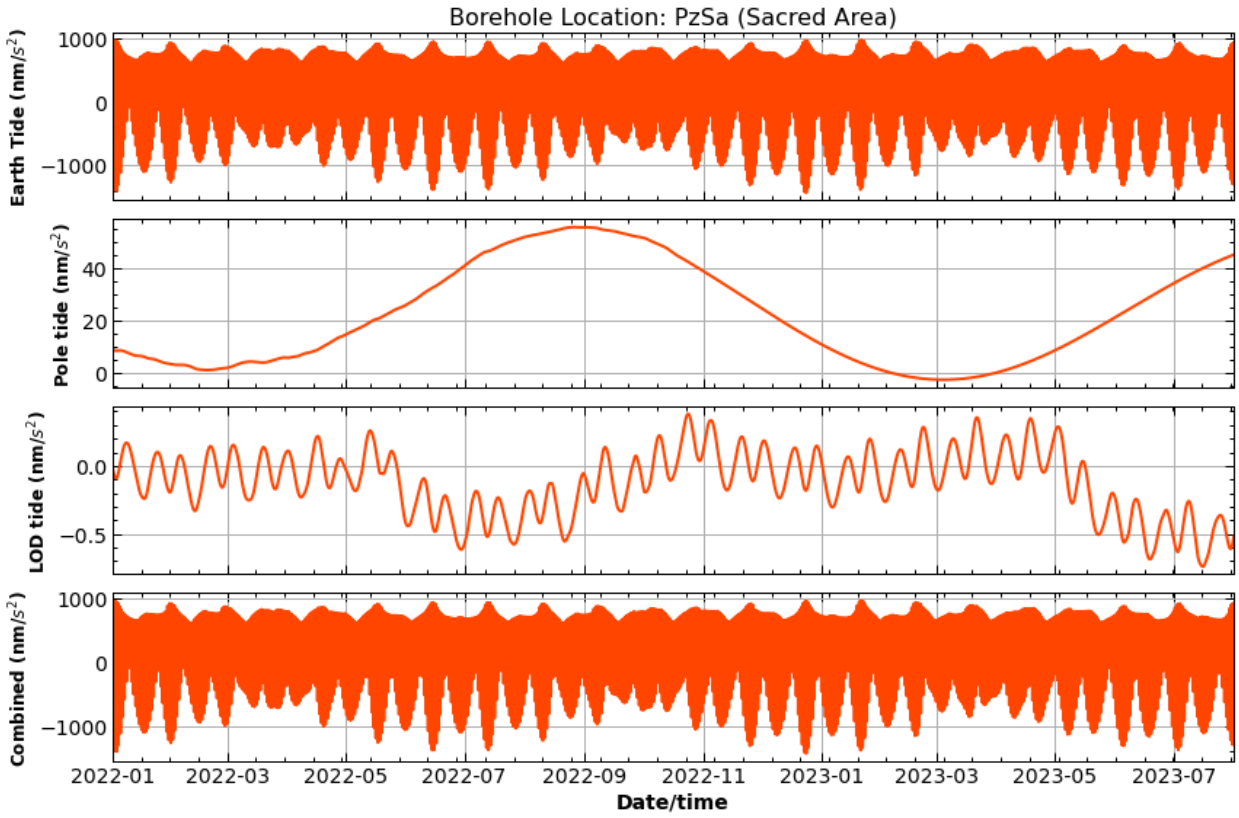

Figure 4.8: Theoretically computed Earth tides model using PyGTide code Rau (2018). The calculation of the variations in gravity on Earth induced by the relative motions of astronomical bodies such as the sun and moon takes into account the pole wobble and the Length of day (LOD) influences to produce the combined effect. An example is this plot of the Earth tides variations at the Sacred Area borehole geolocation.

Table 4.3: Sensor depths in the boreholes

Borehole	Sensor depth
PzSa	7.60m
PzSfh	9.30m
PzTh	6.47m

ature is a vital tool for characterising the subsurface thermal properties, assessing flow parameters

and couple hydraulic properties (e.g. Bucci et al., 2020; Cartwright, 1974; Domenico and Schwartz, 1998). Fluid injection experiments, such as hot water (Yang et al., 2010) or cold water (Shapiro et al., 1997) have been used to estimate the permeability, thermal diffusivity or hydraulic diffusivity of subsurface (rock) sequence. The introduction of hot fluid into the subsurface changes the pore pressure relation and the thermal state of the fluid system. The spatio-temporal distribution of the injected fluid results from the permeability of the medium. Following the relation observed

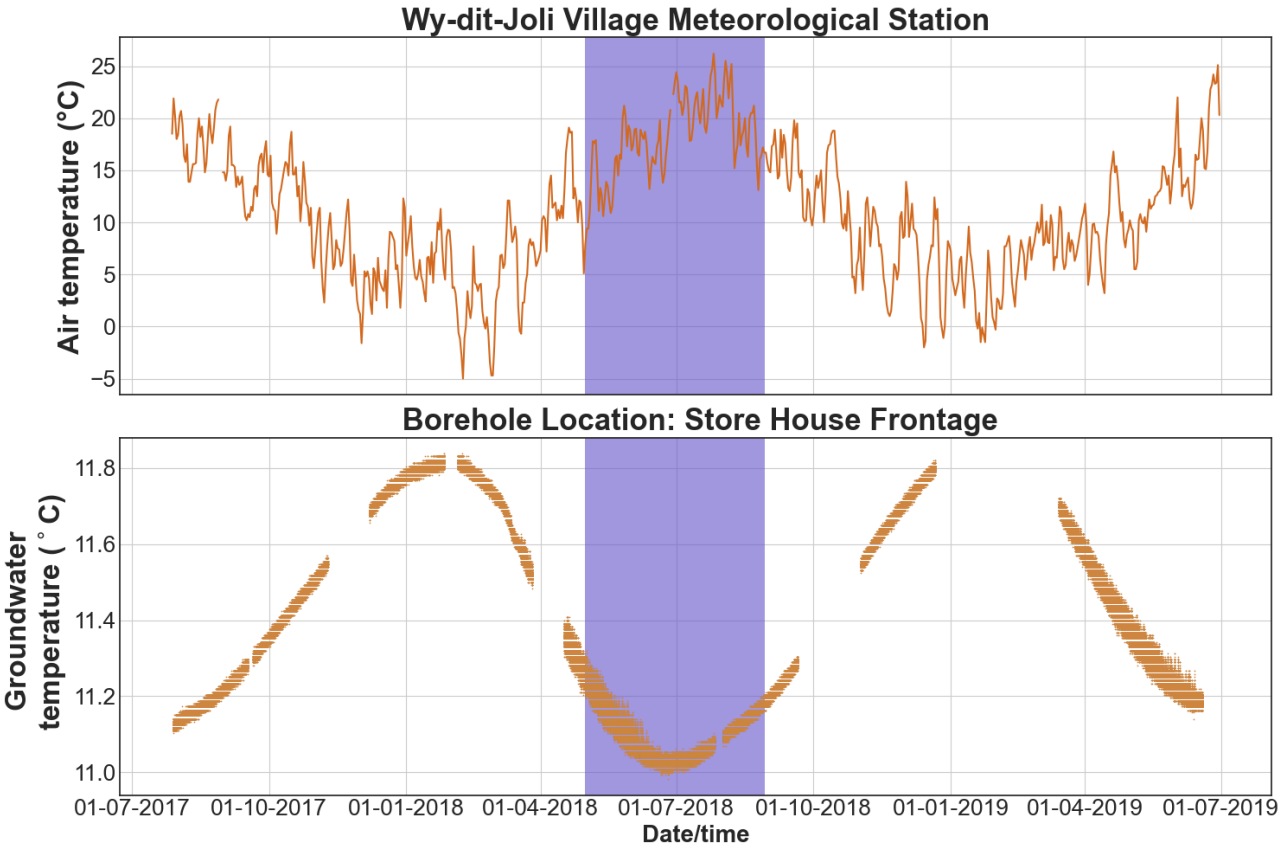

Figure 4.9: Groundwater temperatures recorded in *PzShf* and measured air temperatures.

in the air-water temperatures plot in figure 4.9. The temperatures of the air (at the site) and the water in the boreholes were also recorded during this thesis (Figure 4.10). Both the air and water temperatures were recorded continuously at 60 seconds intervals (Table 4.2). The variations in the air temperatures were measured with the Baro-Diver and compare with the temperatures of the water in PzTh and PzShf recorded with TD-Diver (Figure 4.10).

The temperatures of the water in the boreholes PzTh and PzShf show similar sinusoidal pattern (Figure 4.10). Phase-shifted behavior of air temperature versus borehole water temperatures can be observe in figure 4.10. This shift can be attributed to the difference in the depth of the sensors installed in the boreholes (Table 4.3).

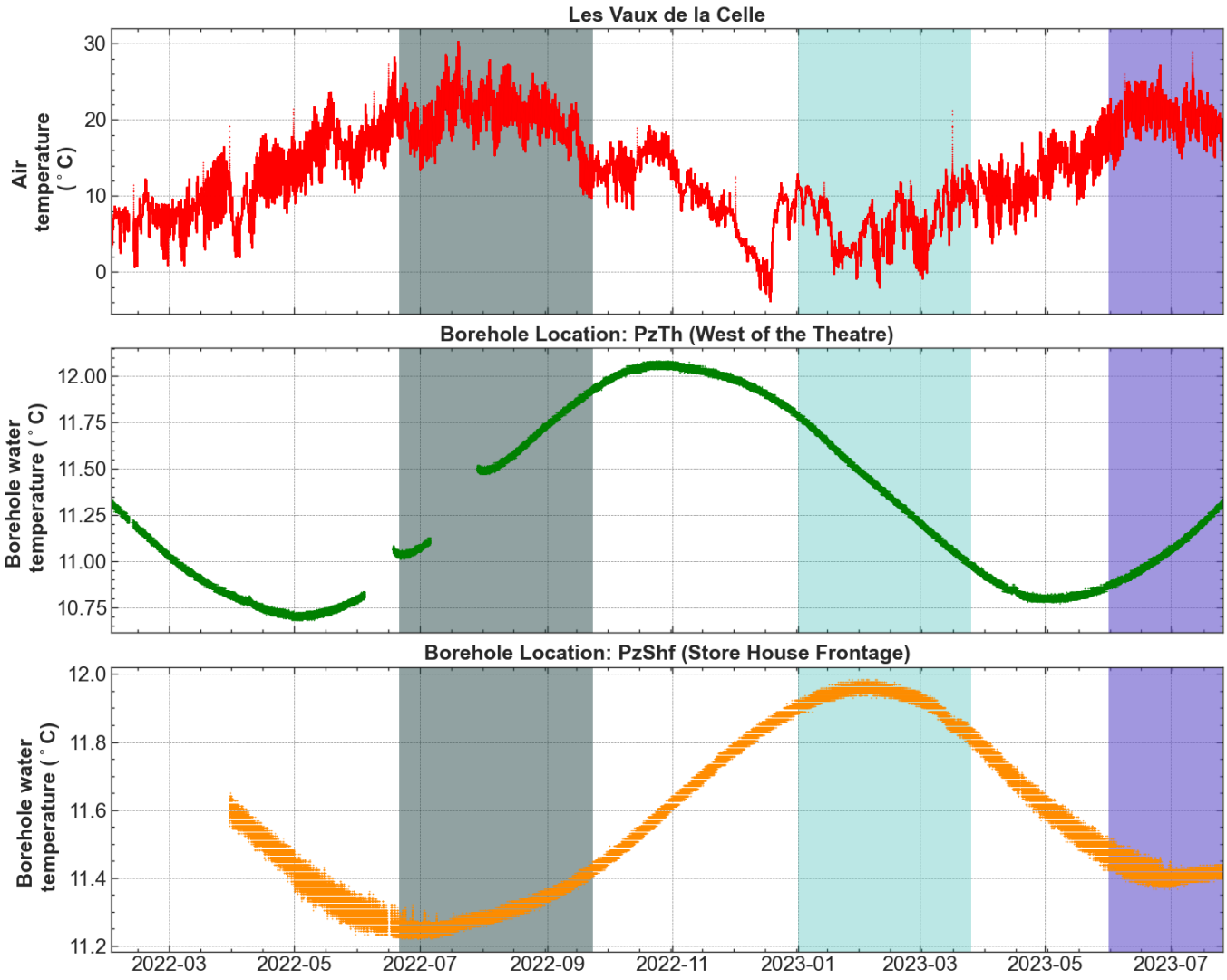

Figure 4.10: Temperatures of the water in the boreholes and the air at the surface.

4.6.2 Theoretical information

Fourier's law described the heat flow from one region to another (equation 4.2). Conceptually, heat is conducted from where the temperature is high to where it is low in a solid or liquid (Domenico and Schwartz, 1998).

$$q = -k\frac{dT}{dx} \tag{4.2}$$

where k, is the thermal conductivity ($Js^{-1}°K^{-1}$) of the medium, $\frac{dT}{dx}$ is the gradient or change in Temperture T and q is the amount of heat (Q) that flow through a unit cross sectional area(A) per unit time t, hence equation 4.3.

$$\frac{dQ}{dt} = kA\frac{dT}{dx} \tag{4.3}$$

The one-dimensional equation by Fourier can be solved with the diffusion equation (equation 4.4) to account for spatio-temporal behaviour of the heat as it travel in time and space (Domenico and

Schwartz, 1998; Yang et al., 2010).

$$\frac{\partial T}{\partial t} = \frac{k}{\rho c_p}\nabla^2 T + \frac{A}{\rho c_p} - \vec{v}\cdot\nabla T \tag{4.4}$$

One analytic solution to the diffusion equation is the complementary error function (equation 4.5).

$$\mathrm{erfc}(\eta) = 1 - \mathrm{erf}(\eta) \tag{4.5}$$

By solving the generalised one dimension diffusion equation for the spatial and time variant of the temperature (equation 4.4). The transient temperature distribution can be estimated with an error function (erf). By classic mathematics the modified erf also known as complementary error function (erfc).

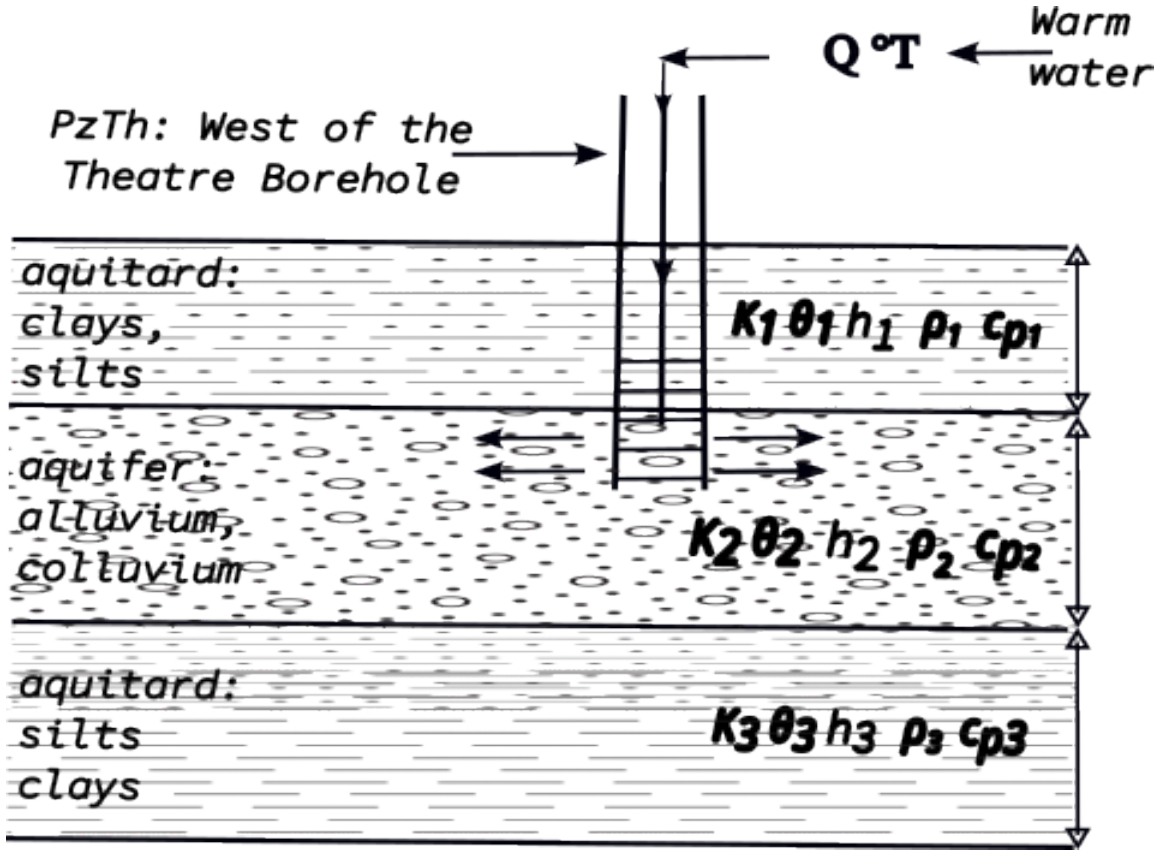

Figure 4.11: Conceptual model of the subsurface showing aquifer overlaid and underlaid the aquiclude at PzTh. $^{\circ}T$ = temperature of warm water pumped at a constant flow rate Q into the borehole, while K, θ, h, ρ, and c_p respectively represent the thermal conductivity, porosity, thickness, density and specific heat the of each bed denoted with a numeric subscript as 1, 2, or 3.

4.6.3 Experimental procedure for the injection tests

For the injection test, the West of Theatre borehole (PzTh), was designated the injection well while the PzSa was the observation well installed with SBE thermal sensors. The concept of the experiment is presented in figure 4.11 with information derived from literature (e.g. see Cartwright, 1974;

Domenico and Schwartz, 1998; Yang et al., 2010). The PzTh penetrates the overlying colluvium and alluvium which include clays and silts into the aquifer which consist of the *Lutetian* Limestone and the Cuisian sand beds. For a site conceptual model, a three-layered aquiclude-aquifer-aquiclude structure is put forward. The first layer is the aquiclude and beneath it is the aquifer and beneath the aquifer is the aquiclude. The acquisition steps is summarised below:

i. Submersible pump was installed in the first bath and hosed or piped to the reservoir placed meters away (Figure 4.12).

ii. The temperature of the water in the bath was recorded with a thermometer.

iii. Water was pumped at a constant rate from the bath to the reservoir.

iv. The time when pumping started and stopped was recorded.

v. The reservoir was kept in the field (for a period of time) to received solar energy and heat the enclosed water.

vi. The temperature of the warm water in the reservoir is measured with a thermometer (Table 4.5).

vii. The submersible was submerged in the reservoir and hosed to the West of the theatre borehole designated PzTh (Figure 4.12).

viii. The temperature of the borehole water in PzTh was recorded in the field note book.

ix. Water was pumped at the same flow rate from the reservoir to PzTh.

x. The time this second pumping began and ended was also recorded.

xi. The data registered by the two piezometers in the Sacred area, PzSa and West of the theater, PzTh boreholes were retrieved (during the routine period of data collection), access and visualized, thereafter treated and analysed.

Thermal tracing experiments and temperature monitoring were performed first by monitoring continuously the air temperatures and measuring the groundwater temperatures in the three water boreholes. The plot of the air and groundwater (or borehole water) temperatures show sinusoidal patterns (Figures 4.9 and 4.10). Qualitatively, the air- borehole water temperature curve patterns alternate reflecting seasonal response to climatic times. The response thus suggests that solar heating and thermal characteristics of the sequence have a plausible effect on the groundwater. It thus, led to the second study on the thermal response of the solid and fluid media in the

Table 4.4: Data sets and acquisition tools: thermal investigations

Aquifer evaluation and thermal test		
Description	**Instrument/Code**	**Sampling interval**
Aquifer test: a. Classic test b. Harmonic pumping	a. TD - Diver b. Submersible pump and accessories	60 seconds
Thermal experiment	TD - Diver SBE temperature logger	10 seconds

archaeological site.

The thermal response of the subsurface to changes in temperatures (diurnal, seasonal, etc) as a function of the thermal diffusivity and hydraulic conductivity of the subsurface and fluid was investigated with field-based thermal tracing experiments. The composite thermal response was assessed in three ways: continuous recording of the water temperatures, the aquifer evaluation test via harmonic pumping, and thermal tracing experiments.

4.6.4 First experiment phase

The first thermal experimental phase was described in subsection 4.6.1. It involved the continuous recording of the groundwater temperatures in the three water boreholes equipped with T-D Divers (Tables 4.5 and 4.5). The results are shown in figures 4.9 and 4.10. This was succeeded by the second and third phases. In the second phase of the experiment, pumping test was performed with pumping, relaxation, and reinjection of the pumped-out water, while the third phase involved the injection of hot water into the west of the theatre borehole for a response model.

4.6.5 Second experiment phase

In the second thermal sub-experiment, a submersible pump was installed below the water levels in the first Gallo-roman bath located south of the temple building (oriented east- west) and hose to an artificial reservoir. The reservoir is made of plastic and has its interior and exterior painted black. The plastic reservoir tank has a capacity (volume) of 1 m^3.

The Submersible pump has 0.5 horsepower (hp) energy usage and a constant **pumping rate** of 35 litres per hour as it pumps water from the first basin into the reservoir.

Table 4.5: Temperature of warm water pump from the reservoir to *PzTh*

Date	Temperature of water	Date	Temperature of water
from Gallo-Roman bath to reservoir		from reservoir to PzTh	
04/07/2022	15.00 °C	06/07/2022	26.50 °C
06/07/2022	16.00 °C	08/07/2022	24.50 °C
08/07/2022	16.00 °C	10/07/2022	27.00 °C
		12/07/2022	31.00 °C

The water-filled reservoir tank was placed 40 meters away from the water source (Gallo-roman bath). Throughout the experiments, the reservoir was placed on wooden (non-conducting) pallets measuring 2.0 × 2.0 × 0.1 m.

The reservoir is kept in the open field to attract and absorb solar energy and heat the enclosed water by convection. From the natural heating that ensued, the reservoir attracts solar radiation and transmits the energy to the water thereby raising the temperature of water in the reservoir to a value much higher than the value of the stored subsurface water temperature. The temperature of the reservoir water was measured before injection into PzSa.

Ideally, for this experiment the water temperature is expected to be higher than the initial temperature of the water in the bath. To perform the injection, the submersible pump was introduced into the reservoir and kept at the base. At the same discharge rate of 35 liters per hour, the hot water in the reservoir was pumped into the west of the theatre borehole. The temporal exposure of the water to solar heating during the experiment was prolonged in the third phase of the experiment (see subsection 4.6.6).

4.6.6 Third experiment phase

The procedure of the experiment described in the second sub thermal experiment was followed in the execution of the third phase of the thermal tracing experiment with the additional installation of three vertically arranged and spaced temperature loggers in the PzSa. The temperature logger manufactured by Sea bird Electronics (SBE) has a data resolution of 0.0001 °C and stores 2.4 million samples at 60 seconds sampling interval in 1669 days. Its measurement sensitivity ranges from -5 to +45 °C with initial accuracy of 0.002 °C .

The SBE sensor has inbuilt capability to convert stored data to retrievable temperature (°C) and

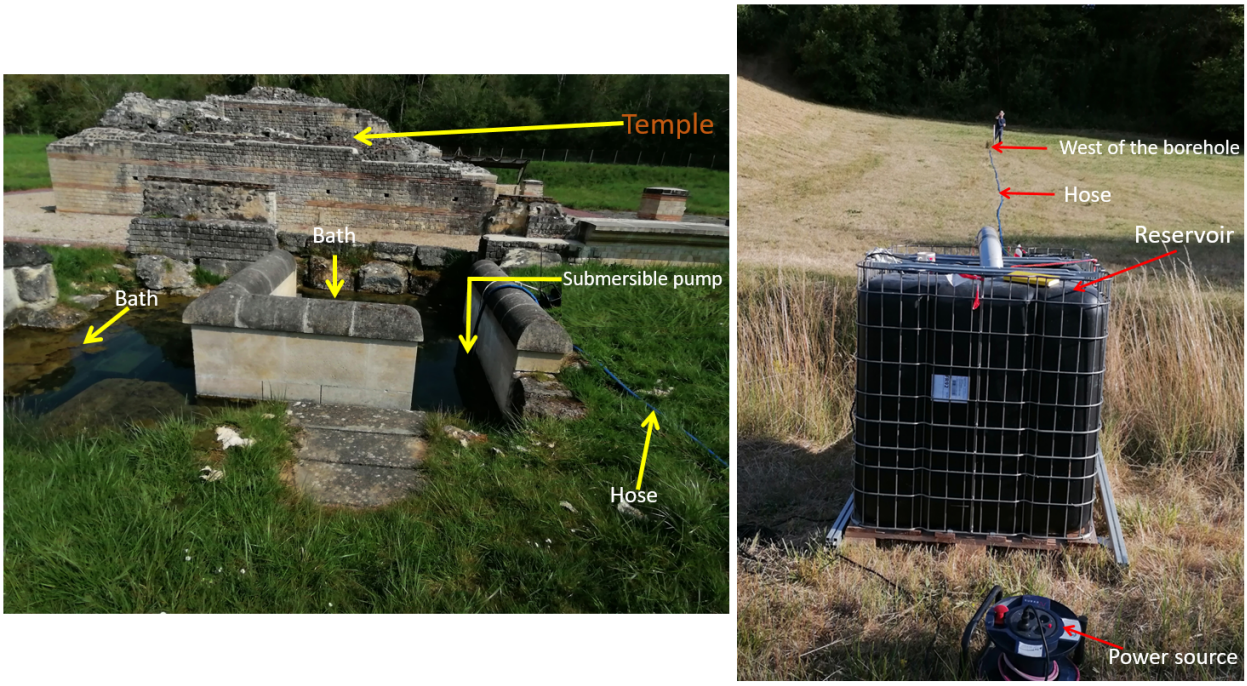

Figure 4.12: Thermal tracing experiments: water from the Gallo-roman baths was pumped and hose into a reservoir kept in the field to be heated by solar radiation and subsequent discharge into PzTh

Date/time output in ASCII format. It has a flexible user-defined sampling interval of 0.5-second to 9 hours. For this operation, the data sampling interval was programmed for 60 seconds.

The three temperature sensors manufactured by Sea-Bird Electronics (SBE) namely SBE 686, SBE 687 and SBE 688 were set up conceptually to aid the identification of possible thermal stratification induced by the introduction of water as it diffuses through the subsurface sequences (Table 4.6 and Figure 4.13). The registered temperature data could conceptually differ in magnitude in an ordered sequence. The retrieved data from the three sensors were compared with the temperature component recorded by the TD diver. The rate of mixing (of hot and cold water) as hot water flow

Table 4.6: Thermal sensors submerged at different depths along the piezometer in the sacred area borehole

ID of temperature sensor	Placed depth (metre)	Diffusion, hot-cold mixing levels
SBE* 686	2.70	Measure surface water
SBE 687	5.50	Intermediate flows
SBE 688	8.20	Lower / bottom flow

from the higher potential, west of the theatre area to the lower elevation points in the sacred area could be registered with variances by the three sensors (Figure 4.13).

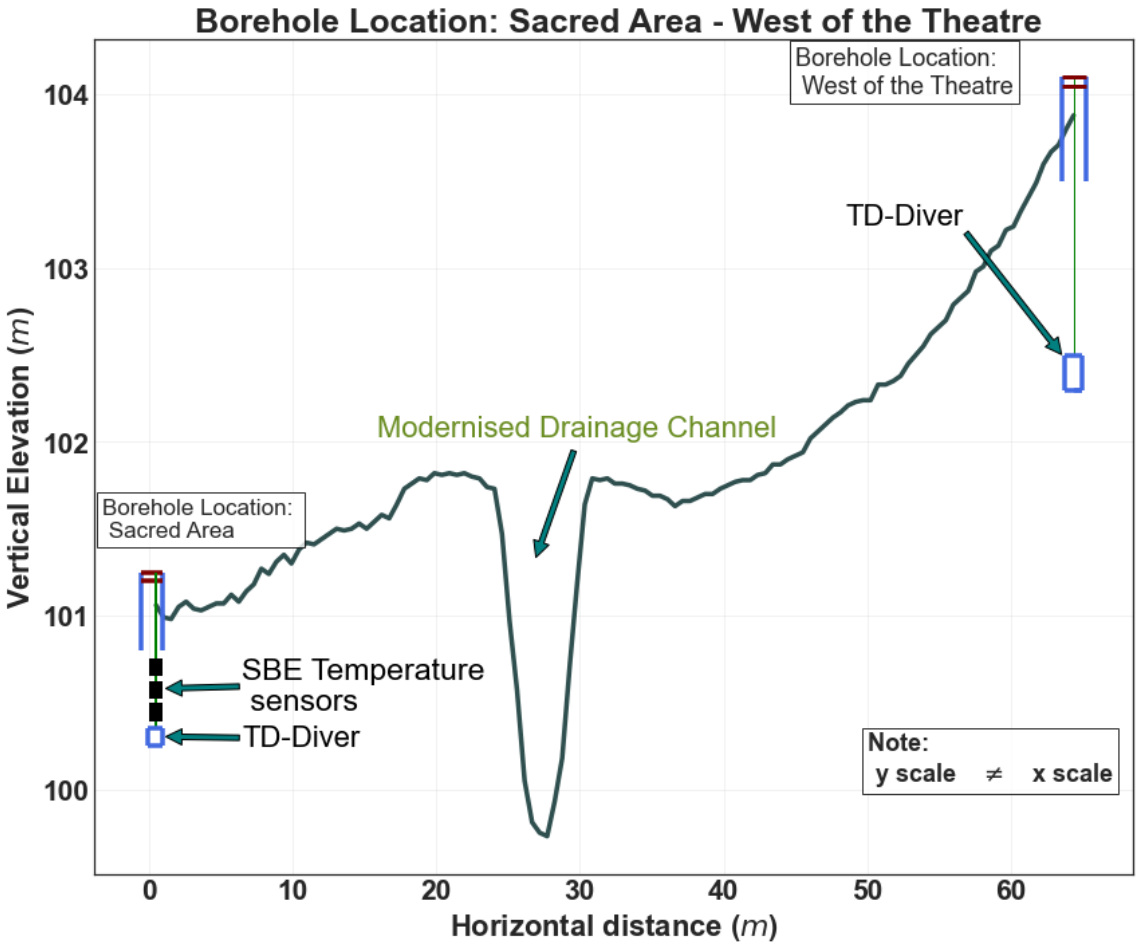

Figure 4.13: Schematic of the topography along the profile from PzSa to PzTh, also included are the temperature sensors and the *TD-Divers (Piezometers)*. The topography data was extracted from a *QGIS* plot of the `digital elevation model` with data acquired with a *theodolite*.

4.7 Aquifer evaluation tests

The aquifer evaluation test was performed to assess the hydraulic behaviour of the aquifer medium, mainly constituted by the Cuisian sand bed and coarse Lutetian limestones. The test was preceded by 3 months of continuous monitoring of the natural electric field (spontaneous potential) for changes in the background potential that may arise from the performance of the field due to rainfall, groundwater flow, extraction or other phenomena that can bring about changes in the hydraulic gradient. The test subdivided into the classic test, pumping with relaxation phase test and harmonic test (e.g. Jörg and Mareike, 2006; Maineult et al., 2008).

4.7.1 Pumping test: type I

1. The classic pumping test experiment is well documented in literature (e.g. Chang et al., 2021; Domenico and Schwartz, 1998; Fetter, 2001; Kuang et al., 2020).

2. The procedure deployed in the execution of the classic aquifer test is outlined thus :

   (a) The tools consist of a 0.50 horse power submersible pump installed below the water level in PzSa (Table A.22). A power source, a container of known volume (1 m^3), a hose and the pump accessories were also involved. The installed T-D Diver and the natural electric field reference electrode were implaced.

   (b) The pump was hose to release the water into a known volume (1 m^3 reservoir).

   (c) Constant rate discharge experiment was performed with a yield of 0.36 litres per second (Table 4.7).

   (d) The water level response to the controlled stress (pumping) was continuously recorded by the T-D Diver in *PzSa*.

   (e) The pumping also has the capacity to induce changes in the natural electric field which can be measured and analysis for flow characteristics of the subsurface layers.

   (f) The onsite *Hydra system* (voltmeter) continued the recording of the natural electric field at the interval of one second.

4.7.2 Pumping test: type II

3. The experiment involves pumping out of water from the borehole for a specified period, and waiting for a time interval for the water levels to recover to a certain extend and re-pumping for the same time interval earlier used and waiting for the same interval for the water levels to recover, and repeating the procedure.

   (a) This experiment had the same procedure as described in the classic test in subsection 4.7.1. But the pumping here is followed by a relaxation period before the pumping resumes.

   (b) The pumping test was performed to assess the response of the aquifer to stress induced by pumping and its recovery rate when the pumping stopped.

   (c) The same tools earlier used for the classic test were deployed for this pumping.

   (d) The water in PzSa was pumped out continuously until it stabilized and its level measured. Thereafter the pumping was stopped.

   (e) A period of relaxation was observed to allow for recovery. It is the time interval between the stoppage and the resumption of pumping.

   (f) The procedure were repeated as stated in subsections 3d and 3e.

   (g) The water levels and the spontaneous potential were continuously recorded in subsections 2d and 2f, respectively.

Table 4.7: Aquifer evaluation test: 27 April, 2022

Pumping phase	**Duration (seconds, s)**	**Reservoir volume (litres, l)**	**Yield (l/s)**
First	168	60	0.35
Second	169	60	0.35
	337		

Average aquifer yield = 0.35 (l/s)

4.7.3 Harmonic pumping test

4. In this test, water was pumped from the borehole to the reservoir and later discharged into the Gallo-Roman bath. The harmonic or periodic test had two steps:

(a) The reference electrode earlier installed in PzSa was removed and installed in the first Gallo-Roman basin (Figure 4.14).

   i. Water was first pumped from PzSa to the 1 m^3 reservoir.

   ii. After some time, the water was discharged from the 1000-liter (1 m^3) reservoir into the Gallo-roman bath.

(b) The time-lapse period of two hours was observed conceptually to permit flow within the subsurface sequence for changes in the water levels and natural electric field.

(c) The procedure in 4(a)i and 4(a)ii was repeated. However the water was injected into PzSa after the observed period of relaxation.

Figure 4.14: The picture on the left shows the materials used for the `injection test` experiment. The image on the right is the zoom of the item at the basins.

4.8 Spontaneous potential (SP) monitoring

4.8.1 Introduction

The measurement of the distribution of passive, natural electrical potential at the ground surface of the Earth and in boreholes is a method in geophysics called Spontaneous Potential Method (Keary et al., 2002; Revil et al., 2006; Telford et al., 1992). Spontaneous potential (SP) are natural

occurring electric field currents in the Earth. Two fundamental SP generating mechanism include electrokinetic and electrochemical activities driven by natural gradients in interfaces or beds with chemical and or electrical charge systems.

The SP response to classic pumping test (Rizzo et al., 2004; Sill, 1983; Titov et al., 2015), harmonic pumping (Maineult et al., 2008) have been used to map groundwater flow structures and directions as well a characterised the subsurface composition in different environments. SP signals have also been used to determine the distribution of the hydraulic heads (Suski et al., 2006) and study the signal inhibitions cycles by decomposing it into constituents (Allègre et al., 2014).

4.8.2 Background field monitoring

The hypothesis of a channel structure (ancient river bed) underlying the alluvium, colluvium, Lutetian Limestones and the Cuisian sands (e.g. BURGEAP, 1992), investigated with electrical methods (e.g. Fores, 2013), has not been substantiated with data and models. It is worth noting that the archaeological site is described as a spring sanctuary because of it age-long relationship with a water source (which can be oberve not only from the emergence of groundwater in the basins but also now at the near surface). The water is attractive to the Gallo-Romans and pilgrims for healing attributed to the roman gods and aesthetics. The flow characteristics (direction, path) of the groundwater has not been scientifically investigated.

The SP experiment is a tool for studying the flow patterns and structures in the subsurface (Sill, 1983; Suski et al., 2006). The flow of groundwater in porous and permeable media in the subsurface generates streaming currents. This movement set up an electric field which can be measured, passively with non-polarizable electrodes partially implanted in the ground.

4.8.3 Theoretical background

Solution to oberved SP anomalies resulting from induce flow via pumping have come up from electrokinetic coupling of the Darcy velocity with elctrical potential (Revil et al., 2006; Rizzo et al., 2004). The Darcy velocity is an expression obtained from the classic Darcy's law of flow in a porous medium (equation 4.6).

$$q = \frac{Q}{A} = K\nabla h \tag{4.6}$$

where the flow rate Q= $\frac{v}{t}$, v is the flow volume per unit time t, through a unit cross section area of a porous material A, ∇h is the hydraulic gradient. The fluid velocity defined as the mean velocity of all possible fluid paths through a porous media given as equation 4.6.

$$u = \frac{Q}{A} \tag{4.7}$$

In a saturated soils, the total current density is express by the relation in equation 4.8.

$$j = -\sigma\nabla\varphi - L\nabla h \tag{4.8}$$

$$\nabla \cdot j = 0 \tag{4.9}$$

By charge conservation law equation 4.9 expressing the total current density is divergence free and the relation in equation 4.10 represent the Poisson relation for electrical potential in an heterogeneous porous medium (Suski et al., 2006; Titov et al., 2015).

$$\nabla(\sigma\nabla\varphi) = -\nabla(L\nabla h) = J \tag{4.10}$$

$$\nabla \cdot (K\nabla h) = S\frac{\partial h}{\partial t} + q \tag{4.11}$$

Equation 4.11 is the diffusion relation (Domenico and Schwartz, 1998), which is solved with boundary condition for the hydraulic head distribution (Titov et al., 2015).

$$L\nabla h = Q_v u \tag{4.12}$$

where L = electrical current coupling (Am^{-2}); σ = electrical conductivity (Sm^{-1}); φ = electrical potential ($volts$, V); h = hydraulic head (m); J = the source term (Am^{-2}); K = hydraulic conductivity (ms-1); S = storage coefficient (m^{-1}); u = Darcy velocity, Q_v = the effective density (of the diffusion layer) per unit pore volume that is drag by the flow of pore water (Revil et al., 2006).

4.8.4 Instrumentation and measurement procedure

4.8.4.1 Data acquisition system

The acquisition set up consists of a Hydra Series II Data Bucket (Fluke Model 2635A) multi-channel multiplexer (a high impedance voltmeter, 1 kΩ) configured to measure and record direct current (DC) voltage in volts), a reference electrode and (eight) field electrodes and accessories (Figure 4.15). The Hydra System is a portable multi-channel digital multimeter with a data resolution of 1μV - 10 mV and accuracy of ± 0.0024%. It is designed for measurements of signals at per second, or per minute rate. The self-potential was monitored for a period of 60 days.

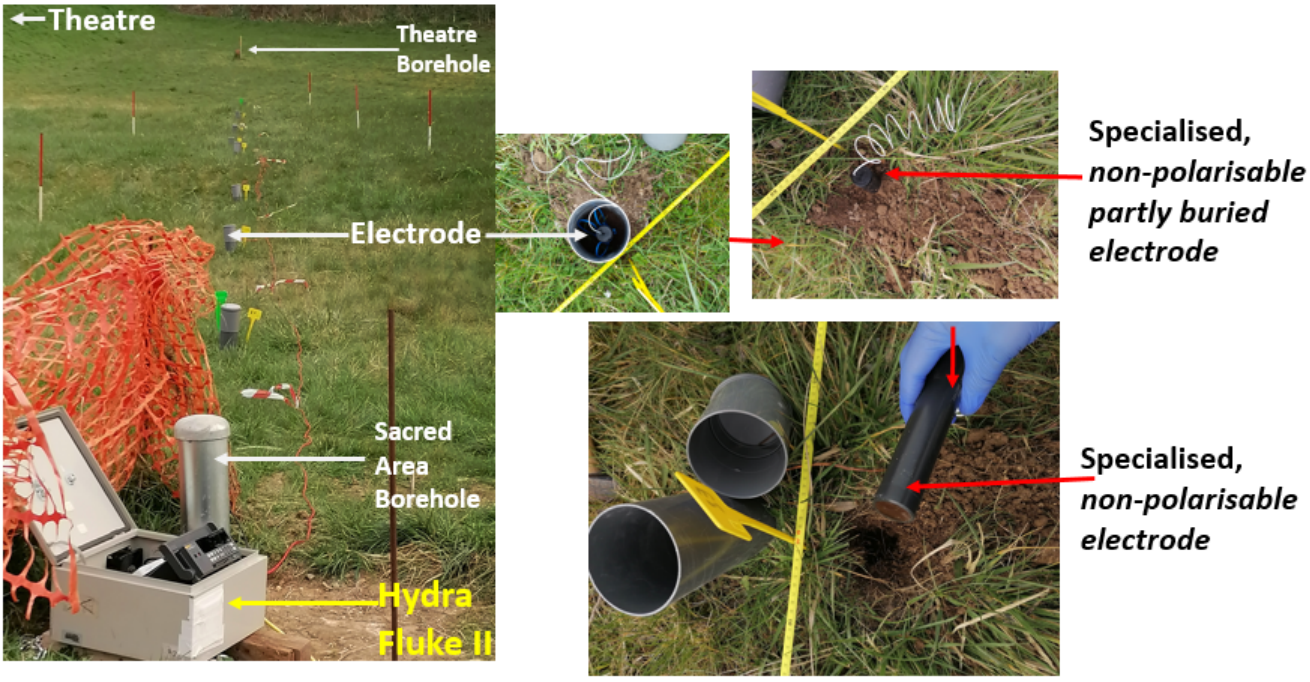

Figure 4.15: Instrument and natural spontaneous potential field acquisition layout

4.8.4.2 Electrodes and environment

A stake consisting of a conducting material was used as *electrode* to establish contact with the earth surface. The electrodes could be designated receivers or transmitters of natural or artificial field such as potentials or currents. Graphite, metallic and non-polarisable electrodes are types of electrodes use in geophysical measurements.

The electrode for SP survey consists of a metal immerse in its own salt. Example of such electrodes include Lead (Pb), silver (Ag) in its sulphate or chloride salt solution. The metal-salt couple of Lead-Lead chloride (Pb-$PbCl_2$) herein referred to as PETIAU electrode was prefer to other non-polarisable electrodes (Cadmium, Copper, Mercury, Lead and Silver) commonly used in geophysical measurements (Petiau and Dupis, 1980).

The unpolarisable PETIAU electrodes were chosen for the survey due to its advantages in noise spectrum, temperature coefficient and stability (Petiau and Dupis, 1980). Compare to non-polarisable electrode like Silver-Silver chloride (Ag-$AgCl_2$) which has a long history in field geophysics. The PETIAU silent characteristics (Petiau and Dupis, 1980), which include noise as low as the one of Ag-$AgCl_2$ at 1 Hz and even lower for the low frequencies (0.4 μV at 0.01 Hz and 1.2 μV at 0.01 Hz for peak to peak value and ΔF=F). Where ΔF= band width (frequency) and F = frequency. The Petiau electrode has longer time stability of the polarisation (1 mV/ month rather than 2 at 10 mV/-month).

Each electrode length is about 20 cm. The electrode was enclosed in 6 cm diameter and 20 cm height cylindrical plastic container (Figure 4.15).

One reference electrode and 8 (eight) field electrodes were arranged in a collinear array along a profile oriented from the borehole the sacred area to the borehole west of the theatre. A 5 cm long cylindrical hole dunged into the earth was use to implanted the field electrodes while the reference electrode was submerge into the PzSa (Figure 4.15).

4.8.4.3 Acquisition procedure

Eight non-polarisable electrodes (NPEs) were partially implanted in the ground at 3 cm depths along a profile were deployed for monitoring natural occurrence of earth potentials.

The reference NPE was inserted into the Sacred Area borehole, designated PzSa and submerged below the water level. The profile was oriented from the borehole located at the Sacred Area to the borehole situated West of remains of the Theatre (Figure 4.15). The set up allowed for continuous sampling of the natural electric field at an interval of 60 seconds.

The instrument is equipped with retrievable data storage device, static random-access memory (SRAM). The SRAM card was used to save and load setup files (instrument configuration: scanning interval (sampling rate), type of measurement, fast or slow measurement rate) and to record or store measure data during field operations. The Memory cards are of different sizes. An empty 256K-byte SRAM cards will store 4, 800 scans of ten channels while a 1M-byte card will store 19, 800 scans of ten channels.
The monitoring of the background self-potential was performed for a period of 60 days at the first instance. Thereafter, the (active) SP data was measured during the period of the pumping experiments.

4.8.5 Monitoring

The SP data was collected in two phases. In the first phase, the natural electric field was monitored for the response of the aquifer system to subsurface water flow. In the second phase, groundwater flow was stimulated through pumping tests experiments. During the pumping experiments described in section 4.7, SP measurements were carried out concurrently.

The response of the natural electric field to the perturbation of the aquifer system caused by arti-

ficially varying the groundwater levels with pumping experiments was monitored to provide parameters for investigating the hydraulic characteristics of the subsurface sequence (see Figure 1.6). The measurements were performed with the PETIAU non-polarisable electrodes (manufactured by SDEC, France) and Hydra Series II Data Bucket (subsection 4.8.4). The electrode consist of lead immersed in a lead chloride solution ($Pb - PbCl_2$) (Figure 4.15).

The SP survey was carried out in the Sacred Area of the site. The sacred area water borehole served as the base station for the reference electrode, RE. The RE was submerged below the static water level, to register minute streaming currents arising from the water levels fluctuations for the establishment of a stabilisation protocol for the field experiments.

4.8.6 Set-up and data acquisition

The SP field instrumentation and procedure was described in section 4.8.4. A submersible pump (Figure and Table A.22) inserted below the water levels in the first Basin (oriented east- west). Conceptually, the aquifer response to the stress introduced by the pumping to cause flow and perturb the natural electric field for the active SP data acquisition.

A sequence of aquifer evaluation experiments ensured the disturbance of the natural hydraulic equilibrium with the aim of initiating flow and generating electric currents known as streaming currents (Allègre et al., 2014; Maineult et al., 2008; Sill, 1983; Suski et al., 2006). To this effect, groundwater flow was stimulated by implementing aquifer evaluation tests at a constant discharge rate. A discharge rate of 0.35 litres per second was obtained after 168 seconds of constant extraction.

Continuous SP signals were measured at 1 minutes interval before, during and after the aquifer evaluation test via constant discharge tests (e.g. Rizzo et al., 2004; Titov et al., 2005), classic and harmonic pumping tests (e.g. Maineult et al., 2008) (see the details on the different pumping tests in section 4.7). The SP monitoring continued for one more month after the pumping experiments.

4.9 Results

The attempt to investigate the aquifer properties using pumping test experiments did not yield the anticipated classic drawdown curve patterns in both the pumping and observations wells (boreholes) to motivate further assessments (Figures 4.16 and 4.17).

Despite this outcome, the field procedure used for the experiments was described in subsections 4.7.1, 4.7.2 and 4.7.3, to provide a view of the steps taken to acquire the data for possible future work.

The plots obtained for each experiment is presented in figures 4.16, 4.18 and 4.19 respectively for the classic pumping test, the traditional pumping test with relaxation phase and the harmonic pumping test.

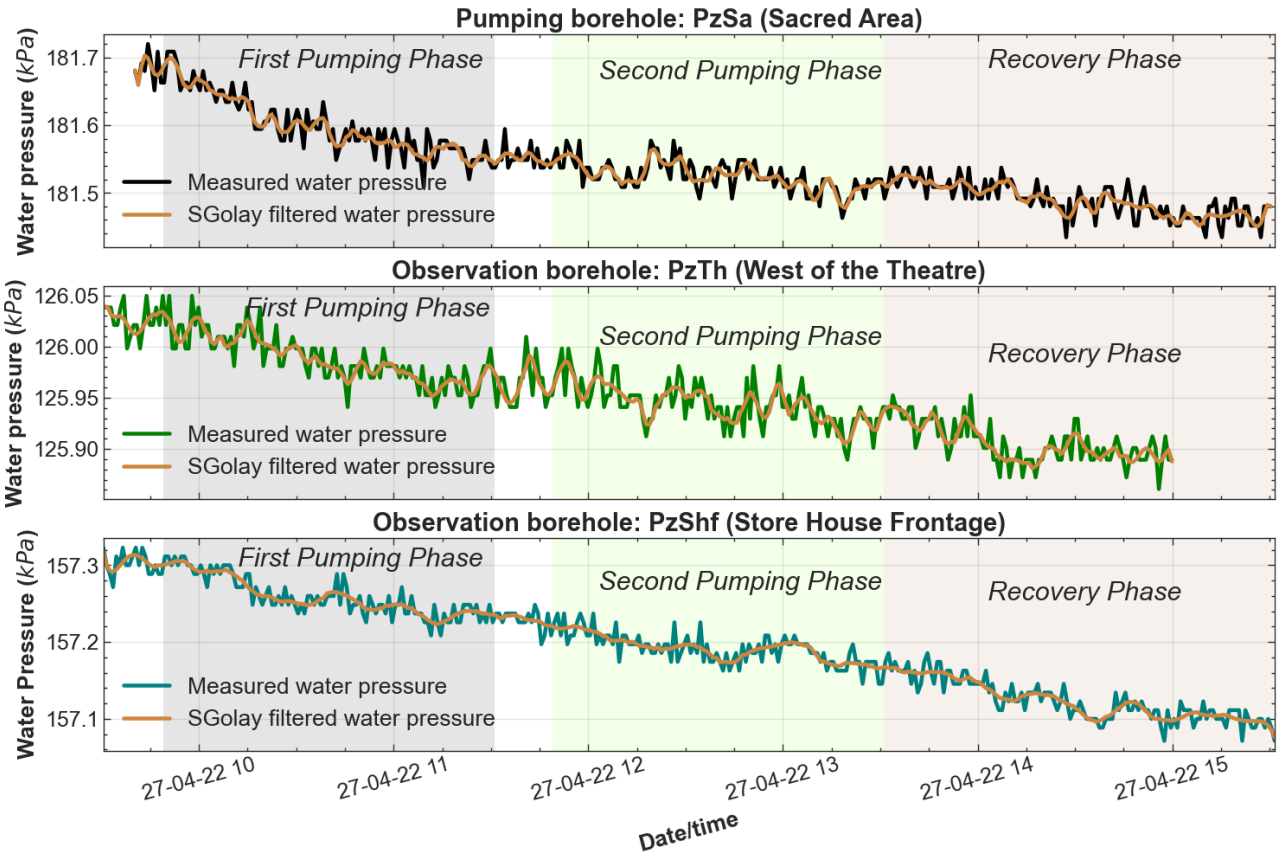

Figure 4.16: Classic pumping experiment with pumping and recovery phases performed at the PzSa borehole and obervations wells PzTh and PzShf.

The time - water pressure data from the classic pumping tests described in subsection 4.7.1 (see Figure 4.16), were filtered using two separate methods.

First, it was filtered using the Savitzky-Golay filter to remove noise and smoothen the data (Chen et al., 2004; Savitzky and Golay, 1964). Secondly, it was treated with the Barometric and Earth tides correction program by Toll and Rasmussen (2007) to remove the impact of barometric pressure and Earth tides to aid the visualization of the drawdown effect. The outcome of the two filtering procedures did not also revealed classic patterns from the pumping tests (Figure 4.17).

The second pumping test experiment described in subsection 4.7.2 had a relaxation phase in-

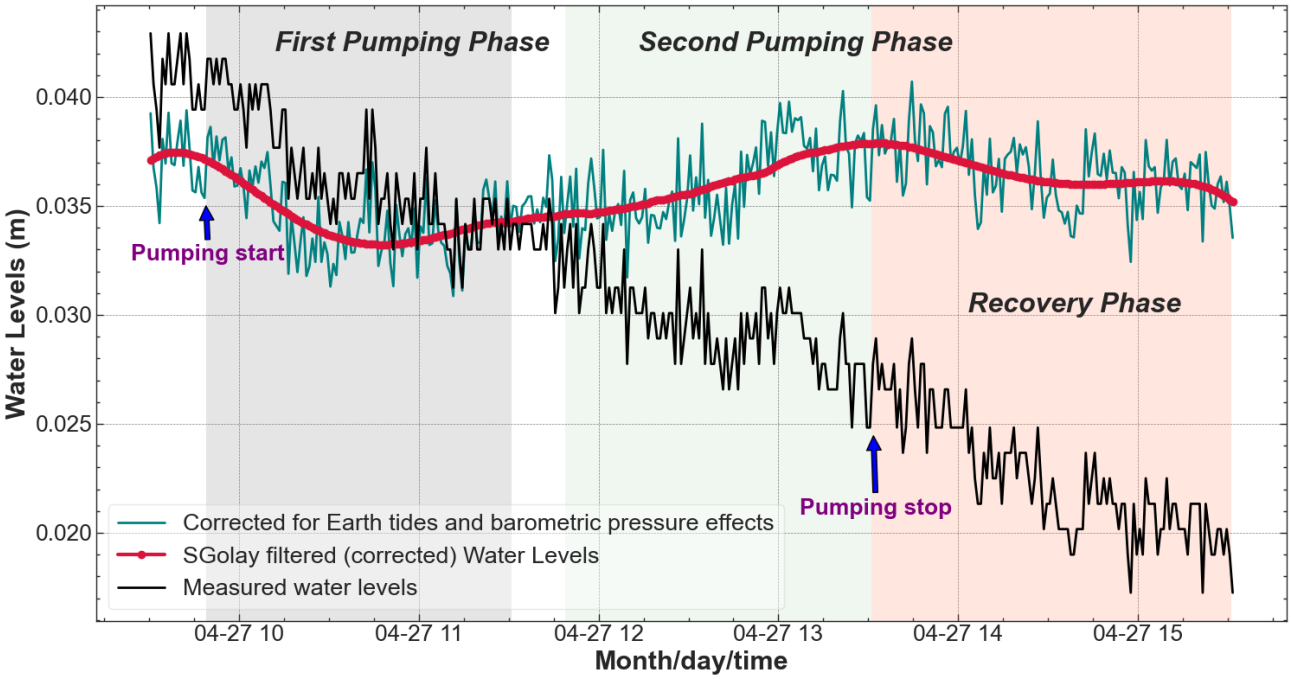

Figure 4.17: Classic pumping experiment with pumping and recovery phases performed at the PzSa borehole filtered to remove the effect of barometric pressure, Earth tides and noise.

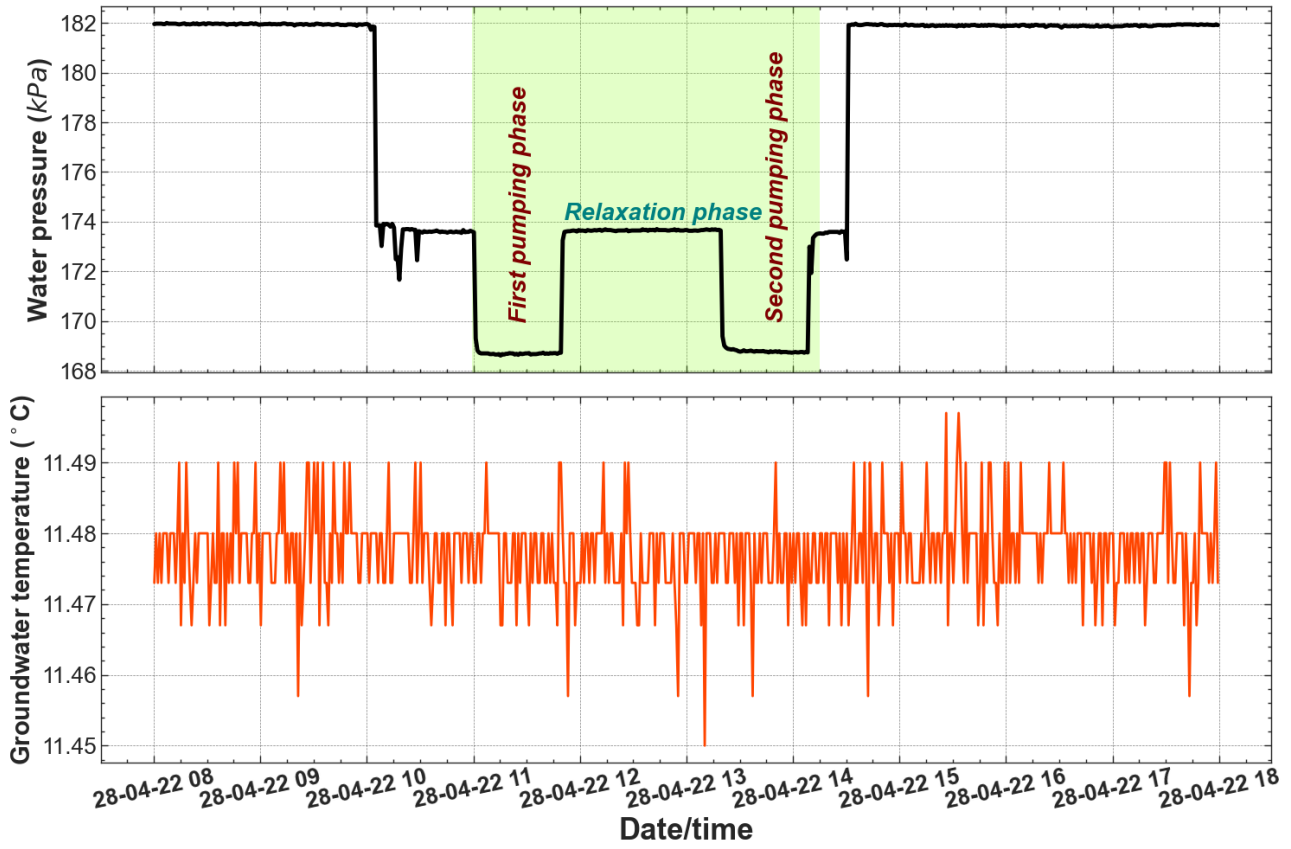

Figure 4.18: Classic pumping experiment with relaxation phase: the response of the water levels in the PzSa borehole with simultaneous recording of the temperatures.

cluded in the pumping exercise to enable the monitoring of the impact of the controlled, applied pressure or change on the aquifer. The sudden raised in the level of the water (in the pumping

borehole, that is, PzSa) can be observed following the stoppage and resumption of pumping (Figure 4.18). The relaxation phase showed no impact on the measured water temperature.

The pattern of the curve suggests the presence of a permeable structure underneath the surface wherein the water rapidly responds to extraction and recharges fast on cessation of pumping.

The third pumping test experiment, called the harmonic pumping test (subsection 4.7.3), had the water pumped into a reservoir and reinjected into the pumping borehole after a time interval. The plot of the water pressure from the harmonic pumping test (Figure 4.19), showed a similar curve pattern as observed in Figure 4.18. The plot of a portion of the response of the borehole water to the injected water clearly showed a rise and fall pattern at the start and end of the injection (Figure 4.20).

This observed decay curve pattern was treated with erf relation. The resulting sigmoid is comparable to a classic erf curve (Figure 4.21 and 4.22).

Qualitatively, the initial curve pattern showed a gradual rise in the temperature as the warm water was injected. It stabilized at a slightly higher than 15.10°C temperature, before gradually decaying to near its starting value. This signifies the capacity of the water that results from warm and cold water mixing), to transmit thermal energy and partly retain it for some time within the sequence.

For each pumping day (e.g. see Figures 4.18, 4.19, 4.20 and 4.21), the response of the borehole water pressure to the pumping was measured alongside the monitoring of spontaneous potential (SP) data which was going on at the site (section 4.8). The SP values were monitored from around the end of February 2023 to June 2023. Herein eight electrodes were used for the survey: 1 reference and 7 emplaced.

The recorded SP (natural electric field) data is shown in figure 4.26 for the classic aquifer evaluation experiment which ran simultaneously with SP monitoring in the vicinity of PzSa.
The maximum recorded amplitude was less than $0.1mV$ and the minimum values lie between -0.16 and $0.19mV$. The minimum were more pronounced SP values between 1st and 5th April 2023. For the entire period of the SP experiment, the highest amplitude fluctuates minimally about $\pm$ $0.0015mV$ (Figures 4.23, 4.24, 4.25 and 4.26). Hence, the observed SP anomalies were qualitatively inspected.

Active SP values were recorded during the classic aquifer test and harmonic pumping test. The amplitude of the recorded did not show significant changes to suggest an anomalous situation

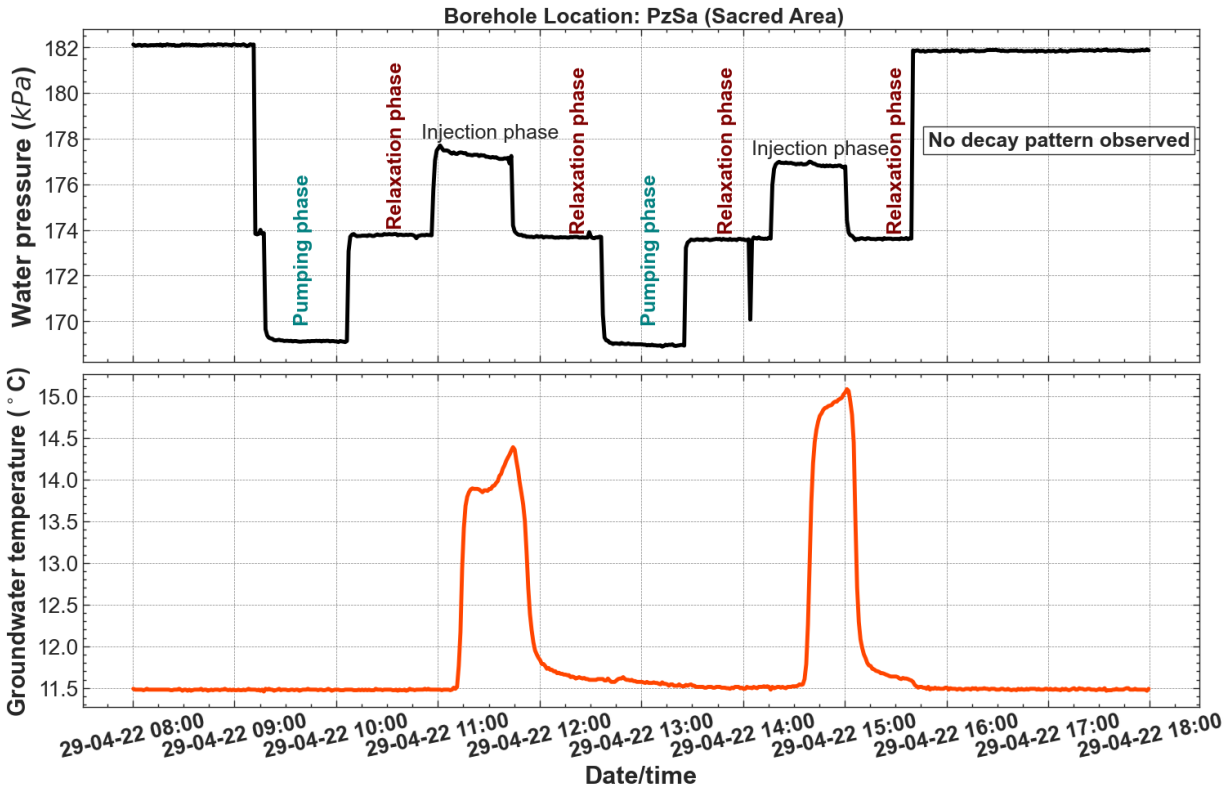

Figure 4.19: Plot of water pressure and temperature respond from the harmonic pumping experiment

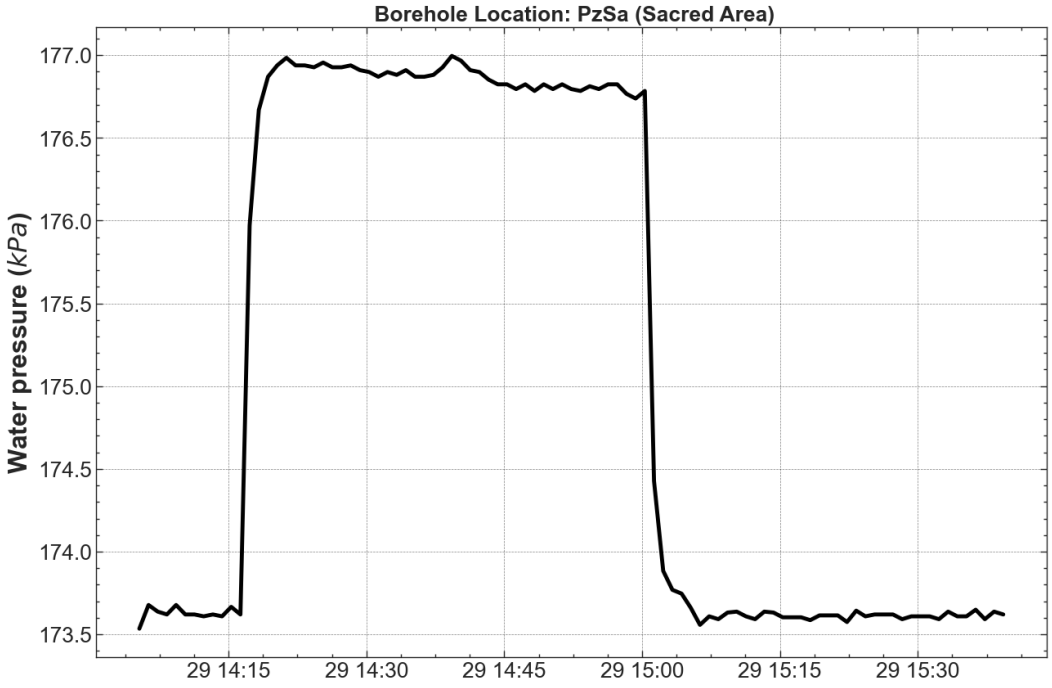

Figure 4.20: Plot of water pressure from the harmonic pumping experiment showing rapid relaxation

compared to figures 4.30, 4.29 and 4.28.

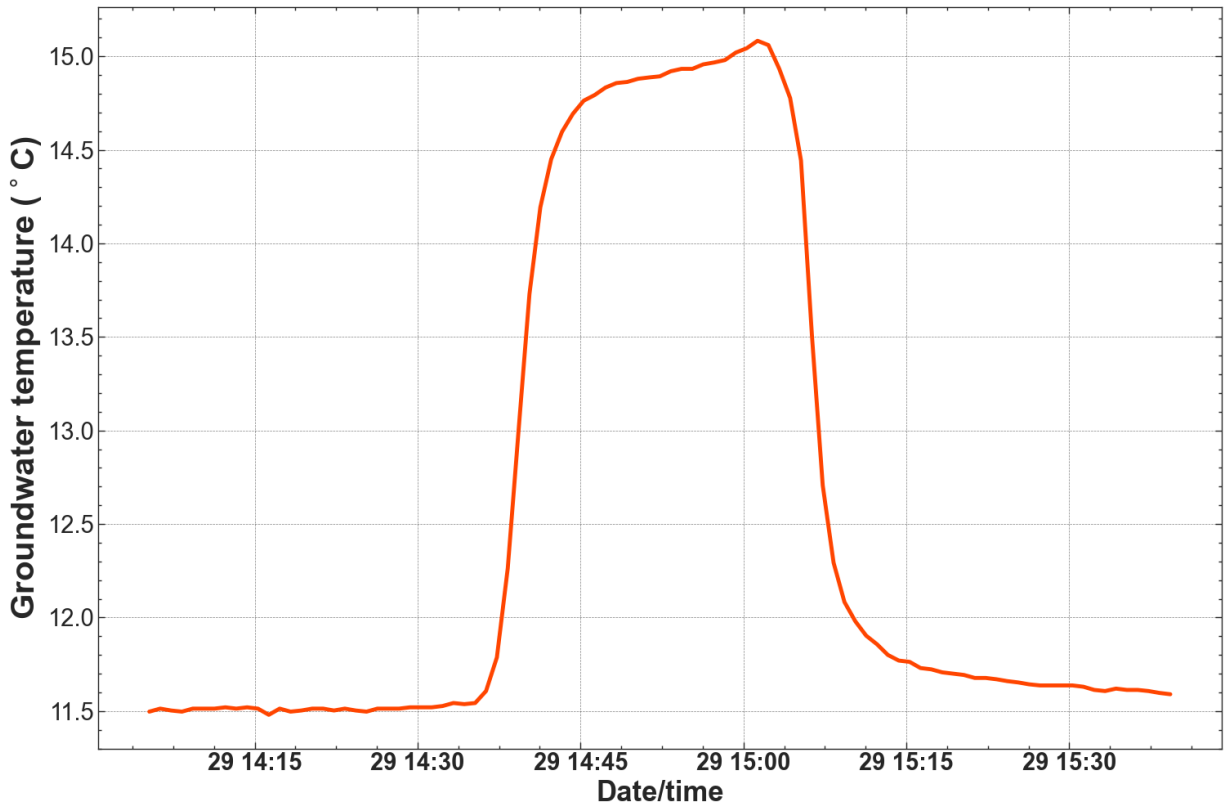

Figure 4.21: Plot of water temperature from the harmonic pumping experiment showing exponential decay pattern

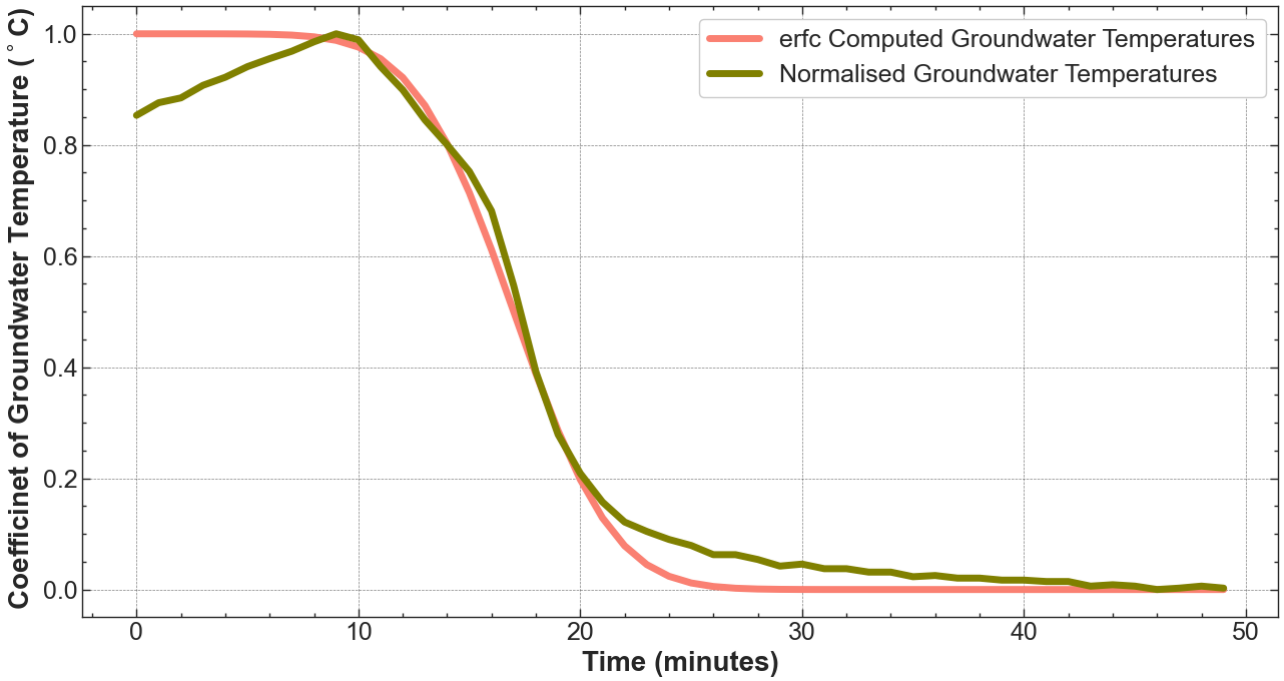

Figure 4.22: Erfc response of the groundwater temperature

The amplitude of the measured potential was below the expected values of hundreds of millivolts. Based on personal communications with my supervisory team, the quantitative evaluation of the SP data did not continue after the passive monitoring and active data acquisition during

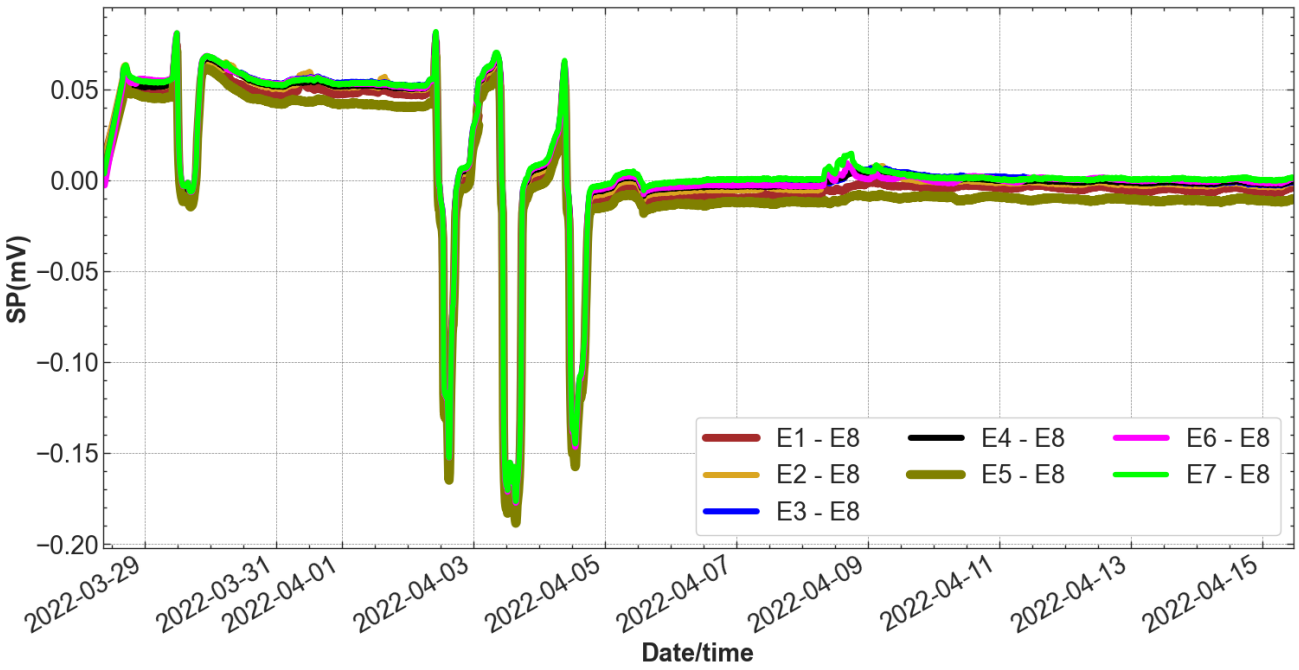

Figure 4.23: Background spontaneous potential monitored at *Les Vaux de la Celle* .

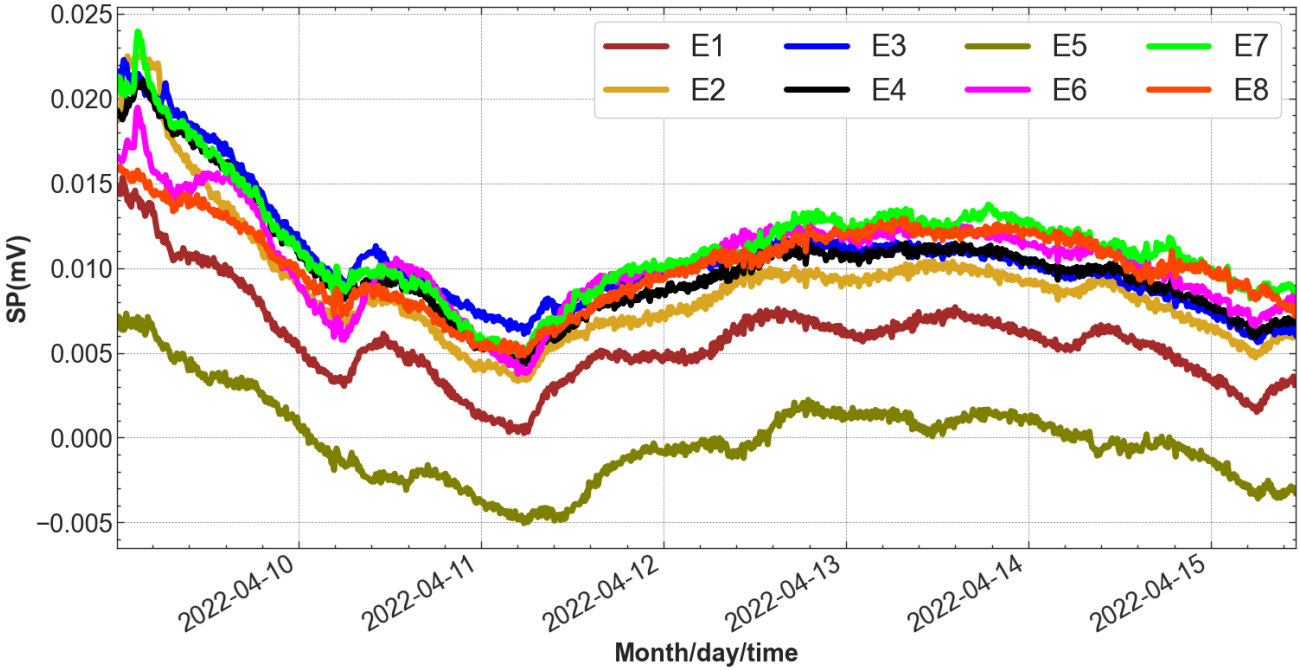

Figure 4.24: Natural spontaneous potential data: background field before the pumping experiments

the pumping phases. Their advice was sequel to the low positive and negative values of the SP anomalies recorded during the two phases of acquisition. The measured response is quite low for hydrogeological analysis compared to values recorded in similar experiments elsewhere. The response of the SP field to induce flow has seen values reaching 8V (see Figure 1 of Titov et al. (2015)). Consequently, the SP data have been archived for teaching, learning, and reference.

However, there are certain characteristics of the data. The monitored data were not relatively sta-

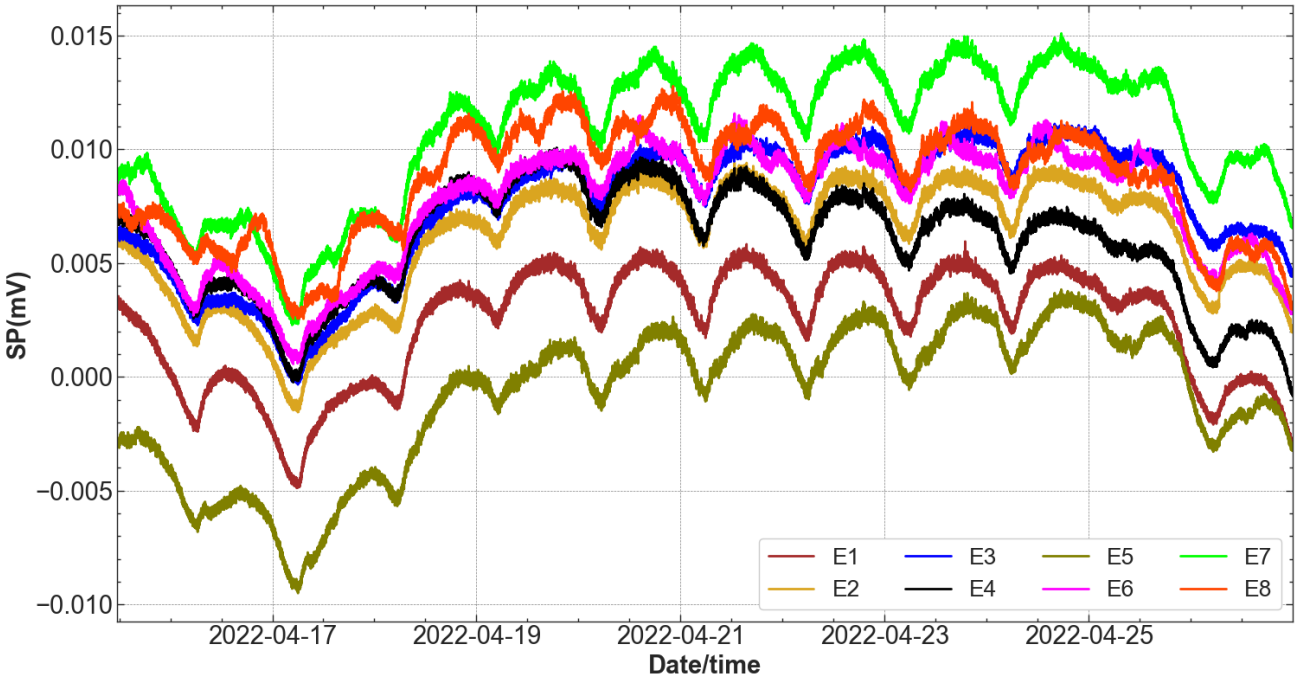

Figure 4.25: Natural spontaneous potential data: a portion of the background field before the pumping experiments

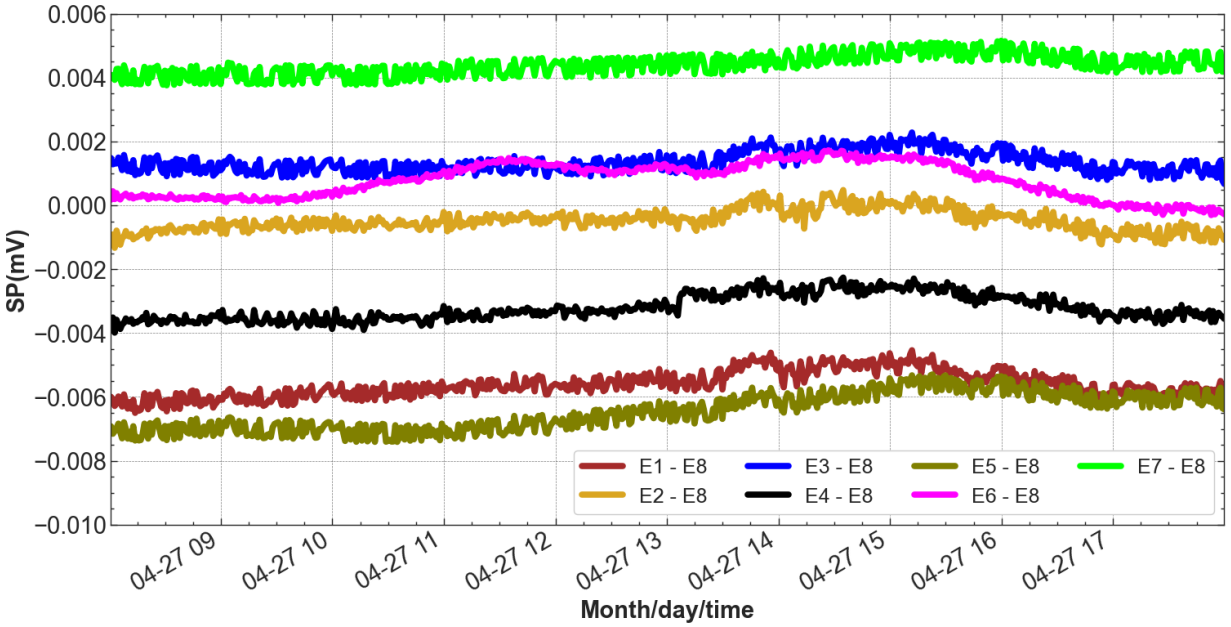

Figure 4.26: Natural electrical spontaneous potential measurements: 27.04.2022 08:00:00 - 27.04.2022 18:00:00 during the harmonic experiment

ble, fluctuations occurred reaching a magnitude of $-0.183mV$ between 1 - 4 April and $< -0.01mV$ on 29 March (Figure 4.23). During the last days of March and the first two weeks of April, the background SP signals were relatively stable between 0.015 and -0.01 mV. The maximum recorded amplitude was 0.08 mV which is well below the amplitude of values used by other researchers for hydrogeological studies with SP anomalies. In some instances, some near-appreciable amplitudes

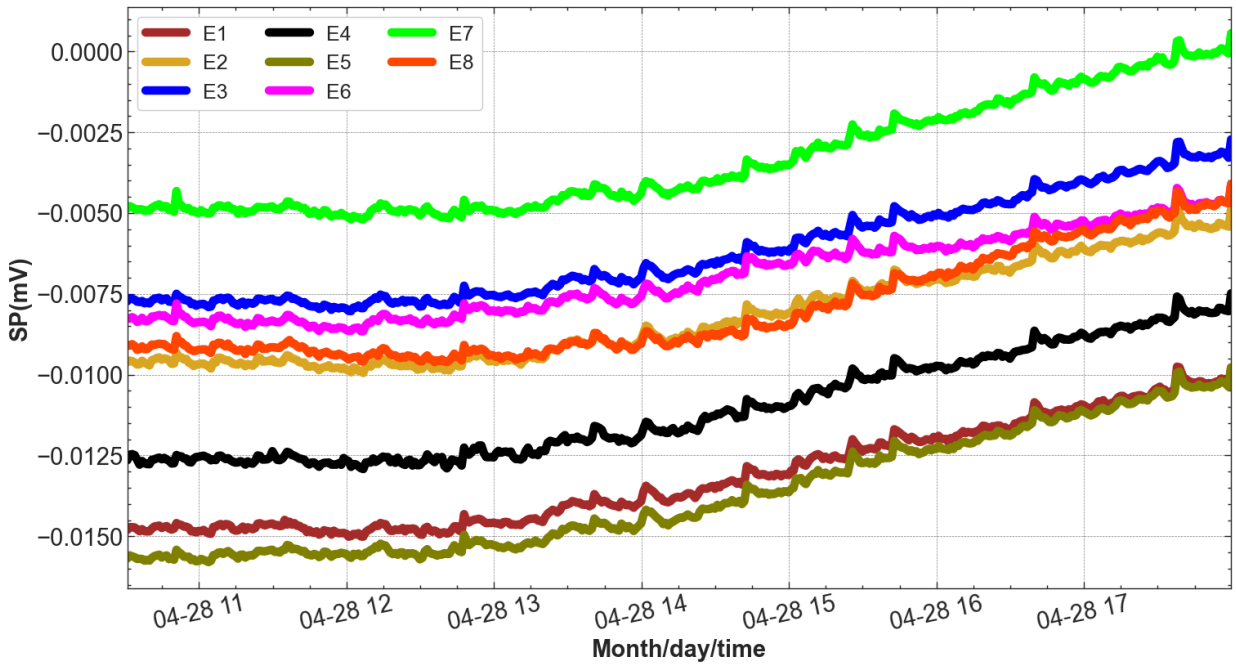

Figure 4.27: Natural electrical spontaneous potential measurements: 28.04.2022 10:00:00 - 28.04.2022 18:00:00 during the pumping experiments

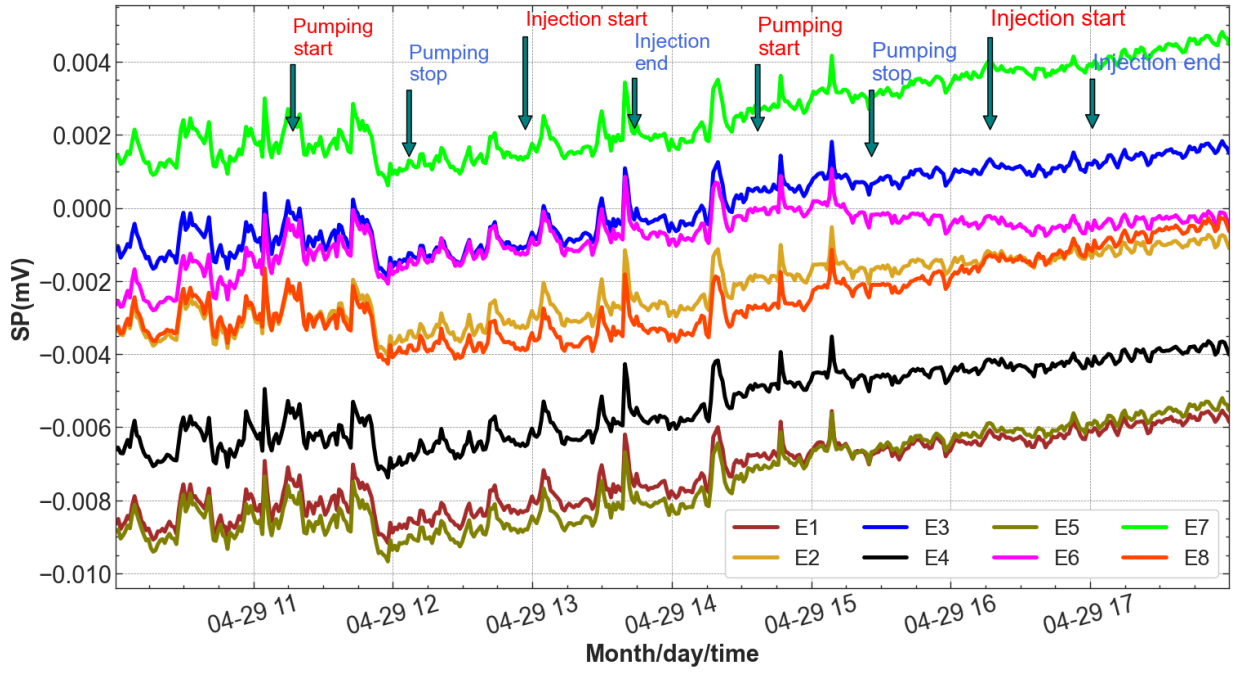

Figure 4.28: Natural electrical spontaneous potential measurements: 29.04.2022 08:00:00 - 29.04.2022 18:00:00 during the harmonic experiments

were observed. For example, positive amplitudes reaching 0.24 mV were attained in figure 4.24 with an instant of -0.005 mV values on 11 April.

For 29 April data were collected, during the harmonic pumping. The SP values fluctuated between 0.005 and -0.008. The magnitude of the anomalies was higher at the E7 electrode which may indi-

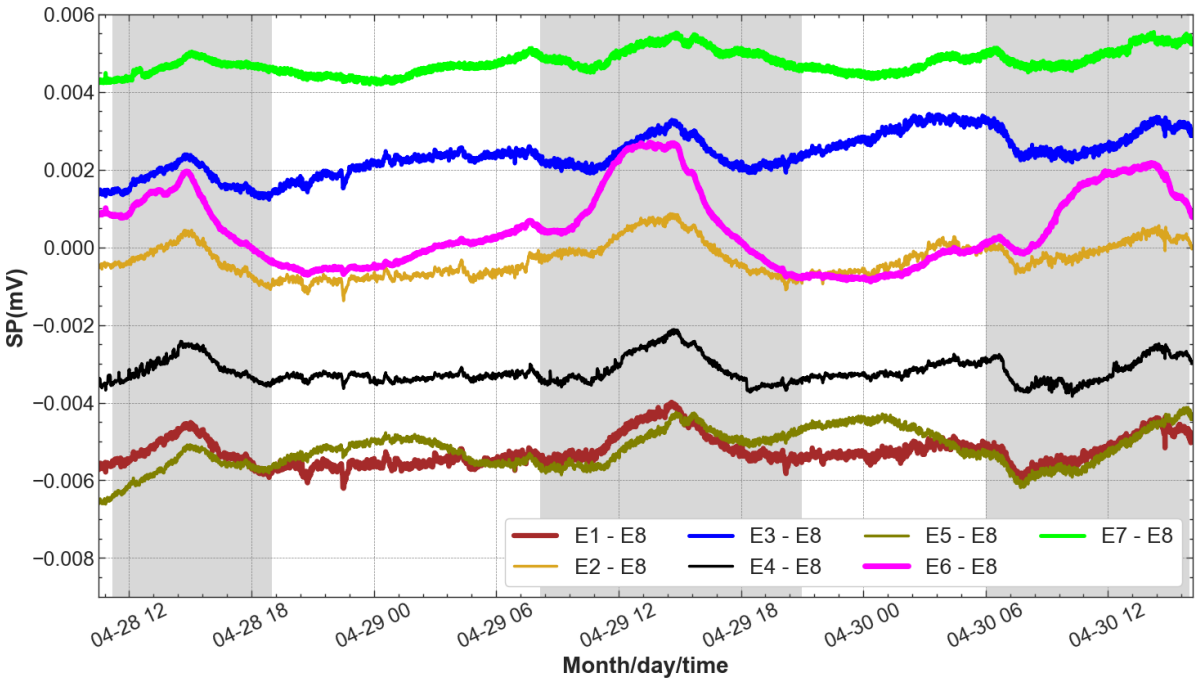

Figure 4.29: Natural electrical spontaneous potential measurements: 28.04.2022 12:00:00 - 30.04.2022 18:00:00

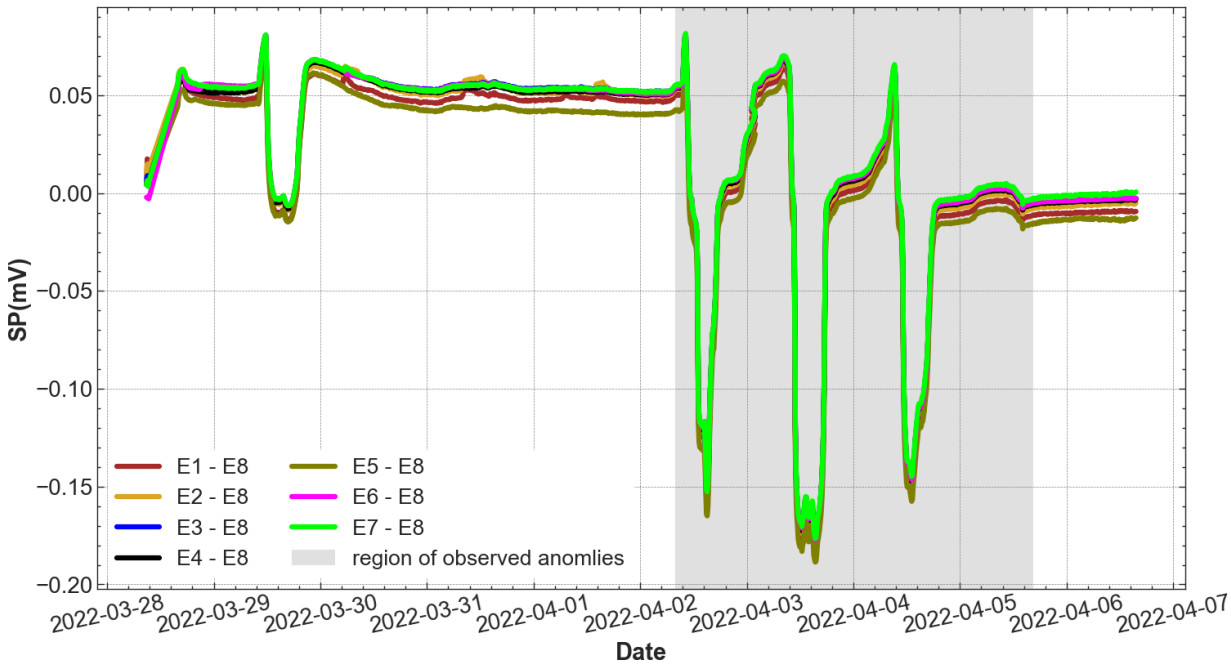

Figure 4.30: Natural electrical spontaneous potential measurements: before pumping experiments zoomed from figure 4.23

cate more flow around the point or path. In each stage of pumping and injection, the fluctuations were significant in number with small peaks, but very small amplitude changes were observed in either the pumping, relaxation, or injection phase. The width of the major peaks was in the range of less than 4 hours with a height of 0.0025 mV in the E6 electrode position. At between 12 - 6

pm, the peak can be seen. The small amplitude did not encourage the fitting of methods such as half-width to estimate the geometry of the anomalies.

The monitored background field (Figures 4.23 and 4.30) is partly shown in figure 4.31, along with the response from the pumping experiments (figure 4.26, 4.27, and 4.28). A portion of the data in figure 4.23 has been replotted in the figure 4.30 to enhance the effect better view of the data.

The erfc model (Figure 4.22) shows a semblance with less than 0.2 $^{\circ}C$ amplitude difference at the initial start, the decay phenomenon varies as the same time rate with the normalized temperatures showing some time step in the 20 th and 30 th minutes before tying up at the 42nd minutes.

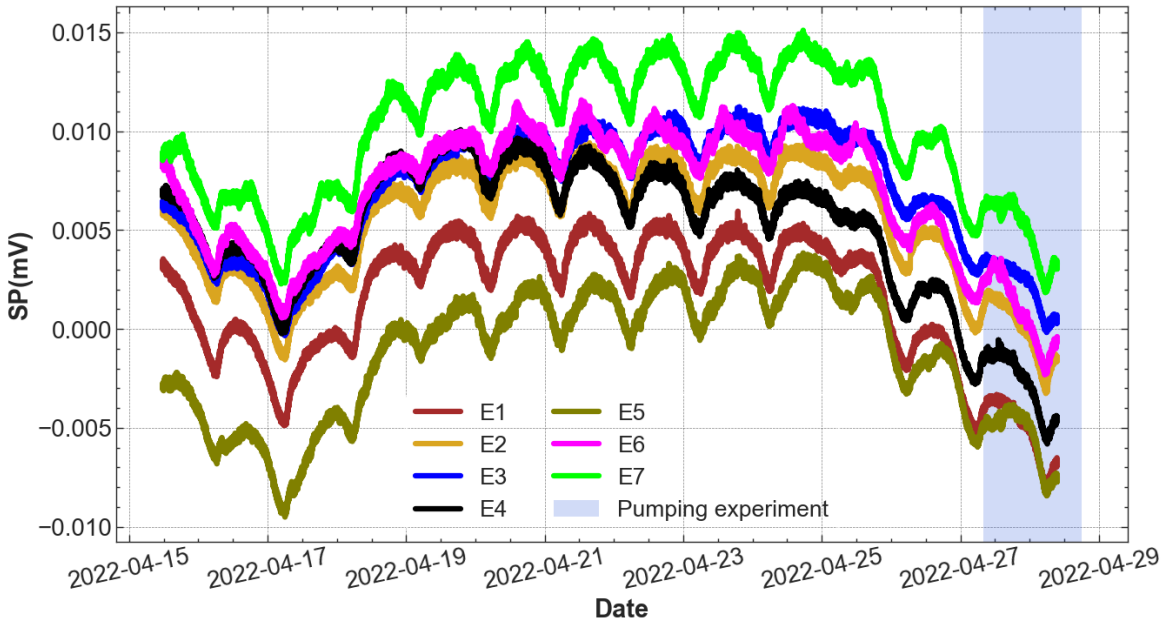

Figure 4.31: Natural electrical spontaneous potential measurements: background and active fields

4.10 Discussion

The following four datasets acquired were analyzed in this chapter: meteorological data, spontaneous potential, thermal tracing, and pumping test data. The meteorological data gives clues to the variability of climatic and environmental conditions.

Specifically, temperatures in the summers of 2021, 2022, and 2023 differ in magnitude but were higher in 2022 (Figure 4.1). This was investigated in subsection 5.4.5 using the water pressure data (Figure 5.6) with Fourier transform. The precipitations (mainly rainfall) were continuous throughout the seasons thus permitting runoff and infiltration to wet the surface and recharge subsurface water, nevertheless, the amount of rainfall was lower in certain periods which included the sum-

mer (Figures 4.2 and 4.3).

As mentioned earlier, the aquifer evaluation test was performed to assess the hydraulic behavior of the aquifers at the site (Bresciani et al., 2020; Domenico and Schwartz, 1998; Fetter, 2001), mainly constituted by the Cuisian sand bed and coarse Lutetian Limestones. The test was preceded by 3 months of continuous monitoring of the natural electric field (spontaneous potential) for the background field.

The monitoring objectives were to acquire the background field for stabilization and observe possible changes in the amplitude of the field that can arise from the performance of the field due to the effects of natural phenomena that can stimulate fluid flow. The flow usually would result from a gradient change that could cause, for example, groundwater to flow thereby generating a measurable potential (Revil et al., 2006; Sill, 1983; Suski et al., 2006; Titov et al., 2015).

During the monitoring period, there were rainy days when infiltration was expected to change the hydraulic gradient and stimulate groundwater flow. Natural mechanisms that encourage subsurface flow were also anticipated to have caused fluid flow and generated streaming currents. However, the monitored data did not provide significant values for hydrogeological analysis as reported. The same situation was also encountered during the active spontaneous potential monitoring experiments performed concurrently with the aquifer test (section 4.8).

This suggests the presence of a permeable subsurface sequence that can be further investigated using other methods. However, the analysis of the water pressure data (Figure 5.6, using theroretical computed Earth tides and response tidal component was useful to overcome the challenge of the aquifer test reported in sections 4.7 and 4.9. It is important that the properties of aquifers on the site have not been determined even by precious researchers and workers (BURGEAP, 1992; Fores, 2013; Group, 1992). This was determined from the analysis of tidal components with associated poroelastic relations (subsection 5.4.7)

The thermal response recorded in figures 4.19 and 4.21 motivated the subsequent experiments described in subsections 4.6.5 and 4.6.6. The idea behind the thermal tracing experiments is as shown in figure 4.13, the injected warm water would flow vertically to mix with the existing groundwater and conceptually flow laterally. Conceptually, by Fourier and Darcian fluxes, the SBE sensors and the TD Diver would record the temperature changes. The analysis of the thermal experiments data was deferred due to time constraints imposed on this study.

4.11 Conclusion

The SP method applied to investigate the response of the subsurface materials and groundwater flow did not submit to appreciable amplitude worthy of analysis. This is an opportunity for testing other methods and models on the site. Thus, the archaeological site is viable for testing non-destructive methods that would provide a real-time representation of the subsurface conditions, materials, and structures.

The SP experiments have unexplored aspects in terms of instrumentation, field procedures and software; sensitivity of instruments to changes in the natural electric field, and profile layouts. A revisit is advocated.

The thermal response of the subsurface water and lithology sequence to natural heating and processes and the experiments performed remain to be evaluated for thermal diffusivity and relations with aquifer hydraulic properties.

In this chapter, we have discussed the types of datasets acquired and outlined the steps taken to obtain them. We provided a first-order treatment of the natural electric field, classical and harmonic pumping, and thermal data sets.

The 2D electrical resistivity data were modeled using standard least squares and robust methods as mentioned in chapter 3.

In the next chapter, we will analyze the borehole water pressure and groundwater temperatures, using the Fourier transform, singular spectral analysis, and wavelet-based semblance methods. The main objective of applying each method is to examine the data for anomalies and interpret them in terms of hydrological, hydrogeological, geological, and other phenomena that would reveal the influences and response of the aquifer.

We first accessed, visualized, and qualitatively analyzed the dataset obtained from monitoring water pressure and temperature in the boreholes. The sequences of datasets acquired at each time interval were then concatenated to produce a series of long-period data. These long time series were subjected to various treatments and the details of the formulation and processing strategy for each method are presented in the next chapter.

CHAPTER 5

Aquifer properties from groundwater pressure data and response to Earth and barometric tides

5.1 Introduction

This chapter investigated the response of the aquifer, its matrix structure, and the water within it to natural forcings due to external sources (barometric and Earth tides) in order to characterize the aquifer property variation with time (Figure 1.7).

Water pressure from three boreholes recorded at 60-second intervals to adequately sample a wide range of events or changes in the borehole water was used for the investigation. The same sampling frequency was used to acquire barometric pressure and model Earth tide data, as well as groundwater and surface (air) temperatures.

Wavelet-based semblance analysis, singular spectrum analysis, and discrete Fourier transform were performed on the water pressure for periodic signals, extraction of harmonic components, phase relationship correlation for a semblance model, and evaluated aquifer response properties. Groundwater level data monitoring find many applications, including short to long term changes in recharge and storage, flow directions, and the determination of aquifer properties (e.g., Table A.4 of appendix B.2). This different information is embedded in the data and can be decomposed to decipher and assess the drivers of the changes in groundwater levels. The idea behind

signal decomposition is that a signal consists of different sinusoids made up of periodic and aperiodic inputs that can be related to the drivers of the change. Each signal can be decomposed into its constituent amplitude and frequency components (e.g. Eriksen and Rehman, 2023).

The concept of signal decomposition can be applied to decompose groundwater levels into sinusoids. Each sinusoid is defined by its amplitude, phase, and period (Figure 5.1). The groundwater pressure signal can be decomposed into their constituent sinusoids to extract harmonic components (Figure 5.1).

A conceptual schematic of the field stress and strain sources (e.g., Earth tides and barometric pressure) that affect groundwater levels at the site is represented in figure 5.2. The schematic conceptualizes the natural and anthropogenic factors and drivers that influence aquifer systems. These influences are recorded in groundwater levels, which can be decomposed into constituent periodic signals and analyzed for their properties and aquifer characteristics using poroelastic parameters (subsection 5.2.4) and model relationship (Cutillo and Bredehoeft, 2011; Detournay and Cheng, 1988; Doan et al., 2008; Fuentes-Arreazola et al., 2018; Hsieh et al., 1988; Kümpel, 1991; Kuang et al., 2020; McMillan et al., 2019; Rau et al., 2022; Rice and Cleary, 1976; Wang and Manga, 2021; Wang, 1993; Zhang et al., 2009).

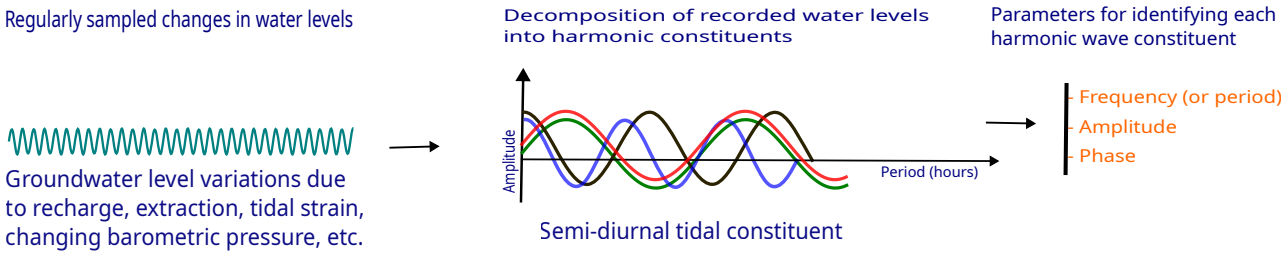

Figure 5.1: Conceptualization of measured groundwater levels decomposition into harmonic components

5.2 Methods

The water pressure data are studied using wavelet-based semblance analysis, singular spectrum analysis (SSA), and discrete Fourier transform (DFT).

The wavelet-based semblance analysis is used to compare two water pressure data sets for flow-varying events as a function of time and wavelength, while the SSA is used to extrac long and short periodic components and the DFT is used to identify diurnal and semi-diurnal harmonic components in the water pressure, groundwater temperature, and barometric pressure data. The steps involved in actualizing the end objectives of the methods are summarized in Figure 5.3. The details of each method are presented in subsections 5.2.1, 5.2.2, and 5.2.3.

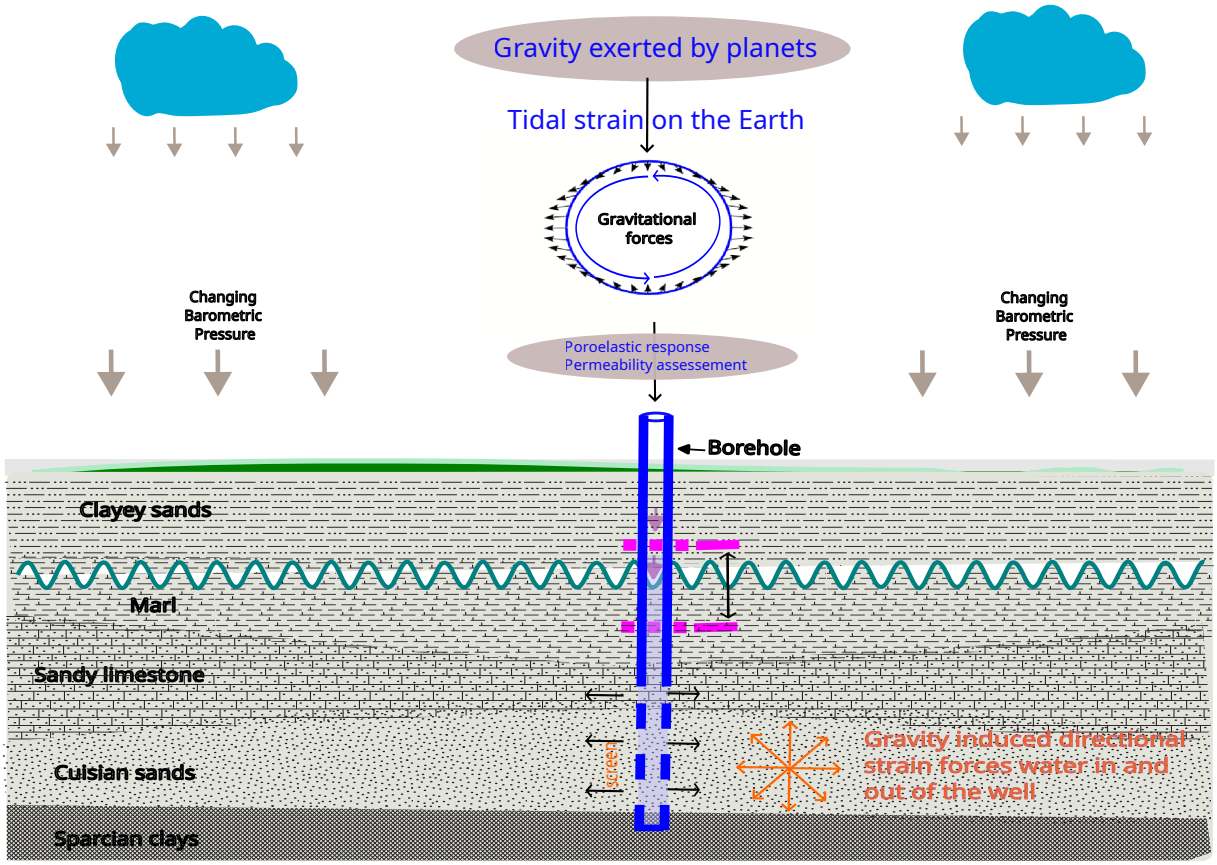

Figure 5.2: Conceptual model of the natural stresses and strains induced by changes in barometric pressure and Earth tides on the subsurface rock sequences and the aquifer systems with the resulting responses recorded in the groundwater levels as variations in the phreatic surface at the Genainville archaeological site. Information on the rock section at the site was derived from the BURGEAP report (BURGEAP, 1992), while the barometric pressure and Earth tides schematic were sourced from (Doan et al., 2006; McMillan et al., 2019; Rau et al., 2022).

5.2.1 Wavelet-based semblance analysis

Wavelet-based semblance analysis of two-time series (e.g., water pressure, water levels, temperatures, Earth tides) evaluates the correlation in the data using phase values to infer temporal or spatial relationships. In this study, the wavelet-based semblance analysis is performed to assess the correlation between water pressure data using phase values to infer spatial connectivity between two permeable beds. To achieve this, the phase response from the continuous wavelet transform CWT of time series data (e.g., water pressure) is correlated with the phase of another CWT water pressure data for a semblance model. The aim is to determine whether the saturated permeable beds or the aquifers in the same vicinity penetrated by two boreholes spatially separated are related by their responses to the same events when viewed in the time-frequency domain.

The theory of the wavelet-based semblance is presented in subsections 5.2.1.1, and 5.2.1.2, the

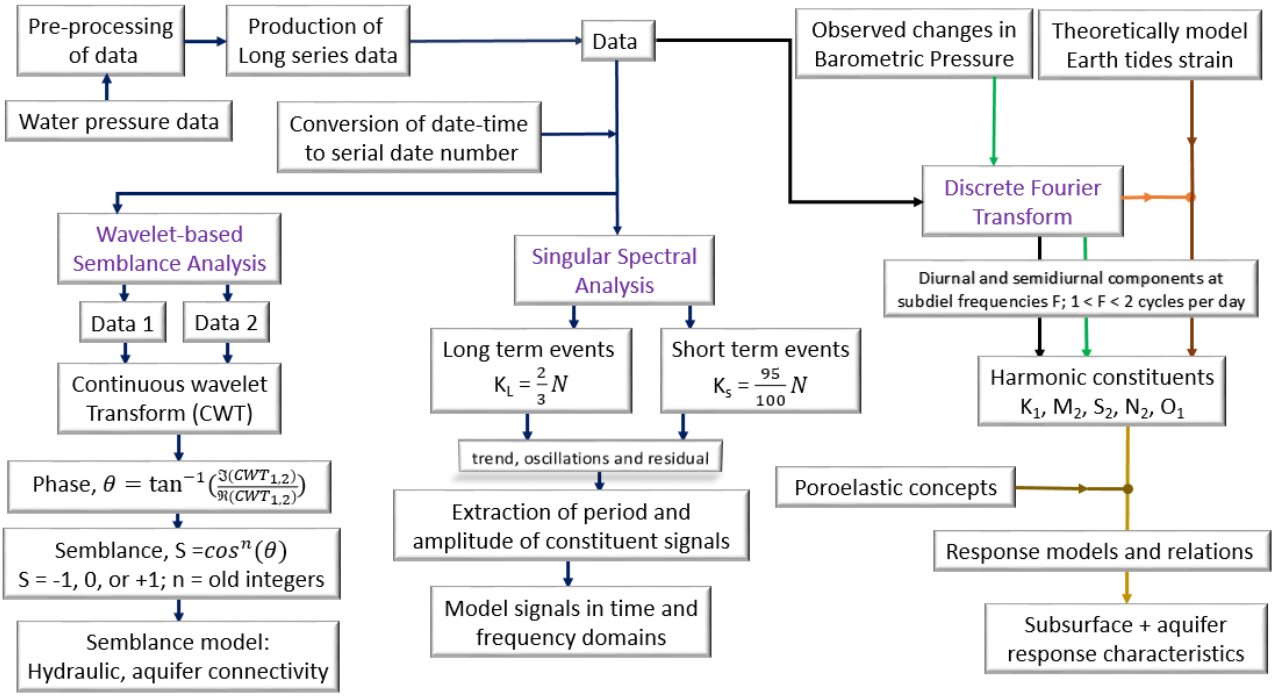

Figure 5.3: A schematic of the pre-processing steps and methods used in this study.

resulting models are described in subsections 5.4.2 and discussed in section 5.5.

Semblance analysis is a method for comparing two data sets for similarities or differences using their phase values (Cooper, 2009; Cooper and Cowan, 2008; von Frese et al., 1997).

Wavelet-based semblance analysis for comparing two-time series was introduced into the geophysical domain by Cooper and Cowan (2008), using the concept of continuous wavelet transform (CWT). Continuous wavelet transform (CWT) is an aspect of wavelet transform. It is a procedure that decomposes data into wavelets by translating and scaling them with a mother wavelet. The transform localizes the frequency content of data over time.

Unlike the Fourier transform (FT), which assumes that the frequency content of data must not change with time (e.g., time series data) or location (e.g., data measured as a function of position), the semblance procedure using the CWT allows two data sets to be compared for phase relationships as a function of both wavelength (or scale) and time (Cooper and Cowan, 2008). Semblance filtering using FT also suffers from the same fate as conventional FT in that it lacks temporal resolution of the data. Despite the limitation of FT, Fourier transform-based semblance analysis compares two-time series based on their phase as a function of frequency (Cooper, 2009). FT-semblance filtering can extract components with any degree of correlation.

The Short Time Fourier Transform (STFT) was developed to examine the frequency content of a

signal within a gived data size in order to constrain time. It suffers from data discretion, which limits it to the sampled space. Compared to the STFT, which was developed to achieve the same objective within a window that limits its coverage, the Wavelet Transform is a windowing technique with variable regional size (Mallat, 2009). CWT provides continuous information about the frequency content over time.

The CWT procedure compares two-time series based on their phase value as a function of both time and wavelength (Cooper, 2009; Cooper and Cowan, 2008). The output semblance function lies between -1 and $+1$. It detects oscillations in two-time series that are out of phase (180° phase difference, $\mathbf{S} = -1$) and in phase (0° phase difference, $\mathbf{S} = +1$) (Cooper and Cowan, 2008; Kosek and Popiński, 1999; Kosek et al., 2010). Using the semblance filtering parameters, it is possible variations in the time series that are in good phase agreement, and to localize anomalies or common oscillations in all possible frequency bands.

Wavelet semblance analysis has been used to compare two-time series data in different domains. These include comparison of gravity and aerogeomagnetic data to locate of anomalies over a profile (Cooper and Cowan, 2008), detection of event-related potentials (ERP) for usage in brain-computer interface (BCI) systems (Saavedra and Bougrain, 2013a), assessing the performance of stocks and bonds in the financial market (Verner and Herbrik, 2017), determining the common signal in geodetic and fluid excitation functions of polar motion (Kosek and Popiński, 1999; Kosek et al., 2010), and monitoring the vibration signal of a dried vacuum pump to resolve its state in time and frequency (Fawazi et al., 2023).

In this study, continuous water pressure data collected from three boreholes at intervals of 60-second intervals over a period of more than one hydrological year were analyzed to assess the local phase behavior. The datasets were routinely retrieved from the TD Divers at intervals before the endpoint of the instrument storage capacity was reached and concatenated to produce long series datasets covering the seasonal and hydrological cycles (see subsections 4.3.1 and 4.3.3).

The datasets from the three boreholes were analyzed in three groups. Group 1 consisted of data from PzSa and PzTh; Group 2 consisted of data from PzSa and PzShf; and Group 3 consisted of data from PzShf and PzTh.

The objective is to assess local relationships within the data sets by comparing two data sets for the hydraulic or spatial response of the subsurface materials using the semblance filtering tech-

nique. The concept of semblance analysis is first discussed using the classical Fourier transform, mentioning the merits and demerits of using the FT. Thereafter, the wave transform is briefly presented, and the concept is used in semblance filtering for correlation between two-time series.

5.2.1.1 Concept of semblance analysis based on Fourier transform

The theory of FT and its implementation using the Fast Fourier Transform algorithm are widely documented (e.g. Cooley and Tukey, 1965; Kong et al., 2021; Milton and Ohira, 2021). It says that a signal is composed of sinusoidal components made up of sine and cosine at different frequencies. Hence, using the FT mathematics, a sampled signal x can be decomposed into its frequency domain components, as expressed in equation 5.1.

$$X(f) = \int_{-\infty}^{\infty} x(t) e^{-2\pi f t} dt \tag{5.1}$$

Where X(f) represents the resulting transform as a function of frequency, f, t indicates the temporal (time) or spatial (space) variability of the data. The phase information is obtained from the relationship between the real X_{re} and the imaginary X_{im} components of the output Fourier transform (equation 5.2).

$$Phase = \tan^{-1}\left(\frac{X_{re}}{X_{im}}\right) \tag{5.2}$$

By using the concept of the Fourier transform to implement semblance analysis **S**. It implies two Fourier-transformed time series data can be represented by equation 5.3.

$$\mathbf{S} = \cos\theta(f) = \frac{\Re_1(f)\Re_2(f) + \Im_1(f)\Im_2(f)}{\sqrt{\Re_1^2(f) + \Im_1^2(f)} \times \sqrt{\Re_2^2(f) + \Im_2^2(f)}} \tag{5.3}$$

Where $\Re_1(f)$ and $\Im_1(f)$ are the real and imaginary parts of the resulting complex quantity from the Fourier transformation of the first time series data. In the same manner, $\Re_2(f)$ and $\Im_2(f)$ are for the second set of data. The f in the expression indicates it is in the frequency domain.

The procedure performs the analysis by first setting a threshold value and, secondly, by separating the Fourier transformed data into two parts. The first part of the Fourier coefficients consists of values above the threshold, while the second part is made of the remaining data.

5.2.1.2 Concept of semblance analysis based on wavelet transform

The wavelet transform-based semblance method has some advantages over Fourier transform semblance filtering, as enumerated in subsection 5.2.1. Furthermore, a mother wavelet is used in

the decomposition procedure to displace and shift the input signal. The mother wavelet is chosen for its orthogonal nature, which results when its real and imaginary parts form a Hilbert transform pair. A mathematical property that is also formed in the Fourier transform. The use of a complex wavelet gives the output of CWT its complex form (Cooper and Cowan, 2008). The scale component in the CWT provides flexibility that allows different values of the scale to be used for accessing different information responses of a transform.

The concept of wavelet transform is to represent a signal in terms of the displaced and shifted versions of a mother wavelet Ψ_t, function (Saavedra and Bougrain, 2013a):

$$\Psi_{a,b}(t) = \frac{1}{\sqrt{|a|}}\Psi\left(\frac{t-b}{a}\right) a, b \in R, \tag{5.4}$$

where a and b denote the respective scale and time shift parameters. There are a number of mother wavelet functions (equation 5.4) such as Morlet function (Cooper and Cowan, 2008) and Shannon function (Kosek et al., 2010) that are commonly used in wavelet transformations.

When a signal x_t is convoluted with the mother wavelet, it results in wavelets with complex properties (equation 5.5).

$$W_{\Psi}^{x}(a,b) = \langle x(t)|\Psi_{a,b}(t)\rangle, \tag{5.5}$$

The steps in the CWT semblance analysis procedure is summarized in figure 5.4.

5.2.1.3 Continuous wavelet transform

Two methods of wavelet transformation are distinguished as a function of the scale and shift parameters: continuous wavelet transform (CWT) and discrete wavelet transform (DWT). In CWT, the scale and shift (translation) parameters are continuous, while in DWT, the parameters are discretized scale $a_j = 2^j$ (dyadic step) and time shift b_j are such that at each scale $j+1$, the resulting coefficient is two-times-less those of the previous scale. In this study, the models were produced using CWT with Morlet mother wavelet. The continuous wavelet transform, herein denoted as W, is conceptually a sliding cross-correlation between a data point $x(t)$ and a reference or mother wavelet chosen from a family of wavelets (equation 5.6)

$$W_{a,b} = \int_{-\infty}^{\infty} x(t)\frac{1}{\sqrt{|a|}}\Psi^*\left(\frac{t-b}{a}\right) dt, \tag{5.6}$$

where a is the scale, b is the displacement or shift time function, Ψ is the mother or reference wavelet, and Ψ^* signifies a complex conjugate of the reference wavelet. The complex property of

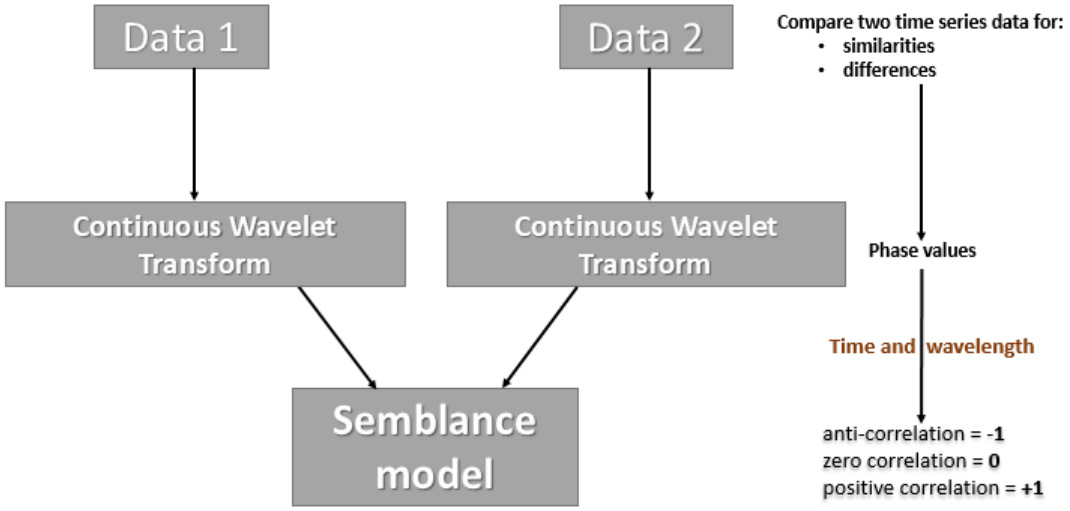

Figure 5.4: Schematic presentation of the semblance analysis steps with the phase response of two signals as a function of time and wavelength.

CWT enables its definition of the phase at each time (or space) and scale. Cooper and Cowan (2008) compared two-time series data using the method of cross-wavelet transform defined by Torrance and Compo (1998) after applying CWT. In the procedure, the resulting cross-wavelet of the two data, W_1 and W_2, can be expressed as $W_{1,2}$ in equation 5.7. Where * signifies a complex conjugate.

$$W_{1,2} = W_1 \cdot W_2^* \tag{5.7}$$

The expression in equation 5.7, is a complex value having an amplitude A, and a phase value θ. The amplitude is given by equation 5.8.

$$A = \left| W_{1,2} \right| \tag{5.8}$$

The phase angle is defined by equation 5.9. Where $\Im$ and $\Re$ represent the respective imaginary and real components of the signal. The phase value ranges between π and $-\pi$.

$$\theta = \tan^{-1}\left(\frac{\Im(W_{1,2})}{\Re(W_{1,2})}\right) \tag{5.9}$$

Semblance S measure, defined in equation 5.10, is a procedure that compares the local phase of two signals for relationships.

$$S = \cos^n(\theta), \tag{5.10}$$

where n is an odd integer that is greater than zero. The correlation output results with -1 representing `inverse correlation`, zero 0 denoting `uncorrelated` and $+1$ defining `correlated` data points.

5.2.2 Singular Spectrum Analysis

Singular Spectrum Analysis (SSA) is a procedure of time series analysis that decomposes, reconstructs, and predicts time series. It is a non-parametric and model-free method of analyzing time series that involves its decomposition, and forecasting. SSA can be applied to all time series data, which means it produces data-driven models (Golyandina et al., 2001). The procedure has useful applications in smoothing, filtering, and reducing noise in time series. It structures the time series into the trend, periodic components, and noise for extraction (Golyandina and Zhigljavsky, 2013; Vautard et al., 1992). It has been widely used to analyze data in economics, climate, meteorology, and the physical and social sciences. It incorporates traditional methods of time series analysis (e.g. Brockwell and Davis, 2016). SSA has been applied to extract periodic information from climate data (Ghil et al., 2002), study characteristic oscillations in spontaneous potential (SP) data, and evaluate SP-groundwater pressure head dynamics and phase relations (Allègre et al., 2014), decompose temperature data for constituent periodicities (e.g. Marques et al., 2006), analyze noise in the coordinate time series of stations (Kong et al., 2023), and assess the response of meteorological and hydrological data to the emission of soil gas radon (Arora et al., 2017). Results with higher accuracy were obtained by Hassani (2007) from SSA treatment of well-known data compared to using Box-Jenskins SARIMA models, the ARAR algorithm, or the Holt-Winter algorithm on the same data (Box and Jenkins, 1976; Box et al., 2015; Brockwell and Davis, 2016).

5.2.2.1 Basic concept

SSA is a methodology that is based on the concepts of matrix-vector products, eigenvalues, and eigenvectors. The main idea of the SSA method of time series analysis is to decompose a signal into its main trend, oscillatory components, and a'structureless' noise. The SSA procedure is implemented in four steps: embedding, decomposition, grouping, and reconstruction (Golyandina and Zhigljavsky, 2013).

A striking property of SSA is its **separability** character. Decomposed signals can be separated into individual oscillation components. Each component can be separated and graphed. The SSA method is effective for extracting seasonality components, periodicity with varying amplitudes, finding trends of different resolutions, and forecasting new time series from reconstructed original data (e.g. Ghil et al., 2002; Hassani, 2007). The basic theory of the SSA herein presented is discussed in Zhigljavsky (2010). Let $x_1, \cdots, x_N$ be a time series of length N. Given a window length

L ($1 < L < N$), we construct the L-lagged vectors $X_i = (x_i, \cdots, x_{i+L-1})^T$, i = 1,2,$\cdots$, K = N - L + 1, and compose these vectors into the matrix in equation 5.11. This matrix has size $L \times K$ and is often called the 'trajectory matrix'. It is a Hankel matrix, which means that all the elements along the diagonal $i + j$ = constant are equal (Deng, 2014).

$$\mathbf{X} = (x_i + j - 1)_{i,j=1}^{L,K} = [X_1 : \cdots : X_K] \tag{5.11}$$

The columns X_j of $\mathbf{X}$ can be considered as vectors in the L-dimensional space $\mathbb{R}^L$. The singular value decomposition of the matrix $\mathbf{X}\mathbf{X}^T$ yields a collection of L eigenvalues and eigenvectors. A particular combination of a certain number l of these eigenvectors determines an l-dimensional subspace $\mathbb{L}$ in $\mathbf{R}^L$, $l <$ L. The L-dimensional data $\{X_1 \cdots, X_K\}$ is then projected onto the subspace $\mathbb{L}$ and the subsequent averaging over the diagonals yields some Hankel matrix $\bar{X}$ which is considered an approximation to $\mathbf{X}$. The time series $\bar{x_1} \cdots \bar{x_N}$, which is in one-to-one correspondence with the matrix $\bar{X}$, provides an approximation to the original series $x_1, \cdots, x_N$.

5.2.2.2 Mathematical models

SSA is implemented in four steps: embedding, decomposition, grouping, and reconstruction of a time series (Figure 5.5). This approach applies to univariate or one-dimensional time series data X_t with finite length N $\{X_t$, t = 1, …, N$\}$. Before commencing the analysis, it is important that X_t is not a series with all zeros and $N > \mathbf{2}$. A vector space also known as the *window length* $\mathbf{M}$ is chosen such that its width is not more than half the length of the univariate time series $\{M \leq N/2\}$. The *embedding* procedure involves the mapping of one dimensional time series $\{X_t\}$ into a multi-dimensional time series $\{X_1, \ldots. X_K\}^{'}$ with vectors $X_i = \{X_i \ldots, X_{i+M-1}\} \in \mathbb{R}^M$, where, K = N - M + 1; $1 \leq i \leq$ K; and the window length parameter is $2 \leq$ M $\leq$ N. The vectors X_i are the lagged vectors, or the *M - lagged* vectors.

The result is a trajectory matrix defined by equation **5.12** and given by the expression in equation **5.13** (e.g. see Hassani, 2007; Kong et al., 2023). The trajectory matrix $\mathbf{X}$ has the structure of a Toeplitz matrix. Typically, with all the diagonal values constant, it means that $i + j$ = constant. The (i, j) part of the matrix is $X_{ij} = X_{i+j-1}$, which indicates that the matrix X takes the same value for a constant value of $i + j$ (Deng, 2014). In simple words, the diagonal has a uniform value.

$$\mathbf{X} = \{X_i, ..., X_K\} = (x_{ij})_{i,j=1}^{M,K} \tag{5.12}$$

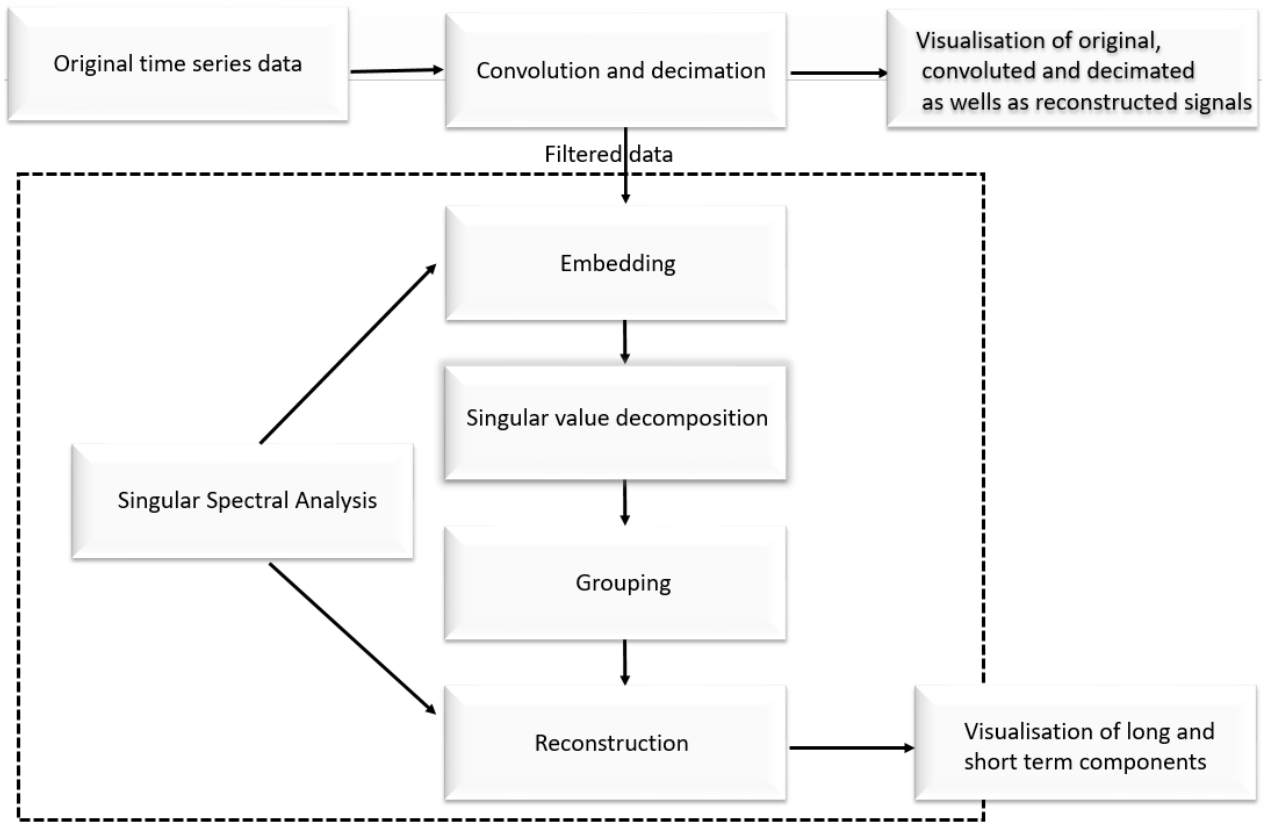

Figure 5.5: The steps involved in singular spectrum analysis

Afterwards,

$$\mathbf{X} = \{X_i, ..., X_K\} = \begin{bmatrix} x_1 & x_2 & \cdots & x_{N-M+1} \\ x_2 & x_3 & \cdots & x_{N-M+2} \\ \vdots & \vdots & \ddots & \vdots \\ x_M & x_{M+1} & \cdots & x_N \end{bmatrix} \tag{5.13}$$

An $M \times K$ matrix where 1 < M < N - M + 1.

The lags or lag values k are derived from the window size, k = 0,..., M - 1. The lags are used in the computation of the covariance between two values X_t and X_{t+k}, where k is the lag or delay. The equations of the M × M covariance matrix are given by equation 5.14:

$$\mathbf{C} = \begin{bmatrix} c(0) & c(1) & \cdots & c(M-1) \\ c(1) & c(0) & \cdots & c(M-2) \\ \vdots & \vdots & \ddots & \vdots \\ c(M-1) & c(M-2) & \cdots & c(0) \end{bmatrix} \tag{5.14}$$

$$where, \qquad C_{(j)} = \frac{1}{N-j} \sum_{i-1}^{N-j} x_t x_{i+j} \qquad \text{and} \qquad j = 0, 1, ..., M-1. \tag{5.15}$$

In some literature, the covariance matrix **C** is given by equation 5.16 (e.g. Allègre et al., 2014; Ghil et al., 2002; Schoellhamer, 2001).

$$C_{i,j} = \frac{1}{N - \left|i-j\right|} \sum_{i=1}^{N-\left|i-j\right|} x_t x_{t+|i-j|} \qquad (i,j) \in [\![1,M]\!]^2 \tag{5.16}$$

In the next step, eigenvalue decomposition is applied to the lagged co-variances (auto variance) matrix to obtain the **eigen values** λ_k and the **eigen vectors** E_K. The eigenelements {(λ_k, E_K): k = 1..., M } of C_x are then obtained by solving equation 5.17 (Ghil et al., 2002).

$$C_x, E_K = \lambda_k, E_K \tag{5.17}$$

Thus, the first component is the trend of the series; it is associated with the first eigenvalue, and usually, it is the long-term trend when it is present. The second and other oscillatory components represent pairs of eigenvalues. The residual component, or noise, is related to the uncoupled eigenvalues. It is usually of a higher rank.

5.2.2.3 Singular value decomposition (SVD)

let {$\mathbf{S} = \mathbf{X}\mathbf{X}^T$} represent the M × M co-variances (auto variance) matrix and $\mathbf{P}\Lambda\mathbf{P}^T$. In this description, $\Lambda = diag(\lambda_1..., \lambda_M)$ is the diagonal matrix of $\mathbf{X}\mathbf{X}^T$ sorted in decreasing order so that $\lambda_1 \geq \lambda_2 \geq \lambda_3... \lambda_M \geq 0$ and $P = (P_1, P_2, P_3, ..., P_M)$ is the corresponding orthogonal matrix of the eigenvectors of $\mathbf{X}\mathbf{X}^T$ (Deng, 2014; Hassani, 2007). The procedure is further explained, thus. Let λ_1, λ_2, $\lambda_3... \lambda_M$ denote the eigenvalues of the matrix **S** {$\mathbf{S} = \mathbf{X}\mathbf{X}^T$} sorted in decreasing sequence $\lambda_1 \geq \lambda_2 \geq \lambda_3 .... \lambda_M \geq 0$. Let the orthogonal eigenvectors of S that correspond to the eigenvalues be represented by B_1, B_2, B_3 .... B_M.

Using the concept, $V_i = X^T \cdot B_i \ / \ \sqrt{\lambda_i}$, where, $i = 1, 2, ...d$, and d is equal to the rank of the matrix X, in which the smallest value of i is such that $\lambda_i > O$. From the classic treatment, the value of d equals the minimum values of M and K.

Consequently, the trajectory matrix is decomposed as X = X_1+ X_2 ... X_d, where $X_i = \sqrt{\lambda_i} \cdot B_i \cdot V_i^T$. The matrices X_i are known as elementary matrices if X_i has one rank. The triple ($\sqrt{\lambda_i} \cdot B_i \cdot V_i^T$) is also known as *ith* eigentriple (ET) of the SVD (Deng, 2014).

The procedure can be explained as a step in obtaining the eigenvalue λ_k from the partial variance (PV) using equation 5.18. The eigenvalues λ_k can be evaluated for the original time series in the

direction specified by the corresponding eigenvectors E_k (Kong et al., 2023). The eigenvector is also known as the empirical orthogonal function.

$$PV(k) = \sum_{k=1}^{\frac{\lambda_k}{M}} \lambda_k \tag{5.18}$$

From the eigenvectors component{E_K, 1 ≤ k ≤ M}, the original time series can be reconstructed to length K {K: K = N- M +1} (equation 5.19)

$$\mathbf{A}_k(t) = \sum_{j=1}^{M} X(t+j-1)E_{k,j}\, t = 1, ..., K \tag{5.19}$$

where $\mathbf{E}_{k,j}$ is the value of the j-th line corresponding to k-th eigenvector as expressed by Kong (2023).

5.2.2.4 Reconstruction

The reconstruction is carried out in two steps known as `eigentriple grouping and diagonal averaging`. The procedure of eigentriple grouping succeeds with the expansion, X = X_1+ X_2... X_d, and the eigentriple regrouping steps the set {$1, 2, 3, ...d$} into the disjoint subsets {$1, 2, ...m$} such { I = I_1+ I_2... I_m} where each I_j contains several $X_i's$. Hence, the equation X = X_1+ X_2 ... X_d becomes X = X_1+ X_2 + X_3... X_d = X_{t_1}+ X_{t_2} + X_{t_3}... X_{t_m}. The Eigentriple of the SSA is as presented in Deng (2014). It is known as an Eigentriple. If m=d with I_j = {j}, where $j = 1, 2, 3, ...d$, the method is referred to as elementary grouping. The concluding step in the SSA procedure is called the *diagonal grouping*. The resultant matrix $X_{I\,j}$ from the grouped decomposition is transformed into a subseries of length N. Let R represent the M× K matrix (see equation **5.12**). Such that R_{ij} is the element of R. R can output a series R_1, R_2, R_3,... R_N given by:

$$R_k(t) = \begin{pmatrix} \frac{1}{t}\sum_{kk}\sum A_k(t-j+1) & 1 \le t \le M-1 \\ \frac{1}{M}\sum_{kk}\sum A_k(t-j+1)E_{k,j} & M \le t \le K \\ \frac{1}{N-t+1}\sum_{kk}\sum_{N+M}^{M} A_k(t-j+1) & K+1 \le t \le N \end{pmatrix} \tag{5.20}$$

Gaps or missing sections in time series may result from different field or laboratory situations in geoscience measurements. For example, in borehole water level or water pressure measurements, gaps in the data may arise from faulty instruments, a time-lapse in data retrieval and instrument reinstallation, or some unforeseen natural occurrence such as flooding or storm events, which can

disrupt the recording process. Restrictions and delays by a lawful authority or other societal elements have also hindered the strict acquisition of continuous data. Hence, time series with gaps or missing data are often used in geosciences, which restricts them to certain types of analysis. The SSA method was modified by Schoellhamer (2001) for use on time series with gaps. Singular spectrum analysis for time series with missing data (SSAM) modifies the SSA calculation of lagged autocorrelation and principal components (Schoellhamer, 2001). The lagged auto-correlation is computed without including the pair of data with a gap as the first step (equation 5.21). The overbar signifies that either a time series with missing data was used or resulted from the computation of a time series with missing data.

$$\bar{c}_j = \frac{1}{N_l} \sum_{l \leq N-j} \bar{x}_l \bar{c}_{l+j} \tag{5.21}$$

$0 \leq j \leq M-1$, for N_l pairs with no missing.

The eigenvalues λ_k and eigenvectors (or empirical orthogonal functions) E_j^k are computed and sorted from the highest to the lowest as in equation **5.13** of the SSA. The eigenvectors contain no missing data. The calculation of the kth principal vector neglects the missing data points (equation 5.22).

$$\bar{a}_j^k = \frac{M}{N_l} \sum_{l \leq N-j} \bar{x}_{i+l} \bar{E}_l^k \tag{5.22}$$

$0 \leq j \leq M-1$, for $N_l x i + l$ pairs with no missing data.

5.2.3 Extraction of harmonic constituents with Discrete Fourier Transform

The discrete Fourier transform (DFT), is used for fast Fourier transform (FFT) computations involving discrete data sets (Milton and Ohira, 2021).

The result of an FFT computation contains the energy distribution over a range of frequencies. A signal or measured data is conceived to consist of different sinusoids. Each sinusoid represents an event or an occurrence at a specific frequency.

In light of the response of aquifer levels to changing environmental and climatic conditions as well as anthropogenic influences, Consider a series of time-variant water pressure data x, measured at a regular interval of time *dt*. The discrete dataset *x(t)* represents a composite of natural and human inducement phenomena.

To examine the constituents in the data for periodic and aperiodic behavior. We transform the

temporal (time domain) data into the frequency domain, decomposing it to output the harmonics in the data using DFT. A time series data x(t) of length N, sampled at a regular interval time *dt* can be represented as equation 5.23:

$$\hat{x}_j = \sum_{k=0}^{N-1} x(t_k) e^{-i\frac{2\pi jk}{N}} \tag{5.23}$$

where k and j are the indices of the sampled discrete data in the respective time and frequency domains. The values of k or $j = 0, 1, 2, ..., N-1$.

The output of the discrete Fourier transform, $\hat{x}_j$, is complex. A complex term or number ($x(w)$) has a real term, x_{re}, and an imaginary term, x_{im}, such that $\hat{x}_j = x_{re} + ix_{im}$ and $i = \sqrt{-1}$. The absolute value of the DFT coefficient, which gives the amplitude information (equation 5.24), while the phase information (θ_j) obtained from equation 5.25, lies within $-\pi \leq \theta_j \leq \pi$.

$$Amplitude = \frac{2}{N}|\hat{x}_w| = \frac{2}{N}\sqrt{x_{re}^2 + x_{im}^2} \tag{5.24}$$

$$Phase = \theta = \tan^{-1}\left(\frac{x_{re}}{x_{im}}\right) \tag{5.25}$$

The DFT coefficients correspond to frequencies: $0, \frac{f_s}{N}, 2\frac{f_s}{N}, ..., N-1\frac{f_s}{N}$, where $f_s = \frac{1}{dt}$, the sampling frequency obtained with regularly spaced data. It is also symmetric, with an equal number of positive and negative frequency components.

The graphical representation of the amplitudes and the corresponding frequencies for the measured borehole water pressure (Figures 5.46, 5.47 and 5.48), theoretical computed areal tidal strain (Figure 5.49), and the barometric pressure variation at the site are shown in figure 5.50.

5.2.4 Concept of poroelasticity

Mathematically, the relationship between applied stress $\Delta\sigma$ and the corresponding strain $\Delta\varepsilon$ is given by equation 5.26.

$$E = \frac{\Delta\sigma}{\Delta\varepsilon} \tag{5.26}$$

Where E, is the Young modulus expressed in Pa, $\Delta\sigma$ the applied stress is in Pa and $\Delta\varepsilon$, the strain is dimensionless.

The concept of elasticity is used to explain the effect and strain produced by the response of a porous medium (e.g., soils) to natural forcings, which include tidal forces and barometric loading. Elastic deformation of rocks and soils in response to an applied stress, changes the volume of the pore space and the pressure of the fluid and its contents (Detournay and Cheng, 1988; Kümpel,

1991; Van Der Kamp and Gale, 1983).

To describe the state of an elastic medium, let us assume, for simplicity, that the rock or soil is isotropic and homogenous. A pure elastic medium is characterized by two elastic coefficients: either a combination of the two lamé constants λ and μ, or the Poisson ratio ν and the bulk modulus K, or the Poisson ratio ν and the Young modulus E, etc. (Doan et al., 2006; Rojstaczer and Agnew, 1989; Wang, 1993). An elastic medium whose pores are filled with fluid is characterized by two additional quantities, which increase to four the number of elastic moduli required to define its state because of the fluid it contains and the pressure exerted by the fluid.

It is adequate to consider the small elemental volume of a porous rock as representative of the field-scale volume. A *fluid-filled porous medium* (typically an aquifer medium) responds to applied stress by producing the usual strains due to the matrix of the porous medium and volume strains due to the changes in the fluid pressure. The constitutive expression by Rice and Cleary (1976), gives the relationship between the stress σ and strain ε in a poroelastic medium (for an isotropic linear material) as equation (5.27):

$$\varepsilon_{ij} = \frac{\beta}{3}\left(\frac{1+\nu}{1-2\nu}\sigma_{ij} - \frac{\nu}{1-2\nu}\sigma_{ij}\delta_{ij} + \alpha p\delta_{ij}\right) \tag{5.27}$$

$$G = \frac{E}{2(1+\nu)} \tag{5.28}$$

$$K = G\frac{2(1+\upsilon)}{3(1-2\upsilon)} \tag{5.29}$$

where σ_{ij} is the stress (force per unit area) in the x_j direction, acting on the surface of a cube whose normals are in the x_i direction; δ_{ij} is the Kronecker delta; kk implies summation for repeated subscripts; ν = Poisson ratio; it relates to the Young modulus E, the shear modulus G, the bulk modulus K in equations 5.28 and 5.29.

The pore pressure p is expressed in terms of α, the Biot-Willis parameter (equation 5.30), such that $0 < \alpha < 1$ and $K \ll K_u$ (the undrained bulk modulus); K_s = the bulk of the matrix structure. The compressibility, β is the inverse of K, ($\beta = \frac{1}{K}$); Equation 5.31, sums the usual strains and provides a relation for the volumetric strain expression for the mean stress and pore pressure.

$$\alpha = \left(1 - \frac{K}{K_s}\right) = 1 - \frac{2G(1+\upsilon)}{3K_s(1-2\upsilon)} \tag{5.30}$$

$$\varepsilon_{kk} = \frac{1}{K}\left(\frac{\sigma_{kk}}{3} + \alpha p\right) \tag{5.31}$$

Using the constitutive equation and the elastic parameters, we can consider two types of flow behaviors in a porous medium: *drained* and *undrained* flow conditions. In the drained deformation, the fluid flows in and out of the medium with the pressure p remaining unchanged. In the undrained condition, fluid neither flows in nor out of the medium during deformation, and the pressure p changes by inducements. In this case, the bulk modulus is now represented by the undrained bulk modulus K_u, which, along with the Biot-Willis parameter α, is used to characterize the elastic response to fluid infiltration (Rice and Cleary, 1976).

Porosity is an intrinsic property of porous materials. It is vital for fluid storage and movement. The ratio of the volume of voids V_v to the total volume V_T of a medium defines its porosity, $\emptyset$; assuming all the pores are interconnected and fully saturated, the volume of the content fluid V_f is equal to the volume of the void space V_v ($V_f = V_v$). The fluid mass content, m, is the mass of fluid per unit volume (equation 5.32).

$$m = \frac{m_f}{V_T} \tag{5.32}$$

where m_f = is the mass of the fluid in a porous material of volume V_T. From the definition of the porosity and the fluid mass content, the mass of the fluid is given by $m = \rho_f \emptyset$ where ρ_f is the density of the fluid. The change in the fluid mass per unit volume, $\Delta m = m_f - m_o$ and the mean stress and the changes in pore pressure are related to the usual strain by the expression in equation 5.33:

$$\Delta m = m_f - m_o = \frac{3\rho(\nu_u + \nu)\left(\sigma_{kk} + \frac{3p}{B}\right)}{2GB(1+\nu)(1+\nu)} \tag{5.33}$$

Where m_o = the reference state mass of the fluid, ν_u = the undrained Poisson ratio, B is the Skempton's coefficient, and $0 < B < 1$. Inputting the bulk modulus and the Biot-WWillis parameter into the expression, it transforms to equation 5.34.

$$\Delta m = \frac{\alpha\rho}{K}\left(\frac{\sigma_{kk}}{3} + \frac{p}{B}\right) \tag{5.34}$$

5.2.4.1 The undrained deformation: build-up coefficients and natural forcing

The undrained conditions signify short-period changes relative to the applied stress (Doan et al., 2008; Van Der Kamp and Gale, 1983; Wang, 1993). It allows for fluid movement and changes in the pore pressure condition. Equation 5.34 is resolved under the undrained condition ($\Delta m = 0$), to obtain the resulting change in the fluid pressure Δp (equation 5.35), which is proportional to the change in the mean stress ($\Delta\sigma_{kk}$). It explains the mechanism for changes in water level in

poroelastic materials, given by $p = \rho g h$ where $\Delta\rho$ is the applied pressure, g is the gravitational acceleration, ρ is the density of water, and Δh the change in the height of the column of water (Sill, 2006).

$$\Delta p = \frac{\Delta\sigma_{kk}}{3} B \tag{5.35}$$

The relations between the drained and undrained elastic parameters provide additional quantities for evaluating the response of fluid-filled pore media to stress. For example, the undrained Poisson ratio ν_u relates to the Skempton coefficient and Biot-Willis parameter through (equation 5.35) (see e.g. Detournay and Cheng, 1988; Rice and Cleary, 1976; Van Der Kamp and Gale, 1983; Zhang et al., 2009).

The Biot-Willis coefficient is a significant component of the effective stress law for volume strain (equation 5.32). The values of α increase with a decrease in the confining pressure. The effective stress for volumetric strain relates to the elastic parameters in equation 5.30 (Wang, 1993). The B, α, K and K_u (or its inverse, the undrained compressibility $\beta_u = \frac{1}{K_u}$) are related by the expression in equation 5.37.

$$\nu_u = \frac{3\nu + \alpha B(1-2\nu)}{3 - \alpha B(1-2\nu)} \tag{5.36}$$

$$\frac{1}{K_u} = \frac{1}{K}(1 - \alpha B) \tag{5.37}$$

5.2.5 Loading efficiency and groundwater parameters

Using ERT, we have obtained refined models of the subsurface structure with more details on the beds, particularly water-bearing beds, and structures. In the next step, we continue with non-destructive investigation by characterizing the subsurface to estimate its physical and mechanical properties.

The fluctuations in the water levels were monitored at a resolution of 1 minute alongside changes in barometric pressure and theoretically computed strains impacted by Earth tides on the subsurface sequences and groundwater.

The three data sets were transformed into the frequency domain using the DFT. Peaks of spectral corresponding to literature-established periodic signals or harmonics were identified and the periods extracted (Cutillo and Bredehoeft, 2011; Ducarme et al., 2006; Merritt, 2004; Munk and MacDonald, 1960).

The amplitude of the dominant diurnal and semi-diurnal peaks in the water pressure (Figures 5.46, 5.47

and 5.48), barometric pressure (Figure 5.50) and Earth tide strain (Figure 5.49b) were computed and shown.

Using the model relation by Jacob (1940), the effect of the changes in barometric pressure on the aquifer (it water and physical property of porosity θ) is given by equation 5.38.

$$\gamma = \frac{\beta_w}{\theta\beta_f + \beta_w} \tag{5.38}$$

where, γ is the loading efficiency (-), β_w = compressibility of fluid (in this case, water) (Pa^{-1}) and β_f = the compressibility of the formation (Pa^{-1}), θ = the aquifer porosity (-). From literature, β_w = 4.59×10^{-10} Pa^{-1}. The expression by Jacob (equation 5.38) was used by Acworth *et al.,* (2016) in computing the specific storage S_s using an expression that involved equation 5.39 and the relation in equation 5.40. The expression by Acworth et al. (2016) was modified by Rau et al. (2022) to equation 5.41.

$$S_s = \rho_w g(\beta_f + \theta\beta_w) \tag{5.39}$$

$$BE = 1 - \gamma \tag{5.40}$$

$$S_s = \rho g \beta_w \frac{\theta}{BE} \tag{5.41}$$

where g is the gravitational acceleration = 9.82 ms^2, ρ_w is the density of water = 998.99 Kg/m^3.

Rau et al. (2022), rearranged the expression in equation 5.41 by involving equation 5.40 in the expression to obtain a relation for computing the porosity from specific storage derived from the response of Earth tides (equation 5.42). The relations by Acworth et al. (2016), Rau et al. (2022), and other workers have involved the poroelastic properties (section 5.2.4) of fluid-filled porous media in the computations and derivation of relationships for aquifer response to stress and strain. The aquifer porosity and Skempton coefficient can be calculated with equations 5.42 and 5.43. The Biot-Willis parameter is given by equation 5.44 or 5.45, where K is the bulk modulus, and K_s is the bulk modulus of the formation.

$$\theta = \frac{S_s BE}{\rho g \beta_w} = \frac{S_s}{\rho g \beta_w}(1 - \gamma) \tag{5.42}$$

$$B = \frac{3\gamma(1-\upsilon)}{2\alpha(1-2\upsilon)\gamma + (1+\upsilon)} \tag{5.43}$$

$$\alpha = 1 - \frac{K}{K_s} = 1 - \frac{\beta_s}{\beta} \tag{5.44}$$

$$\alpha = (1 - \frac{K}{K_s}) = 1 - \frac{2G(1+\upsilon)}{3K_s(1-2\upsilon)} \tag{5.45}$$

Using the concept of poroelasticity (Bredehoeft, 1967; Cutillo and Bredehoeft, 2011; Hsieh et al., 1987; Rau et al., 2022; Van Der Kamp and Gale, 1983), aquifer parameters can be estimated from the effect of Earth tides using equation 5.46 with compressibility, shear modulus, undrained bulk modulus derived from equations 5.47, 5.48, 5.49 and 5.50.

$$S_s = -\left[\left(1-\frac{K}{K_s}\right)\left(\frac{1-2v}{1-v}\right)\left(\frac{2\bar{h}-6\bar{l}}{R.g}\right)\right]\frac{\Delta A^{ET^{pot}}}{\Delta h} \tag{5.46}$$

where $\Delta A^{ET^{pot}}$ is the amplitude of the tidal component in Earth potential, Δh = the amplitude of the corresponding tidal component in the water pressure variations, g, and R are the respective literature values of gravitational acceleration and radius of the Earth taken as 9.82 ms^{-2} and 6371 km. The love numbers $\bar{l}$ = 0.07 and $\bar{h}$ = 0.6, are dimensionless parameters that summarize the elastic properties of the earth, while the Poisson ratio, v = 0.25, compressibility of the solid grains, $\beta_s = 1/K_s$, K_s = bulk modulus of the solids, while compressibility, $\beta = 1/K$, K = bulk modulus.

$$\beta = \theta\beta_f\left(\frac{\gamma}{1-\gamma}\right) \tag{5.47}$$

$$G = A^{ET}\frac{\rho g}{(1-BE)} \tag{5.48}$$

$$K^u = K - \frac{4}{3}G \tag{5.49}$$

$$B = \gamma\frac{\beta^u}{\beta} \tag{5.50}$$

5.3 Data and model used

5.3.1 Water pressure data

The details of the acquisition, instruments, and description of the water pressure data and barometric pressure data are contained in Chapter 4. The plot of the water pressure is reproduced here (Figure 5.6).

5.3.2 Earth tides model

Theoretical Earth tide parameters were computed using the *PyGTide* code by Rau (2018), based on the *ETERNA PREDICT* program by Wenzel (1996), at intervals of *1 minute* (Table 4.2). The synthetic tides were calculated for the three water borehole locations. The input variables used for the computation include the geo-parameter of the location, the sampling rate of the solid Earth

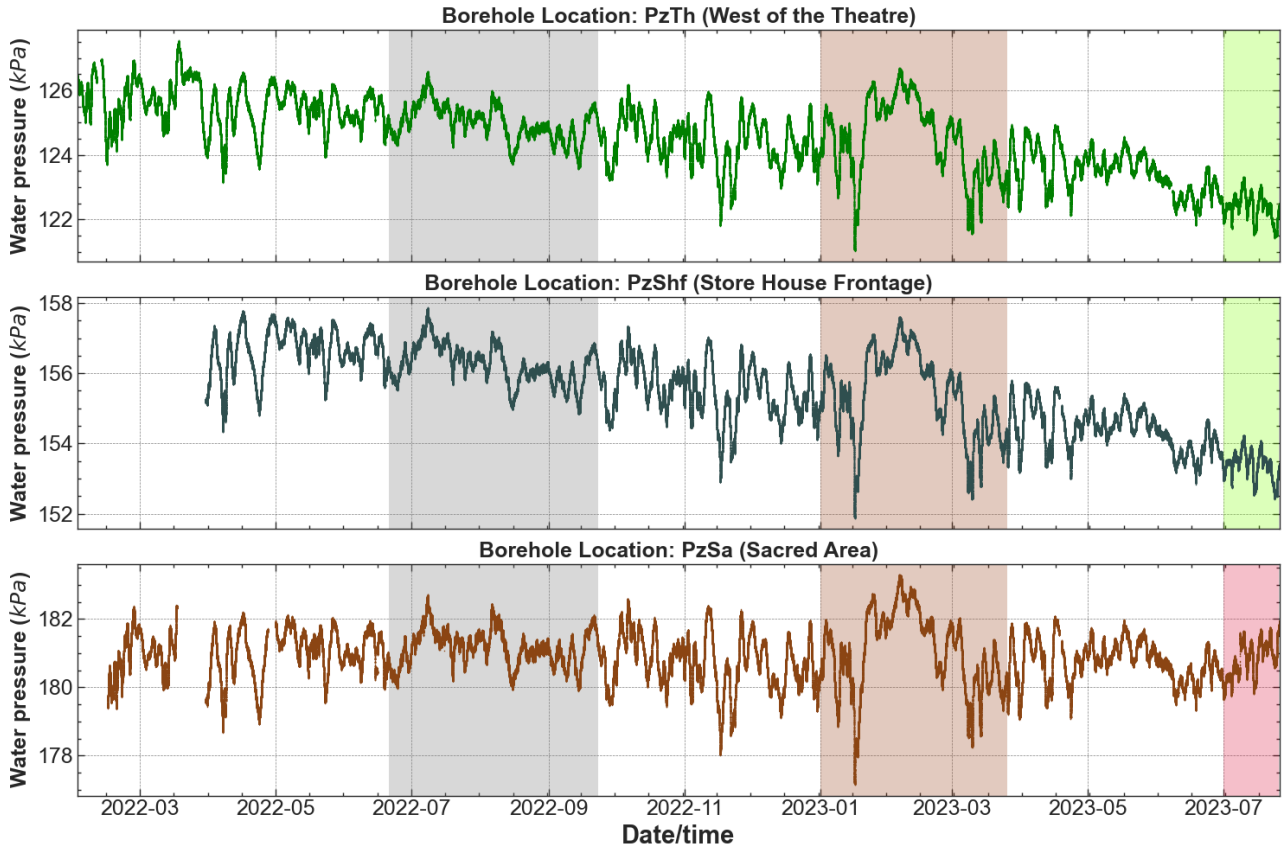

Figure 5.6: Borehole water pressure in the three boreholes acquired at the same period from January 2022 to July 2023. Minor gaps in the data are due to retrieval and re-installation procedures were between 10 and 15 minutes, while major gaps were caused by instrument failure or disruptions in the acquisition sequence by non-anthropogenic influences.

tides, the start date, and the duration (Table 4.1). The duration defines the calendar period or the date of interest, while the geo-parameter of the location provides the longitude, latitude, and elevation data. PyGTide is *ETERNA PREDICT* wrapped using the Python programming code. It is based on the latest tidal catalogue which included the *PREDICT* by Kudryavtse (2004). *PyGTide* has the advantages of input from the updated tidal catalogue and comparative accuracy over similar software used for Earth tides computation, e.g., TSoft (Van Camp and Vauterin, 2005).

The output of *PyGTide* incorporates the effects of pole wobble and length of day influences in the computation of the combined Earth tides effect (Rau, 2018; Rau et al., 2020). The computed combined tides were used in this analysis and referred to as Earth tides in this thesis.

Models of theoretically computed earth tides have been compared with field measurements in terms of both accuracy and precision. Figure 5.7 is a computed theoretical Earth tides model for *PzSa*. Typically, tidal data can be analyzed from two perspectives: amplitude and phase. The ratio of tidal data amplitude to the theoretical tide amplitude is associated with poroelastic properties

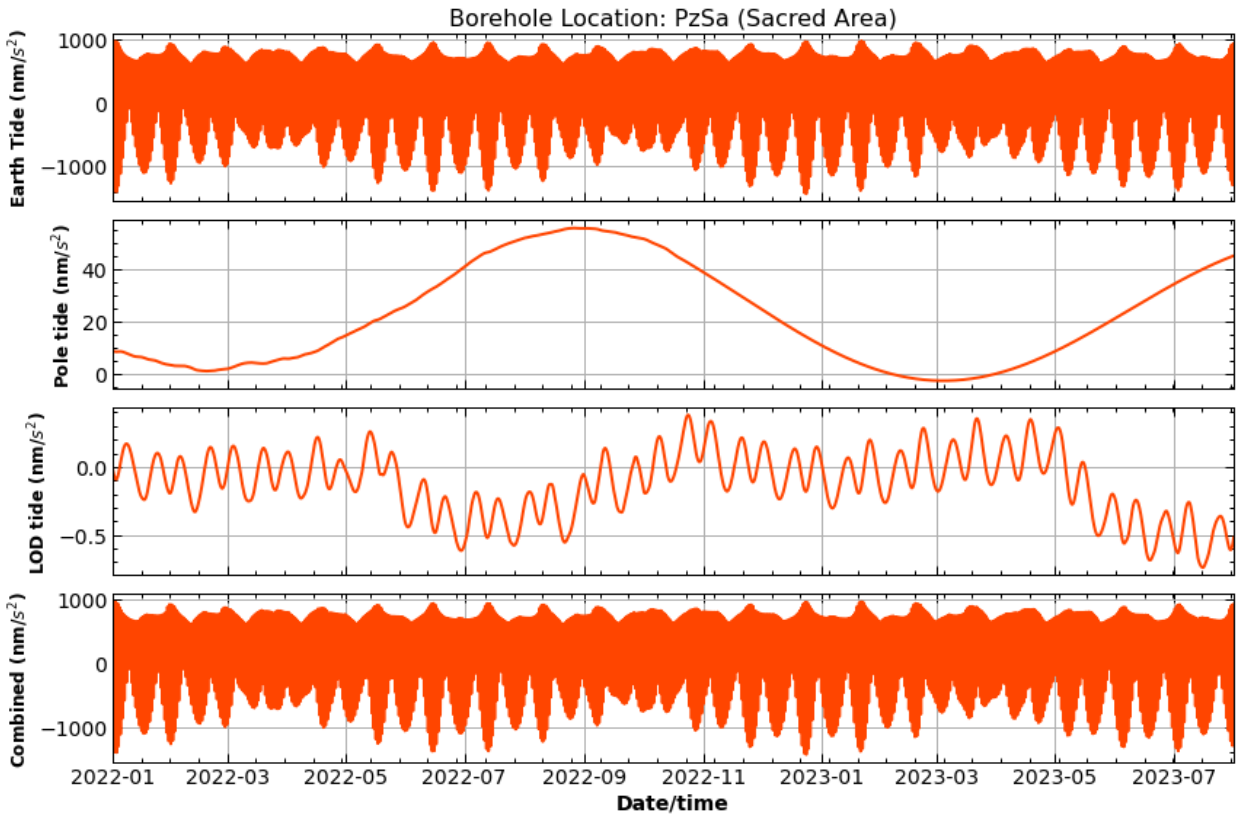

Figure 5.7: Theoretically computed Earth tides model using PyGTide code Rau (2018). The calculation of the variations in gravity on Earth induced by the relative motions of astronomical bodies such as the sun and moon taken into account the pole wobble and length of day (LOD) influences to produce the combined effect. An example is the Earth tides variations for the site at the Sacred Area borehole geolocation.

of the formation, including Skempton's coefficient, bulk modulus, and Poisson's ratio (Cutillo and Bredehoeft, 2011; Gao et al., 2020; Hsieh et al., 1988; Sato et al., 2022; Sun et al., 2019; Wang and Manga, 2021; Zhang et al., 2009). Aquifer flow properties, such as permeability, are more closely related to phase changes between tidal data and the theoretical tide (Doan et al., 2008; Gao et al., 2020).

5.3.3 Filtering of water pressure

Fluctuations in groundwater levels are caused by several factors that impose stress and strain on the aquifer systems (Doan et al., 2008). Figure 5.8 is an example of a long-series data plot showing variations in measured water pressure and groundwater temperatures from PzShf arising from different natural and, or human-related influences. Using the model equations 5.51 and 5.52 (e.g. see Rasmussen and Mote, 2007; Rasmussen and Crawford, 1997; Spane, 2002; Toll and Rasmussen, 2007), the change ΔW in aquifer water pressure corresponding to a change in the borehole water

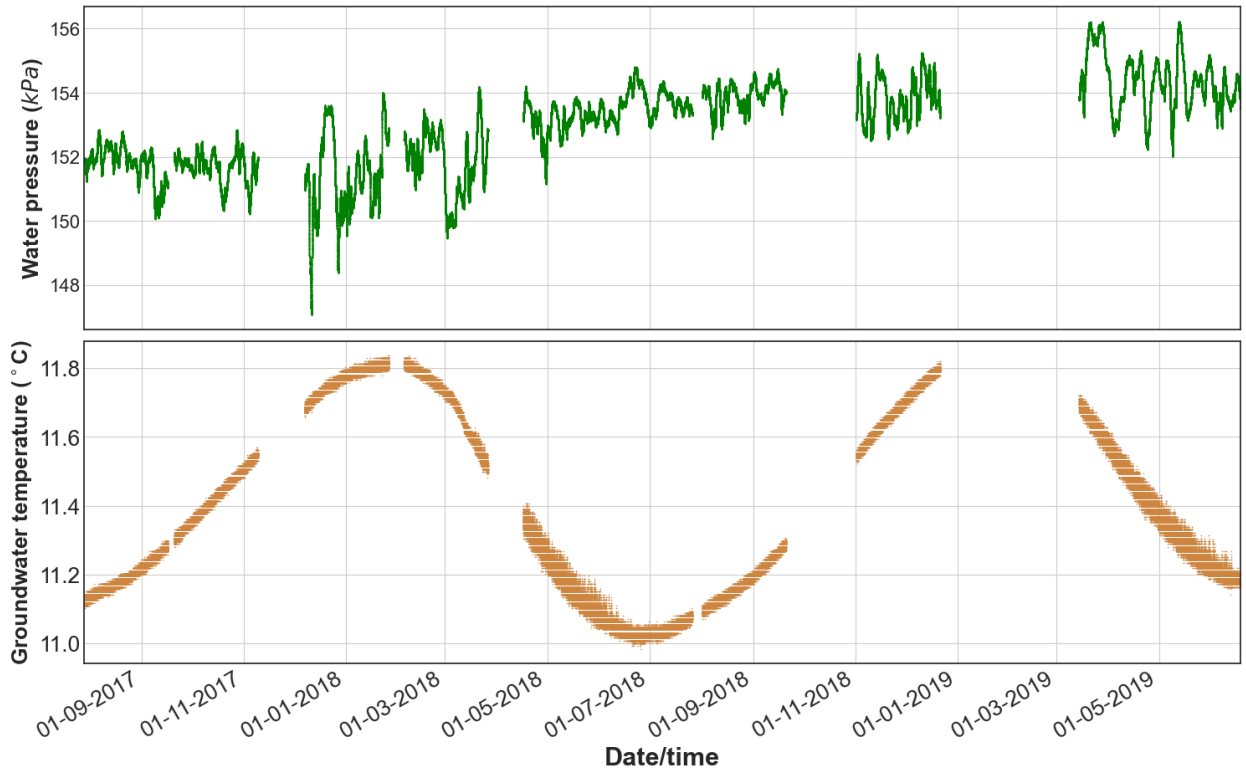

Figure 5.8: Observed fluctuations in water pressure and groundwater temperatures in *PzShf* from 2017 to 2019. The gaps in the plots were either due to instrument failure or delays in retrieving the data, which momentarily halted it continuous recording.

pressure due to variations in barometric pressure, ΔB_p and Earth tides effect ε can be removed.

$$\Delta W = \sum_{\tau=0}^{5} \mu(t) \cdot \Delta B_p(t-\tau) + \varepsilon(t) \tag{5.51}$$

where ΔB_p is the change in barometric pressure over time interval t, $\mu(t)$ is the unit barometric response function at the lag τ, and $\varepsilon(t)$ is the finite sum of the principal solar and lunar tidal components that are likely to affect water levels given by equation 5.52.

$$\varepsilon(t) = \sum_{\tau=0}^{5} (a_i \cos\omega_i t + b_i \sin\omega_i t) \tag{5.52}$$

Where a_i and b_i are the Earth tide coefficients, and the frequencies $\omega_i = \frac{2\pi}{P_i}$ correspond to the ith principal diurnal or semidiurnal tidal components with period, P.

The fluctuations in the measured water pressure due to Earth tides and barometric pressure were removed using the regression deconvolution technique described in (2007) and in a computer program known as barometric and Earth tide correction (BETCO) by Toll and Rasmussen (2007). The correction procedure with BETCO uses barometric pressure and Earth tide measurements collected at the same intervals as the measured water pressure.

The software, BETCO was applied to the measured water pressure data from PzSa. The result of

the correction is shown in figure 5.9. Similarly, the BETCO procedure was applied to measure water pressure in PzShf from the store house frontage borehole. The results of the procedure are visualized on a tripartite plot that contains the corrected water pressures with barometric pressure and rainfall data (Figure 5.10).

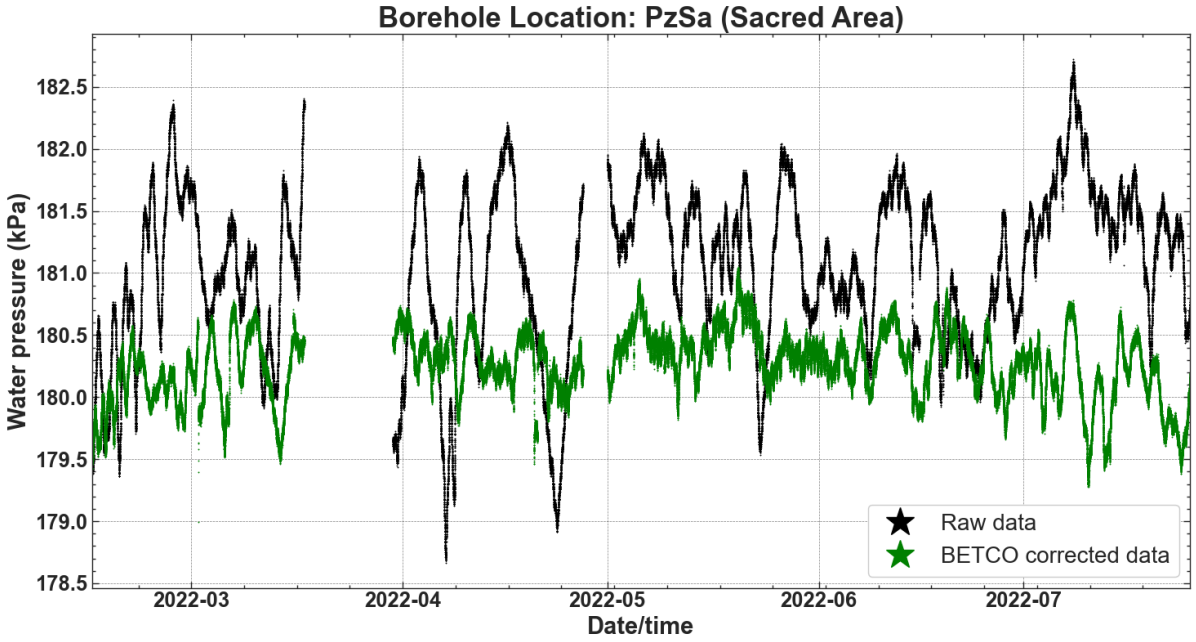

Figure 5.9: Measured water pressure was corrected with the BETCO program (Toll and Rasmussen, 2007) to remove the effect of barometric pressure and Earth tides.

5.4 Results

5.4.1 Observed borehole water pressure

The observed water pressure (Figure 5.6), fluctuates from the minimum values of 121.03 kPa, 151.88 kPa, and 177.14 kPa to the maximum values of 183.29 kPa, 157.88 kPa, and 157.88 kPa, respectively, in PzTh, PzShf, and PzSa. The respective mean of 124.45 kPa, 155.50 kPa, and 180.93 kPa was computed for the listed. The maximum, mean, and minimum recorded barometric pressure were 103.26 kPa, 100.68 kPa, and 96.16 kPa (Figure 4.7).

A significant variation occurred between January and March 2023 with a prominent upward trend, followed by a sharp decline in March 2023. These changes continue until mid-June, when the water pressure in PzTh and PzShf fluctuate with a downward trend, except for PzSa, which shows an upward increase. The pattern of the fluctuations of the recorded water pressure in the three boreholes is similar but differs in amplitude.

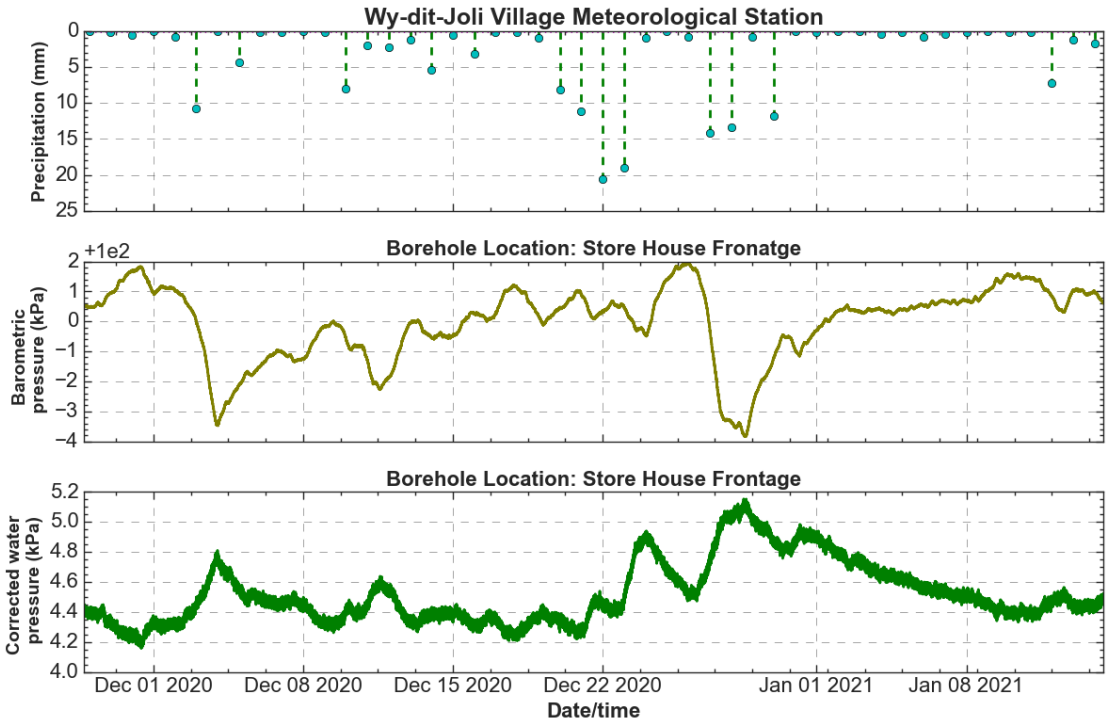

Figure 5.10: Precipitation, barometric presssure, and measured water pressure were corrected with the BETCO program (Toll and Rasmussen, 2007) to remove the effect of barometric pressure and Earth tides at *PzShf*.

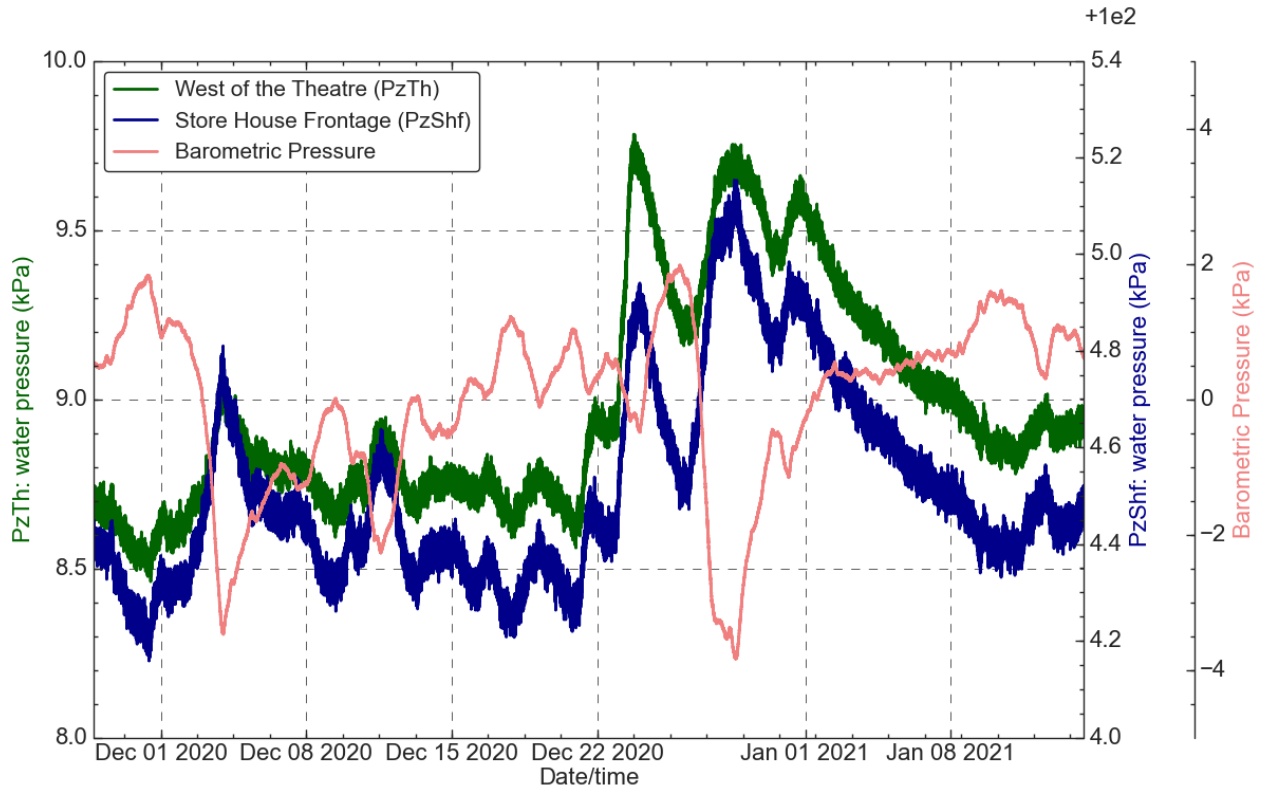

Figure 5.11: Barometric pressure and measured borehole water pressure *PzTh* and *PzShf* were corrected with the BETCO program (Toll and Rasmussen, 2007) to remove the effect of barometric pressure and Earth tides.

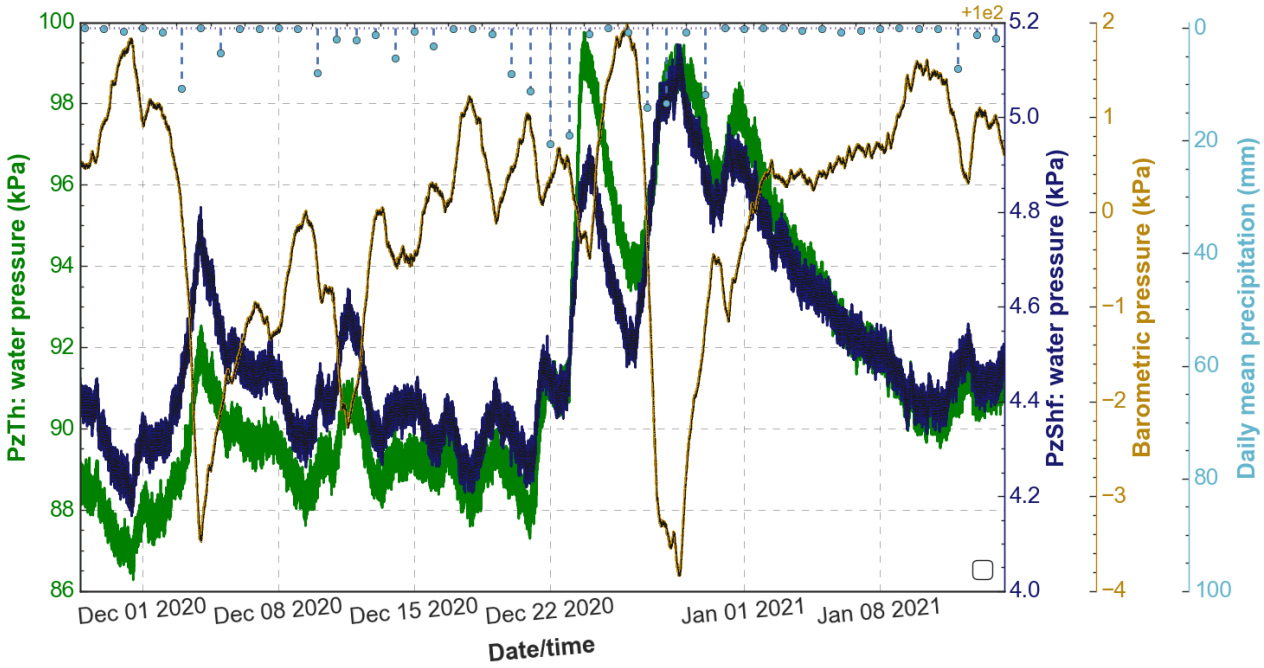

Figure 5.12: Precipitation, barometric pressure, and measured borehole water pressure *PzTh*, and *PzShf*, were corrected with the BETCO program (Toll and Rasmussen, 2007) to remove the effect of barometric pressure and Earth tides.

5.4.2 Semblance models

The pre-processing treatment for the semblance analysis includes extraction of the date-time and water pressure columns of each dataset and alignment of the date-time and water pressure data of two boreholes to ensure data length uniformity (e.g., PzTh with PzShf or PzSa and PzShf). Then, the date-time component of the data was transformed into serial date format (Appendix C.3.2).

Two types of data were used for the analysis: raw field data and filtered data. In the second type of data, influences, stresses, and strains such as barometric pressure and Earth tides that impact the aquifer systems were removed with the barometric and Earth tide correction (BETCO) computer program (Toll and Rasmussen, 2007), before the implementation of the semblance analysis. The treatment with BETCO ensured that fluctuations due to barometric pressure and Earth tides were removed and that the changes in water pressure data were mainly due to the aquifer properties.

The analysis was carried out on two categories of data sets: multi-seasonal (two years) and seasonal (three months). The seasonal data consist of measured water pressure data from PzTh and PzShf inclusive of data from PzSa. The data from PzSa was used in its raw form and compared with a BETCO-corrected version of it (Figures 5.13 and 5.14). In figure 5.13, the uncorrelation events, **S** = -1, appear widespread, indicating the hydraulic response of the two signals differs in phase.

The uncorrelated events are indicators of the impact of the filtering effect, which removed the influence of barometric pressure, Earth tides, and noise (non-periodic, structureless components). The features on the semblance plot of the raw and filtered data from PzSa are pronounced at a scale of 500 or higher, while at lower scales the correlation is less sharp. The anomalies in the longer data set in figure 5.14 are poorly resolved compared to the quality of resolution obtained with shorter data sets in figure 5.13.

The second seasonal data covered November 2020 to January 2021 (Figure 5.15). In the hydrographs, which are part of figure 5.15, two peak periods are noticed, centered around 24^{th} December and 1^{st} January. The obvious fluctuations in the water pressure in both plots are similar in pattern; however, the PzShf shows less sharp peaks. The water pressure in the PzShf have a higher amplitude than in the PzTh. The amplitude decreased from the mid-first week of January and did not return to the initial values preceding the observed rise in the third week of December (Figure 5.15). The behavior of the water in the two boreholes is compared for temporal and spectral information.

The CWT procedure was implemented at a scale of 80. At this wavelength, the models obtained from the CWT for the two data correlated well around the peaks in December and January. The data was anti-correlated between 60 and 80 wavelengths around the 1^{st} and 17^{th} of December. The correlations and anti-correlations, or zero events, are resolved in the regions with rise and decrease, or relatively minute variations.

In the second seasonal dataset, which covered February to April 2021 (Figure 5.16), the amplitude of the water pressure in PzShf is higher than that in PzTh. The changes in the water pressure are more pronounced in the PzShf hydrograph. The CWT anomalies are correlated at the wavelength of 1440. The generality of the semblance plot is correlated with this scale.

The anti-correlations between 1000 and 1400 wavelengths were well observed in March. Prominent events are well resolved in the first part of the two CWT plots. The anomalies are strongly correlated as events in the semblance relation model, with scattered occurrences of anticorrelated events.

The comparison of data sets for assessing relationships, behavior patterns, or similarity was more meaningfully visualized with short period series (compare Figure 5.17 with Figure 5.15); these short-term relationships in hydraulic interactions are strongly correlated in the figures.

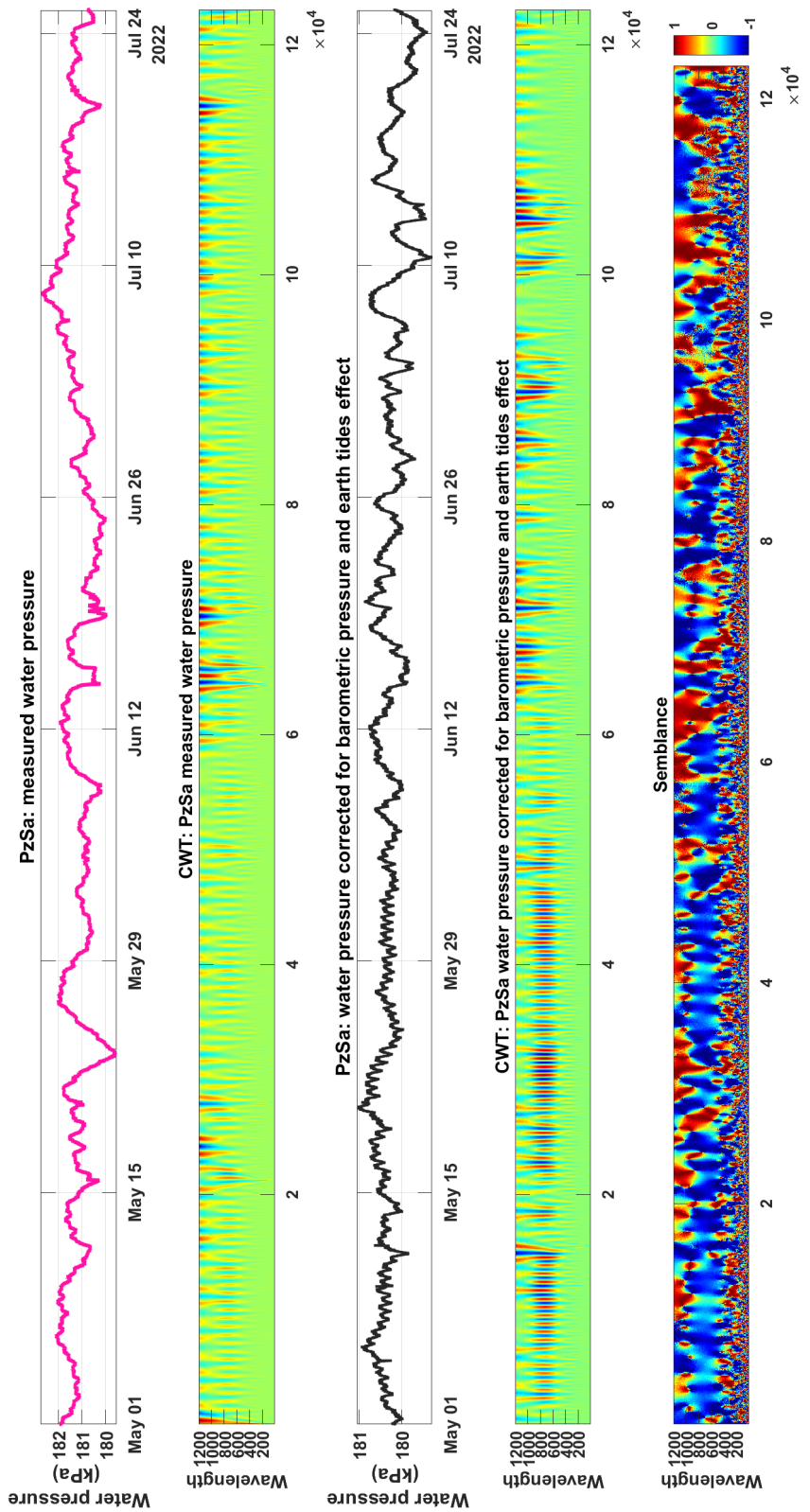

Figure 5.13: Wavelet-based semblance analysis of (May - June, 2022) measured water pressure and water pressure corrected for barometric pressure and Earth tides effect. Positive correlation in red, **S** = + 1, anticorrelation in blue, **S** = -1, zero correlation in green, **S** = 0. *PzSa* refers to a borehole equipped with a piezometer at the Sacred Area.

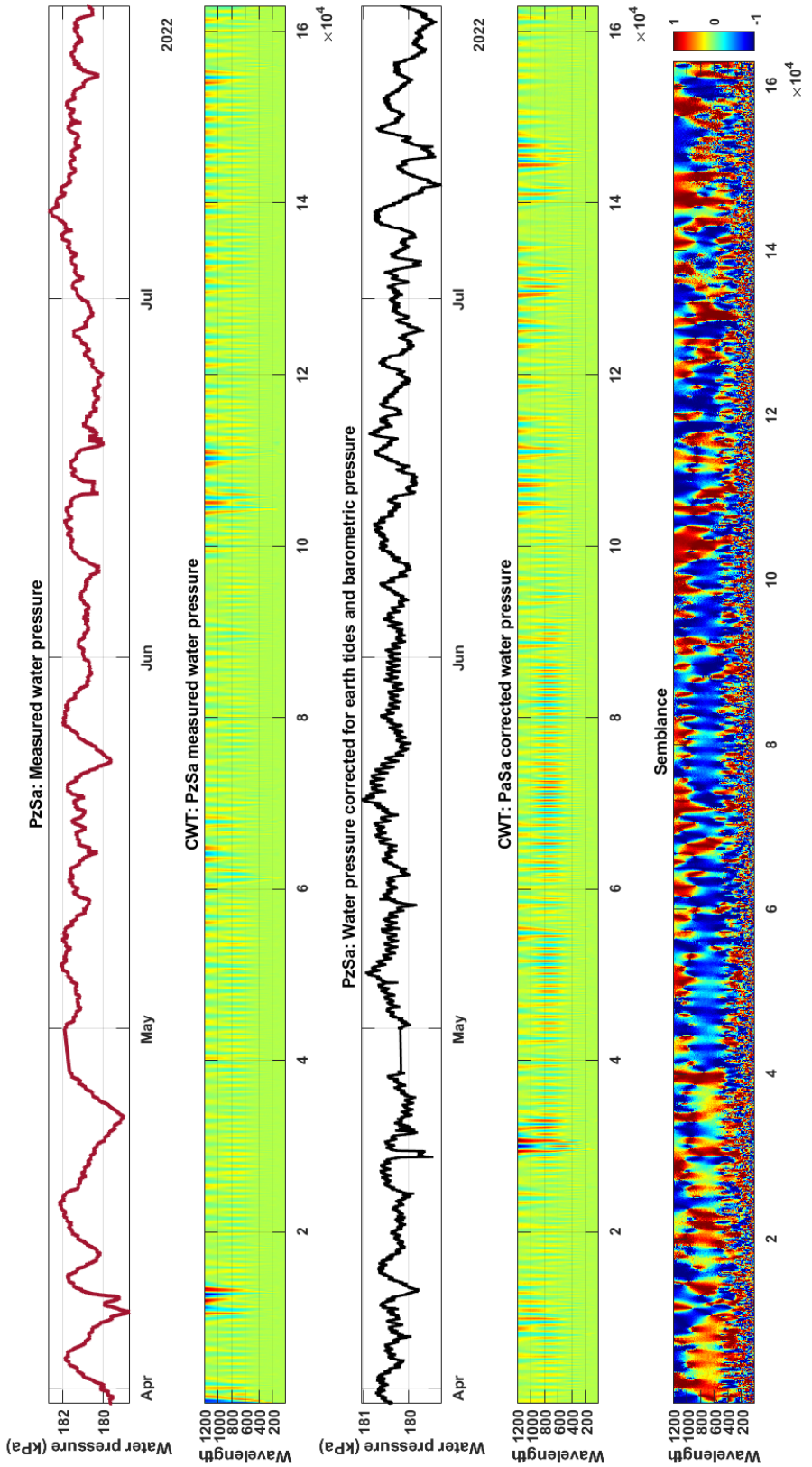

Figure 5.14: Wavelet-based semblance analysis of (April - July, 2022) measured water pressure and water pressure corrected for barometric pressure and earth tides effect. Positive correlation in red, **S** = + 1, anticorrelation in blue, **S** = -1, zero correlation in green, **S** = 0. *PzSa* refers to a borehole equipped with a piezometer at the Sacred Area.

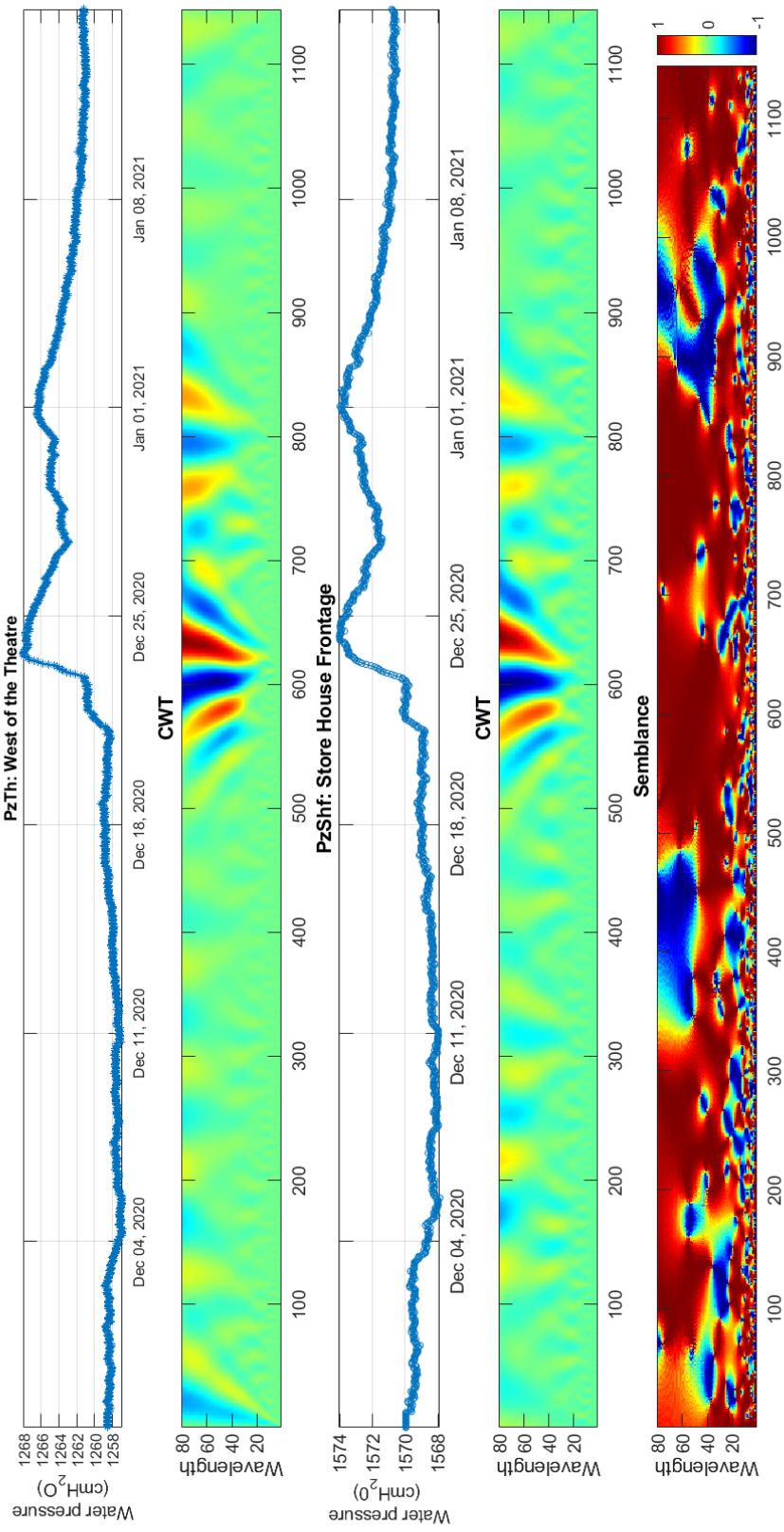

Figure 5.15: Wavelet-based semblance analysis of water pressure data corrected for barometric pressure and Earth tides effect at a scale of 80. Positive correlation in red, **S** = + 1, Anticorrelation in blue, **S** = -1, zero correlation in green, **S** = 0. Borehole AF refers to *PzTh* (West of the Theatre), while Borehole BC is *PzShf* (Store house frontage).

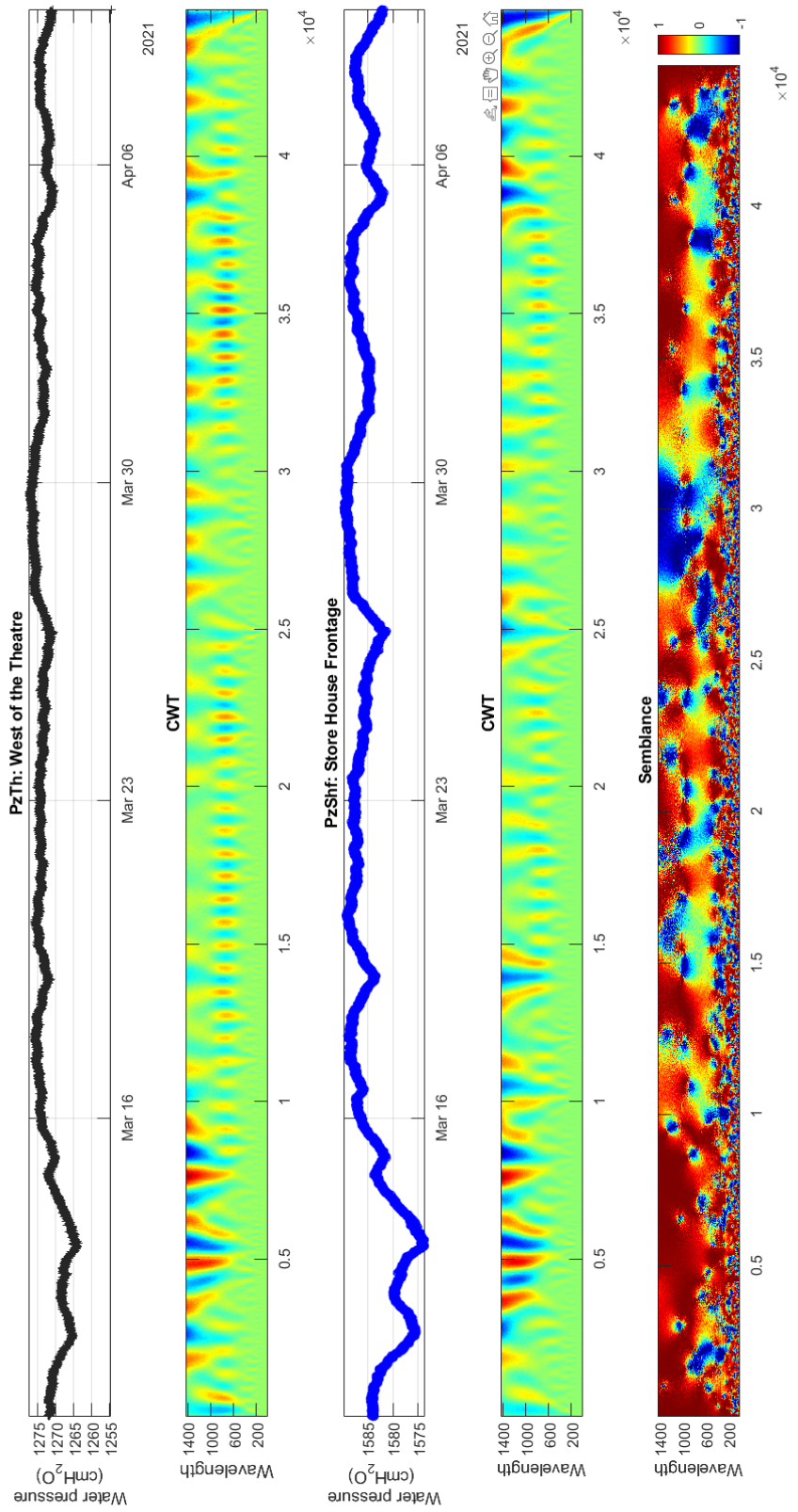

Figure 5.16: Wavelet-based semblance analysis of water pressure (short-period data) at a scale equal to 1440. Positive correlation in red, **S** = + 1, anticorrelation in blue, **S** = -1, zero correlation in green, **S** = 0. Borehole AF refers to *PzTh* (West of the Theatre), while Borehole BC is *PzShf* (Store house frontage).

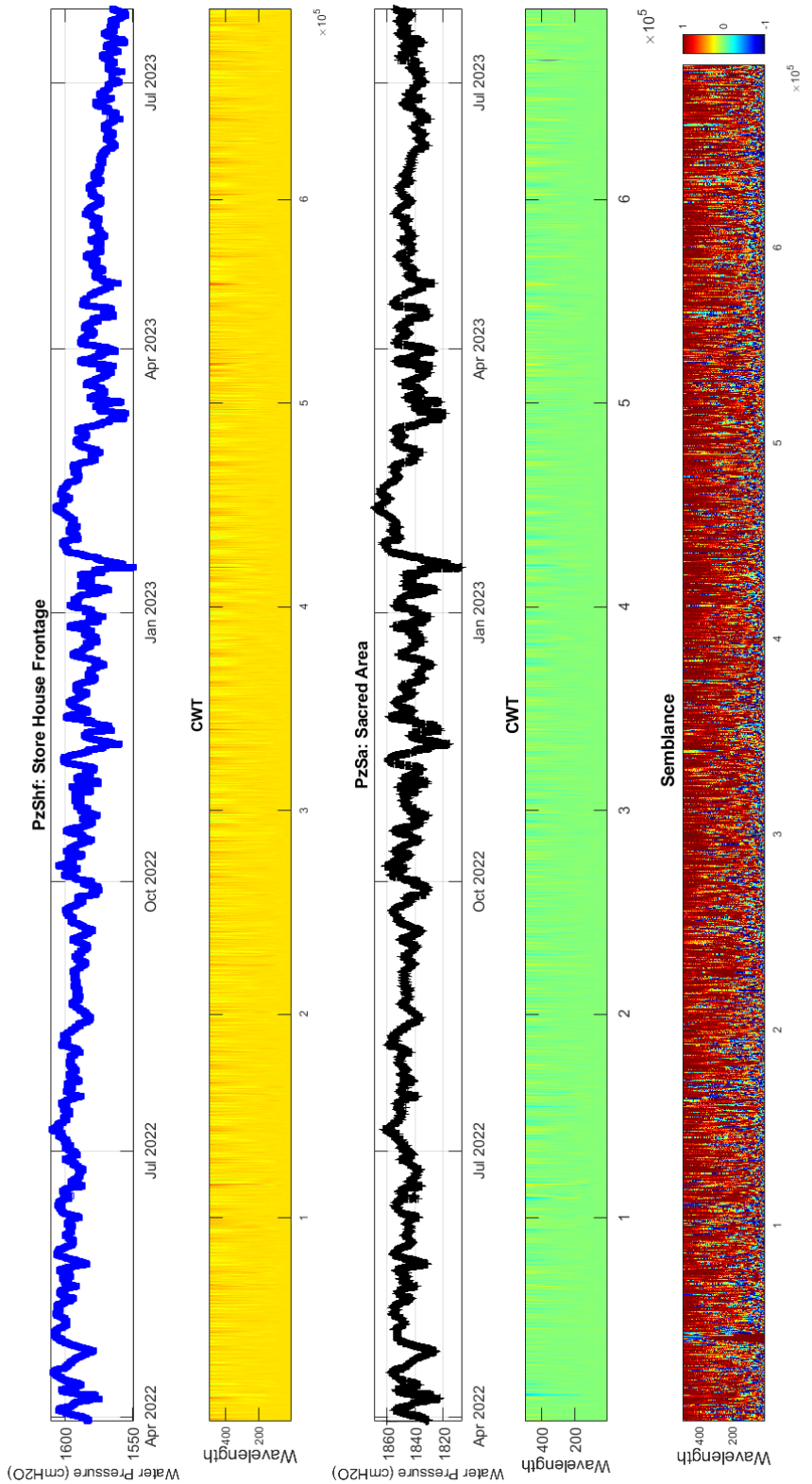

Figure 5.17: Wavelet-based semblance analysis of water pressure (long-period data) at a scale of 1440. Positive correlation in red, **S** = + 1, anticorrelation in blue, **S** = -1, zero correlation in green, **S** = 0. Borehole AF refers to *PzTh* (West of the Theatre), while Borehole BC is *PzShf* (Store house frontage).

It can be interpreted as a response to short-period influences with relatively small amplitudes but periodic at the site. Hydrologically related response of the aquifer. Thus, it can be inferred that the aquifer medium is spatially interconnected.

Figures 5.15 and 5.16 are models obtained for different data on the site. The length of the data seems to affect the clarity of the results obtained. By comparing figures 5.13 and 5.14, it is obvious that the figure 5.13, has a better resolution of anomalies compared to figure 5.14. Hence, the temporal impact of fluctuations can be monitored and assessed for sudden and rapidly occurring hydrologic and meteorological events perturbing the aquifer water pressure.

5.4.3 Singular spectrum analysis

Continuous water pressure data was acquired at 60-second intervals from three water boreholes designated *PzShf*, *PzTh*, and *PzSa* (Figure 4.4, Table 4.1) at the archaeological site (Barrière and Vermeersch, 2016; Cholet and Delestre, 1992). The data was retrieved periodically from the TD Diver sensors and concatenated to produce a long series of data of a certain length (Figure 5.6). The SSA was applied to a sampled time series X_t of finite length N, $\{X_t, t = 1, ...N\}$ in two phases. In the first phase, the method was applied to a long series of data sets for each borehole, water pressure or temperature, and the barometric pressure and air temperature data measured at the site. In the second phase, the method was applied to a series of overlapping sub-data sets using the sliding window method (section 5.4.3.2). The data was sampled at 60 minutes (1 hour) for the SSA.

To compute the long-term and short-term oscillations in the data. A certain amount of the measured data was intuitively used for the computation by applying the expressions in equations 5.53 and 5.54. The quantity of data used to perform the computation for the long-period events $\{k_L\}$ is given by equation 5.53. In simple terms, two-thirds of the length of the data was analyzed for long-term events.

$$k_L = \frac{2}{3}N \tag{5.53}$$

The short-term events $\{k_S\}$ were analyzed using ninety-five percent of the data (equation 5.54).

$$k_S = 0.95N \tag{5.54}$$

The concept of using a certain amount of the data (equations 5.53 and 5.54) for the computation of long and short period events is based on personal communications with F. Lopes, a research engineer, Muséum National d'Histoire Naturelle (MNHN), Paris, France.

A sampling rate of 60 minutes was chosen for the analyses of the long-series data sets. The sampling rate corresponds to the window length earlier described in section 5.2.2.2. The length of the vector space was wide enough to include all possible periodic events that influence groundwater levels at sub-daily to seasonal or annual scales without exceeding half of the length of the time series {M ≤ N/2} (e.g. see Kong et al., 2023).

5.4.3.1 SSA on long series data

5.4.3.1.1 Sacred Area (*PzSa*)

(a) Data preparation and decomposition The original time series (e.g., water pressure data from $PzSa$), a one-dimensional (1-D) data was accessed and visualized in the time domain as shown in the upper left-hand of figure 5.18 and a convolution procedure applied to it. The convoluted data was filtered to remove noise and reconstructed to obtain the signal. The reconstructed signal shares a similar pattern with the original and filtered use for the reconstruction data (e.g., Figure 5.18). The filtered data is used for the analysis. It was sampled at 60-minute intervals. The mean of the data was computed. The variance, or the difference between the amplitude of the time series and its mean, was used for the interactive SSA. Two-thirds of the data (filtered) involved decomposition procedures, while 95% or 0.95 of the data was analyzed for short-period events (equations 5.53 and 5.54).

The singular value decomposition procedure disaggregated the signal into constituent components, which include the trend, the oscillating components, and the residual or noise (figure 5.19).

The trend is a generalized structure of the tendency of the signal. It covers the beginning to the end of the propagation of the signal.

(b) Extraction of period

Each oscillating component has a period, or frequency, at which it occurs. Hence, based on the frequency of oscillation, the first twenty components were obtained (Figure 5.18 and table A.9 of appendix E.5). The maximum oscillating period of each component was extracted from the plot of its amplitude and period, first for the long-term components and subsequently for the short-term components. In each term, the corresponding eigenvalue and period were recorded (table A.9 of appendix E.5). Thereafter, each component was separated

from the signal and visualized in the time and frequency domains. The plot of a component in the frequency domain is a spectrum that shows the amplitude as it varies with the period or time. The modulation of the amplitude of a component is one of the peculiarities of the SSA compared to the globalization of peaks in FFT and its correspondence to a frequency event or the expression of an amplitude at a frequency. The oscillations were individually separated and visualized by the component, both in time and frequency.

(c) Grouping and regrouping

This stage comes after the extraction of the periods with the corresponding eigenvalue. The grouping and regrouping stages involve two approaches. In the first step, eigenvalues with a closely related period were regrouped into the same group.

Example: in table A.9 of appendix E.5, components with eigenvalues 11 and 12 were regrouped into the same eigenvalue. Eigenvalues 5 and 6 were also grouped for the same reason of the same or nearly the same period. The second step was reordering the data after the magnitude of the period was rearranged, starting with the highest value and going all the way through to the lowest. In the grouping (reordering), the eigenvalue was used as the index of a corresponding period. Therefore, group 1, group 2, group 3, group 4, group 5, group 6, *etc*, corresponds to eigenvalue 19, 7, 1, 2, 3:4, 8, *etc*.

Thus, the computation is reordered in a sequence of decreasing magnitudes of the periods, using the eigenvalues as an index. The resulting computation has a sequence of components arranged as follows: $g(19) = 1$, $g(7) = 2$, $g(1) = 3$, $g(2) = 4$, $g(3:4) = 5$, $g(8) = 6$, $g(9:10) = 7$, $g(17:18) = 8$, $g(5:6) = 9$, $g(13) = 10$, $g(11:12) = 11$, $g(16) = 12$, $g(15) = 13$, $g(14) = 14$, and $g(20) = 15$.

The method of grouping was implemented for the short-term constituents (Table A.9 of appendix E.5). The eigenvalues and the corresponding periods were first grouped for terms with similar or nearly similar periods and arranged in order of decreasing values, starting with the highest periods. The eigenvalues served as the index in the grouping. From table A.9 of appendix E.5, the eigenvalue of 20 has the highest or largest period; hence, it is regrouped thus, $g(20) = 1$. Similarly, the grouping was carried out consequently: $g(10) = 2$, $g(9) = 3$, $g(7:8) = 4$, $g(5:6) = 5$, $g(1:2) = 6$, $g(3:4) = 7$, $g(13) = 8$, $g(12) = 9$, $g(11) = 10$, $g(14:15) = 11$, $g(18:19) = 12$, and $g(16:17) = 13$.

The SSA procedure was repeated with the ordered sequence of eigenvalues with descending periods, and the outcome is presented as figures 5.20, 5.21, 5.22, 5.23, 5.24 and 5.25, for the Sacred Area (PzSa) borehole water pressure data at the Sacred Area.

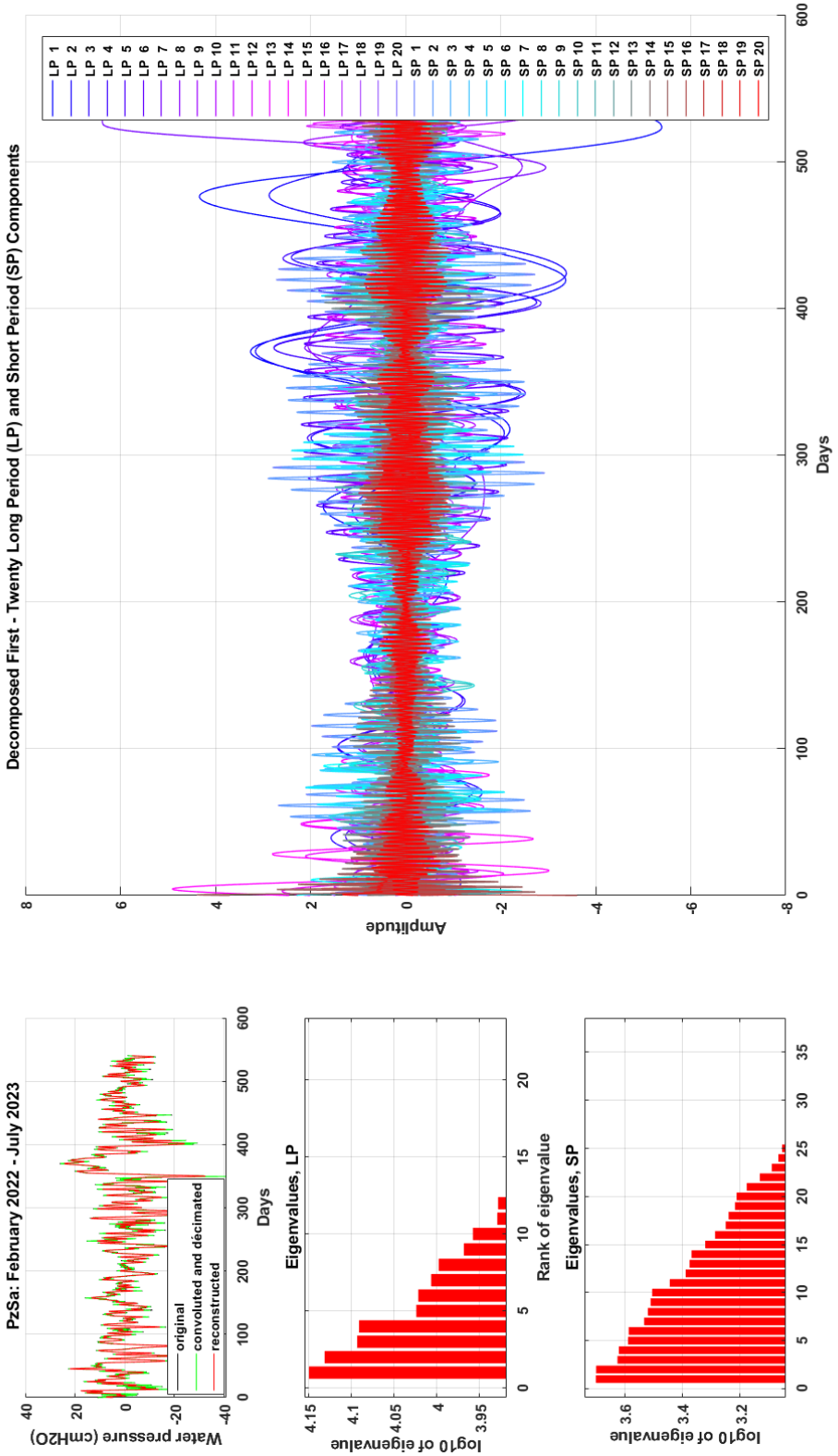

Figure 5.18: Singular spectrum analysis: decomposition of water pressure data from Sacred Area borehole into components.

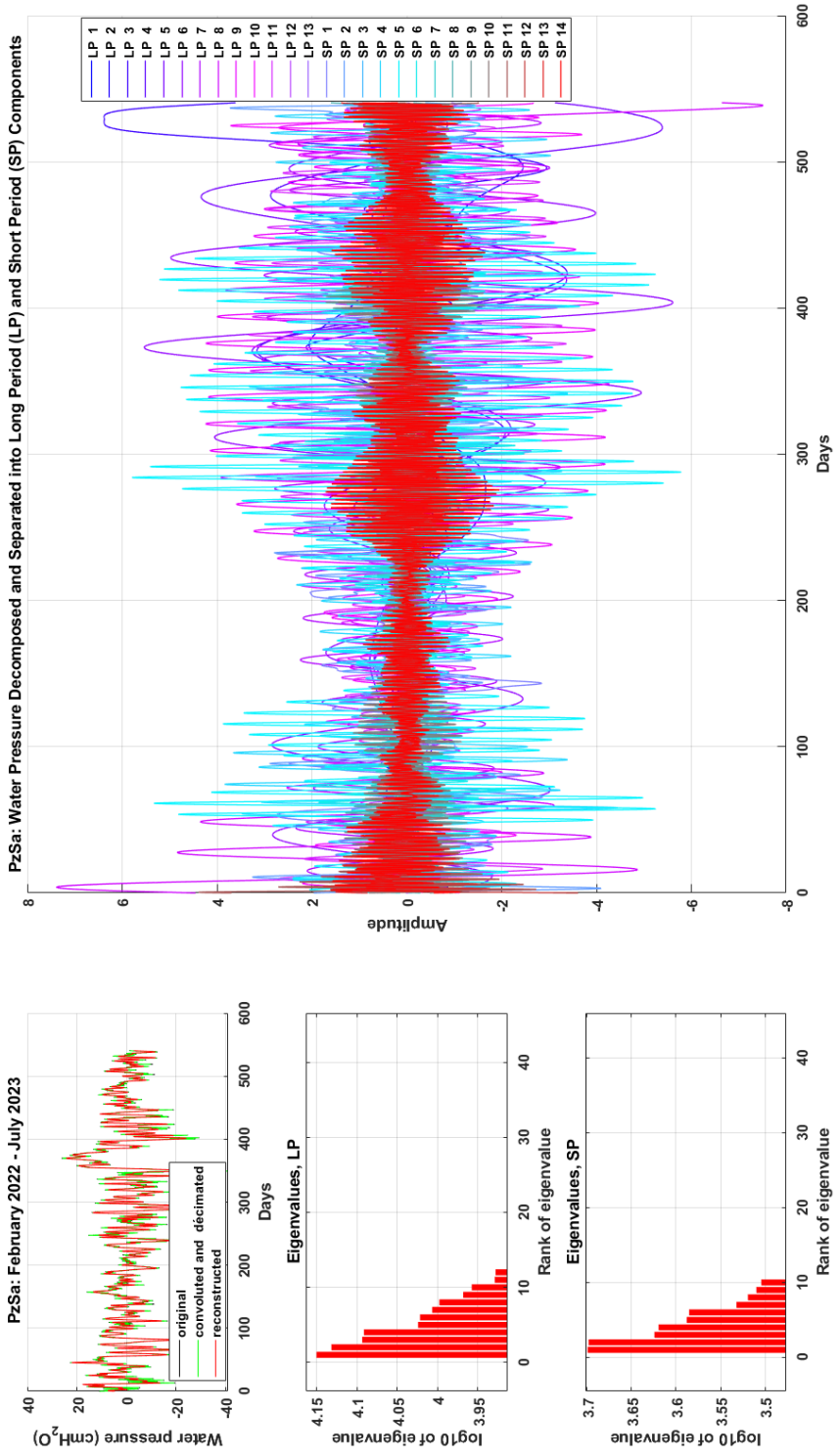

Figure 5.19: Singular spectrum analysis: decomposition of water pressure data from Sacred Area borehole into components after eigenvalue grouping.

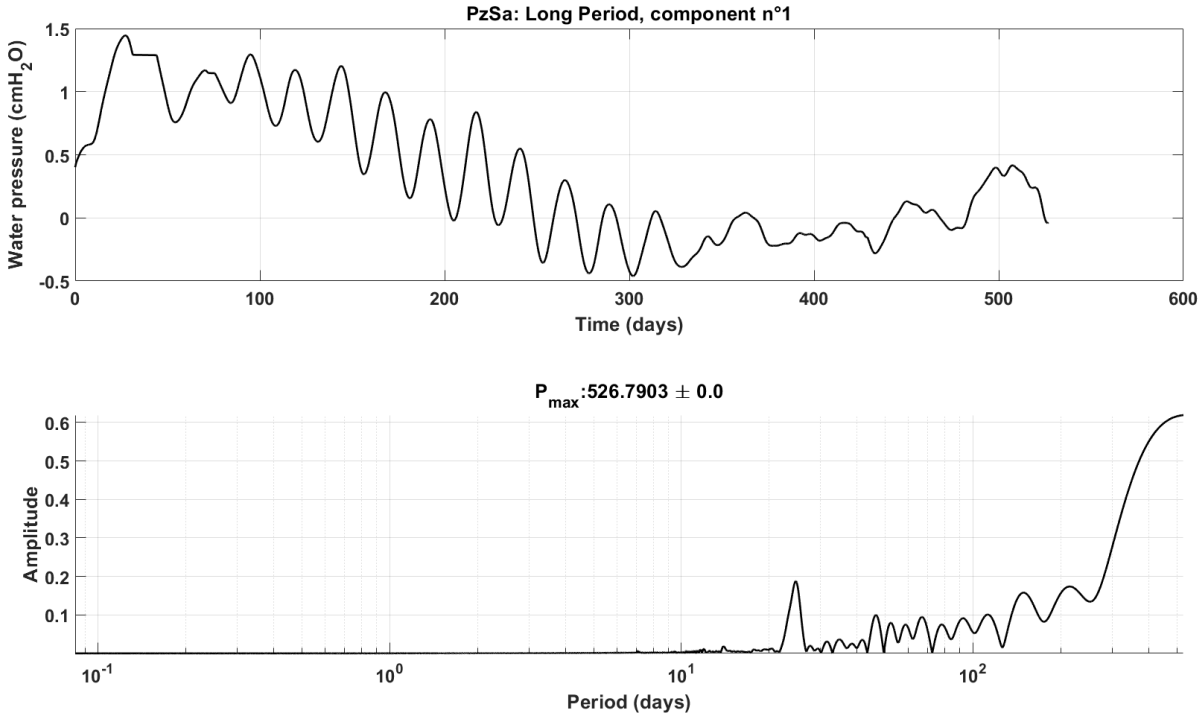

Figure 5.20: The trend extracted from the decomposition of water pressure data of the Sacred Area borehole as the first component and expressed in time and frequency domains. The varying of the trend can be observed in both time and frequency.

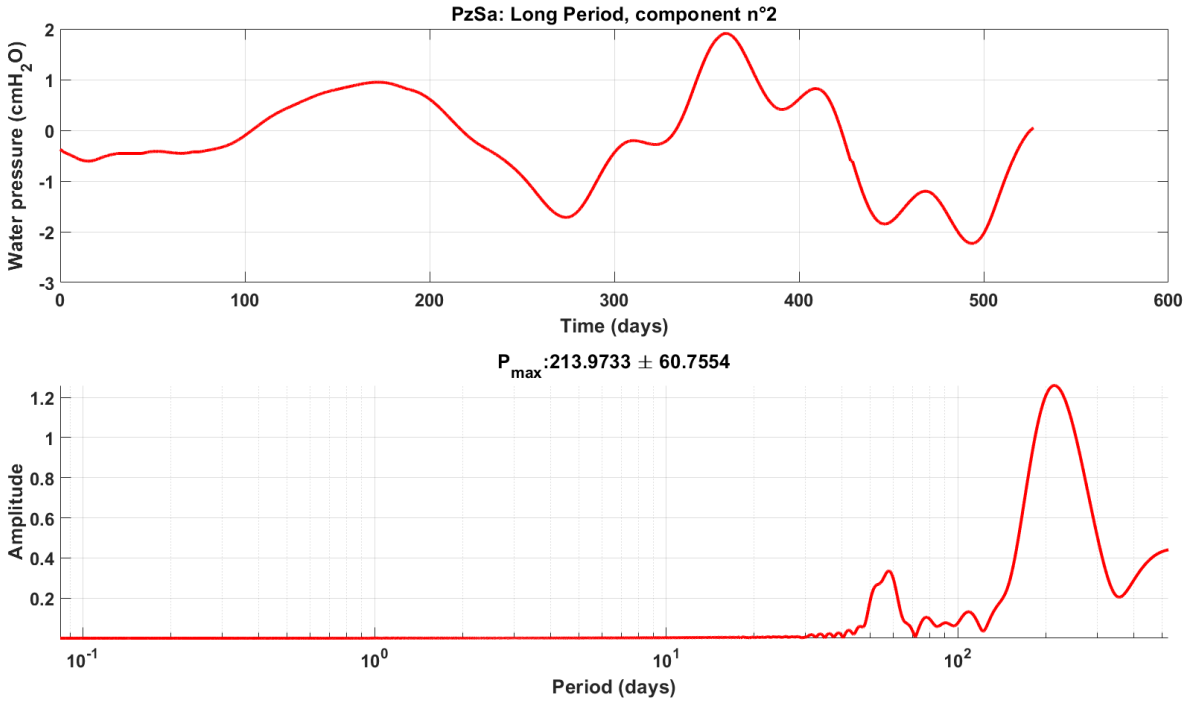

Figure 5.21: The second component from the Sacred Area has a period of 214 days. It has a large variation length with some short form of varying amplitude.

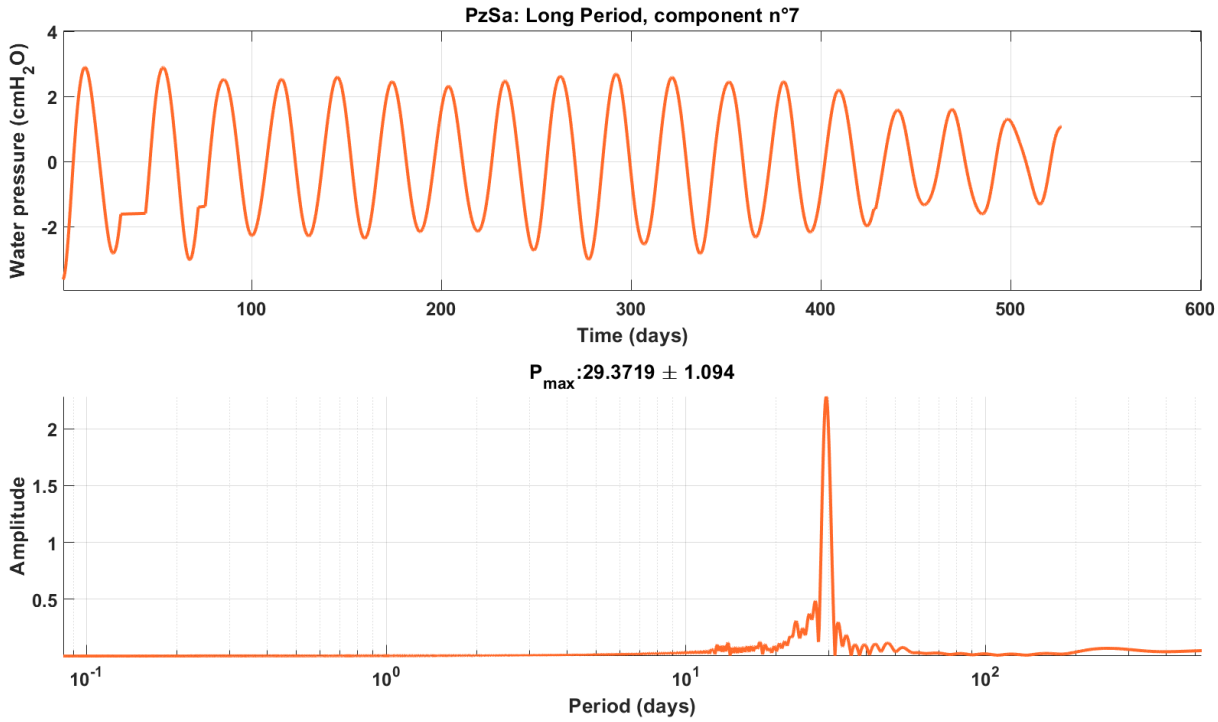

Figure 5.22: The seventh component has a period of about 29.4 days. It shows repeated patterns occurring at intervals. The period correspocorrespondsncorrespondsding to a natural cyclic of the lunar phase.

5.4.3.1.2 Store House Frontage (PzShf) The SSA procedure was applied to a second set of water pressure data acquired from the Store House borehole (PzShf) from March 2022 to July 2023 (Figure 5.26). This data has multiple seasonal components. It covers the four known seasons: **spring** (March, April, May), **summer** (June, July, August), **autumn** (September, October, November), and **winter** (December, January, February).

Embedded in water pressure time series are also impacts or effects from the variability of harmonic and non-periodic events caused by nature and man. An example is the phenomenon of climate change, which causes prolonged rainfall, storms and extreme events that affect hydrological processes.

The data is a long series of data that will permit different scales of climatic and environmental influences, as well as anthropogenic and other natural factors causing fluctuations in groundwater levels, to be studied. The complex processes that cause changes in water levels can be individually isolated and studied for periodic and aperiodic behaviors.

Following the grouping and regrouping criteria earlier outlined. SSA was applied to the long series data in two ways:

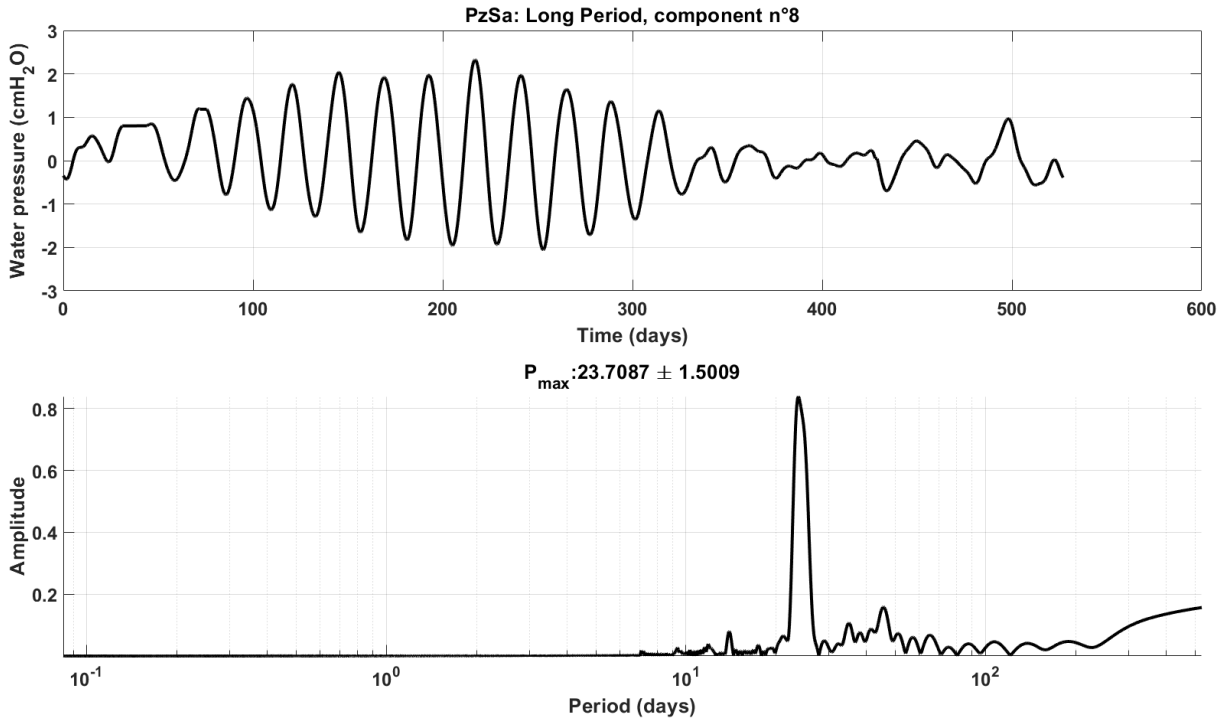

Figure 5.23: The eighth component has an oscillation period of 24 days. It shows a stable cyclic pattern from about day 100 to a little higher than day 300. The period was inferred to relate to the effect of a solar cycle (e.g. Temmer et al., 2005).

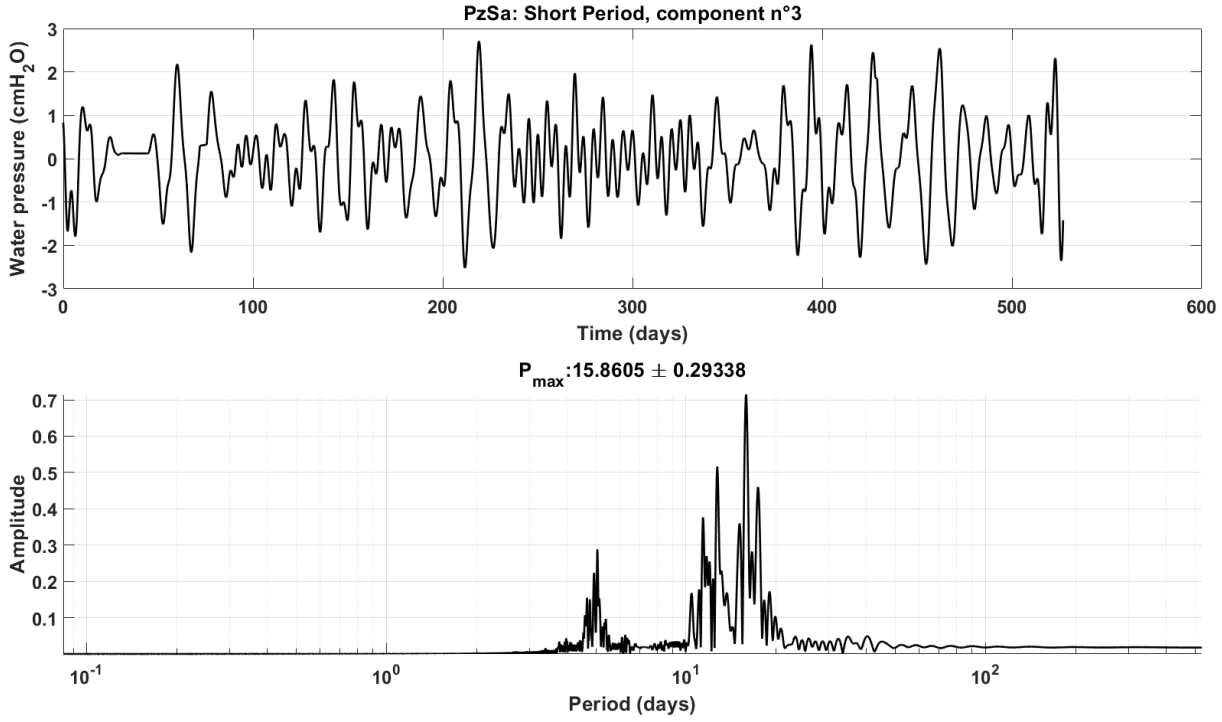

Figure 5.24: The third short term component has a period of 16.0 days. It is indicative of a signal with a period is within the lunar influence.

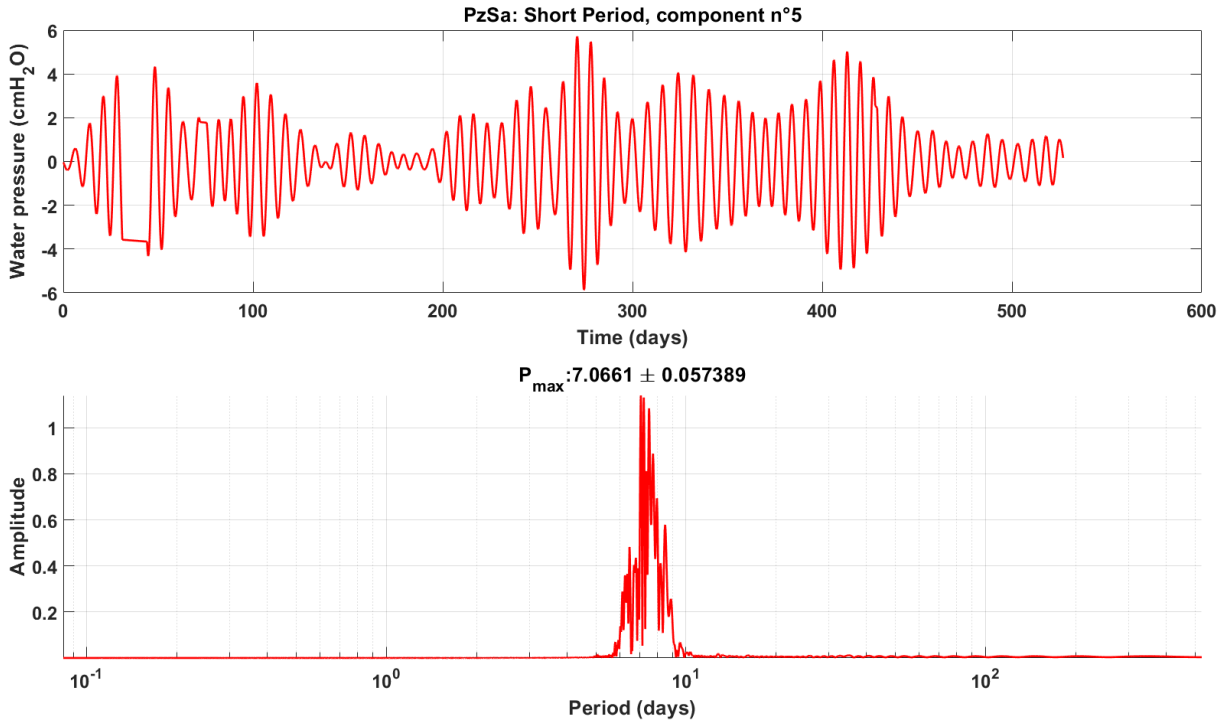

Figure 5.25: The fifth short-term component has a period of 7.0 days. It is indicative of signal with regular patterns occurring at intervals with significant variations in its amplitude. It can be seen as a weekly event that influences the water levels. The period is within the the half lunar phase.

i. Before grouping

ii. After grouping

In the first step The SSA procedure was applied to the data. The first twenty decomposed components and the residual were extracted using the eigenvalues and the corresponding period. The extracted components are shown in table A.10 of appendix E.5.

The second step involves grouping and reapplication of the SSA. Let each component represent a group. The grouping is done in an orderly sequence, from the period with the highest to the lowest value. There is a second criterion for grouping, eigenvalues with approximately the same period were grouped. Thereafter, the components were reordered from the highest to the lowest values of the period. The regrouping procedure considers each eigenvalue as the index of a group.

For example, in table A.10 of appendix E.5, under the short period components, eigenvalue 20 has the highest period, hence, it is group as g(20)= 1. It was followed by eigenvalues 10 and 8, consequently, g(10) = 2 and g(8) = 3. The expression g(10) = 2, implies eigenvalue 10 is now in group 2.

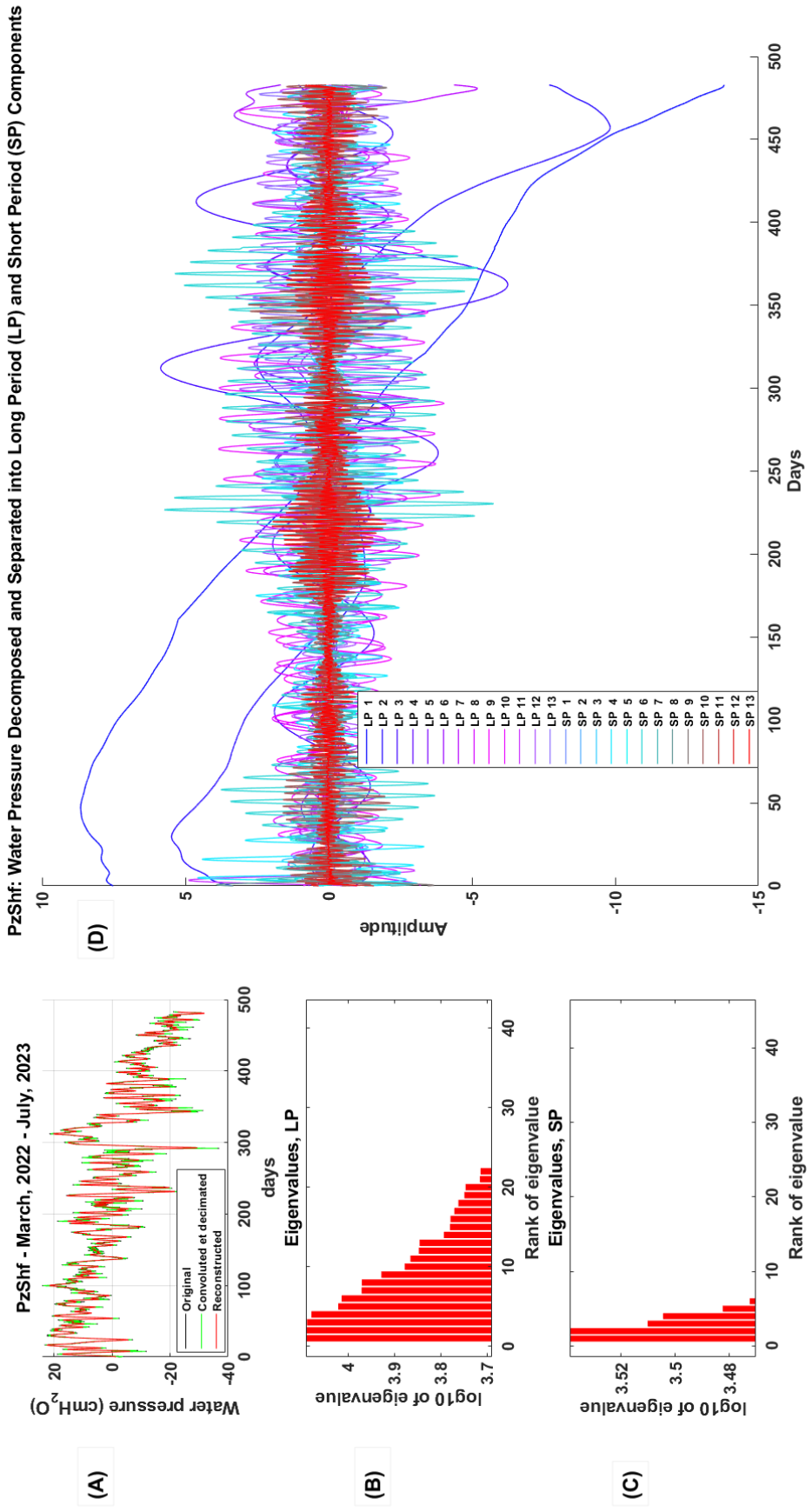

Figure 5.26: Singular spectrum analysis: decomposition of water pressure data from the borehole at the Store House Frontage into constituents after eigenvalue grouping.

For the second grouping criterion, eigenvalues 1 and 2 have nearly the same period; therefore, g(1:2) = 6, in line with earlier criteria of descending order of magnitude of values. The short-term components were grouped as follows: g(20) = 1, g(10) = 2, g(8) = 3, g(5:6) = 4, g(4) = 5, g(1:2) = 6, g(3) = 7, g(7) = 8, g(9) = 9, g(11:12) = 10, g(13:14) = 11, g(17:18) = 12, g(15:16) = 13, and g(19) = 14. The long-term components were also grouped following the steps and guide discussed as g(1) = 1, g(2) = 2, g(3:4) = 3, g(5) = 4, g(6) = 5, g(9) = 6, g(14) = 7, g(10: 11) = 8, g(17:18) = 9, g(7:8) = 10, g(19:20) = 11, g(12:13) = 12, g(15:16) = 13. After the grouping and regrouping, the SSA was reapplied to the same data. The outcome is the eigenvalues used as an index, with corresponding values (in this case, the periods) decreasing from the highest to the lowest.

A composite plot produced by interactively applying the SSA procedure to the data is shown in figures 5.26 and 5.27 5.29, 5.28 A-D, consisting of the time treatment of the data and spectrum of the decomposed components as well as the eigenvalues of the `Long Period` (LP) and `Short Period` (SP) components.

Figure 5.26 A is the spectrum of components decomposed from the water pressure measured in *PzShf* from March 2022 to July 2023. Each color strand represents a component. A component is isolated based on its period or frequency.

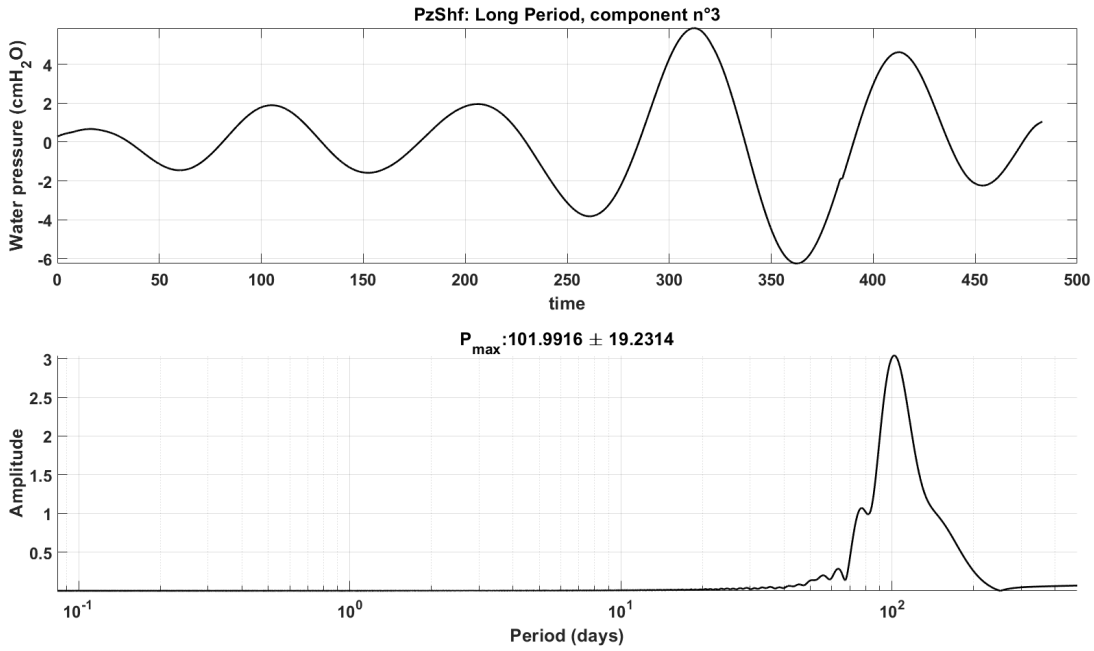

Figure 5.27: The third long-term component obtained from PzShf has a period of 101.0 days. It depicts a periodic signal that is more active towards the end of the year.

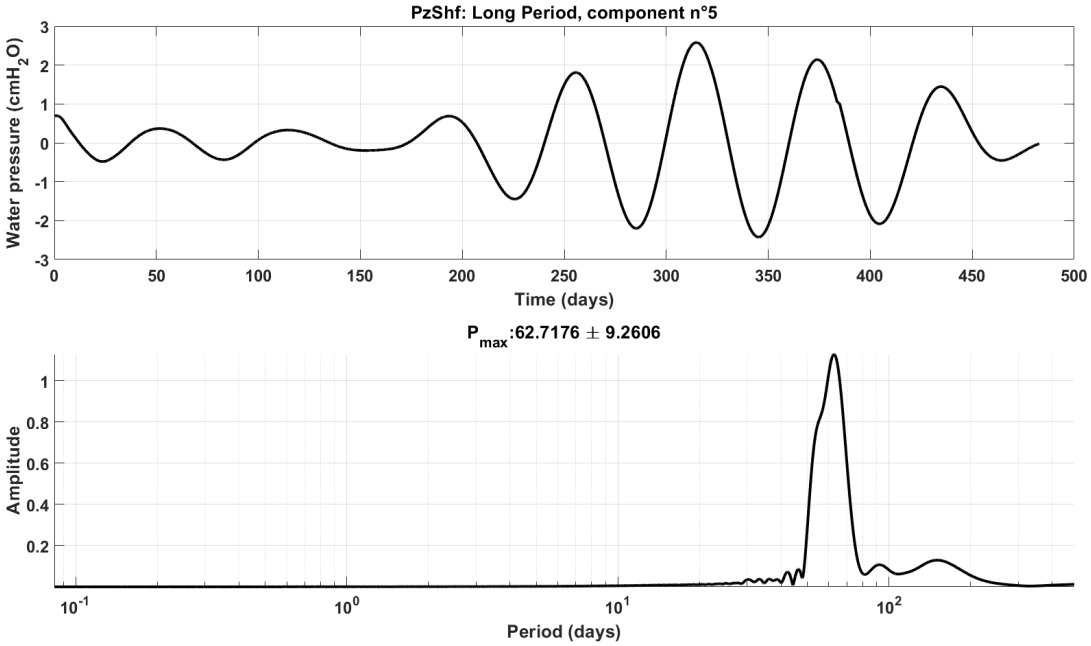

Figure 5.28: The fifth long-term component obtained from PzShf has a period of 62.70 days. It has a periodic behavior that became pronounced in its later parts, as revealed by the plot.

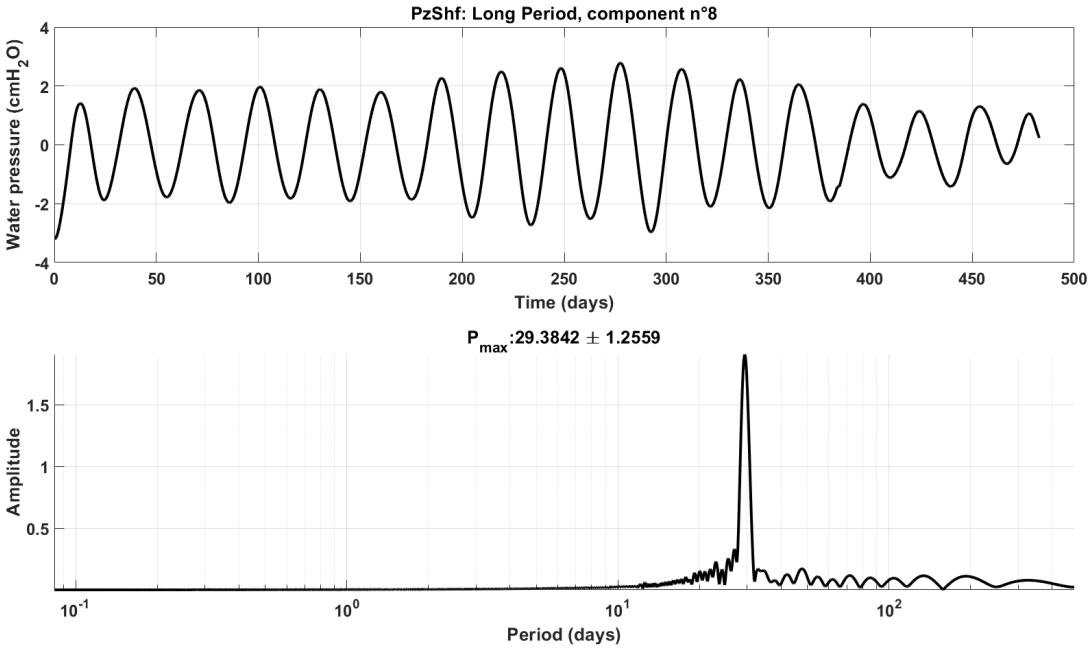

Figure 5.29: The eighth component obtained from PzShf has a period of 29.40 days. It is periodic signal, as observed in its sinusoidal behavior. The period aligns with the *lunar* phase timing.

5.4.3.1.3 West of the Theatre (PzTh) The measured water pressure in the *PzTh* was also treated with the SSA to decompose the data into components and for possible extraction of periodic phenomena or signals. Data from February 2022 to June 2023 was preprocessed, and the date time part of the dataset was converted to a serial date number as required by the SSA code written in

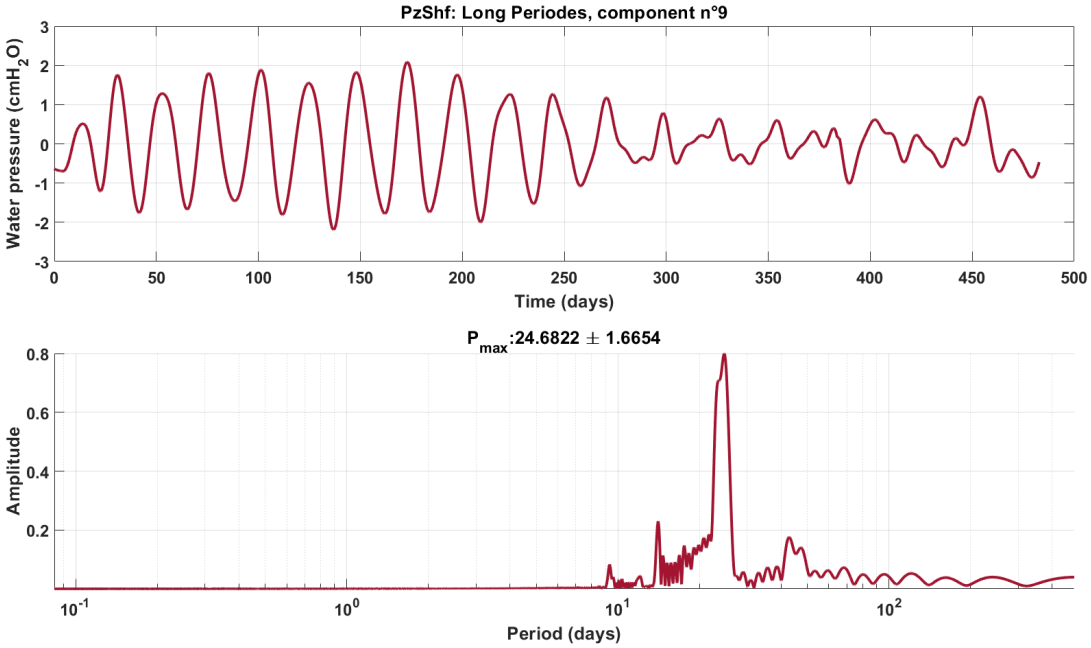

Figure 5.30: The ninth long-term component obtained from PzShf has a period of 24.80 days. It is a periodic signal, as observed in its sinusoidal behavior. The period aligns with the lunar phase timing.

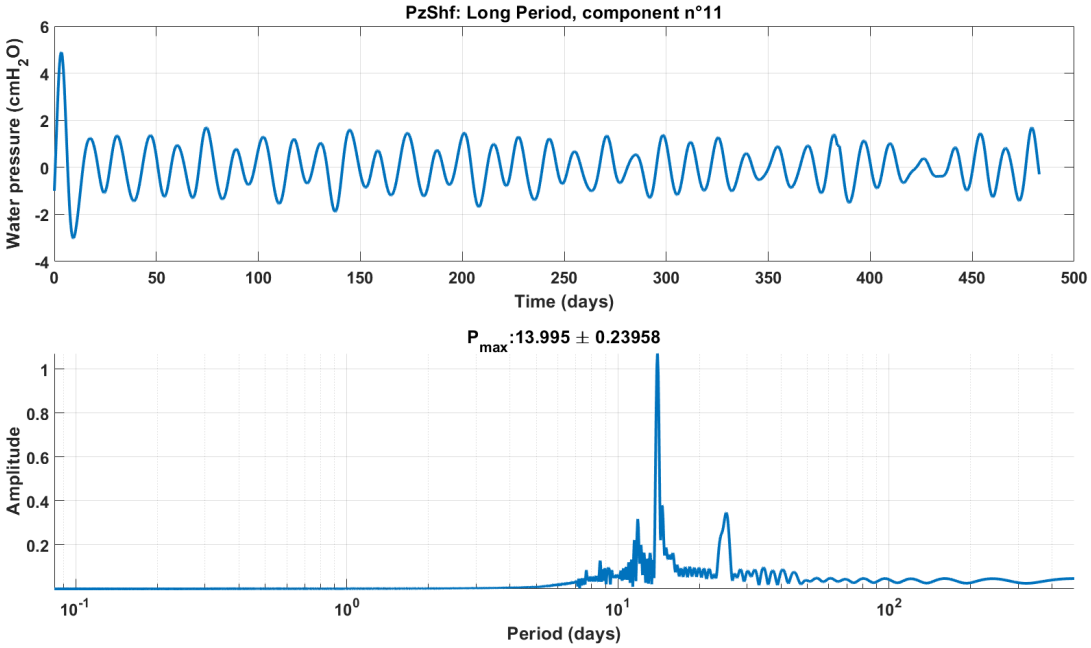

Figure 5.31: The eleventh long-term component obtained from *PzShf* has a period of 14 days. It is a periodic signal, as observed in its sinusoidal behavior. The period aligns with the *lunar* phase timing.

the MATLAB programming language.

The steps to convert the date time to the serial number documented in the Python programming

language are given in appendix C.3.2. The input file for the SSA code was structured into two columns. The first column had the serial date number, while the second column contained the data (water pressure or temperature). The input file was prepared in the Windows Notepad program. The file name ends with the .dat extension.

The first twenty outputs from the SSA treatment of the data are shown in table A.11 of appendix E.5. The output consists of the long and short-period components of the data. Following the regrouping criteria explained in the traditional implementation of the SSA, the LP components with the same or nearly identical periods were grouped. The procedure was carried out as follows: g(1) = 1; g(2) = 2; g(3) = 3; g(4) = 4; g(5) = 5; g(6) = 6; g(9:10) = 7; g(17) = 8; g(13:14) = 9; g(7:8) = 10; g(15:16) = 11; g(11:12) = 12; g(18:19) = 13; g(20) = 14; After the regrouping, the SSA procedure was reapplied to the data. Before the reapplication of the SSA to the data, the short-period components were regrouped following the same criteria. Consequently, g(1) = 1; g(2) = 2; g(3) = 3; g(4) = 4; g(5) = 5; g(6:7) = 6; g(8) = 7; g(9) = 8; g(10:11) = 9; g(12:13) = 10; g(14) = 11; g(15) = 12; g(16) = 13; g(17:18) = 14; g(19:20) = 15;.

Following the regrouping, the SSA was applied to the data, and the output is presented in figures 5.32, 5.33, 5.34, 5.35, 5.36, 5.37 and 5.38.

The decomposed components consist of the trend, the oscillations, and the residual. One of the visible advantages of the SSA method is the separation of components into individual constituents, including trend, oscillating components, and residuals. Each component signifies an event with either a physical or anthropogenic precursor. The trend is the generalized long-term structure of the water levels as it responds to recharge, extraction, flow, and hydro-meteorological impacts.

It signifies the annual to multi-year behavior of the water source. Similarly, the SSA was applied to data sets from the storehouse borehole acquired in parts of the years 2017, 2018, and 2019. The procedure was performed to extract the first twenty long and short-period components (Table A.12 of appendix E.5).

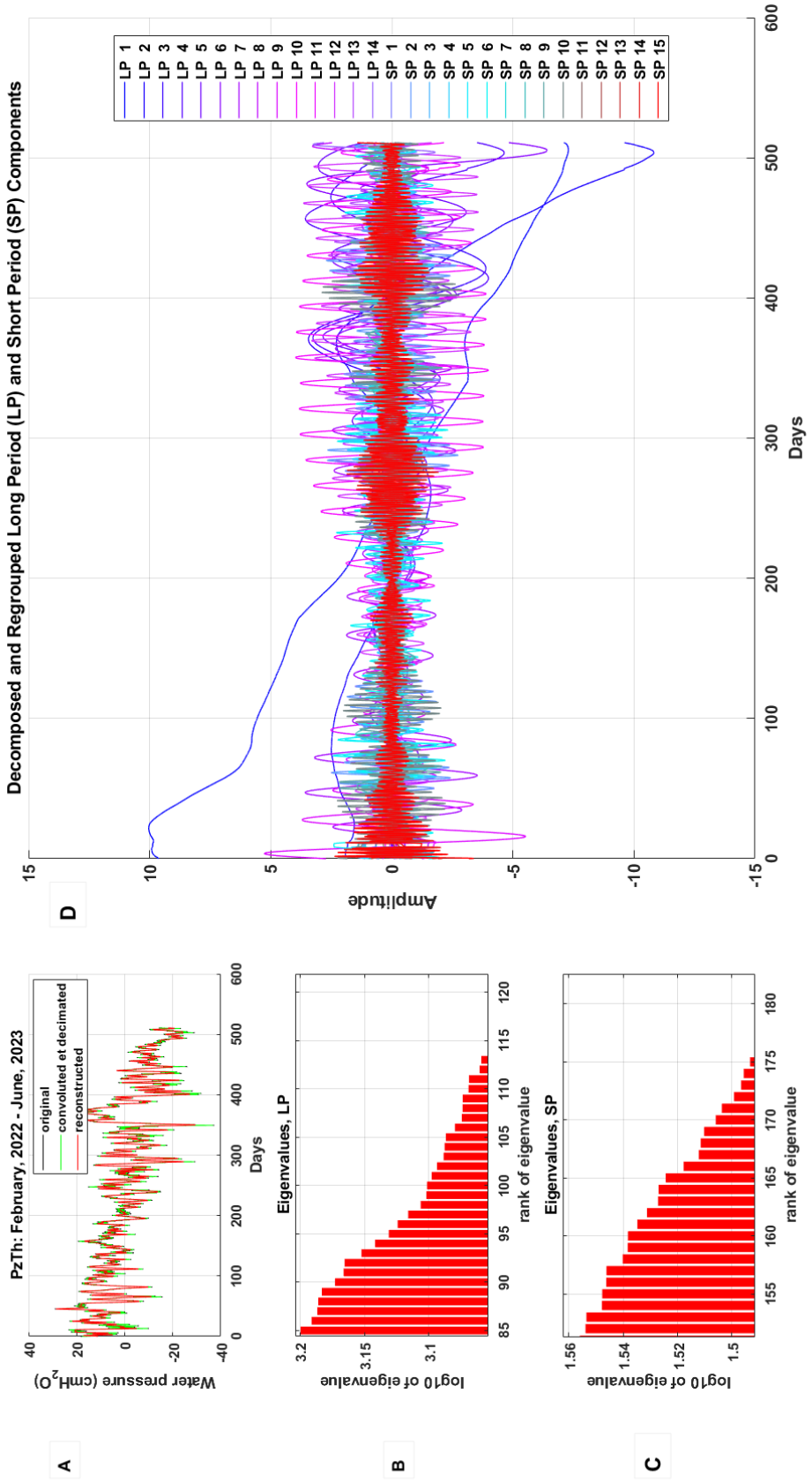

Figure 5.32: The decomposed and regrouped long and term components from the West of the Theatre.

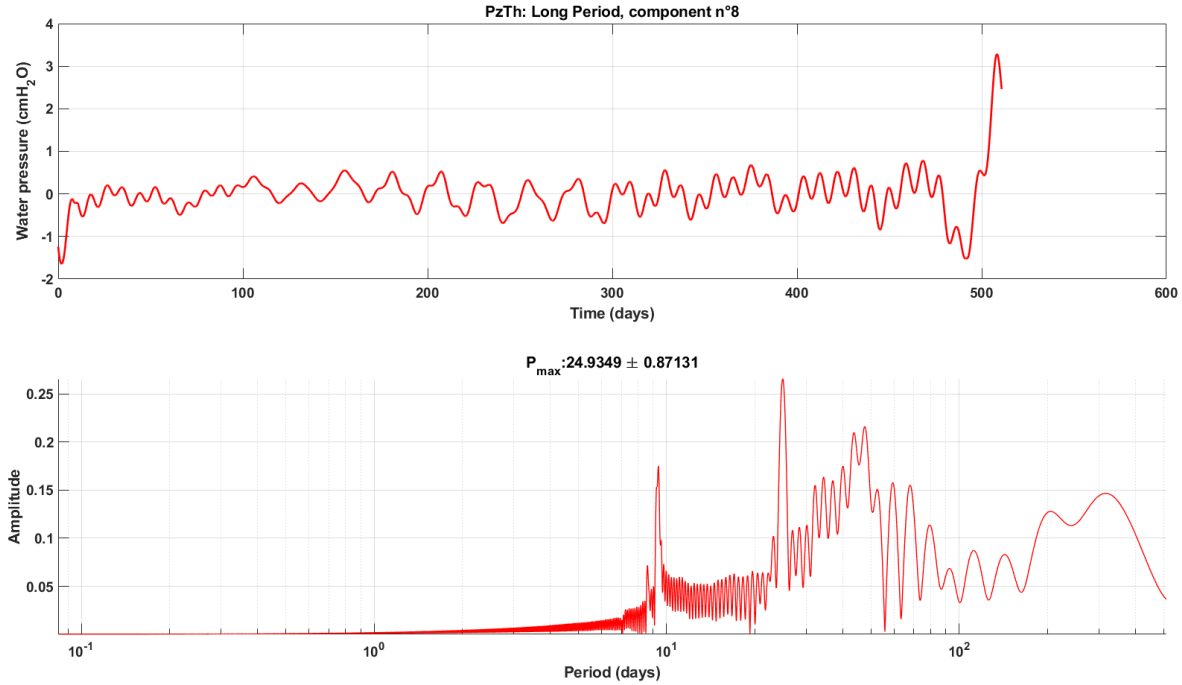

Figure 5.33: The eighth component of the long term signals from the West of the Theatre.

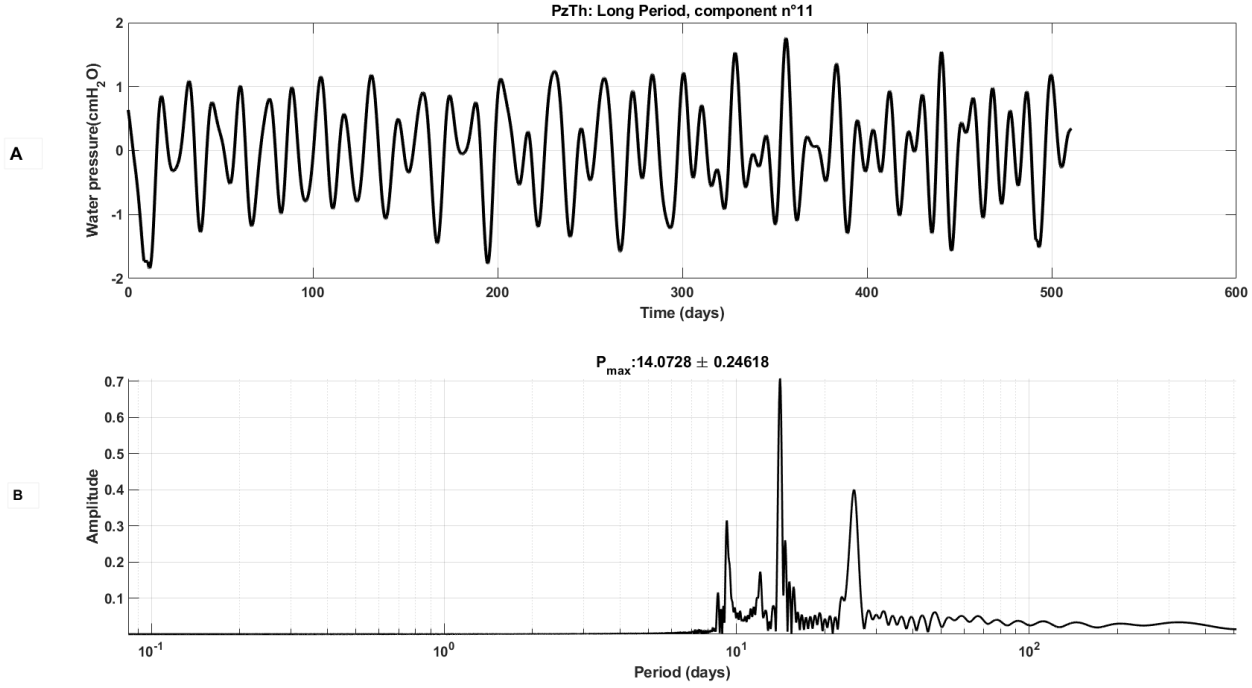

Figure 5.34: The eleventh component of the long term signals from the West of the Theatre.

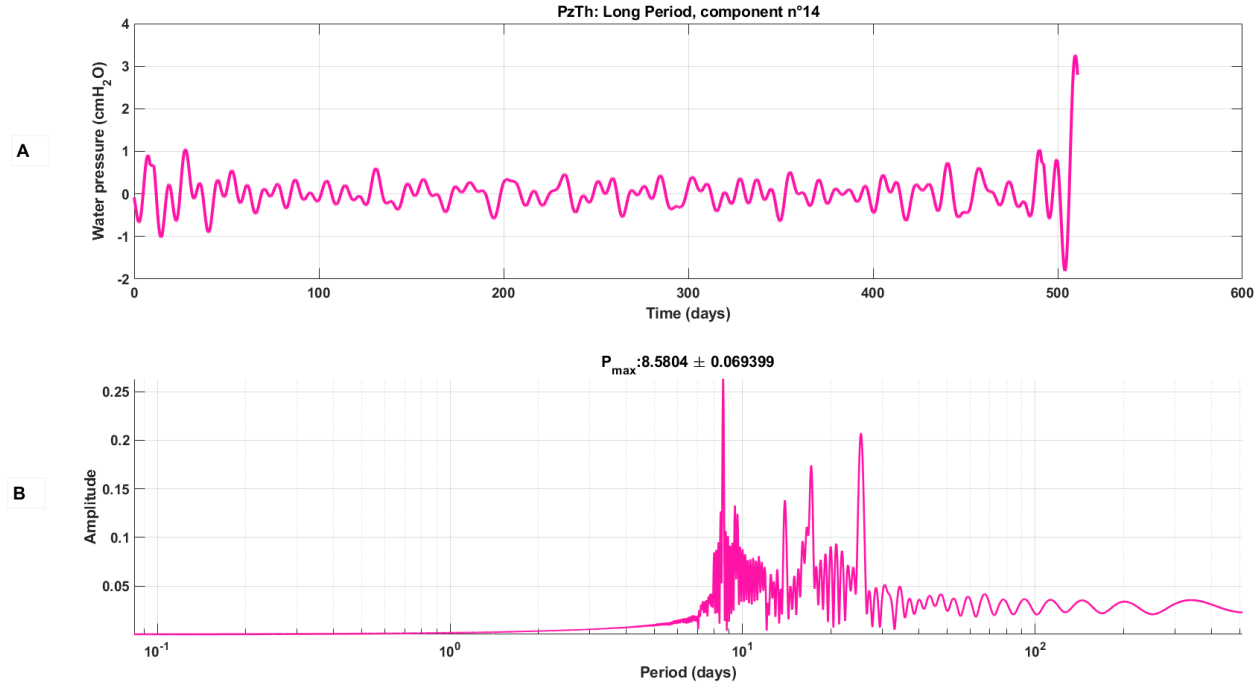

Figure 5.35: The fourteenth component of the long term signals from the West of the Theatre.

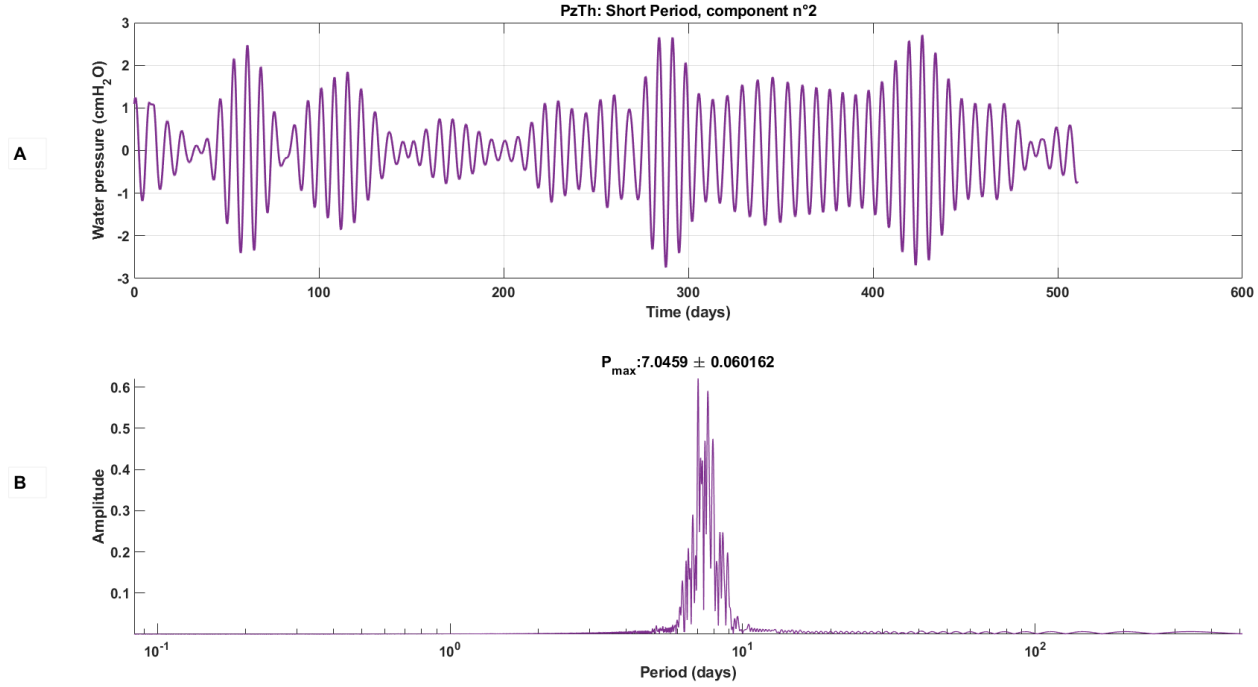

Figure 5.36: The second component of the short term signals from the West of the Theatre.

5.4.3.1.4 SSA applied to groundwater temperature data The groundwater temperatures measured in PzShf (Figure 5.8) for years 2017, 2018, and 2019 were decomposed using the SSA method. The spectrum obtained after regrouping is presented in figure 5.39. Ten LP and eight SP strands

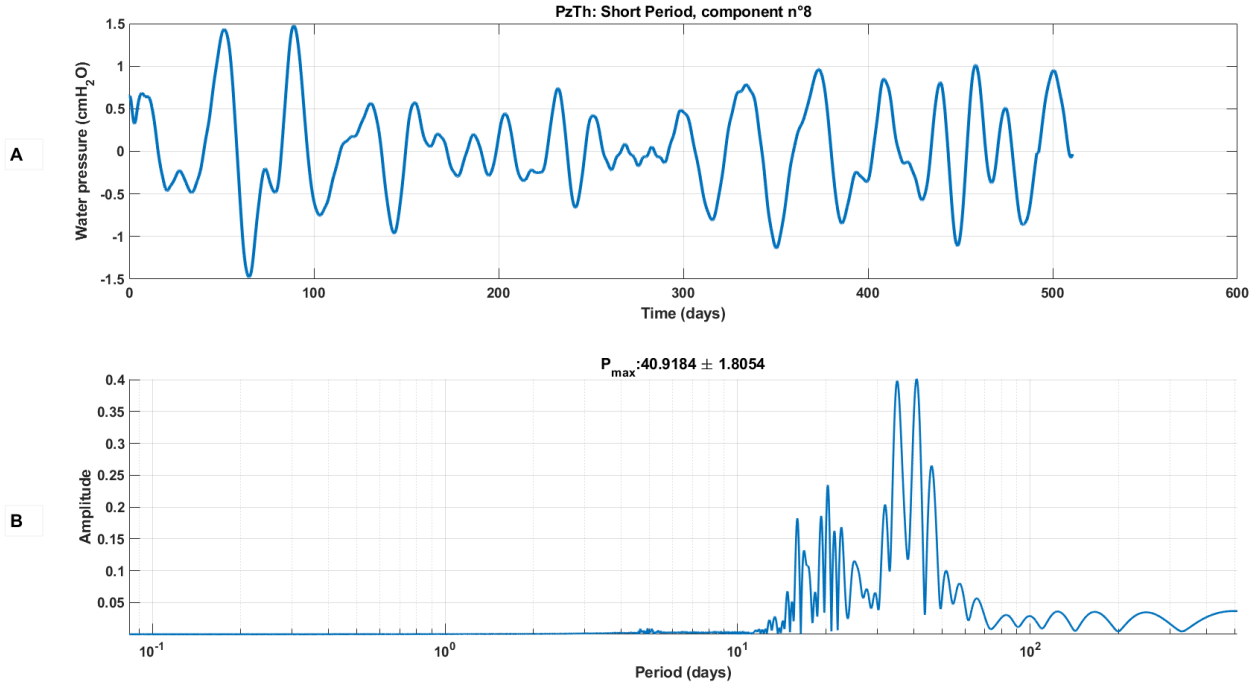

Figure 5.37: The eighth component of the short term signals from the West of the Theatre.

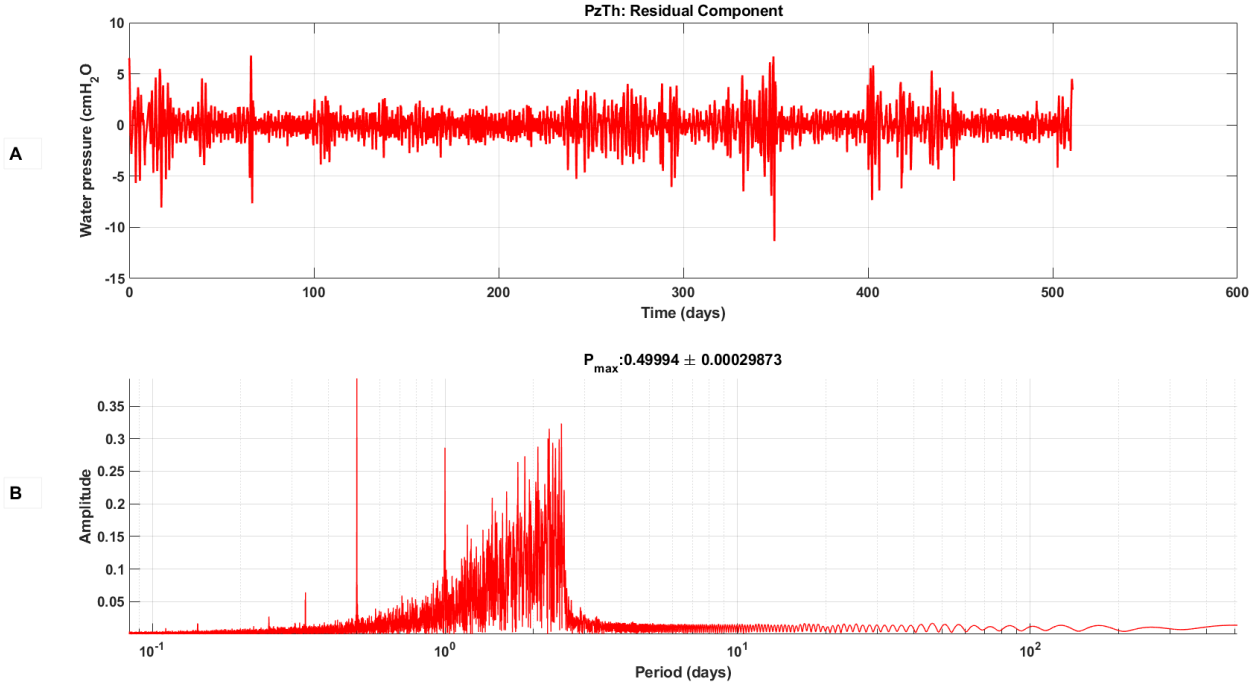

Figure 5.38: The residual component of the short term signals from the West of the Theatre.

represent the different contributors to the changes in the temperature values. Two prominent components, LP 1 and LP 2, depict the long-term temperature structure of the water (Figure 5.39).

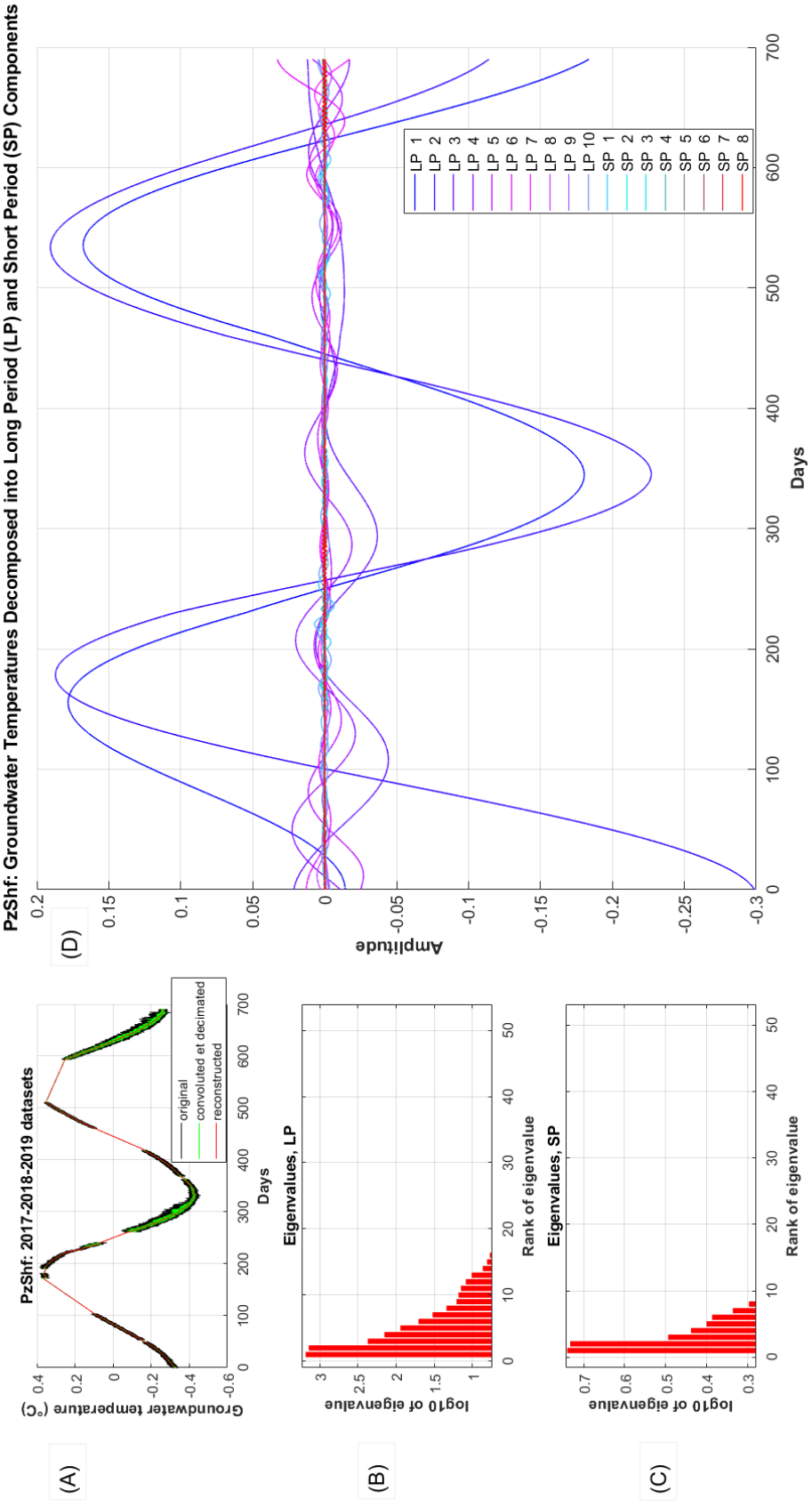

Figure 5.39: Singular spectrum analysis: decomposition of groundwater temperatures from year 2017 - 2019 in PzShf into long and short term components.

5.4.3.2 Sliding window method

In data analysis, sliding windowing is the procedure of selecting, for analysis, a subset of a larger data set at a regular interval with an overlap of a fixed size. A section or portion of data is selected, and a mathematical procedure is applied to that section or portion. The approach is also known as the overlapping window technique. Other windowing techniques include hopping, season, tumbling, and snapshots.

The sliding method is useful for pattern identification in time series (Chou and Ngo, 2016; Mozaffari et al., 2014). It was applied using established mathematical solutions. For example, in a Fourier transformation, it is useful for resolving the frequency components in time.

Sliding window techniques have applications in many fields, including hydrological studies (e.g., see Kulanuwat et al., 2021) and environmental studies (e.g. see Wagner and Michalewicz, 2008).

To analyze data using this method, two parameters are required: the size of the window (*window size*) and a time or temporal *step*.

By windowing the water pressure data, the evolution of the amplitudes can be studied, and changes can be identified over time. It will also allow certain oscillations to be identified and associated with a particular period or season. In this study, the SSA was applied to the sliding windowing year of 2018 water pressure data acquired in the PzShf borehole. The window size of 14 days and a time step of 7 days were chosen (Figure 5.40). The two-week window size conceptually includes all categories of daily and sub-daily inducements that influence water pressure. Using the defined parameters, two-week window size, and one-week step, the sub-data were: D1 - D14, D7 - D21, D14 - D28, etc., for 91 days (January-March 2018). Where D1 represents Day One data and D1 - D14 is the window size.

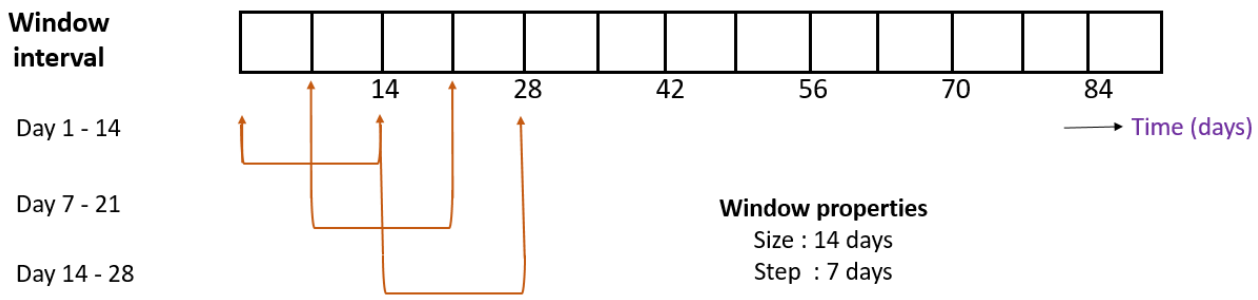

Figure 5.40: A schematic showing the window interval and step applied to implement the windowing technique.

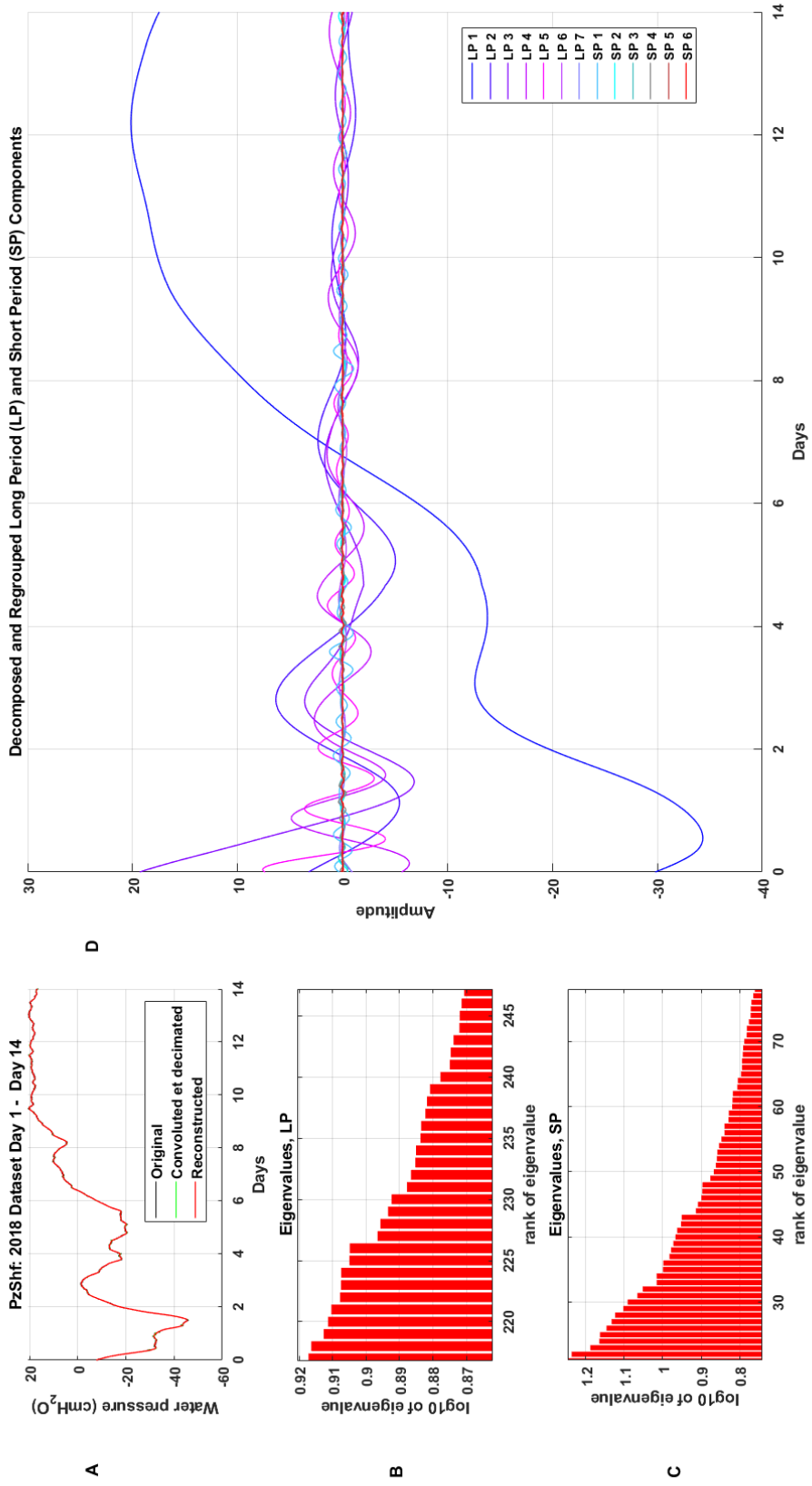

Figure 5.41: Singular spectrum analysis: decomposition of the year 2018 water pressure from PzShf into long and short-term components using a sliding window size of 14 days and a window interval of 7 days for subsequent steps.

For each windowed dataset, the resulting decomposed long and short-period oscillations are visualized, and the periods extracted (e.g., Figures 5.41 and 5.42; Table A.13 in appendix E.5). Constituents with the same period were paired and reprocessed. The resulting first five long and short constituents are shown (e.g., Figures 5.41 and 5.42). The tidal potential components and other influences are identified (Table A.14 in appendix E.5), following a similar guide (e.g. Acworth et al., 2016; Rau et al., 2020).

Using the SSA, the sub-data was first decomposed into components and subsequently constrained in frequency and time. Furthermore, the amplitude of the components observed in the window techniques was visualized to idealize the magnitude and changes in the amplitudes with time (Figures 5.43, 5.44 and 5.45).

The results of the SSA treatment of the long series data sets from the three boreholes (see Figure 5.6) and the windowed portion of the data sets acquired in the year 2018 (Figure 5.8) are herein presented. In each dataset, the long- and short-term events are investigated (equations 5.53 and 5.54).

The analysis was performed in two stages. The first stage saw the decomposition of the dataset into components that include the trend, oscillations, and residual, as shown in figure 5.18.

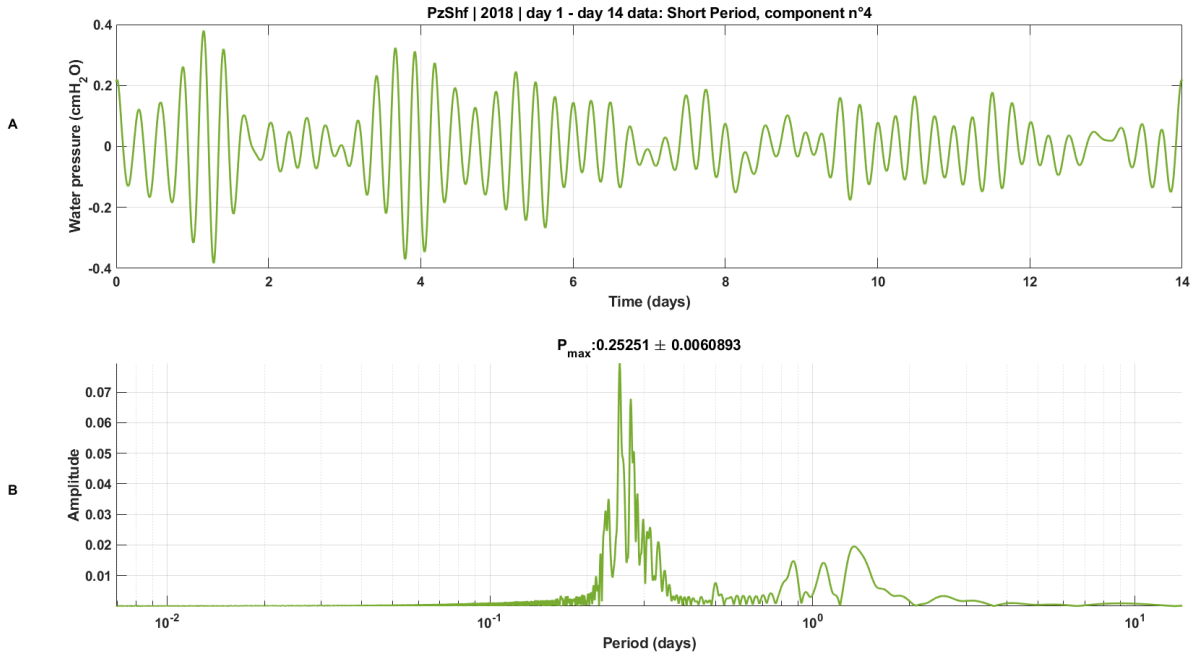

Figure 5.42: Singular spectrum analysis: the temporal and spectral visualization of a short term signal with 0.25 days in a window size of day 1–day 14 from year 2018 water pressure in PzShf.

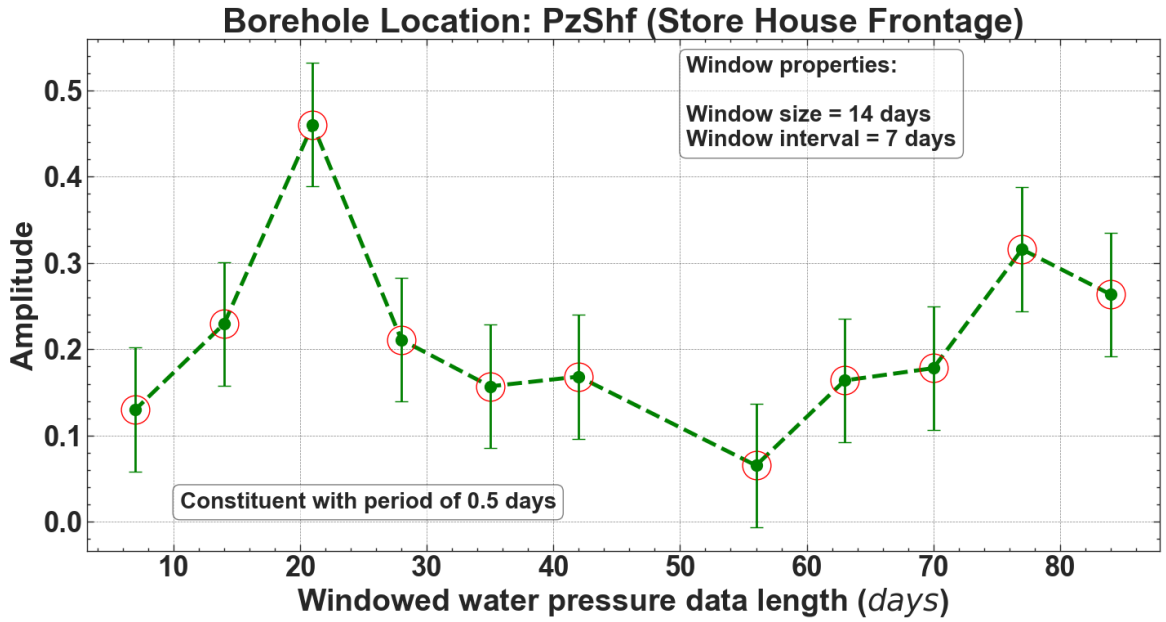

Figure 5.43: The changes in the amplitude of signals with 0.5 days period observed in the window intervals analysis.

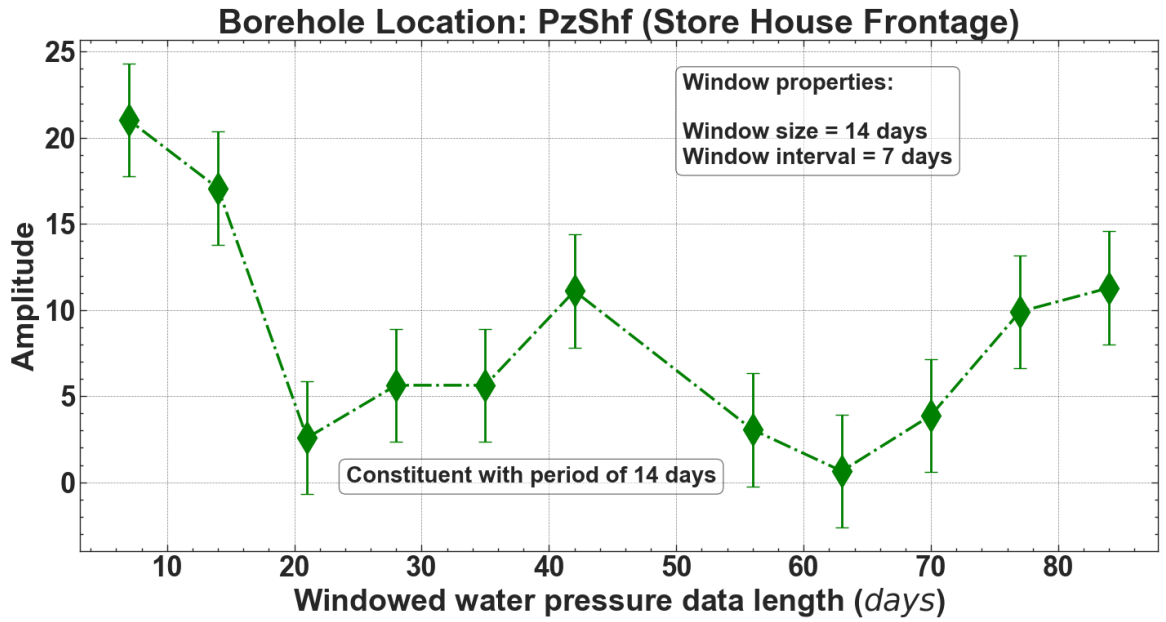

Figure 5.44: The changes in the amplitude of signals with 14 days period observed in the window intervals analysis.

The second stage followed the regrouping of the closely related components; it saw the eigentriple computation separate the trend, oscillations, and residue from the data. Each identified oscillating component is represented by a time and spectrum plot. It thus permits the modeling of each separated signal in the frequency and time domains. Its amplitude information is modeled in both the time and frequency domains. The frequency information can be visualized, and the maximum oscillation period can be extracted.

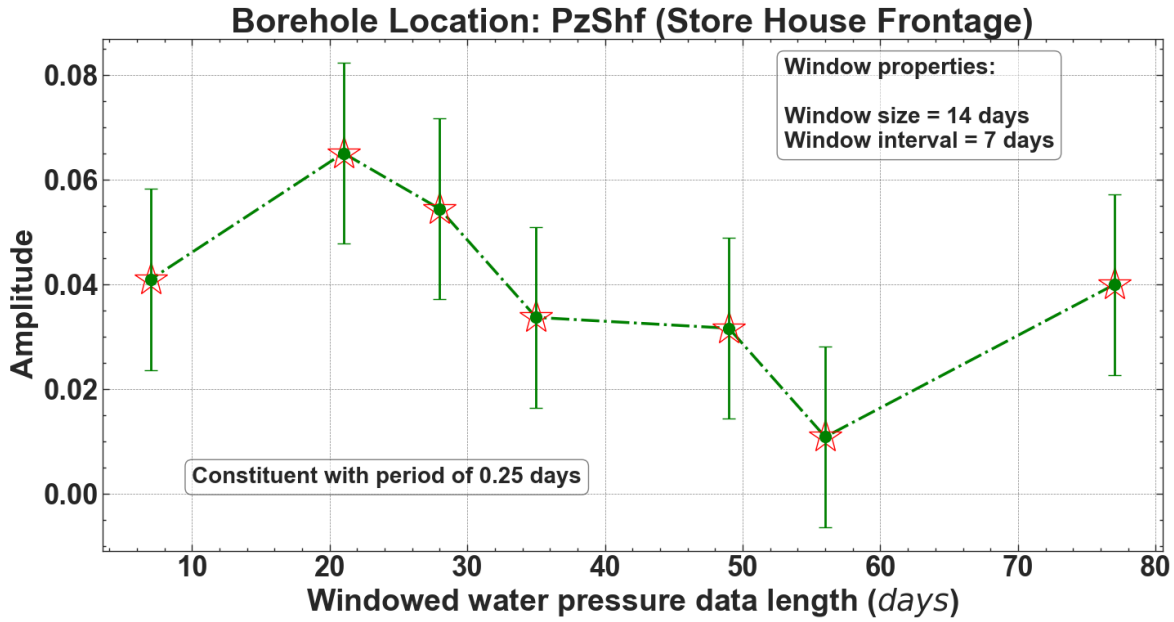

Figure 5.45: The changes in the amplitude of signals with 25 days period observed in the window intervals analysis.

Begin with the PzSa water pressure data, which covered 14 February 2022 to 26 July 2023, spanning 527 days (see Figure 5.6). In the first stage of decomposition, a finite number of 20 components were outputted each for the long-period and short-period events (Figure 5.18). The second stage involved the regrouping of components within the same period. It produced 15 long-term components and 12 short-term components (Figure 5.19).

The long-term trend has a period of 526.7903 days, confirming the length of the day set used (figure 5.20). In figure 5.20, periodic oscillations can be observed from day 100 to day 300, with a trend decreasing in amplitude. The oscillations beyond day 300 were less pronounced and did not show patterns that repeated over time. The amplitude fluctuates, reaching its highest in the later part of the spectrum. Following the trend is the long-term behavior of the water levels in the borehole, it represents the annual behavior of the signal with an amplitude value of 1.23 (figure 5.21). The short-term oscillating components obtained in PzSa with the periods of 29 and 24 days are graphed in figures 5.22 and 5.23,

For the water pressure data from PzShf (Figure 5.6), 13 LP and 13 SP components were obtained after the regrouping exercise (Figure 5.26). The model signal in Figure 5.27 from PzShf is interpreted as a quarterly or seasonal event or a signal with amplitude higher towards the end of the plot. Figures 5.28, 5.29, 5.30 and 5.31 are periodic signals extracted from PzShf with respective periods of 62.70, 29.40, 24.8, and 14 days among the other LP and SP signals.

The PzTh water pressure data (Figure 5.6), was decomposed, the periods extracted (Table A.11 in appendix E.5), and reprocessed (Figure 5.32), 13 LP and 15 SP were obtained. Some of the long components are shown in figures 5.33, 5.34, and 5.35. Some of the short term events include figures 5.36, 5.37 and 5.38.

As explained in subsection 5.4.3.2 (see also Figure 5.40), a window size of 14 days and a time step of 7 days were used to implement the SSA on the 2018 data from the PzShf (see, e.g., Table A.13 in appendix E.5). The resulting signals were identified for each window interval, and the associated period or frequency is shown in table A.14 of appendix E.5. Each period that corresponds to a known harmonic component is identified for its presence as an Earth tide constituent and also for its presence in groundwater or barometric pressure.

By convention, an alphabet is used in the nomenclature of harmonic wave components, each constituent is identified by a capital letter and a subscript, usually a number. The subscript of 1 or 2, respectively, represents an event that occurs once or two times in a day. The subscript of 1 or 2 indicates daily or semi-diurnal events.

In the table A.14 in appendix E.5, the semi-diurnal (S-D) signals largely dominated by the K_2 and S_2 components are prominent and can be seen in each window interval.

Figures 5.43, 5.44 and 5.45 show how the respective amplitude of signals identified with a period of 0.5, 14, and 25 days changes over the 91 days investigated by the window.

In table A.13 of appendix E.5, the periods of 0.25, 0.33, and 0.5 days correspond to the periods of S_4, S_3, and S_2 harmonic components of solar origin, e.g., see table 5.1. It is an indication of the impact of solar radiation or heating on the Earth's surface. It is an effect of atmospheric and Earth tides that impact groundwater, causing changes in its levels.

The treatment of the groundwater temperatures was considered to test the capacity of the SSA on not only the water pressure data but also temperature data. Figure 5.39 shows the strands in the composite data reflecting the different heating and inducement responsible for changes in the temperature.

5.4.4 Extraction of harmonic components

We applied a window function before computing the DFT of the water and barometric pressure data sets to minimize the effect of spectral leakage and enhance the spectrum representation. The

Table 5.1: Major harmonic components of the tidal potential (Cutillo and Bredehoeft, 2011; Ducarme et al., 2006; Munk and MacDonald, 1960)

Earth Tides Components	Period (hours)	Period (days)	Frequency (cycles per day)	Description
O_1	25.82	1.0758	0.9295	Principal lunar
K_1	23.93	1.3721	1.0029	Lunar solar
M_2	12.42	0.5175	1.9324	Principal lunar
S_2	12.00	0.5000	2.0000	Principal solar
N_2	12.66	0.5275	1.8957	Lunar elliptic
Shallow Water Tides				
S_3	8.000	0.3333	3.0000	Principal solar
S_4	6.000	0.2500	4.0000	Principal solar

Hanning window function, a pure cosine function, was applied to the datafrom the Numpy package using the Python programming language (Harris et al., 2020).

The results of the product of the windowed and measured data were the input data for the DFT. The DFT computation was executed in the Python programming language (Harris et al., 2020; Swarztrauber, 1982; Van Rossum and Drake, 2009). By windowing, the data length was weighted to normalize the amplitude of the FFT output. The window procedure evened out non-periodic waveforms and distributed the spectral energy within a precise frequency band (Lyon, 2009).

The prominent peaks of the spectrum within the diel cycles of wave harmonics were extracted at corresponding frequency (period) points for each data set (Figures 5.46, 5.47, 5.48, 5.49 and 5.50). Five harmonic constituents within the semi-diurnal and diurnal periods considered relevant for groundwater studies were identified in the Earth tides, barometric, and water pressure data sets (Acworth et al., 2016; Rau et al., 2020, 2022). The five components (O_1, K_1, M_2, S_2, and N_2) constitute about 95% of the Earth tides considered important in groundwater studies (Table 5.1).

The results are herein presented in units of time (period) instead of the traditional frequency (cycles per time) norm to accommodate the diversity of the expected readers. For example, harmonic components with 12-hour and 24-hour oscillation periods correspond respectively to the frequencies of 2.0 cycles per day and 1.0 cycles per day (Table 5.1).

In the PzTh, PzShf, and PzSa, the semi-diurnal principal solar component S_2 with a period of 12

hours is the dominant harmonic, followed by the diurnal luni-solar component K_1, which has a period of 23.93 hours. The S_2 component has the highest amplitude in PzSa. The M_2 was seen in the PzTh with a much smaller amplitude.

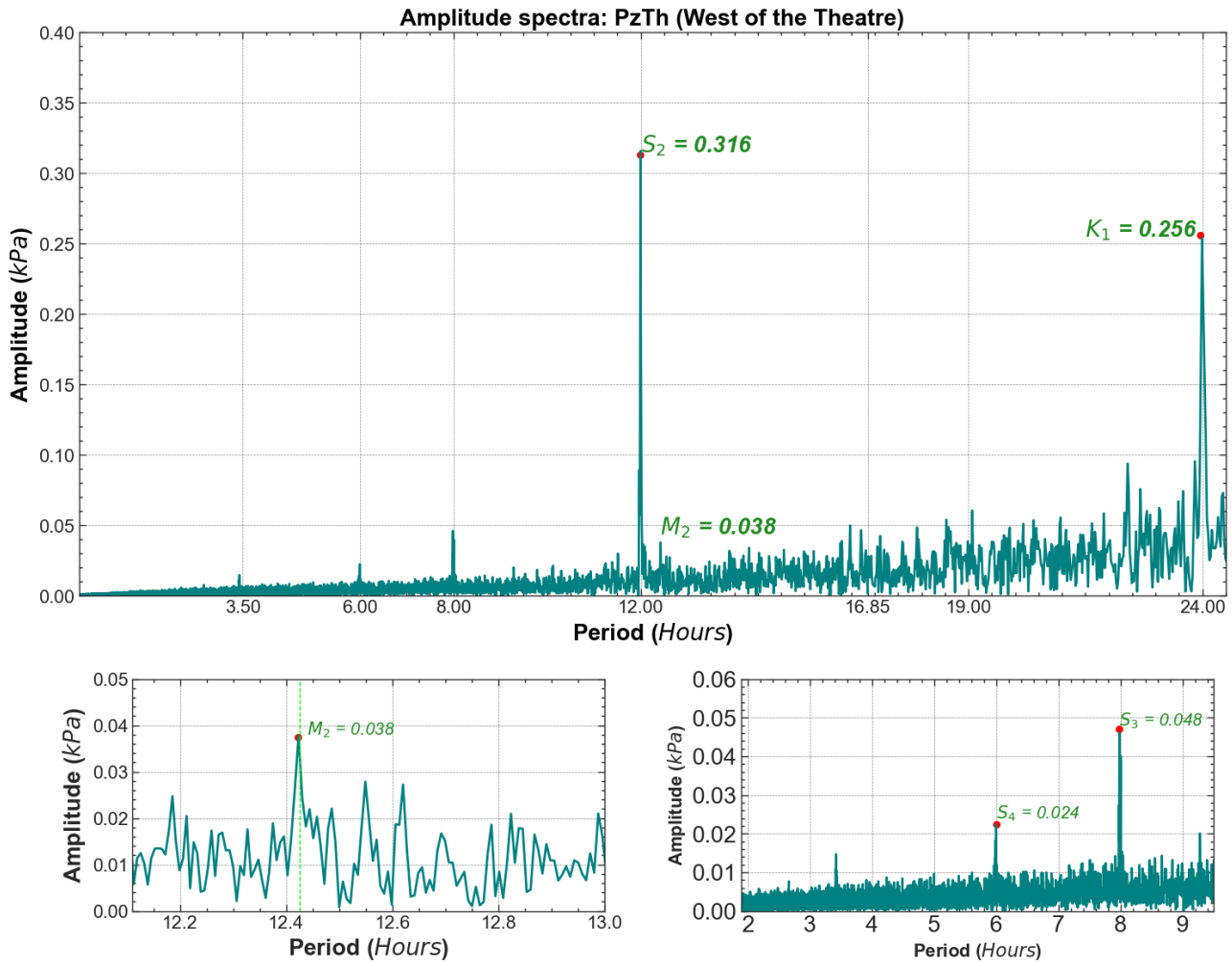

Figure 5.46: Amplitude spectra showing the harmonic components in the measured water pressure in PzTh (West of the Theatre).

5.4.4.1 Form ratio

The form ratio function is a classification scheme derived from the ratio of the sum of amplitudes of two diurnal and two semi-diurnal tidal constituents (equation 5.55):

$$F = \frac{K_1 + O_1}{M_2 + S_2} \tag{5.55}$$

It measures the diurnal tidal inequality in a region. It gives a qualitative description of the prevalence of a combined number of diurnal harmonic constituents over the same number of semi-diurnal components. It is a tool for recognizing the predominance of tidal strength. Table 5.2 gives the range of values used in the identification of the predominance of diurnal, semi-diurnal, or

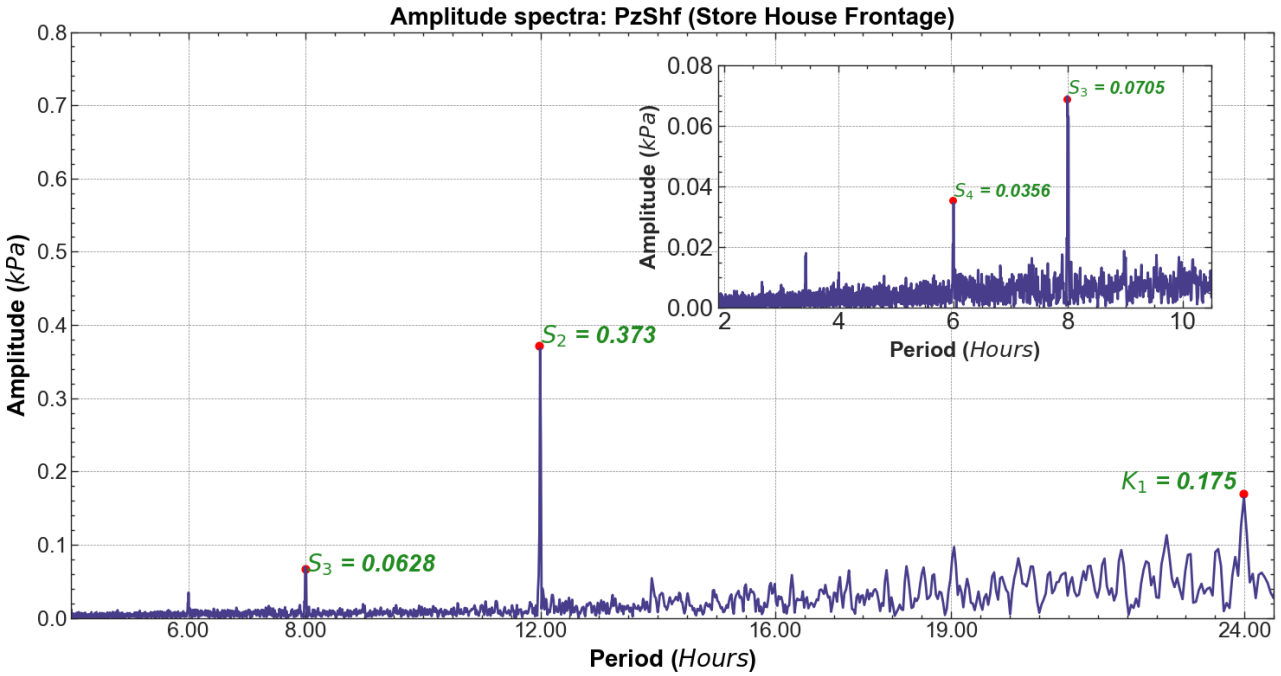

Figure 5.47: Amplitude spectra showing the harmonic components in the measured water pressure in PzShf (Store House Frontage).

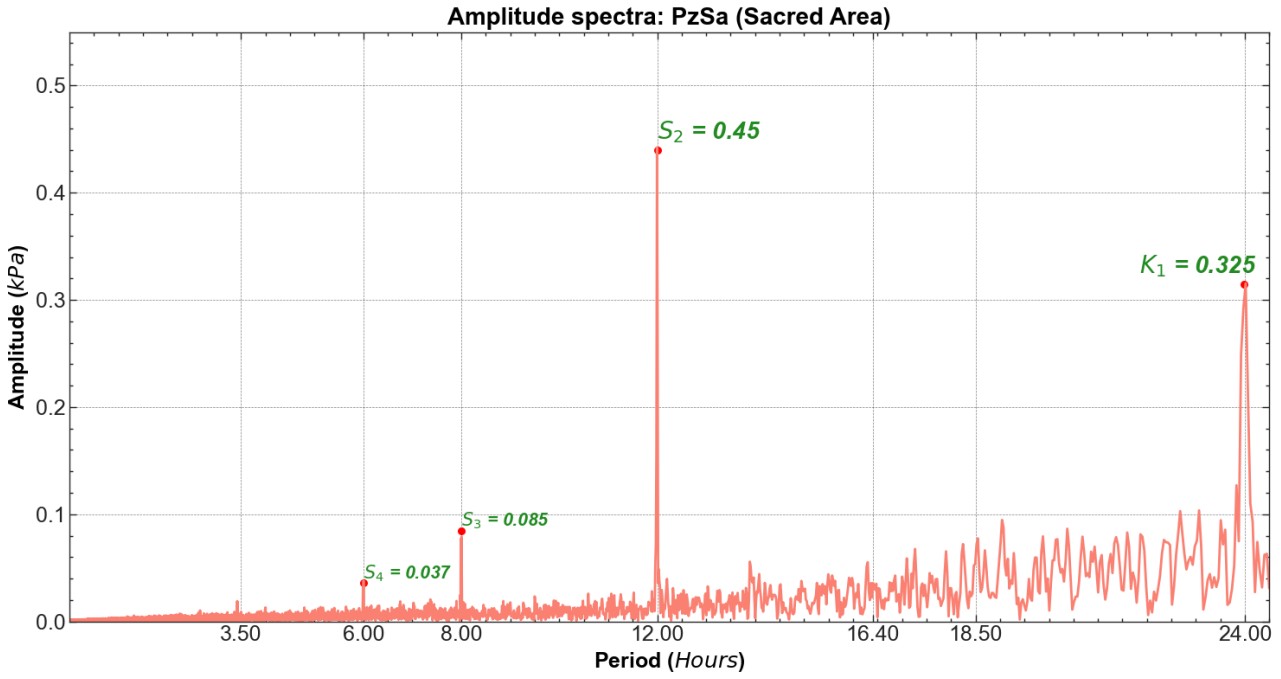

Figure 5.48: Amplitude spectra showing the harmonic components in the measured water pressure in PzSa (Sacred Area).

mixed tides in an area. From the ratio, the expected response of the water levels can be anticipated, and mitigation can be planned. The periodic nature of Earth tide effects is represented in figure 4.8 while the strain impacted by tidal effects is modeled in figure 5.49. The form ratio of the tidal strain (Figure 5.49b), computed using equation 5.55 indicates the presence of mixed domi-

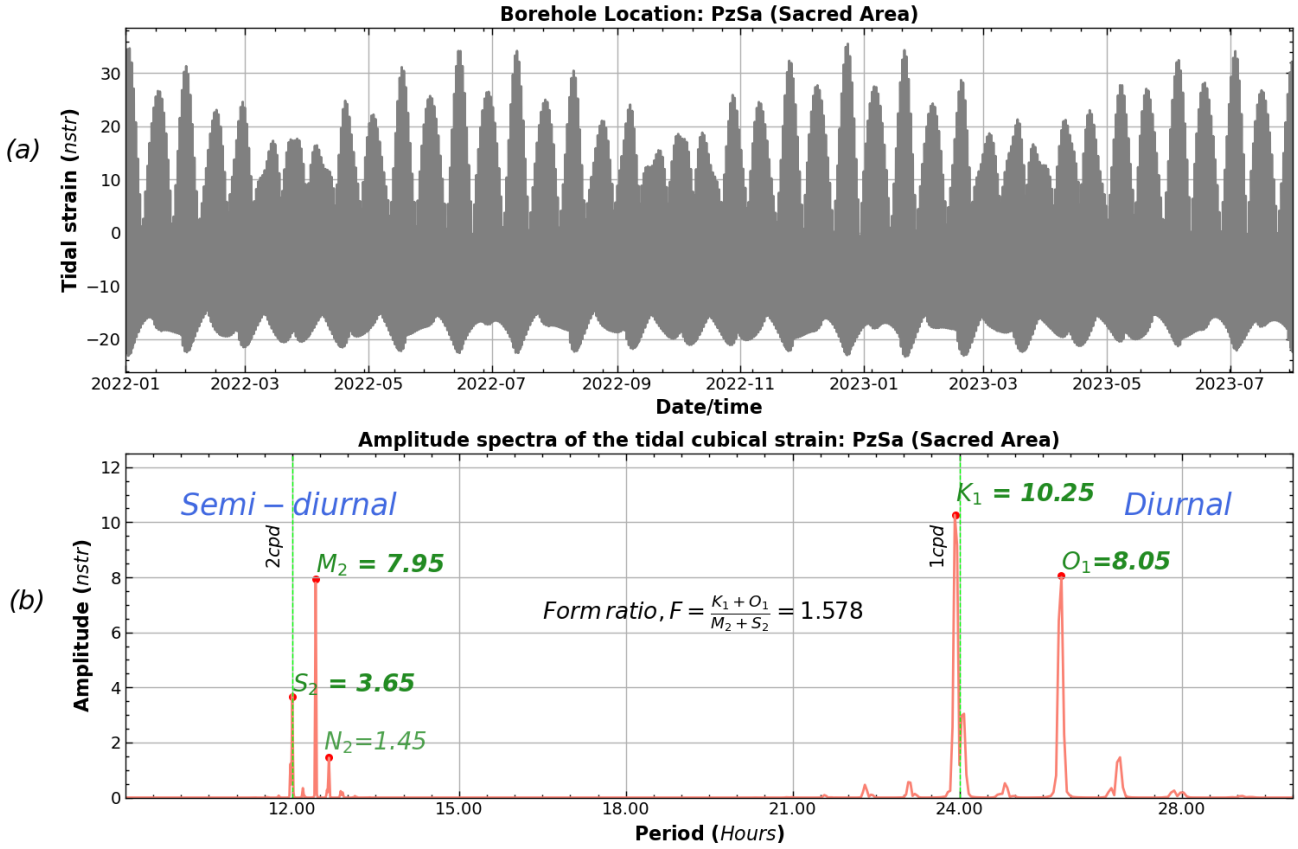

Figure 5.49: Theoretically computed Earth tides areal strain (Figure 5.49a) and spectra (Figure 5.49b) for the *PzSa*. The tidal strains have a dominant diurnal impact on the subsurface in the site from their form ratio of 1.578.

Table 5.2: Form ratio

Form Ratio, F	**Description**	Tidal response
0.00 – 0.25	Semi-diurnal tides	2 Highs, 2 Lows per day, similar strength
0.25 – 1.50	Mixed, dominantly semi-diurnal tides	2 Highs, 2 Lows per day, unequal in heights and uneven spacing
1.50 – 3.00	Mixed, dominantly diurnal tides	2 Highs, 2 Lows per day, but different strength
> 3. 00	Diurnal tides	1 High, 1 Low per day

nantly diurnal tides (Table 5.2).

The DFT procedure on the water pressure produced two dominant constituents within the 12–24-hour period, which are the S_2 and K_1. The amplitude of the S_2 from the spectrum of the water in PzTh is 0.316, while K_1 = 0.256 and M_2 = 0.043 (Figure 5.46). For the PzShf, the S_2 amplitude is 0.373 and K_1 is 0.175, the ratio is 3:1 (Figure 5.47). In PzSa, the S_2 is the prominent component

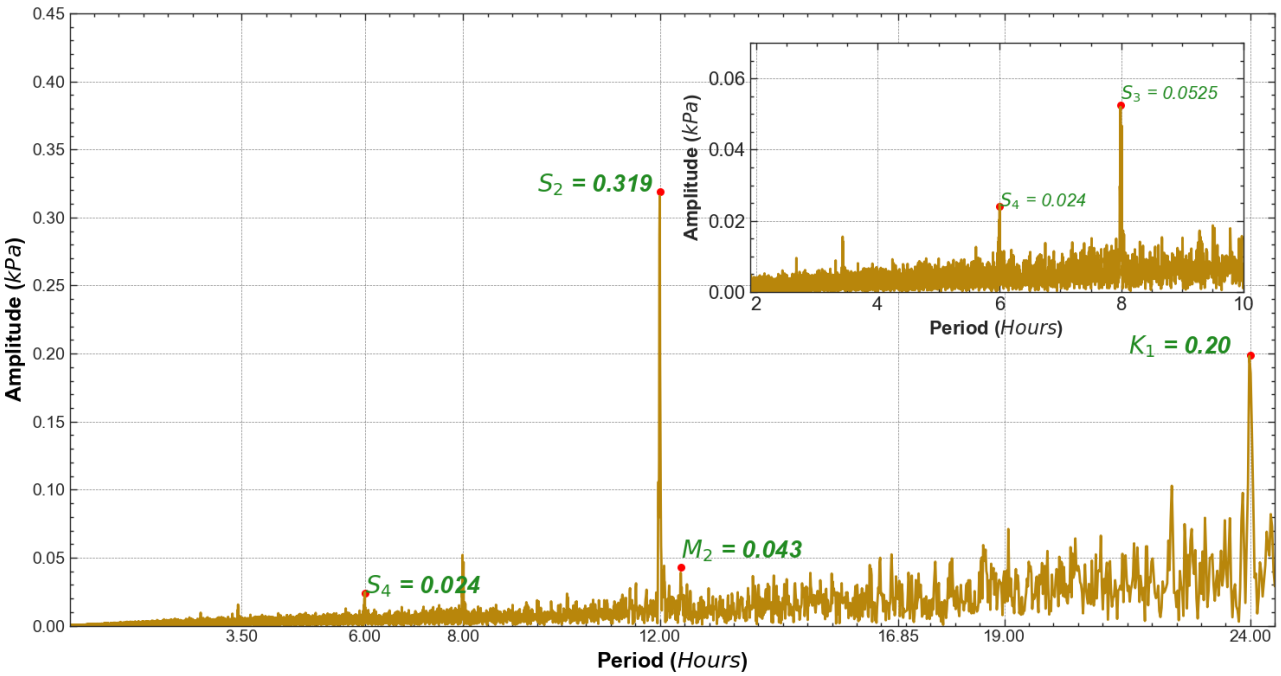

Figure 5.50: The spectra of harmonic components from the barometric pressure showing the dominance of the semi-diurnal S_2 wave in the long series data acquired at site from November, 2020 to July, 2023.

with an amplitude of 0.45, while the K_1 has a value of 0.325 (Figure 5.48). No occurrence of O_1 and N_2 components was identified at the site. The components in the barometric pressure are S_2 with an amplitude of 0.319 and K_1 with an amplitude of 0.20 (Figure 5.50). The traditional five harmonics are not all present in the water, or barometric pressure data at this site. The Earth tide strain (Figure 5.49), has all five components with a form ratio of 1.58. The computed form ratio of the water in the boreholes (Figure 5.6), shown in table 5.3, indicates the dominance of mixed semi-diurnal tides.

Table 5.3: Form ratio values computed from the amplitude of tidal components

	Amplitude of tidal components				
Location	K_1	S_2	M_2	Form ratio	Remarks
PzSa	0.325	0.450		**0.72**	Mixed, dominantly semidiurnal tide
PzShf	0.175	0.373		**0.46**	Mixed, dominantly semi-diurnal tide
PzTh	0.256	0.316	0.043	**0.81**	Semidiurnal tide

5.4.5 Seasonality and harmonic components variability

The S_2 harmonic constituent is the principal solar semi-diurnal constituent. It has a period of 12 hours (a frequency of 0.5 cycles per day). It comes from atmospheric oscillations due to the gravitational forces of the sun and moon and from oscillations of the sun's thermal effects on the Earth's surface.

In other words, the S_2 harmonic constituent is produced by the stress exerted due to the gravitational attraction of the sun and moon on the Earth and by the sun's thermal effect. It thus has both tidal and solar heating sources. The semi-diurnal tides are a reliable and global phenomenon that causes a response in hydraulic heads (Acworth et al., 2016; Merritt, 2004).

The amplitude of the tidal component was monitored during the summer period, which usually spans from June to September. The summer is known for longer periods of solar heating on the Earth's surface; hence, the component was monitored for variability in its amplitude for qualitative inference to solar heating.

This difference in amplitude can be viewed as input from increasing solar heating if it is assumed that the tidal forces remain unchanged as the global warming scenarios continue. The amplitude of S_2 in the year 2022 was higher than that for the year 2023 (Figures 5.51 and 5.52). Compare the respective values of 0.415 and 0.565 in year 2022 to 0.359 and 0.385 in year 2023. The value of 0.462 for 2022 was also higher than the value of 0.356 for 2021 in PzTh (Figure 5.53). The results agree with reports of the 2022 temperature as the hottest or warmest summer (Ballester et al., 2023; Guinaldo et al., 2023; Lindsey and Dahlman, 2023).

5.4.6 Aquifer confinement type identification using tidal components

The presence or dominance of some of the harmonic components in the spectra of the water pressure data has provided information for identifying the type of aquifer confinement. Using the scheme by Rahi and Haliban (2013) shown in table 5.4. The response of the main harmonics within two prominent subdiel periods (12-hour < T < 24-hour) identified in the spectrums of the decomposed groundwater was used following the scheme by Rahi and Haliban (2013) to identify the signature of the aquifer confinement type at the site (Table 5.5). From the response of the aquifer water, the M_2 was seen only in PzTh, though at a comparatively lower amplitude. The absence of M_2 in PzShf and PzSa is a pointer to the prevailing confinement conditions. Thus, the unconfined aquifer type dominates (taking an end-member definition), which with spatial variations, the con-

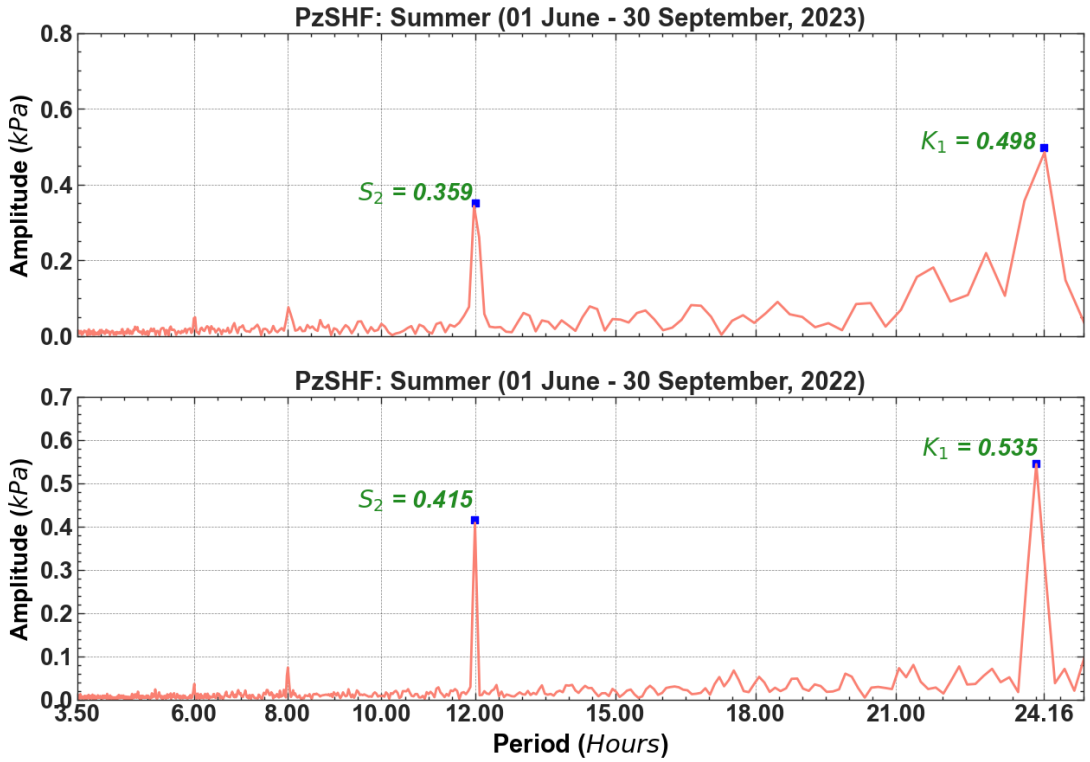

Figure 5.51: Changes in the amplitudes of the K_1 and S_2 harmonic components in the summer of years 2022 and 2023 at *PzShf*.

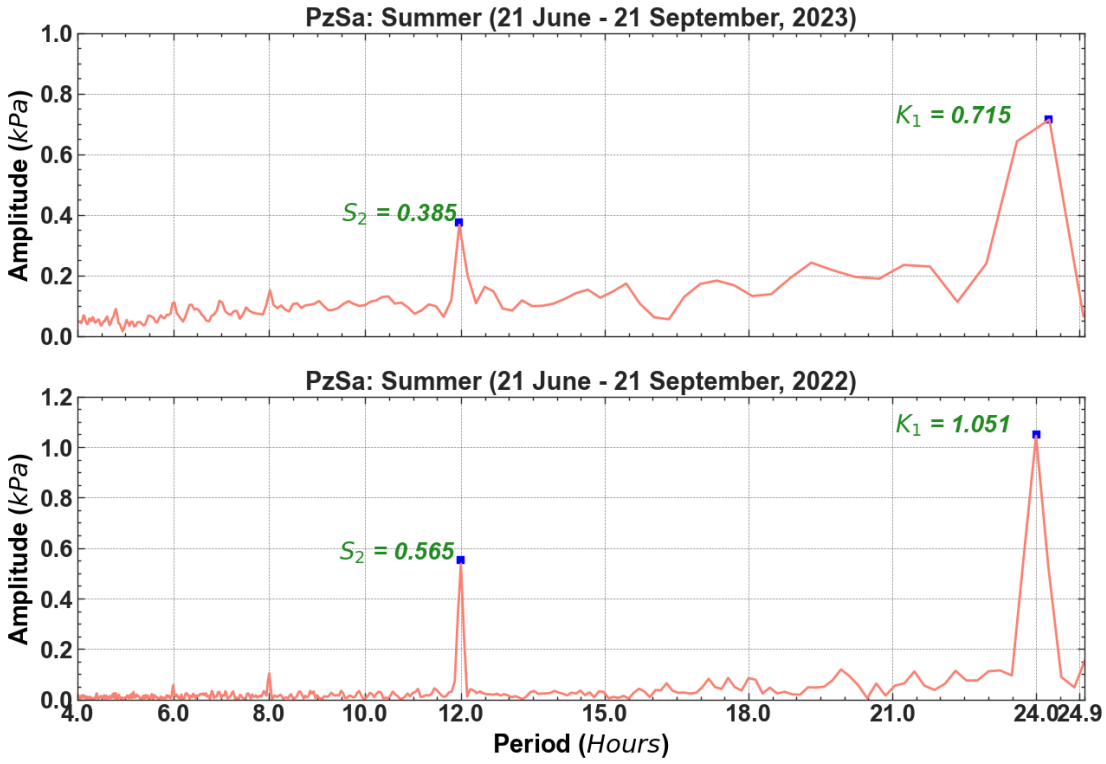

Figure 5.52: Changes in the amplitudes of the K_1 and S_2 harmonic components in the summer of years 2022 and 2023 at *PzSa*.

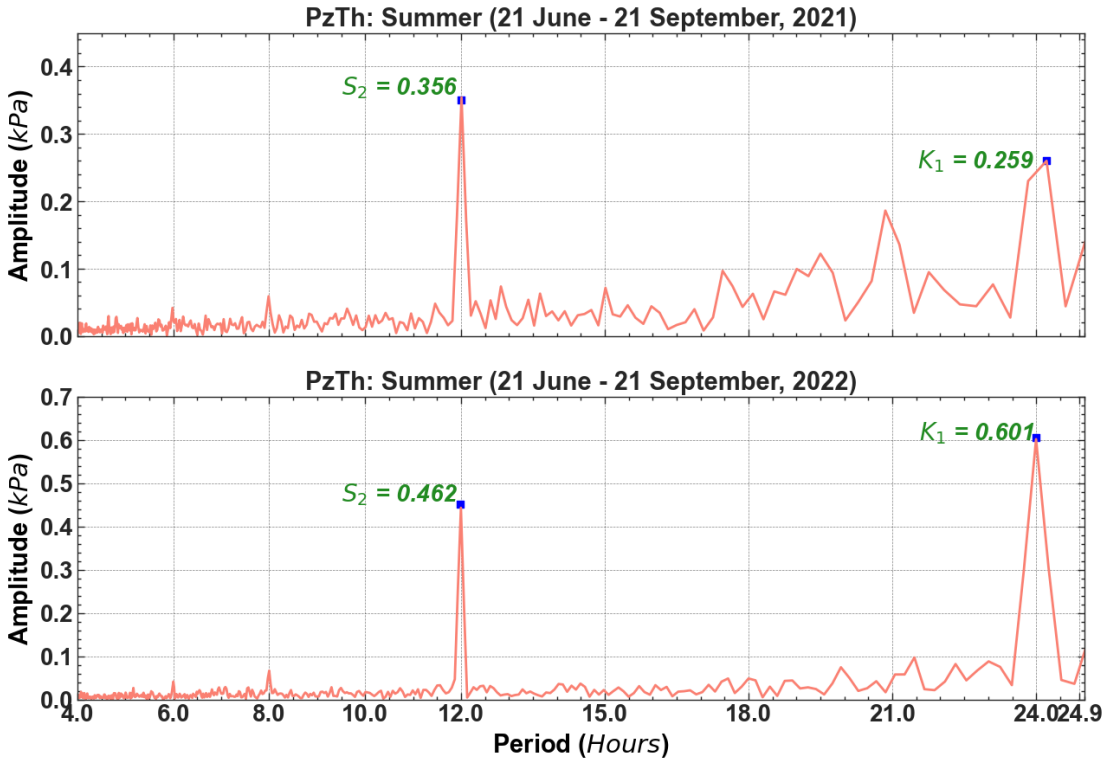

Figure 5.53: Changes in the amplitudes of the K_1 and S_2 harmonic components in the summer of years 2022 and 2023 at *PzTh*.

Table 5.4: Aquifer confinement types identification based on the response from periodic natural disturbance (Rahi and Halihan, 2013)

Tidal wave component	**Confined**	**Semi-confined**	**Unconfined**
O_1	Present	May be present	Not present
K_1	Present	Present	May be present
M_2	Present, dominant	Present	Not present
S_2	Present	Present, dominant	May be present
N_2	Present	May be present	Not present

Table 5.5: Identification of aquifer confinement types

Borehole location	**Harmonic component**	*Aquifer types and response to harmonic signals*		
		confined	semiconfined	unconfined
Sacred Area, *PzSa*	K_1, S_2	Present	**Present**	Uncertain
Theatre, *PzTh*	K_1, S_2, M_2	Present	**Present**	
Store House, *PzShf*	K_1, S_2	Present	**Present**	Uncertain

finement conditions would tend toward semi-confinement, as can be inferred from the presence of M_2 observed only in PzTh (Larocque et al., 1998; Turnadge et al., 2019; Wang et al., 2018; Weeks, 1979). The dominance of the S_2 and K_1 tidal components suggests a semi-confinement.

5.4.7 Aquifer storage characteristics

Using the method by Cutillo and Bredehoeft (2011), the loading efficiency γ was determined from a regression model of the pore pressure and barometric pressure (Figure 5.54). The total pore pressure was computed after removing the effect of earth tides in the water pressure with TSoft software (Van Camp and Vauterin, 2005). The procedure involved obtaining the total pore pressure by summing the barometric and measured water pressure at each time step. The total pore pressure is fitted with a simple tidal model in the TSoft software (Van Camp and Vauterin, 2005).

From the model of the relationship between the total pore pressure and the barometric pressure, the loading efficiency γ of 58% gave a clue to the effect of the barometric efficiency (Figure 5.54). The relation in equation 5.40 was used to estimate the barometric efficiency, BE, after obtaining the loading efficiency γ. The BE value of 0.4152 (41.52 %) was determined. From equation 5.41,

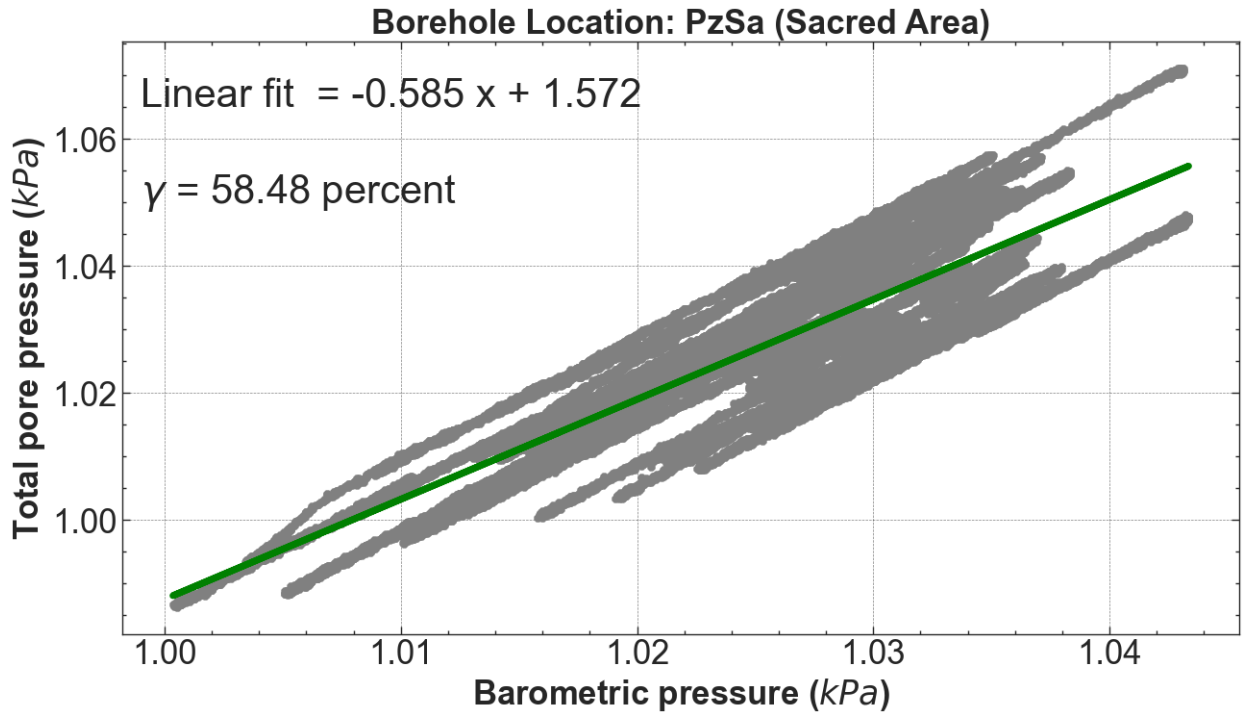

Figure 5.54: Total pore pressure and barometric pressure relation for February–June 2022.

the specific storage of the aquifer can be calculated with analytical values of the porosity typical of sand and poroelastic parameters (Table 5.6 and subsection 5.2.4). Using the model equation by

Rau *et al*, a plot of the S_s and the analytical values of θ normalized by γ is shown in figure 5.55.

The result models the specific storage and porosity values. From the model in figure 5.55, the specific storage S_s of $2.38491 \times 10^{-6}\ m^{-1}$ corresponds to the porosity of 0.3750; the S_s value of $2.00689 \times 10^{-6}\ m^{-1}$ corresponds to the porosity of 0.3164; and the S_s value of $2.53083 \times 10^{-6}\ m^{-1}$ is associated with the porosity of 0.3996.

The specific storage coefficient S_c is given a porosity value (e.g., 30%) typical of sands to represent the *Cuisian* sand beds. For lack of experimental values and also in this case where the pumping tests proved problematic (sections 4.7 and 4.9). The aquifer thickness from the lithology section in figures 2.9 and 2.10 is used. A thickness D of 8.5 m was used to estimate the specific storage coefficient $S_c = S_s \times D$. Also, specific storage was estimated from the earth tides effect using equa-

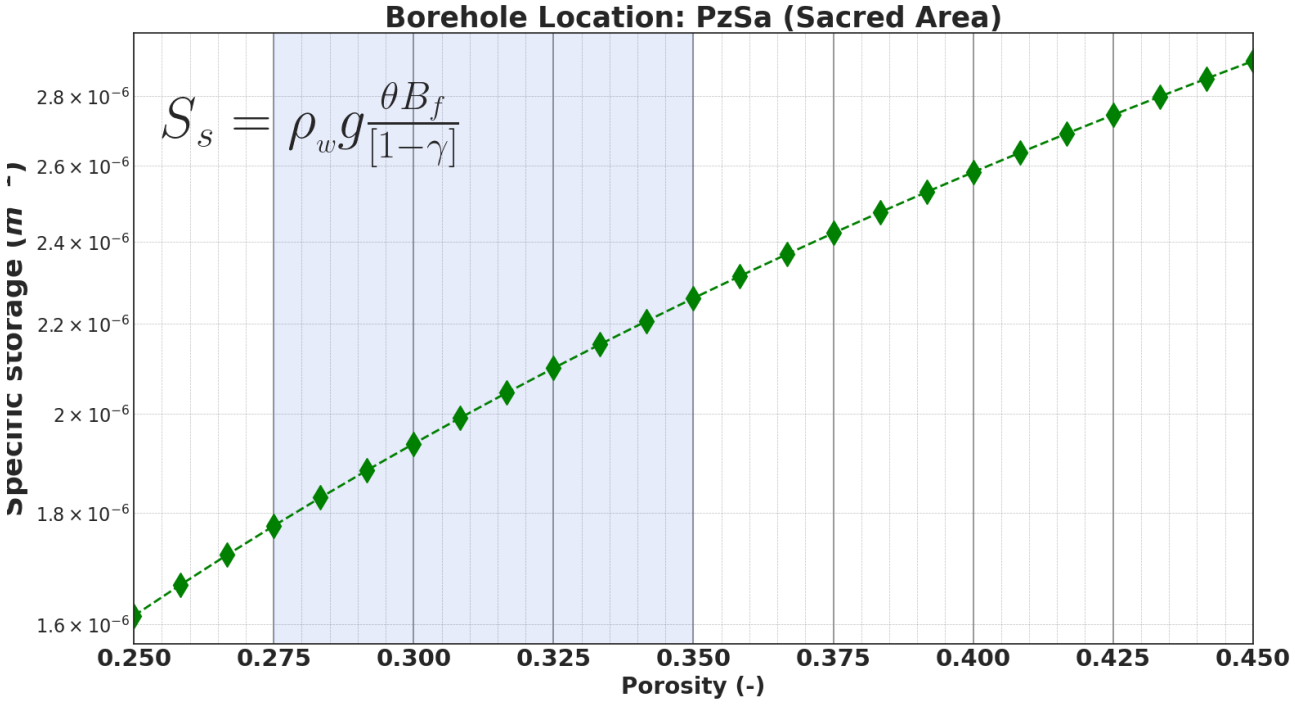

Figure 5.55: Analytical relationship between specific storage and porosity with parameters derived from tidal efficiency and fluid compressibility.

tion 5.46. The theoretical Earth potential was estimated using the PyGtide code (Rau, 2018). The amplitude of the M_2 tidal component computed was extracted from the tidal potential and water pressures sequel to the DFT (subsection 5.2.3). The amplitude of M_2 component was obtained from figure 5.46, and 1.179 from the theoretical computed tidal potential. Two assumptions are relied upon to apply the model equation 5.46: the minus sign indicates the head in the aquifer reduces while the tide generating potential increase (Cutillo and Bredehoeft, 2011; Merritt, 2004). Incompressibility of the solids is assumed, hence $1/K_s = 0$.

Table 5.6: Input parameters for poroelastic computation

Description	Symbol	Value (SI unit)
Density of water	ρ_w	1000.00 Kgm^{-3}
Compressibility of the fluid	β_w	4.59×10^{-10} Pa^{-1}
Poisson ratio	v	0.25
Compressibility of the formation	β_f	3.8×10^{-8} Pa^{-1}
Porosity of sand	θ	$0.25 - 0.45^*$
Gravitational Acceleration	g	9.82 ms^{-2}

Domenico and Schwartz (1998); Fetter (2001); Rice and Cleary (1976); *Range of values used for analytical evaluation

The specific storage of $2.60 \times 10^{-7} m^{-1}$ compares reasonably with values obtained using the analytical values in subsection 5.4.7 from barometric pressure effects. From equation 5.42, the porosity θ with specific storage from equation 5.46 and the loading efficiency (Figure 5.54). The θ value is 0.0239. Using the same method, Cutillo and Bredehoeft (2011) and Rau et al. (2022) obtained similar values for porosity. The next step in the evaluation procedure of the mechanical properties was the computation of the bulk compressibility of the material., β^u, assuming undrained conditions and vertical uniaxial loading. Using the loading efficiency γ = 58.48% from figure 5.54 and β_f, the compressibility of the fluid, in this case water, (table 5.6) with θ (equation 5.47).

The resulting value of $\beta = 1.548 \times 10^{-11} Pa^{-1}$ further motivates the derivation of the undrained bulk modulus $1/K^u$ and Skempton coefficient, B, by the method of Rau et al. (2022) in equations 5.49 and 5.50. Where $\beta = 1/K$ and $\beta^u = 1/K^u$; and G = the shear modulus (equation 5.48), $A^{ET} = A^{ET}_{M_2}$ = the amplitude of the M_2 tidal component. From the model equations 5.47, 5.48, 5.49 and 5.50. The Skempton coefficient of 0.585 was obtained after the computation of the compressibilities, and G. B = 0.585 is compared with values in table 5.7 (Kümpel, 1991; Kümpel et al., 1999; Kümpel, 1997) for information on the saturation. This implies a highly saturated subsurface. The values obtained compare with values for different geological formations in Rau et al. (2022).

Table 5.7: Description of saturation with the Skempton parameter

typical:	Saturation > 99%	Saturation < 95%
	B > 0.5	B < 0.1

5.4.8 Climate change signatures from Earth tides: preliminary interpretation

The S_2 component (a semi-diurnal tidal component) has thermal and tidal origin (Acworth et al., 2016; Rau et al., 2020). It is modulated by the S_3 and S_4 components due to its relationship with solar heating of the Earth surface (Acworth et al., 2016; Rau et al., 2020). The dominant presence of the S_2 component is observed in all the spectrums (Figures 5.46, 5.47, 5.48, 5.49 and 5.50). Its amplitude was compared during the summer periods in 2021, 2022, and 2023 (Figures 5.51, 5.52 and 5.53).

The year 2022 amplitudes were significantly higher than the 2023 values obtained at all points. This outcome motivated the comparison of temperatures for the years 2022 and 2023 (Figures 5.51 and 5.52; also see Figure 4.1). The year 2022 temperatures were notably higher than the year 2023

From this, it is hypothesized that water levels are potential signatures for detecting the impact of environmental variability caused by rising temperatures (Figure 4.1). The impact reflects the amplitudes of the solar tides, e.g., S_2 component. The inference is drawn from the effect of thermal or solar radiation on the S_2 tidal component, which has not only atmospheric origin but also has an Earth tide (Acworth et al., 2016).

The results agree with reports of the 2022 temperature as the hottest or warmest summer (Ballester et al., 2023; Guinaldo et al., 2023; Lindsey and Dahlman, 2023). This rise in temperature impacts adversely on heritage and archaeological materials (Hollesen et al., 2016, 2018). The harmonic components are herein proposed as a tool for climate change monitoring. Other climate change monitoring facilities include cloud cover, surface water, etc (Karl et al., 1995).

5.5 Discussion

From the long-period data sets (equation 5.53), trends and events with large periods are extracted, and the converse is expected for the computation of short-period events (equation 5.54). The trend signifies the long-term behavior of the water levels in the aquifer as it responds to the general changes due to inputs, extractions, and other changes in the hydraulic gradient.

By windowing the data, a similar feat, synonymous with the short-term Fourier transform, is achieved. First, the signal conceived as a composite of different inputs is decomposed within a period (window), which allows the amplitude of a signal to be computed and extracted. The second benefit of the windowing technique in the SSA is that the amplitude variation in time can be constrained.

This is important as the days when a particular signal was ineffective (inactive) can be ascertained and monitored while assessing the impact of other signals.

From each plot obtained, the signature of an event, inducement, or phenomenon can be deciphered and related to an established or known event in nature or cause of inducement. In a few instances, a prediction can be made based on the signal's period (or frequency), or its historical precedence.

The signature of the spring-neap cycle is interpreted from figures 5.22 and 5.29 while the lunar forthnight event is in figure 5.31. The periods of 24 days (Temmer et al., 2005) and 27 days (Poblet and Azpilicueta, 2018) correspond to the signatures of solar activities recorded in the data. An example can be observed from the models of the signals extracted from PzTh shown in figures 5.32, 5.33, 5.34, and 5.35. The short-term signals (e.g., Figures 5.36, and 5.37) identified in PzTh have periods that correspond to solar and lunar periods. This indicates the influence of the lunar and solar events on the response structure of the aquifer system, causing fluctuations in the water levels and their impact on the aquifer matrix.

The residual component of the water pressure in each borehole (e.g., Figure 5.38, also see tables A.9, A.10 and A.11) has a period of 0.5 days. Thus, it can be concluded that the aquifer system is significantly impacted by the signal with a period of 0.5 days, which is equivalent to the period of the S_2 harmonic component.

With the DFT method; signals, influences, and drivers of changes in the groundwater levels with periods between 12-24h, were detected. Components with higher than 24 hours were not considered. These components with lower periods have implications for daily to sub-daily fluctuations of the water levels. The dominance of S_2 suggests the prevalence of thermal heating or impacted radiation from atmospheric and Earth tides (see e.g. Rahi and Halihan, 2013; Zhang et al., 2009).

The identified S_2 and K_1 harmonic components have signatures that were interpreted by Rahi and Haliban(2013) in assigning the response to aquifer confinement (Table 5.4). From this study, an unconfined aquifer tending towards semi-confined aquifer confinement type is inferred by the response of the K_1 and S_2 components (Table 5.5).

The form ratio is important for identifying the dominant tidal harmonic behavior (Table 5.2). In semi-diurnal sites, M_2 and/or S_2 components tend to have the largest amplitude, whereas in diurnal sites, K_1 and/or O_1 tend to dominate (Stephenson, 2016). Four types of behavior are expected

from the typical information derived from the form ratio, as follows:

1. Semi-diurnal SD: 2 nearly equal high waters and 2 nearly equal low waters approximately uniform spaces over each lunar day

2. Mixed, semi-diurnal MSD: 2 high waters and 2 low waters each lunar day, but marked by inequalities in height and irregular spacing.

3. Mixed, mainly diurnal MD: sometimes 2 unequal high waters and low waters at irregular spacing over a lunar day, and sometimes only 1 high water and 1 low water in a day.

4. Diurnal SD: 1 high water and 1 low water approximately uniform spaces over a lunar day

The amplitudes of the main components were extracted from the spectrum of the water pressure of PzTh, PzShf, and PzSa (Figures 5.46, 5.47 and 5.48) and used for the form ratio computation (Table 5.3). Hence, semi-diurnal tide dominates other tides at the site, based on the computed form ratio values. (Table 5.2).

The effect of natural forcings at the site was used to investigate the properties of the subsurface and the aquifer medium. Two properties - specific storage and Skempton's coefficient - were estimated non-invasively using this approach (subsection 5.2.4 and 5.4.7). These parameters relate to the presence and saturation state of the subsurface. It has been shown that the response of water in wells and boreholes to Earth tides and other forcings can be analyzed to derive corresponding harmonic components. From the analysis, the amplitude ratio of a harmonic component in water and earth tides can be related to poroelastic parameters to evaluate the hydraulic and physical properties of the subsurface. In this study, the Skempton's coefficient, a parameter that provides information about the saturation state of the subsurface, was calculated using poroelastic relations and the amplitude ratio of tidal harmonic components. This result can be useful for evaluating the saturation state of the subsurface over time and for monitoring groundwater rise. The value of B obtained from this study showed that the subsurface was saturated at the time of this investigation (subsection 5.4.7 and Tabletable 5.7); see also Kümpel (1991); Kümpel et al. (1999); Kümpel (1997). This information is useful for planning dewatering schemes and managing the rise in water levels. The two parameters evaluated assumed bulk responses of the subsurface and variation in one (vertical) direction. The precise depth of the investigation remains to be determined.

5.6 Conclusion

The semblance analysis has been applied to study the temporal and spectral behavior of two water pressure data sets. The method is effective with short-term data spanning some weeks. The semblance anomalies were clearly defined in the data set, which covered some weeks up to about three months. The contrast was seen in the long series as the features observed in the short-term (that span weeks) data were not well defined in the long-series data. The long series data covered over 12 (twelve) months.

With the semblance method, the response of two wells or borehole water to a field situation or inducement can be analyzed and monitored for a relationship based on the nature of correlation. It can be seen in the obtained plots, that strong correlations exist within the water pressure data, suggesting a spatial connection between the aquifer beds (the saturated permeable layer in the vicinity of the drilled boreholes are spatially connected to each other).

It can also be deduced that the observed positive correlation is a clue that the subsurface transmissivity of the water-bearing rocks is positive. It implies that the flow is readily accomplished. It is a possible indication of a corresponding response to environmental inputs and changes in water levels. Water pressure recorded in the boreholes were also investigated using the SSA to learn more about the factors causing variations in the levels. The amplitude and period of each identified signal, factor, or event were computed to determine the magnitude and duration of the impact assessed. For example, the identified short-period signal with a period of 7 days has an amplitude larger than the other signals identified in PzSa, indicating its prevalence and dominant influence in causing the fluctuations in the vicinity.

The advantage of the SSA method exploited in this research is the separatability of oscillating components based on their period. This benefit herein, is the ability to extract a sinusoid and study its temporal and spectrum characteristics compared to the sum of harmonics in the FT method. With the SSA, weekly, monthly, annual, and other long-period influences in groundwater can be identified and extracted.

The windowing technique implemented with the SSA permits us to study the changes in amplitude with time of a signal or event as the data length extends. A specific signal's occurrence time can be identified, and its influence can be tracked. In other words, it is possible to pinpoint, the actual time when a specific periodic signal drove the fluctuations and track its effects. The win-

dowing procedure is also a way of monitoring the variations in the amplitude or relative strength of the same signal with time. It permits attributing a physical or reported event to a periodic signal within a time frame.

A particular signal can be investigated in the three boreholes. For example, signals with 7-day periods appear in the short-period events computed in both PzSa (Figure 5.25) and PzTh (Figure 5.36).

With the SSA, a periodic signal can be extracted and attributed to a phenomenon using the period of the signal corresponding to established astronomical events or periods in hydrological cycles or climatic conditions or to predictable or known human-related inducements. Compared to the Fourier transform method, SSA permits the visualization of the changes in the signals' amplitude over time.

The DFT investigation has revealed the presence of daily and sub-diel signals that also influence the groundwater system. The principal semi-diurnal solar harmonic component S_2 dominates the other components. It implies the rise of the water levels proportional to the strength of the signal twice daily to wet the heritage walls, foundations, and buried artifacts.

The variations in the amplitude of the S_2 harmonic components are a tool for inferring climate change signatures from the analyses of the groundwater levels. The amplitude responded accordingly to correspondingly higher temperatures recorded in 2022, compared to the years before and after it (Figures 5.51, 5.52 and 5.53).

This study has shown that subsurface and aquifer properties can be estimated not only from classical pumping test experiments but also from the analysis of tidal harmonic components from Earth tides and measured borehole water pressure data associated with poroelastic parameters. This approach provides a solution for estimating aquifer properties in problematic areas where the classical approach is difficult to perform. The estimated parameters, such as Skempton's coefficient, can be used to monitor the saturation state of the subsurface.

Therefore, the steps used to derive the parameter in this thesis can be followed to non-invasively assess the saturation state of the subsurface sequence at the site over time. It is therefore recommended that a monitoring scheme be established that includes the assessment of Skempton's parameters at regular intervals.

CHAPTER 6

General discussion

6.1 General discussion

Non-invasive methods of investigation were pursued through the monitoring of natural forcing effects and environmental parameters such as temperature and solar heating. Natural forcings, which result principally from stress exerted on the Earth by the gravitational effects of astronomical bodies, chiefly the sun and the moon, and barometric loading from changes in the atmospheric pressures, were the principal periodic phenomena utilized in the assessment of the aquifer properties using well-documented procedures. For example, the amplitude of a tidal response component in borehole water is compared with the corresponding component in the theoretical tide to obtain a value (ratio) for use in computations such as equation 5.46 to estimate aquifer-specific storage (Bredehoeft, 1967; Gao et al., 2020; Hsieh et al., 1987; Rau et al., 2022).

The research context was outlined, and the objectives were set out as mentioned in section 1.3. The principle of minimum intervention routinely applied to field-based experiments in archaeological settings was diligently observed, mainly to avoid damage to the buried artifacts and historic ruins during the execution of the different experiments summarized in Figure 6.1.

The field experiments involved monitoring and analyses of water pressure variations, and the application of geophysical and hydrogeological methods to assess the subsurface and aquifer properties (Figure 6.2). Figure 6.1, is a schematic representation of the non-invasive methods used to

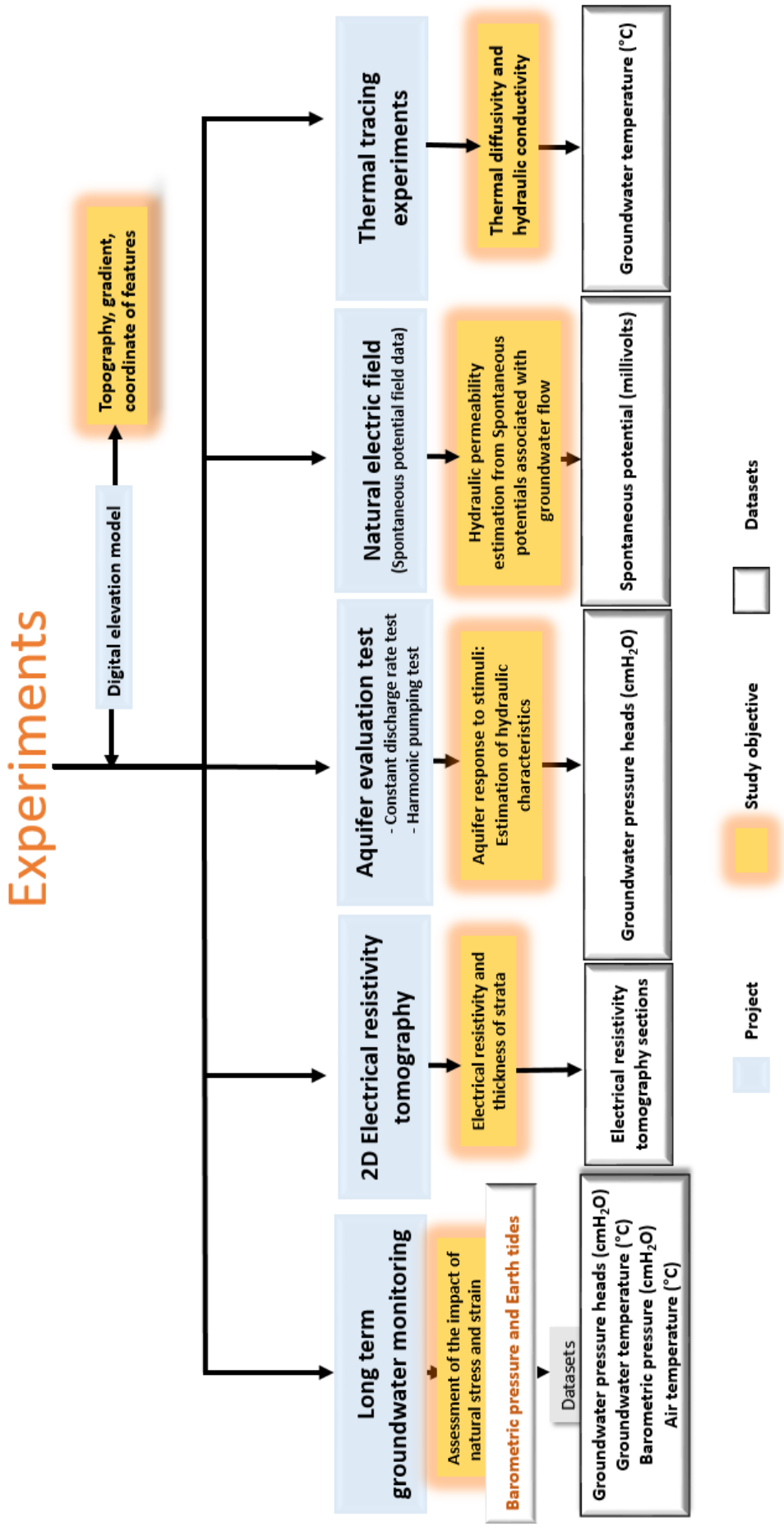

Figure 6.1: Pictorial outline of the onsite experiments and the acquired data sets

investigate the subsurface and the drivers of groundwater fluctuations in the site (Figure 6.3). The influence of natural and human activities on the aquifer and water saturation state can be studied using this method to constrain temporal and spatial events, signals, and forces.

An event, or a signal that triggers a change in the water pressure at a specific period can be constrained and its impact mitigated through innovative ways that incorporate the hydraulic, geological, and mechanical properties of the subsurface and buried archaeological materials.

A recap of the main methods and some of the results obtained is shown in figure 6.2, while as earlier mentioned, figure 6.1 summarizes the field-based experiments carried out to non-invasively investigate the subsurface (Figure 6.3). Figure 6.1 outlined the experiments. Each experiment is identified under the key project. Following each project (experiment) is the study objective, which outlines the essence of the experiment. The datasets in figure 6.1 were acquired with profiles and points in figure 6.3. Afterward, the types of datasets acquired are subsequently indicated. First,

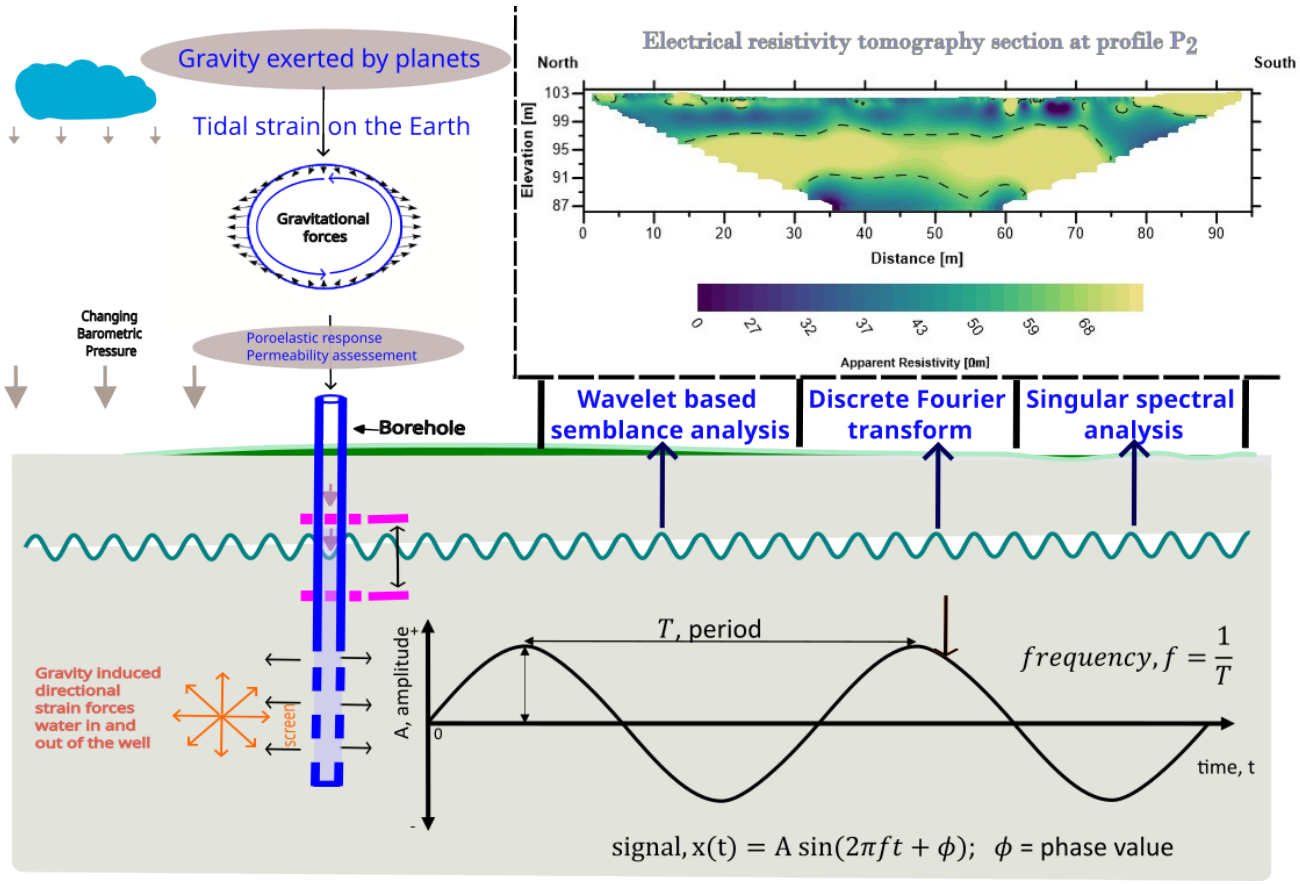

Figure 6.2: A composite schematic showing one of the 2D electrical resistivity sections (top right), a model of barometric pressure and tidal forces exerted on the Earth by the planets causing its deformation, and the fluctuations of groundwater in wells and boreholes with the methods used for the analysis of the data.

the relationship between the hydro-meteorological variables and inflow into the subsurface was

discussed using the watershed in chapter 2. Runoff and infiltration are explained as processes of the hydrological cycle initiated by precipitation and directed by differential elevation as inflow into the valley. They favor the movement of water into the valley where the artifacts and the ruins are located, as shown by the model of flow direction in Figure 2.13. One major outcome of the surface flow and infiltration in the model is the groundwater, which is water stored in pores and voids beneath the Earth's subsurface. The response of the groundwater to diverse impacts and influences either from natural or anthropogenic sources was studied, and interesting outcomes were revealed in the plots and models obtained in chapters 3, 4 and 5.

6.1.1 Data and scale

However, the passive measurements of water level fluctuations in the boreholes were both insightful and an incentive to the subsequent investigation, which revealed a variety of influences attributed to natural and anthropogenic activities, together with variability in climatic and environmental conditions.

Two criteria were set for the passive data: first, it was expected **to cover at least more than one hydrological year**. This was achieved as continuous measurements from the previous years, 2017–2019, were continued to 2023 (figures 5.6 and 5.8). The year 2022–2023 water pressure data are shown in figure 5.6 with fluctuations in a similar manner except for the period from July 2023 in PzSa (Sacred Area). This deviation in the response trend may indicate a variation in a property within the radial distance of influence of the borehole. This can be attributed to the heterogeneous nature of the subsurface.

This hypothesis of spatial heterogeneity was partially deduced from the tomographic sections in figures 3.8 and 3.10 (interpreted as the limestone bed and its weathered components, saturated colluvial materials; see also figures 3.12 and 3.14, which were thinner in figures 3.9 and 3.13).

The second criterion for the passive data was to adequately sample all responses to forcing; hence, a sampling rate of 60 seconds was used to allow for the detailing of changes and drivers of the changes within the simple space. Rau (2020) recommends the use of data acquired at sub-hourly intervals for at least three months to meet the ≈28-day period suitable for harmonic least squares evaluation in tidal analysis (Schweizer et al., 2021). The importance of data length was duly outlined by Acworth et al. (2016) by emphasizing a theoretical data length of 14.76 days, which should

be double ($\gtrsim$ 1 month) to achieve the minimum length of time series required to assess the two major semi-diurnal tidal components of M_2 and S_2 and for it to be distinguished. This requirement was superseded in this research, which enables the consideration of a wide range of variables in the groundwater (water pressure variations) data.

6.1.2 Subsurface structure from ERT models

A detailed mapping of the subsurface at the cultural area, opposite the remains of the amphitheater, was performed using electrical resistivity tomography (ERT). The ERT survey also covered the *Open Aire* and the frontage of the temple building traversing the paved road (Figure 6.3).

ERT method is a multidimensional imaging base on the electrical resistivity contrast bed adjoining beds (Arjwech et al., 2020; Loke, 1994, 1999), which have impacted archaeological studies by re-

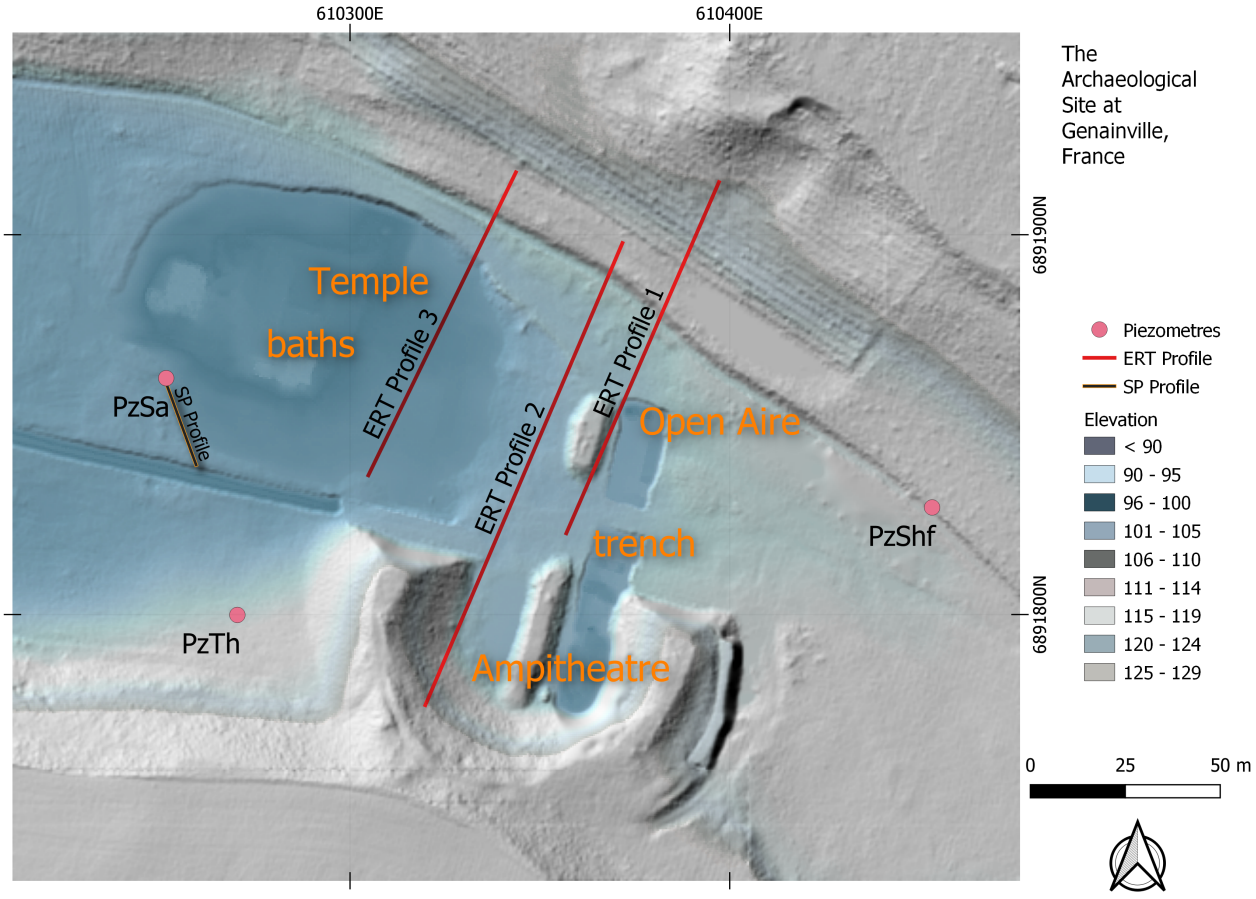

Figure 6.3: A map of the archaeological site showing the locations of the piezometers installed in three boreholes, electrical resistivity tomography (ERT) profiles, spontaneous potential (SP) profile, archaeologic trench, the remains of the theater, temple, baths, and the *Open Aire* area.

vealing the outlined geometries of artifacts and buried historical materials and anomalies (Deiana et al., 2018; Epov and Chemyakina, 2009). Smooth subsurface models were obtained using the

inversion method of Loke and Barker (1996), to produce finer images of the subsurface structure. The outcome of the ERT is a finer picture of the subsurface model in figures 3.8, 3.9 and 3.10. The interpretation is based on the information derived from the subsurface geology in figures 2.10 and 2.16 as well as figure 2.2.

A three-layer model for the subsurface is consequently deduced from the same models in figures 3.12, 3.13, and 3.14. The first layer has a depth range of 5–7 m; it houses the alluvial and colluvial materials, which contain buried cultural materials dated to the period of the site occupation by the Gallo-Romans. The permeable, saturated sections of the first layer, in hydrogeological terms, constitutes the near-surface aquifer top.

The results in figures 3.8 and 3.12 laid to rest the idea put forward by the archaeologists during the 2019 and 2020 excavation campaigns (e.g. Barrière, 2021), of a possible existence of building walls buried in the rubble of a previous building uncovered in 2016 in the *Open Aire* zone. The idea prompted successive archaeological activities at this location, reaching less than two meters (< 2 m) in depth. From the ERT sections, there is no feature with a range of resistivity values corresponding to a resistive structure with a spatial extent that can represent either a wall structure or a building foundation. The ERT is a viable tool for scientific archaeological expeditions, as seen in the sections. The investigations can now focus on reconstructing the recovered items and linking their spatial extent with cultural information.

The second modeled layer from the ERT section of figures 3.9 and 3.13 provided the geometric parameters for defining the foundation of the theater. From there, the depth of the ruin reached 2.5 m at the lower section of the *Cavea* and a bout 4 m at the upper section. The delineated depths will be a useful guide for the archaeological community in planning and executing related activities. The second layer is estimated to be about 4 - 5 m thick and consists of colluvium, and other rock sequences and historical or cultural materials. It is a tool for reconstruction, as the tomo model of the area beneath the theatre can be compared with the situation in the field and missing or broken parts can be replaced at the exact location.

The model of the subsurface structure beneath profile P_2 (Figures 3.9 and 3.13) also gives credence to the saturated near-surface beds in Figures 3.12 and 3.13 and supports human activities within 2 m depths other than buildings or structures housing humans. The *Open Aire* zone and the paved road used as access to the temple building from the eastern section have shown variable contrast in the resistivity values with depths not exceeding 2 m, which support human activities in the cen-

tral part of the site at a less invasive scale.

At the base of the ERT model (P_2) is a very conductive interface 10 - 12 m from the surface. From geological information, e.g., see BURGEAP (1992); de Lamotte et al. (2022); Garnier and Dessevre (2004); Garnier (2004); Garnier and Lemaire (2006), the *Cuisian* sand is the main aquifer and constitutes the groundwater reservoir. Similarly, from the geological information in figures 2.3, 2.10 and 2.16. This conductive bed is interpreted as a water-saturated sequences of geological layers. The layers, according to the geological information, are at the top of the *Sparnacian* clay with sands from the Cuisian beds. The sands are porous; hence, the bed can retain water within the sequences. This will give a conductive response to the ERT method. This explains the observed low resistivity values in the ERT section at P_2. From this inference, the conductive is interpreted as the **aquifer** bed.

Using information from field observations, subsurface geology of the site, and the ERT models (e.g., Figures 2.10, 2.16, 3.9, and 3.13), the tomographic model delineates the aquifer body 10 - 12 m below the surface. Hence, at the site (Les Vaux de la Celle), the aquifer base is located at the *Cuisian* sand-*Sparnacian* clay interface. The conductive layers and sections in the ERT models suggest saturation. This means the aquifer extends from the top of the *Sparnacian* clay bed to the near-surface. From the lithology log and subsurface geological information (Figures 2.10 and 2.16), the geological materials at this point of the sand-clay interface in the subsurface to the near-surface include mainly sands, colluvial materials, and silts. As explained in the previous section, these are mainly porous media capable of receiving, storing, and releasing water from their pore spaces.

6.1.3 Semblance models and spatial connectivity of saturated beds

The theory of wavelet-based semblance is presented in subsection 5.2.1.2, and the resulting models are described in subsection 5.4.2 and discussed in section 5.5.

The wavelet-based semblance analysis investigated the water pressure by comparing two data sets using their phase components extracted from continuous wavelet transform CWT. By comparing the phase behavior of the data (signals), the response to the same inducement can be constrained in time and frequency. This approach compares the hydrostratigraphic relationship (via spatial connectivity) between aquifer units using water pressure data. The phase correlation is positive if the water pressure are spatially connected via the same saturated, permeable source. And would

imply the water pressures' homogeneous response in time.

Hence, it can be hypothesized that spatial connectivity entails similarity in phase response and is interpreted as the absence of a vertically impervious layer. The models produced in figures 5.15, 5.16 and 5.17 showed more areas correlated both in time and frequency with positive events. Areas where the correlation was not recorded are minimal. Likewise, out-of-phase events are sparsely distributed. The phase correlations offer a more meaningful alignment of two signals to the same source and response frame to the same stimuli. Compare this hypothesis with figures 5.13 and 5.14. After removing barometric and Earth tide influences, the water was largely uncorrelated (negative correlation) with water from the same source. An explanation can be advanced: the water levels at the archaeological site are faced with inducements that cause them to fluctuate. The dominant inducements are the barometric and Earth tide effects. According to the literature, the fluctuations affect the hydrostatic equilibrium of the subsurface and can hasten the deterioration of the buried materials.

The models from this thesis compare with similar models of relationships established between two data sets impacted by the same agent of change (forcing) or spatial heterogeneity. Cooper and Cowan (2008) applied the semblance method on gravity and pseudo gravity over the Vrededfort dome impact structure and Witwatersrand basin to show where and the scales on which the remnant magnetization exists. This was achieved at a wavelength of 125–150 km.

The comparison using phase is different from the visual inspections method, which compares trends and patterns, or the cross-correlations, which compare cause and effect, or strength of response (Box and Jenkins, 1976; Box et al., 2015; Larocque et al., 1998; von Frese et al., 1997; Wang et al., 2023). Other methods include the frequency method, which assumes the data must not change with time or location (Cooper, 2009), or comparing the amplitude of spikes (Acworth et al., 2016; Bloomfield, 2013; Cooley and Tukey, 1965; Neto et al., 2016; Swarztrauber, 1982; Turnadge et al., 2019). The phase-based method compares two data sets as a function of frequency (Fawazi et al., 2023; Saavedra and Bougrain, 2013a,b). The model has applications in many fields. For example, bond yield and stock values (Verner and Herbrik, 2017), two different geophysical (spatial) data (Cooper and Cowan, 2008), and this thesis (water pressure data). From the semblance analysis of water pressure, it can be inferred that the aquifer units in the site are spatially connected, hence the dominance of the strongly correlated events, indicating a simultaneous response to the same stimuli or inducements.

6.1.4 Model of aquifer responses from singular spectrum analysis

Periodicity is an important type of information in hydrological signals and is mainly caused by Earth's revolution and rotation, geological processes, human activities, and other physical factors (Kottegoda, 1980; Rosenquist et al., 2010; Xie et al., 2021). Various tools have evolved for studying periodicity in signals and time series data, particularly hydrological data. The extraction of periodic events from borehole water levels or water pressure data usually involves the classic Fourier transform, harmonic analysis for tidal response models, and other frequency domain methods (Bloomfield, 2013; Lyon, 2009; Machiwal and Jha, 2006; Marques et al., 2006; Swarztrauber, 1982). The outcome of the transform is usually a spectrum of amplitudes with the corresponding frequencies. This has over the years allowed the spikes or peaks with corresponding frequencies as components to be extracted and identified with known physical events (Bloomfield, 2013; Vautard et al., 1992).

The idea behind data decomposition is to conceptualize a signal as a composite of many stimuli, each with its specific characteristics. A signal consists of periodic and non-periodic components (Golyandina and Zhigljavsky, 2013; Hassani, 2022; Schoellhamer, 2001; Zhigljavsky, 2010). It is the record of the responses to inputs and changes. In the same manner, changes in groundwater levels are representative of the different natural and anthropogenic events and factors causing the fluctuations. By decomposing the data, we can extract a particular event and study its characteristics and influence in terms of its amplitude and period. This study, like others who have applied the SSA method to decompose a signal into components (e.g. see Arora et al., 2017; Kong et al., 2023; Tomé et al., 2018). The objective here emphasizes the ability of the SSA to isolate an event, influence, or natural phenomenon into individual components in the composite data.

The objective sought was achieved because, first, the data was decomposed into components based on the period, and second, the events were isolated, allowing the variability of the amplitude to be modeled in both the frequency and time domains. This feat is difficult to actualize with the traditional Fourier transform, which produces a spectrum of the data with peaks identified with corresponding frequencies to represent an event.

6.1.5 Estimation of aquifer properties

This study used three methods to assess the response of groundwater levels and evaluate the properties of the subsurface and aquifer using passively acquired water pressures (chapter 5). Two of

these methods are not among the classic methods used for groundwater level analysis but were used in this study for a new approach: wavelet-based semblance analysis and singular spectrum analysis. From the classic Fourier transform, the amplitude and phase of the main components (subsections 5.2.3 and appendix F.6). The amplitude and phase of each extracted harmonic component are documented in tables A.15, A.16 and A.17 (of appendix G.7) for the water pressure data and table A.18 (of appendix G.7) for the Earth tide strain.

The phase, θ computed from equation 5.25, represents a lag or lead between the forcing and the water levels. By convention, $\theta < 0$ is a phase lag, and $\theta > 0$ is a lead (Agnew, 2005). The difference between the phase of a tidal component in the water pressure θ^{WP} and its corresponding component in the Earth tide strain θ^{ET} is estimated as the phase shift. The computed phase shift, $\theta^{WP} - \theta^{ET}$, for each tidal component is documented in tables A.19, A.20 and A.21 of appendix G.7.

Hsieh et al. (1987) presented a model equation for phase shift as a function of the time needed for the water to move in and out of the well. The method of considering phase difference hinges on the aquifer hydraulic properties of diffusivity, transmissivity, and storage coefficient (Cooper Jr. et al., 1965; Gao et al., 2020; Gieske and De Vries, 1985). It conceptualizes time lag as negative and time lead as positive to assess the relative difference between a response or disturbance tidal component and the corresponding harmonic component around a phase value (Gao et al., 2020; Zhang et al., 2023). The time factor concept differs from the idea expressed by Gao et al. (2020) who sees phase shift as the response of an aquifer whose surfaces are bound by a rigid bed to compression. Fluctuations in the tidal amplitude and phase shift induce changes in the hydraulic properties. Variations in phase shifts are related to permeability changes (Gao et al., 2020; Zhang et al., 2023). Small phase shifts are attributed to higher permeability, while large phase differences are related to low permeability. The response amplitude is attributed to the aquifer's compressibility properties, and thus to its water saturation state.

6.1.6 Aquifer confinement type

In the tidal response models in figures 5.46, 5.47 and 5.48 produced from the DFT of the waters in wells (boreholes) PzTh, PzShf, and PzSa (Figure 6.3). The S_2 and K_1 tidal components are the expressions of the periodic events in the waters. Additional responses from the interaction of the solar tides were observed by the presence of shallow tides, mainly S_3 and S_4 components. No response was observed for the O_1, and N_2 tidal components. A small response M_2 was seen in

figure 5.46.

The absence of O_1 and N_2 was equally observed by Turnadge et al. (2019) in the spectrum of water from three wells in the Peel aquifer region (Superficial, Rockingham, and Leederville). The M_2 Earth tide component was also not seen in the tidal response models in figures 5.47 and 5.48, except for the model in figure 5.46. It can be concluded that all five tidal components considered important for groundwater studies may not be present in some environments (Table 5.1). Hence, the implication for the present or absence of M_2 is related to the confinement conditions. Relatively large amplitudes of M_2 are a marker for the semi-confinement or confined conditions in a vicinity. The inference was drawn from the assessment model and earlier discussion in subsection 5.4.6.

In literature, the groundwater confinement status of an aquifer is discussed concerning its exposure to atmospheric conditions (existence of vertical flow) and its spatial variability (Acworth et al., 2016; Gao et al., 2020; Turnadge et al., 2019; Wang et al., 2018, 2019). The aquifer confinement types were identified in subsection 5.4.6 using the tidal response models outlined by Rahi and Halihan (2013).

The DFT method is a robust approach for assessing the spatial and temporal variability of the confinement in aquifer (Turnadge et al., 2019). In the aquifer confinement models by Rahi and Halihan (2013) applied by Turnadge et al. (2019) and other researchers, the amplitude of M_2 tidal component was a key factor in some of the references mentioned, while in this research, the amplitudes of S_2 and K_1 tidal components were the key inputs for assessing the confinement types at the site. The aquifer confinement aquifer deduced is unconfined to semi-confined for the site from the dominance of S_2 and K_1 tidal components.

The implications for recharge in an unconfined aquifer setting include that recharge can occur from downward seepage through the unsaturated zone, through lateral groundwater flow, or upward seepage from the underlying strata (Domenico and Schwartz, 1998; Fetter, 2001). Therefore, the DFT method for examining data for tidal components is cost-effective and valuable for assessing aquifer thickness and areas of aquifer leakage. From the confinement type identification models, the characteristics of the bed overlying the aquifer can be inferred. In unconfined (with variability to semi-confined) conditions, the beds overlying the aquifer medium are relatively permeable and close to the land surface.

CHAPTER 7

General conclusion, perspectives and recommendations

7.1 General conclusion

The pilot site of Genainville combined natural phenomenon of geological and hydrogeological interests expressed by the hydraulic behavior of the aquifer with the onsite human-engineered materials and crafts contained in the building structures and buried artifacts. Hence, there is a need for non-destructive, passive assessments for its preservation. The site presents a suitable location for testing geophysical and geological methods and models that will further advance archaeological and heritage site preservation in addition to geophysical and geological studies.

From the ERT models, some generalized inferences are plausible. First, the upper or near-surface layers show variations in resistivity values, implying a bed with mixed materials, including cultural objects, lined surfaces, and variable geological sequences. Secondly, the near-surface bed has a variable thickness of 5 - 7 m and consists of loose and porous materials with the potential to store and transmit fluid. This bed is directly in contact with the artifacts in the subsurface and the regional (*Cuisian*) aquifer.

In the light of the ongoing variability in climate and environmental conditions associated with events such as prolonged rainfall and flooding, the beds would become readily saturated and hold water longer before draining, thereby exposing the buried cultural items to conditions different from it usual stable state and increase their susceptibility to destruction.

With the increasing impact of the global climate change conditions, extreme events such as prolonged and intense rains, more water is expected to be held in the subsurface pores and voids, this will tend to increase the weathering state and also increase the thickness of the weathered column. Hence, the site would inevitably be confronted with the need for mitigation measures to curtail impacts or menaces from the likelihood of rising water levels and flooding events (Abboud et al., 2018; Cobby et al., 2009).

Tidal phenomena at the site are expected to cause fluctuations in the water levels at amplitudes corresponding to the tidal energy and periodically at the frequency of prevalence of the main components. These components (obtained from the DFT) are the semi-diurnal S_2 and the diurnal K_1. The semi-diurnal events are expected to dominate the drivers of fluctuations, going by the value obtained from the model form ratio equation.

The semblance method assesses the phase behavior of a two-time series for similarities or differences. It is a comparison of two data sets using their phase values. For the semblance analysis, two types of data sets were used. The first was filtered from barometric pressure and Earth tides, while the second was the raw data directly recorded in the field. The semblance effect is much more pronounced in the unfiltered data when compared to the filtered data.

From the response of the data, the correlation can identify periods when both water levels respond to field inputs or influences and periods when the fluid behaves differently. The semblance models suggest the response of the fluids in the boreholes is in phase. Hence, the aquifer at the site is hypothesized as a body of laterally connected medium that is neither separated nor compartmentalized by an impervious unit of materials. In any case, the spatial-geometric structure of the aquifer is yet to be fully recognized or mapped.

The semblance effect is more readily evaluated with short-series data than long-series data to emphasize seasonal or monthly events.

The general inference from this analysis suggests homogeneous sequences at the levels of the installed boreholes and spatially connected flow structures that enable fluid interactions. The strong and positive correlation aligned this view with observed similarity in response patterns over the time series.

From the spatial and temporal alignment of the semblance anomalies, the response to stress and strain by the aquifer medium in the CWT models suggests some differences in both model struc-

tures. From this, it can be inferred that there is a localized difference in the hydraulic or physical properties of the lithology. Generally, the response structure in the semblance models gives credence to the same aquifer medium undergoing the same natural and or anthropogenic variability. This study has shown that two borehole water levels, water pressures, or hydro-meteorological series can be investigated for semblance relationships.

The SSA as a data decomposition method is introduced to explore its property of separateability. After decomposing a signal into components, the next goal is to display the amplitude of a signal component as it varies in time. With the SSA, the different factors and drivers of the changes in the data (groundwater levels, temperatures, etc.) can be isolated based on their period (frequency).

The SSA method produces a trend that represents the long-term (annual, seasonal, monthly) pattern of the data, the oscillating components (events, drivers of changes), and a residual. The oscillating components represent the response, e.g., of the water levels to the drivers of its fluctuations. Each oscillating component was modeled in the time and frequency domains. The SSA has the added benefit of enabling signal decomposition and separation into individual events. Various events recorded in the groundwater time series are decomposed into one or more components based on their constituent frequencies. This refinement is a kind of approach that allows an oscillation to be identified and graphed. The period of each wave, oscillation, or event is readily extracted and related to an astronomical event, seasonality, or a human-induced phenomenon.

In the frequency domain, the signal's amplitude was graphed with the period to show how it changes during impact. The maximum period attained by the oscillation is computed, extracted, and used to identify a phenomenon.

The residual component contains different signals and drivers. In the measured water pressure data, the residual component also contains an amplitude with a period of 0.5 days, which is herein interpreted as the signature of a semi-diurnal tide.

The SSA method, unlike the traditional Fourier transform, permits each driver, stress, or influence to be individually identified based on the parameter of the period. This introduction also accounts for different long-term and short-term factors influencing the water pressures.

Traditionally, the Fourier transform herein implemented in its discrete form, or discrete Fourier transform (DFT), results in a spectrum with peaks corresponding to a frequency interpreted as events, inputs, and forcings. In DFT, the outcome or amplitude of the signals is not resolved in

time. The lack of time resolution in the Fourier transform is solved in the SSA as the individual signals can be extracted from the signal and expressed in both time and frequency domains. With SSA, a signal's amplitude is visualized as it varies.

In the study, the advantage offered by natural, periodic forcings was exploited to passively characterize the hydro-geo-mechanical properties of the subsurface without perturbing the environment with pumping or injection, and during long term period.

Periodic signals in the groundwater were identified using the discrete Fourier transform method, from which the diurnal and semi-diurnal components were extracted. The amplitude ratios of the tidal components were computed and associated with poroelastic relations to derive properties of the subsurface sequence. The confinement status was evaluated as largely unconfined, with variability in semi-confined conditions. The aquifer-specific storage and porosity were estimated. It can be deduced from the plots or models produced from the semblance analysis, that the aquifer layer at the site is spatially connected, implying no impervious bed separates or acts as a barrier to fluid flow. Separatability of the signals in the aquifer was achieved with SSA, which permits the different behaviors of the aquifer to be monitored over time.

7.2 Perspectives

In this study, the aquifer and its properties have been studied using 2D ERT and poroelastic relations, assuming a 1D (vertical) direction of variation. The study using 1D poroealstic relationships can be extended to 2D and 3D, which should reflect the Earth's structure. Thus, it is worth verifying the physical parameters of the aquifer with 2D and 3D models using ERT and electromagnetic methods.

The feature imaged and mapped in the section beneath ERT profile P_3, as the ancient Gallo-Roman road and parts of the sacred area, can be investigated with modern dating tools to derive archaeological and cultural information for documentation and also studied to ascertain the type of construction materials used.

The SP measurements were inspected for changes in amplitudes before the pumping test (background SP monitoring) and during the pumping test (active SP monitoring). As earlier reported, the magnitude of the observed SP response did not show appreciable changes in the background or active SP values to ensure anomalies and therefore motivate further hydrogeological studies. To

perturb the natural electric field and stimulate subsurface water flow at a higher frequency. The pumping rate can be increased using a submersible pump of higher power to produce different flow rates for comparison. The duration of the pumping should span from hours to days to allow for considerable lowering of the water level. In a classic example, 48 hours of pumping is suggested to achieve or obtain a stable water level before performing the test experiment. Secondly, the density of the electrodes can be increased for a large sample area and dense data sets.

The model poroelastic equations assume a uniaxial, vertical relationship to the aquifer properties (Van Der Kamp and Gale, 1983). This assumption is used to derive most model equations that relate tidal and barometric effects to the aquifer properties. This constraint results only in one (vertical) response direction, without considering the 3-dimensional (3-D) view of the Earth's structure. Models developed in 3D give a broader view of the effects of stress and strain and allow aquifer properties to be assessed in different directions and their variations with time.

The thermal response of the subsurface water and lithology sequence to natural heating and processes, in addition to the other experiments performed, remains to be evaluated for thermal diffusivity and relations with aquifer hydraulic behaviors.

7.3 Recommendations

This historic site is proposed and presented to the scientific community as a location suitable for testing new and known methods and models that have been considered, developed, or hypothesized for application to explain the complex relationships at the site.

The groundwater temperature time series acquired with the water pressure data were not analyzed due to time constraints. It is imperative to study the data using modern and established methods to derive information that would relate the hydrothermal properties of the waters to flow and environmental conditions.

Some parameters, such as the natural spontaneous potential field response, induced polarization structure, and thermal characteristics of the subsurface, are opportunities for testing the much-talked-about new models with other non-destructive methods. For future studies, the temperature and thermal datasets should be revisited to quantitatively assess the thermo-hydrological response of the sequences as well as their impact on the cultural materials.

Parameters such as Skempton's coefficient can be used to monitor the state of saturation of the subsurface. Therefore, the steps used to derive the parameter in this thesis can be followed to non-invasively assess the state of saturation of the subsurface sequence, that is, the groundwater level at the site. It is therefore recommended that a monitoring scheme be implemented to assess the Skempton parameter at regular intervals.

Bibliography

J.M. Abboud, M.C. Ryan, and G.D. Osborn. Groundwater flooding in a river-connected alluvial aquifer. *Journal of Flood Risk Management*, 11(4):e12334, 2018. doi: https://doi.org/10.1111/jfr3.12334. URL https://onlinelibrary.wiley.com/doi/abs/10.1111/jfr3.12334.

ACIA. *Impacts of a Warming Arctic: Arctic Climate Impact Assessment*. Cambridge University Press, 2004. ACIA Overview report.

R. Ian Acworth, Landon J. S. Halloran, Gabriel C. Rau, Mark O. Cuthbert, and Tony L. Bernardi. An objective frequency domain method for quantifying confined aquifer compressible storage using earth and atmospheric tides. *Geophysical Research Letters*, 43(22):11,671–11,678, 2016. doi: https://doi.org/10.1002/2016GL071328. URL https://agupubs.onlinelibrary.wiley.com/doi/abs/10.1002/2016GL071328.

D. C. Agnew. Earth tides: An introduction. https://www.unavco.org/education/professional-development/short-courses/course-materials/strainmeter/2005-strainmeter-course-materials/tidenote.pdf, 2005. Accessed online: 19 February 2024.

V. Allègre, A. Maineult, F. Lehmann, F. Lopes, and M. Zamora. Self-potential response to drainage–imbibition cycles. *Geophysical Journal International*, 197(3):1410–1424, June 2014. ISSN 0956-540X. doi: 10.1093/gji/ggu055. URL https://academic.oup.com/gji/article/197/3/1410/653424. Publisher: Oxford Academic.

M. M. Amin. The effect of underground water on heritage sites (a case study on graeco-roman

cemeteries in alexandria). *Journal of Association of Arab Universities for Tourism and Hospitality*, 14(1):65 – 78, 2017. ISSN 1687-1863. doi: 10.21608/jaauth.2017.50037. URL https://jaauth.journals.ekb.eg/article_50037.html.

P. V. N. Araújo, V. E. Amaro, L. S. Aguiar, C. C. Lima, and A. B. Lopes. Tidal flood area mapping in the face of climate change scenarios: case study in a tropical estuary in the brazilian semi-arid region. *Natural Hazards and Earth System Sciences*, 21(11):3353–3366, 2021. doi: 10.5194/nhess-21-3353-2021. URL https://nhess.copernicus.org/articles/21/3353/2021/.

R. Arjwech, P. Sriwangpon, K. Somchat, P. Pondthai, and M. Everett. Electrical resistivity tomography (ert) data for clay mineral mapping. *Data in Brief*, 30:105494, 2020. ISSN 2352-3409. doi: https://doi.org/10.1016/j.dib.2020.105494. URL https://www.sciencedirect.com/science/article/pii/S2352340920303887.

B. R. Arora, Arvind Kumar, Vivek Walia, Tsanyao Frank Yang, Ching-Chou Fu, Tsung-Kwei Liu, Kuo-Liang Wen, and Cheng-Hong Chen. Assesment of the response of the meteorological/hydrological parameters on the soil gas radon emission at hsinchu, northern taiwan: A prerequisite to identify earthquake precursors. *Journal of Asian Earth Sciences*, 149:49–63, 2017. ISSN 1367-9120. doi: https://doi.org/10.1016/j.jseaes.2017.06.033. URL https://www.sciencedirect.com/science/article/pii/S1367912017303437. Tectonics, Volcanism and Geo-energy in East Asia.

E. R. Atwood. Preserving the Taj Mahal: India's struggle to salvage cultural icons in the wake of industrialization. *Penn St. Envtl. L. Rev. 101*, 11(1), 2002.

J. Ballester, M. Quijal-Zamorano, R. F. Méndez Turrubiates, F. Pegenaute, F. R. Herrmann, J. M. Robine, X. Basagaña, C. Tonne, J. M. Antó, and H. Achebak. Heat-related mortality in Europe during the summer of 2022. *Nature Medicine*, 29(7):1857–1866, July 2023. ISSN 1546-170X. doi: 10.1038/s41591-023-02419-z. URL https://doi.org/10.1038/s41591-023-02419-z.

P. Barone and C. Ferrara. Non-invasive moisture detection for the preservation of cultural heritage. *Heritage*, 1(1):163–170, August 2018.

V. Barrière. Genainville - Vaux-de-la-Celle: fouille programmée (2018). *Archéologie de la France - Informations [En ligne]*, 2018. URL https://journals.openedition.org/adlfi/112382. mise en ligne le 26 novembre 2021, consulté le 17 novembre 2023.

V. Barrière. Fouilles archéologiques à Genainville (2019-2020). quand des moutons redessinent l'histoire du site gallo-romain. *Amis du Vexin français*, 76, May 2021. URL https://hal.science/hal-03218555.

V. Barrière and D. Vermeersch. La construction monumentale sur le site des "Vaux de la Celle"à Genainville (Val d'Oise). In *A la romaine ! Résidence privée, construction publique en Gaule du nord* , pages p. 115–118. 2016. URL https://hal.science/hal-01670985.

V. Barrière et al. *Les Vaux-de-la-Celle: Un Aventure Archéologique*. Privat Patrimoine, Toulouse, France, 2019.

V. Barrière. Le site antique des Vaux-de-la-Celle à Genainville. *Amis du Vexin français*, 75:22–33, 2020. https://hal.science/hal-03154057.

J. Beer and A. Seither. Groundwater and cultural heritage. *Quaternary International*, 368:1–4, May 2015. doi: 10.1016/j.quaint.2015.04.025.

P. Bloomfield. *Fourier analysis of time series: An introduction*. John Wiley & Sons, Inc., United States, second edition, 2013.

A. Bonazza and A. Sardella. Climate change and cultural heritage: Methods and approaches for damage and risk assessment addressed to a practical application. *Heritage*, 6(4):3578–3589, 2023. ISSN 2571-9408. doi: 10.3390/heritage6040190. URL https://www.mdpi.com/2571-9408/6/4/190.

G. E. P. Box and G. M. Jenkins. *Time Series Analysis: Forecasting and Control*. Holden-Day series in time series analysis and digital processing. Holden-Day, 1976. ISBN 9780816211043. URL https://books.google.fr/books?id=1WVHAAAAMAAJ.

G. E. P. Box, G. M. Jenkins, G. C. Reinsel, and G. M. Ljung. *Time series analysis: forecasting and control*. John Wiley & Sons, 2015.

John D. Bredehoeft. Response of well-aquifer systems to earth tides. *Journal of Geophysical Research (1896-1977)*, 72(12):3075–3087, 1967. doi: https://doi.org/10.1029/JZ072i012p03075. URL https://agupubs.onlinelibrary.wiley.com/doi/abs/10.1029/JZ072i012p03075.

E. Bresciani, R. N. Shandilya, P. K. Kang, and S. Lee. Well radius of influence and radius of investigation: What exactly are they and how to estimate them? *Journal of Hydrology*, 583:

124646, 2020. ISSN 0022-1694. doi: https://doi.org/10.1016/j.jhydrol.2020.124646. URL https://www.sciencedirect.com/science/article/pii/S0022169420301062.

P. J. Brockwell and R. A. Davis. *Introduction to Time Series and Forecasting*. Springer, Switzerland, third edition, 2016.

V. Brunet-Gaston. Décor baroque ou perspective illusoire : le complexe « théâtre et temple » de Genainville (Val d'Oise)1. *Études lett.*, (1-2):119–128, May 2011.

A. Bucci, M. Lasagna, D. A. De Luca, F. Acquaotta, D. Barbero, and S. Fratianni. Time series analysis of underground temperature and evaluation of thermal properties in a test site of the po plain (nw italy). *Environmental Earth Sciences*, 79(185), 2020. URL https://doi.org/10.1007/s12665-020-08920-9.

BURGEAP. Hydrogeological study of the archaeological site at genaainville. Technical Report BUREAP Group Report N° 1169, Genainville, France, 1992.

J. Cao, B. Mai, H. Chen, Y. Li, and J. Wang. Investigation and analysis of groundwater-derived damage to the shahe ancient bridge site in xi'an, china. *Heritage Science*, 9(99), 2021. URL https://doi.org/10.1186/s40494-021-00573-6.

W. Carruthers. How egypt's aswan dam washed away nubian heritage. 2023. https://newlinesmag.com/essays/how-egypts-aswan-dam-washed-away-nubian-heritage/, accessed online: 14 December, 2023.

K. Cartwright. Tracing shallow groundwater systems by soil temperatures. *Water Resources Research*, 10(4):847–855, 1974. doi: https://doi.org/10.1029/WR010i004p00847. URL https://agupubs.onlinelibrary.wiley.com/doi/abs/10.1029/WR010i004p00847.

S. W. Chang, S. S. Memari, and T. P. Clement. PyTheis—a python tool for analyzing pump test data. *Water*, 13(16), 2021. ISSN 2073-4441. doi: 10.3390/w13162180. URL https://www.mdpi.com/2073-4441/13/16/2180.

F. Chen, H. Guo, P. Ma, H. Lin, C. Wang, N. Ishwaran, and P. Hang. Radar interferometry offers new insights into threats to the angkor site. *Science Advances*, 3(3):e1601284, 2017. doi: 10.1126/sciadv.1601284. URL https://www.science.org/doi/abs/10.1126/sciadv.1601284.

Jin Chen, Per. Jönsson, Masayuki Tamura, Zhihui Gu, Bunkei Matsushita, and Lars Eklundh. A simple method for reconstructing a high-quality ndvi time-series data set based on the savitzky–golay filter. *Remote Sensing of Environment*, 91(3):332–344, 2004. ISSN 0034-4257. doi: https://doi.org/10.1016/j.rse.2004.03.014. URL https://www.sciencedirect.com/science/article/pii/S003442570400080X.

R. Chmielewski and P. Muzolf. Selected problems of protection of historic buildings against the rainwater and the groundwater. *MATEC Web of Conferences*, 174:03012, 01 2018. doi: 10.1051/matecconf/201817403012.

L. Cholet and X. Delestre. Le Sanctuarie Gallo-Romaines de Genainville. *Archeologia*, 278(1):54 – 59, 1992. https://doi.org/10.1111/j.1745-6584.2006.00254.x.

L. Cholet, D. Morize, N. Jobelot, and D. Vermeersch. Les habitats situés à l'Oest de l'aire culturelle. In *Céramiques Gallo-romianes du Val-d'Oise*, number 5 in Archéologie en Val-d'Oise, pages 174 – 205. Service départmental d'archéologie du Val-d'Oise, 1996. ISBN 9782907459082.

J.-S. Chou and N.-T. Ngo. Time series analytics using sliding window metaheuristic optimization-based machine learning system for identifying building energy consumption patterns. *Applied Energy*, 177:751–770, 2016. ISSN 0306-2619. doi: https://doi.org/10.1016/j.apenergy.2016.05.074. URL https://www.sciencedirect.com/science/article/pii/S0306261916306717.

J. F. Claerbout and F. Muir. Robust modeling with erratic data. *GEOPHYSICS*, 38(5):826–844, 1973. doi: 10.1190/1.1440378. URL https://doi.org/10.1190/1.1440378.

A. Clark. *Seeing beneath the soil: Prospecting methods in archaeology*. B. T. Batsford Ltd, 1990.

D. Cobby, S. Morris, A. Parkes, and V. Robinson. Groundwater flood risk management: advances towards meeting the requirements of the eu floods directive. *Journal of Flood Risk Management*, 2(2):111–119, 2009. doi: https://doi.org/10.1111/j.1753-318X.2009.01025.x. URL https://onlinelibrary.wiley.com/doi/abs/10.1111/j.1753-318X.2009.01025.x.

J. W. Cooley and J. W. Tukey. An algorithm for the machine calculation of complex fourier series. *Mathematics of computation*, 19(90):297–301, 1965.

G. R. J. Cooper. Wavelet-based semblance filtering. *Comput. Geosci.*, 35(10):1988–1991, oct 2009.

ISSN 0098-3004. doi: 10.1016/j.cageo.2008.10.017. URL https://doi.org/10.1016/j.cageo.2008.10.017.

G. R. J. Cooper and D. R. Cowan. Comparing time series using wavelet-based semblance analysis. *Computers and Geosciences*, 34(2):95–102, 2008. ISSN 0098-3004. doi: https://doi.org/10.1016/j.cageo.2007.03.009. URL https://www.sciencedirect.com/science/article/pii/S0098300407001185.

H. H. Cooper Jr., J. D. Bredehoeft, I. S. Papadopulos, and R. R. Bennett. The response of well-aquifer systems to seismic waves. *Journal of Geophysical Research (1896-1977)*, 70(16): 3915–3926, 1965. doi: https://doi.org/10.1029/JZ070i016p03915. URL https://agupubs.onlinelibrary.wiley.com/doi/abs/10.1029/JZ070i016p03915.

M Coppola, F Di Benedetto, CA Garzonio, E Pecchioni, and AP Santo. Groundwater damages on the historic buildings of cairo: the case of the medieval walls of mokattam limestone. *IOP Conference Series: Materials Science and Engineering*, 949(1):012004, nov 2020. doi: 10.1088/1757-899X/949/1/012004. URL https://dx.doi.org/10.1088/1757-899X/949/1/012004.

P. A. Cutillo and J. D. Bredehoeft. Estimating aquifer properties from the water level response to earth tides. *Groundwater*, 49(4):600–610, 2011. doi: https://doi.org/10.1111/j.1745-6584.2010.00778.x. URL https://ngwa.onlinelibrary.wiley.com/doi/abs/10.1111/j.1745-6584.2010.00778.x.

B. M. Das and K. Sobhan. *Principles of Geotechnical Engineering*. Cengage Learning, United Kingdom, 8th SI edition, 2014.

C. de Groot-Hedlin and S. Constable. Occam's inversion to generate smooth, two-dimensional models from magnetotelluric data. *GEOPHYSICS*, 55(12):1613–1624, 1990. doi: 10.1190/1.1442813. URL https://doi.org/10.1190/1.1442813.

D. Frizon de Lamotte, J. Douçot, A. Frizon de Lamotte, et al. *Curiosités Géologiques du Vexin*. BRGM éditions, 2022.

R. Deiana, G. Leucci, and R. Martorana. New perspectives on geophysics for archaeology: A special issue. *Surv Geophys*, 39:1035–1038, 2018. https://doi.org/10.1007/s10712-018-9500-4.

R. Deiana, G. P. Deidda, E. D. Cusí, P. van Dommelen, and A. Stiglitz. Fdem and ert measurements for archaeological prospections at nuraghe s'urachi (west-central sardinia). *Archaeological Prospection*, 29(1):69–86, 2022. doi: https://doi.org/10.1002/arp.1838. URL https://onlinelibrary.wiley.com/doi/abs/10.1002/arp.1838.

C. Deng. Time series decomposition using singular spectrum analysis. Master's thesis, East Tennesse State University, March 2014.

E. Detournay and A.H-D. Cheng. Poroelastic response of a borehole in a non-hydrostatic stress field. *International Journal of Rock Mechanics and Mining Sciences & Geomechanics Abstracts*, 25(3):171–182, 1988. ISSN 0148-9062. doi: https://doi.org/10.1016/0148-9062(88)92299-1. URL https://www.sciencedirect.com/science/article/pii/0148906288922991.

M.-L. Doan, E. E. Brodsky, R. Prioul, and C. Signer. Tidal analysis of borehole pressure: A tutorial. Schlumberger-Doll Research Report, 2008. URL https://www.isterre.fr/IMG/pdf/tidal_tutorial_SDR.pdf.

M.-L. Doan, E. E. Brodsky, R. Prioul, and C. Signer. Tidal analysis of borehole pressure a tutorial. 2006. URL https://api.semanticscholar.org/CorpusID:131382647.

P. A. Domenico and F. W. Schwartz. *Physical and Chemical Hydrogeology*. John Wiley and Sons, Inc., New York, United States of America, second edition, 1998.

B. Ducarme, A. P. Venedikov, J. Arnoso, and R. Vieira. Analysis and prediction of ocean tides by the computer program vav. *Journal of Geodynamics*, 41(1-3):119–127, 2006.

H. Dunleavy. Ice dam bursts theaten to increase sunny day floods as hotter temperatures melt glaciers. InsideClimate News, 2021. URL https://insideclimatenews.org/news/03072021/ice-dam-glaciers-sunny-day-floods-alaska/. Date accessed: 27-11-2023.

P. J. Edwards, K. W.J. Williard, and J. E. Schoonover. Fundamentals of watershed hydrology. *Journal of Contemporary Water Research & Education*, 154(1):3–20, 2015. doi: https://doi.org/10.1111/j.1936-704X.2015.03185.x. URL https://onlinelibrary.wiley.com/doi/abs/10.1111/j.1936-704X.2015.03185.x.

M. I. Epov and M. A. Chemyakina. Geophysical methods in the research of archaeological sites in Western Siberia and Altai: results and perspectives. *ArcheoSciences. Revue d'archéométrie*,

(33 (suppl.)):271–274, October 2009. ISSN 1960-1360. doi: 10.4000/archeosciences.1682. URL http://journals.openedition.org/archeosciences/1682. ISBN: 9782753509436 Number: 33 (suppl.) Publisher: Presses universitaires de Rennes.

T. Eriksen and N. ur Rehman. Data-driven nonstationary signal decomposition approaches: a comparative analysis. *Scientific Reports*, 13(1):1798, January 2023. ISSN 2045-2322. doi: 10.1038/s41598-023-28390-w. URL https://doi.org/10.1038/s41598-023-28390-w.

N. Fawazi, A. Azraei, W. M. Haziq, and M. Hakimi. Wavelet based semblance analysis for vibration signal monitoring of a dried vacuum pump. *AIP Conference Proceedings*, 2798(1):020026, 07 2023. ISSN 0094-243X. doi: 10.1063/5.0154236. URL https://doi.org/10.1063/5.0154236.

C. W. Fetter. *Applied Hydrogeology*. Pearson Education International, United States of America, fourth edition, 2001.

B. Fores. Geophysique appliquée sur le gallo-romain des Vaux-de-la-Celle, genainville (95). Rapport master 2, Université de Cergy-Pontoise, September 2013.

M. A. Fuentes-Arreazola, J. Ramírez-Hernández, and R. Vázquez-González. Hydrogeological Properties Estimation from Groundwater Level Natural Fluctuations Analysis as a Low-Cost Tool for the Mexicali Valley Aquifer. *Water*, 10(5):586, May 2018. doi: 10.3390/w10050586. URL https://www.mdpi.com/2073-4441/10/5/586. Number: 5 Publisher: Multidisciplinary Digital Publishing Institute.

X. Gao, K. Sato, and R. N. Horne. General solution for tidal behavior in confined and semi-confined aquifers considering skin and wellbore storage effects. *Water Resources Research*, 56(6):e2020WR027195, 2020. doi: https://doi.org/10.1029/2020WR027195. URL https://agupubs.onlinelibrary.wiley.com/doi/abs/10.1029/2020WR027195. e2020WR027195 10.1029/2020WR027195.

C. Garnier and A. Dessevre. Evaluation du risque de non atteinte des objectifs de bon état qualitatif et quantitatif des masses d'eau souterraines du bassin seine normandie. Géologie Hydrogéologie Du Bassin Paris, 2004. Avancées Perspect., 201–219.

F. Garnier. Étude hydrogéologique du site archéologique de genainville et de ses environs. *Mémoire d'Aptitude à la Géologie*, 325, 2004. Institut Géologique Albert-de-Lapparent.

F. Garnier and D. Lemaire. Étude hydrogéologique du site archéologique de Genainville. *Courrier Scientifique du parc naturel régional du Vexin française*, 2:52–58, May 2006.

M. Ghil, M. R. Allen, M. D. Dettinger, K. Ide, D. Kondrashov, M. E. Mann, A. W. Robertson, A. Saunders, Y. Tian, F. Varadi, and P. Yiou. Advanced Spectral Methods for Climatic Time Series. *Reviews of Geophysics*, 40(1):3–1–3–41, 2002. ISSN 1944-9208. doi: https://doi.org/10.1029/2000RG000092. URL https://agupubs.onlinelibrary.wiley.com/doi/abs/10.1029/2000RG000092. _eprint: https://agupubs.onlinelibrary.wiley.com/doi/pdf/10.1029/2000RG000092.

A. Gieske and J.J. De Vries. An analysis of earth-tide-induced groundwater flow in eastern botswana. *Journal of Hydrology*, 82(3):211–232, 1985. ISSN 0022-1694. doi: https://doi.org/10.1016/0022-1694(85)90018-6. URL https://www.sciencedirect.com/science/article/pii/0022169485900186.

N. Golyandina and A. Zhigljavsky. *Singular Spectrum Analysis for Time Series*. Springer, Heidelberg, 2013. URL http://www.springer.com/series/8921.

N. Golyandina, V. Nekrutkin, and A.A. Zhigljavsky. *Analysis of Time Series Structure: SSA and Related Techniques*. Chapman and Hall/CRC, 1st edition, 2001. URL https://doi.org/10.1201/9780367801687.

ESIRIS Group. Etude geotechigue de conception mise en place d'un abri de temple. Technical report, UDAP - Unité Départmentale de l'Architecture et du Patrimoine, Les Vaux de la Celle, Genainville, France, 1992.

T. Guinaldo, A. Voldoire, R. Waldman, S. Saux Picart, and H. Roquet. Response of the sea surface temperature to heatwaves during the france 2022 meteorological summer. *Ocean Science*, 19(3):629–647, 2023. doi: 10.5194/os-19-629-2023. URL https://os.copernicus.org/articles/19/629/2023/.

K. Harper. The Environmental Fall of the Roman Empire. *Daedalus*, 145(2):101–111, 04 2016. ISSN 0011-5266. doi: 10.1162/DAED_a_00380. URL https://doi.org/10.1162/DAED_a_00380.

K. Harper. *The Fate of Rome: Climate, Disease, and the End of an Empire*. Princeton University Press, Princeton, 2018. ISBN 9781400888917. doi: doi:10.1515/9781400888917. URL https://doi.org/10.1515/9781400888917.

C. R. Harris, K. J. Millman, S. J. van der Walt, R. Gommers, P. Virtanen, D. Cournapeau, E. Wieser, J. Taylor, S. Berg, N. J. Smith, R. Kern, M. Picus, S. Hoyer, M. H. van Kerkwijk, M. Brett, Allan Haldane, J. F. del Río, M. Wiebe, P. Peterson, P. Gérard-Marchant, K. Sheppard, T. Reddy, W. Weckesser, H. Abbasi, C. Gohlke, and T. E. Oliphant. Array programming with NumPy. *Nature*, 585(7825):357–362, September 2020. ISSN 1476-4687. doi: 10.1038/s41586-020-2649-2. URL https://doi.org/10.1038/s41586-020-2649-2.

Fekri A. Hassan. The aswan high dam and the international rescue nubia campaign. *The African Archaeological Review*, 24(3/4):73–94, 2007. ISSN 02630338, 15729842. URL http://www.jstor.org/stable/40743449.

H. Hassani. Singular spectrum analysis: Methodology and comparison. *Journal of Data Science*, 5: 239 – 257, 2007.

H. Hassani. Singular spectrum analysis: Methodology and comparison. *Journal of Data Science*, 5 (2):239–257, 2022. ISSN 1680-743X. doi: 10.6339/JDS.2007.05(2).396.

R.W. Healy, T.C. Winter, J.W. LaBaugh, and O.L. Franke. Water budgets: Foundations for effective water- resources and environmental management. *U.S. Geological Survey Circular 1308*, page 90 p, 2007.

D. A. Hepp and T. Terberger. Post-glacial develompent of the climate and prominent climate extremes in the west hemispere, 2023. URL https://nihk.de/fileadmin/_processed_/6/4/csm_Klimakurve-v4-2022-02-15-en_b2b7887454.jpg. [Online; accesed July 27, 2023].

O. R. Hermawan and D. P. E. Putra. The effectiveness of wenner-schlumberger and dipole-dipole array of 2D geoelectrical survey to detect the occurring of groundwater in the gunung kidul karst aquifer system, yogyakarta, indonesia. *Journal of Applied Geology*, 1(2):71–81, 2016. URL https://dx.doi.org/10.22146/jag.26963.

J. Hollesen, H. Matthiesen, A. B. Møller, A. Westergaard-Nielsen, and Bo Elberling. Climate change and the loss of organic archaeological deposits in the Arctic. *Scientific Reports*, 6(1):28690, June 2016. ISSN 2045-2322. doi: 10.1038/srep28690. URL https://doi.org/10.1038/srep28690.

J. Hollesen, M. Callanan, T. Dawson, R. Fenger-Nielsen, T. Friesen, A. Jensen, A. Markham, V. Martens, V. Pitulko, and M. Rockman. Climate change and the deteriorating archaeo-

logical and environmental archives of the arctic. *Antiquity*, 92(363):573–586, 06 2018. doi: 10.15184/aqy.2018.8.

I. P. Holman, D. M. Allen, M. O. Cuthbert, and P. Goderniaux. Towards best practice for assessing the impacts of climate change on groundwater. *Hydrogeology Journal*, 20:1–4, 02 2012. doi: 10.1007/s10040-011-0805-3.

P. A. Hsieh, J. D. Bredehoeft, and J. M. Farr. Determination of aquifer transmissivity from earth tide analysis. *Water Resources Research*, 23(10):1824–1832, 1987. doi: https://doi.org/10.1029/WR023i010p01824. URL https://agupubs.onlinelibrary.wiley.com/doi/abs/10.1029/WR023i010p01824.

P. A. Hsieh, J. D. Bredehoeft, and S. A. Rojstaczer. Response of well aquifer systems to Earth tides: Problem revisited. *Water Resources Research*, 24(3):468–472, 1988. ISSN 1944-7973. doi: https://doi.org/10.1029/WR024i003p00468. URL https://agupubs.onlinelibrary.wiley.com/doi/abs/10.1029/WR024i003p00468. _eprint: https://agupubs.onlinelibrary.wiley.com/doi/pdf/10.1029/WR024i003p00468.

C. E. Jacob. On the flow of water in an elastic artesian aquifer. *Eos, Transactions American Geophysical Union*, 21(2):574–586, 1940. doi: https://doi.org/10.1029/TR021i002p00574. URL https://agupubs.onlinelibrary.wiley.com/doi/abs/10.1029/TR021i002p00574.

W. Jia, L. Yin, M. Zhang, X. Zhang, J. Zhang, X. Tang, and J. Dong. Quantification of groundwater recharge and evapotranspiration along a semi-arid wetland transect using diurnal water table fluctuations. *Journal of Arid Land*, 13(5):455, 2021. doi: 10.1007/s40333-021-0100-7. URL http://jal.xjegi.com/EN/abstract/article_772.shtml.

M. Jing, R. Kumar, F. Heße, S. Thober, O. Rakovec, L. Samaniego, and S. Attinger. Assessing the response of groundwater quantity and travel time distribution to 1.5, 2, and 3 °c global warming in a mesoscale central german basin. *Hydrology and Earth System Sciences*, 24(3):1511–1526, 2020. doi: 10.5194/hess-24-1511-2020. URL https://hess.copernicus.org/articles/24/1511/2020/.

R. Jörg and M. Mareike. Periodic pumping tests. *Geophysical Journal International*, 167(1):479–493, 10 2006. ISSN 0956-540X. doi: 10.1111/j.1365-246X.2006.02984.x. URL https://doi.org/10.1111/j.1365-246X.2006.02984.x.

M. Karegar, T. Dixon, R. Malservisi, J. Kusche, and S. Engelhart. Nuisance flooding and relative sea-level rise: The importance of present-day land motion. *Scientific Reports*, 7, 09 2017. doi: 10.1038/s41598-017-11544-y.

T. R. Karl, V. E. Derr, et al. Critical issues for long-term climate monitoring. *Climatic Change*, 31: 185 – 221, 1995.

P. Keary, M. Brooks, and I. Hill. *An Introduction to Geophysical Exploration*. Blackwell Science Ltd, United Kingdom, 2002.

H.-J Kümpel. Poroelasticity: Parameters reviewed. *Geophysical Journal International*, 105:783–799, 06 1991. doi: 10.1111/j.1365-246X.1991.tb00813.x.

H.-J Kümpel, G. Grecksch, Klaus Lehmann, Dorothee Rebscher, and K. Schulze. Studies of in situ pore pressure fluctuations at various scales. *Oil & Gas Science and Technology-revue De L Institut Francais Du Petrole - OIL GAS SCI TECHNOL*, 54:679–688, 11 1999. doi: 10.2516/ogst:1999057.

C. Kneisel and C. Hauck. Electrical methods. In C. Hauck and C. Kneisel, editors, *Applied Geophysics in Periglacial Environments*, pages 1–248. Cambridge Univeristy Press, New york, 01 2008. ISBN 9780521889667. doi: 10.1017/CBO9780511535628.

Q. Kong, T. Siauw, and A. M. Bayen. *Python Programming and Numerical methods: A Guide for Engineers and Scientists*. Academic Press, United Kingdom, 2021.

Q. Kong, L. Zhang, J. Han, C. Li, W. Fang, and T. Wang. Analysis of coordinate time series of doris stations on eurasian plate and the plate motion based on ssa and fft. *Geodesy and Geodynamics*, 14(1):90–97, 2023. ISSN 1674-9847. doi: https://doi.org/10.1016/j.geog.2022.05.001. URL `https://www.sciencedirect.com/science/article/pii/S1674984722000416`. Contemporary research in Geodynamics and Earth Tides.

W. Kosek and W. Popiński. Comparison of spectro-temporal analysis methods on polar motion and its atmospheric excitation. *Artificial Satellites*, 34(2):65–75, 1999.

W. Kosek, W. Popinski, and T. Niedzielski. Wavelet based comparison of high frequency oscillations in the geodetic and fluid excitation functions of polar motion. In Nicole Capitaine, editor, *Proc. Journée 2010 "Systèmes de référence spatio-temporels"*, Observatoire de Paris, pages 168–171, October 2010.

N. T. Kottegoda. *Analysis of hydrologic time series*, pages 20–66. Palgrave Macmillan UK, London, 1980. ISBN 978-1-349-03467-3. doi: 10.1007/978-1-349-03467-3_2. URL https://doi.org/10.1007/978-1-349-03467-3_2.

X. Kuang, J. J. Jiao, C. Zheng, J. A. Cherry, and H. Li. A review of specific storage in aquifers. *Journal of Hydrology*, 581:124383, 2020. ISSN 0022-1694. doi: https://doi.org/10.1016/j.jhydrol.2019.124383. URL https://www.sciencedirect.com/science/article/pii/S0022169419311187.

S. M. Kudryavtsev. Improved harmonic development of the earth tide-generating potential. *Journal of Geodesy*, 77(12):829–838, 2004. ISSN 1432-1394. doi: 10.1007/s00190-003-0361-2.

L. Kulanuwat, C. Chantrapornchai, M. Maleewong, P. Wongchaisuwat, S. Wimala, K. Sarinnapakorn, and S. Boonya-aroonnet. Anomaly detection using a sliding window technique and data imputation with machine learning for hydrological time series. *Water*, 13(13), 2021. ISSN 2073-4441. doi: 10.3390/w13131862. URL https://www.mdpi.com/2073-4441/13/13/1862.

H.-J. Kümpel. *Tides in water saturated rock*, pages 277–291. Springer Berlin Heidelberg, Berlin, Heidelberg, 1997. ISBN 978-3-540-68700-9. doi: 10.1007/BFb0011467. URL https://doi.org/10.1007/BFb0011467.

N. Lal. The Taj Mahal: Monumental neglect. *The Diplomat*, 2018. URL https://thediplomat.com/2018/07/the-taj-mahal-monumental-neglect/. Accessed: 12/01/2024.

M. Larocque, A. Mangin, M. Razack, and O. Banton. Contribution of correlation and spectral analyses to the regional study of a large karst aquifer (charente, france). *Journal of Hydrology*, 205 (3):217–231, 1998. ISSN 0022-1694. doi: https://doi.org/10.1016/S0022-1694(97)00155-8. URL https://www.sciencedirect.com/science/article/pii/S0022169497001558.

M. Lee, Y. You, S. Kim, K. T. Kim, and H. S. Kim. Decomposition of water level time series of a tidal river into tide, wave and rainfall-runoff components. *Water*, 10(11), 2018. ISSN 2073-4441. doi: 10.3390/w10111568. URL https://www.mdpi.com/2073-4441/10/11/1568.

Y. Li, C. Zhang, C. Chen, and H. Chen. Calculation of capillary rise height of soils by swcc model. *Advances in Civil Engineering*, 2018:1–10, 08 2018. doi: 10.1155/2018/5190354.

R. Lindsey and L. Dahlman. Climate change: Global temperature, 2023. https://www.climate.gov/news-features/understanding-climate/climate-change-global-temperature, Accessed online: 09-01-2024.

J. Liu, J. Wassermann, C.D. Nguyen, and et al. IR thermography imaging of water capillary imbibition into porous stones of a gallo-roman site. In T. Hughes, J. & Howind, editor, *Science and Art: A Future for Stone: Proceedings of the 13th International Congress on the Deterioration and Conservation of Stone*, volume 1, pages 391–398, Glasgow, 6-10 September 2016. Paisley: University of the West Scoland.

M. H. Loke. *The inversion of two-dimensional resistivity data.* PhD thesis, Univ. of Birmingham, 1994.

M. H. Loke. *Electrical imaging surveys for environmental and engineering studies: A practical guide to 2-D and 3-D surveys.* Penang, Malaysia, 1999.

M. H. Loke and R. D. Barker. Rapid least-squares inversion of apparent resistivity pseudosections by a quasi-newton method1. *Geophysical Prospecting*, 44(1):131–152, 1996. doi: https://doi.org/10.1111/j.1365-2478.1996.tb00142.x. URL https://onlinelibrary.wiley.com/doi/abs/10.1111/j.1365-2478.1996.tb00142.x.

L. López-González, M. Gomez-Heras, R. Otero-Ortiz de Cosca, S. Garcia-Morales, and R. Fort. Coupling electrical resistivity methods and gis to evaluate the effect of historic building features on wetting dynamics during wind-driven rain spells. *Journal of Cultural Heritage*, 58: 209–218, 2022. ISSN 1296-2074. doi: https://doi.org/10.1016/j.culher.2022.10.009. URL https://www.sciencedirect.com/science/article/pii/S1296207422001832.

D. Lyon. The discrete fourier transform, part 4: Spectral leakage. *Journal of Object Technology*, 8: 23–34, 11 2009. doi: 10.5381/jot.2009.8.7.c2.

D. Machiwal and M. K. Jha. Time series analysis of hydrologic data for water resources planning and management: A review. *Journal of Hydrology and Hydromechanics*, 54(3):237 – 257, January 2006.

A. Maineult, E. Strobach, and J. Renner. Self-potential signals induced by periodic pumping tests. *Journal of Geophysical Research: Solid Earth*, 113(B1), 2008. doi: https://doi.

org/10.1029/2007JB005193. URL https://agupubs.onlinelibrary.wiley.com/doi/abs/10.1029/2007JB005193.

S. Mallat. *A Wavelet Tour of Signal Processing*. Academic Press, Boston, third edition, 2009. ISBN 978-0-12-374370-1. doi: https://doi.org/10.1016/B978-0-12-374370-1.00015-X. URL https://www.sciencedirect.com/science/article/pii/B978012374370100015X.

C.A.F. Marques, J.A. Ferreira, A. Rocha, J.M. Castanheira, P. Melo-Gonçalves, N. Vaz, and J.M. Dias. Singular spectrum analysis and forecasting of hydrological time series. *Physics and Chemistry of the Earth, Parts A/B/C*, 31(18):1172–1179, 2006. ISSN 1474-7065. doi: https://doi.org/10.1016/j.pce.2006.02.061. URL https://www.sciencedirect.com/science/article/pii/S1474706506002968. Time Series Analysis in Hydrology.

T. C. McMillan, G. C. Rau, W. A. Timms, and M. S. Andersen. Utilizing the impact of earth and atmospheric tides on groundwater systems: A review reveals the future potential. *Reviews of Geophysics*, 57(2):281–315, 2019. doi: https://doi.org/10.1029/2018RG000630. URL https://agupubs.onlinelibrary.wiley.com/doi/abs/10.1029/2018RG000630.

H. Mekonnen, Z. Bires, and B. Kassegn. Practices and challenges of cultural heritage conservation in historical and religious heritage sites: evidence from north shoa zone, amhara region, ethiopia. *Heritage Science*, 10, 10 2022. doi: 10.1186/s40494-022-00802-6.

M. L. Merritt. Estimating hydraulic properties of the floridan aquifer system by analysis of earth-tide, ocean-tide, and barometric effects, collier and hendry counties, florida. *Water-Resources Investigations Report*, 2004. URL https://api.semanticscholar.org/CorpusID:55689801.

B. Mille. *Les grands bronzes du sanctuaire des Vaux de la Celle à Genainville*, pages 264–267. 01 2019.

J. Milton and T. Ohira. *Mathematics as a Laboratory Tool: Dynamics, Delays and Noise*. Springer Nature, second edition, 2021.

P.-H. Mitard. La tête en tôle de bronze de Genainville (Val d'Oise). *Gallia*, 40(1):1–33, 1982. doi: 10.3406/galia.1982.1851. URL https://www.persee.fr/doc/galia_0016-4119_1982_num_40_1_1851.

P.-H. Mitard. La nécropole protohistorique de Génainville (Val d'Oise). *Revue archéologique de Picardie*, 1(1):33–38, 1983. doi: 10.3406/pica.1983.2982. URL https://www.persee.fr/doc/pica_0752-5656_1983_num_1_1_2982. Included in a thematic issue : Les celtes dans le nord du bassin parisien.

P.-H. Mitard. Val- d'Oise. le site Gallo-romain des Vaux de la Celle à Genainville. *Bulletin Monumental*, 142(4):444–446, 1984. doi: 10.3406/bulmo.1984.6437. URL https://www.persee.fr/doc/bulmo_0007-473x_1984_num_142_4_6437.

P.-H. Mitard et al. Le Sanctuaire Gallo-romaine de Genainville (Val d'Oise). *Bulletin archéologique du Vexin francaise*, 1993.

L. Mol and P. R. Preston. The writing's in the wall: A review of new preliminary applications of electrical resistivity tomography within archaeology. *Archaeometry*, 52(6):1079–1095, 2010.

M. Moník, Z. Lenďáková, J. J. Ibáñez, J. Muñiz, F. Borell, E. Iriarte, L. Teira, and F. Kuda. Revealing early villages – Pseudo-3D ERT geophysical survey at the pre-pottery neolithic site of kharaysin, jordan. *Archaeological Prospection*, 25(4):339–346, 2018. doi: https://doi.org/10.1002/arp.1713. URL https://onlinelibrary.wiley.com/doi/abs/10.1002/arp.1713.

Ladan Mozaffari, Ahmad Mozaffari, and Nasser Azad. Vehicle speed prediction via a sliding-window time series analysis and an evolutionary least learning machine: A case study on san francisco urban roads. *Engineering Science and Technology, an International Journal*, 6, 12 2014. doi: 10.1016/j.jestch.2014.11.002.

W. H. Munk and G. J. F. MacDonald. The rotation of the earth. Cambridge University Press, London, 1960.

D. C. Neto, H. K. Chang, and M. Th. van Genuchten. A mathematical view of water table fluctuations in a shallow aquifer in brazil. *Groundwater*, 54(1):82–91, 2016. doi: https://doi.org/10.1111/gwat.12329. URL https://ngwa.onlinelibrary.wiley.com/doi/abs/10.1111/gwat.12329.

C. C. Okpoli. Sensitivity and Resolution Capacity of Electrode Configurations. *International Journal of Geophysics*, 2013:608037, October 2013. ISSN 1687-885X. doi: 10.1155/2013/608037. URL https://doi.org/10.1155/2013/608037. Publisher: Hindawi Publishing Corporation.

P. Orième. Découverte de vestiges Gallo-romains sur le territoire de la commune de Genainville (Seine-et-Oise) : pavillon, théâtre, thermes. *Bulletin Conférence des Sociétés Savantes de Seine-et-Oise*, (14), 1937.

G. Petiau and A. Dupis. Noise, temperature coefficient, and long time stability of electrodes for telluric observations*. *Geophysical Prospecting*, 28(5):792–804, 1980. doi: https://doi.org/10.1111/j.1365-2478.1980.tb01261.x. URL https://onlinelibrary.wiley.com/doi/abs/10.1111/j.1365-2478.1980.tb01261.x.

F. L. Poblet and F. Azpilicueta. 27-day variation in solar-terrestrial parameters: Global characteristics and an origin based approach of the signals. *Advances in Space Research*, 61(9): 2275–2289, 2018. ISSN 0273-1177. doi: https://doi.org/10.1016/j.asr.2018.02.016. URL https://www.sciencedirect.com/science/article/pii/S0273117718301339.

K. A. Rahi and T. Halihan. Identifying aquifer type in fractured rock aquifers using harmonic analysis. *Ground water*, 51(1):76–82, 2013. URL https://doi.org/10.1111/j.1745-6584.2012.00925.x.

T. Rasmussen and T. Mote. Monitoring surface and subsurface water storage using confined aquifer water levels at the savannah river site, usa. *Vadose Zone Journal - VADOSE ZONE J*, 6, 05 2007. doi: 10.2136/vzj2006.0049.

T. C. Rasmussen and L. A. Crawford. Identifying and Removing Barometric Pressure Effects in Confined and Unconfined Aquifers. *Ground Water*, 35(3):502–511, May 1997. ISSN 0017-467X, 1745-6584. doi: 10.1111/j.1745-6584.1997.tb00111.x. URL http://doi.wiley.com/10.1111/j.1745-6584.1997.tb00111.x.

G. C. Rau. PyGtide: A Python module and wrapper for ETERNA PREDICT to compute gravitational tides on earth. *Zenodo*, 2018. URL https://.doi:10.5281/zenodo.1346260.

G. C. Rau, M. O. Cuthbert, R. I. Acworth, and P. Blum. Technical note: Disentangling the groundwater response to earth and atmospheric tides to improve subsurface characterisation. *Hydrology and Earth System Sciences*, 24(12):6033–6046, 2020. doi: 10.5194/hess-24-6033-2020. URL https://hess.copernicus.org/articles/24/6033/2020/.

G. C. Rau, T. C. McMillan, M. S. Andersen, and W. A. Timms. In situ estimation of subsurface hydro-geomechanical properties using the groundwater response to semi-diurnal earth and at-

mospheric tides. *Hydrology and Earth System Sciences*, 26(16):4301–4321, 2022. doi: 10.5194/hess-26-4301-2022. URL https://hess.copernicus.org/articles/26/4301/2022/.

A. Revil, K. Titov, C. Doussan, and V. Lapenna. Applications of the self-potential method to hydrological problems. In Harry Vereecken, Andrew Binley, Giorgio Cassiani, Andre Revil, and Konstantin Titov, editors, *Applied Hydrogeophysics*, pages 255–292, Dordrecht, 2006. Springer Netherlands. ISBN 978-1-4020-4912-5.

J. R. Rice and M. P. Cleary. Some basic stress diffusion solutions for fluid-saturated elastic porous media with compressible constituents. *Reviews of Geophysics*, 14(2):227–241, 1976. doi: https://doi.org/10.1029/RG014i002p00227. URL https://agupubs.onlinelibrary.wiley.com/doi/abs/10.1029/RG014i002p00227.

E. Rizzo, B. Suski, A. Revil, S. Straface, and S. Troisi. Self-potential signals associated with pumping tests experiments. *Journal of Geophysical Research: Solid Earth*, 109(B10), 2004. doi: https://doi.org/10.1029/2004JB003049. URL https://agupubs.onlinelibrary.wiley.com/doi/abs/10.1029/2004JB003049.

S. Rojstaczer and D. C. Agnew. The influence of formation material properties on the response of water levels in wells to earth tides and atmospheric loading. *Journal of Geophysical Research*, 94 (B9):12403 –12411, 1989.

S. E. Rosenquist, J. M. Moak, A. D. Green, and O. P. III Flite. Understanding hydrologic variation through time-series analysis. In *Proceedings of the 2010 South Carolina Water Resources Conference, held October 13-14, 2010, at the Columbia Metropolitan Convention Center*, 10 2010.

C. Saavedra and L. Bougrain. Wavelet-based semblance for p300 single-trial detection. In *International Conference on Bio-inspired Systems and Signal Processing*, 2013a. URL https://api.semanticscholar.org/CorpusID:6291423.

Carolina Saavedra and Laurent Bougrain. Wavelet-based semblance for p300 single-trial detection. Jan 2013b. doi: 10.5220/0004191001200125.

C Sabbioni, P Brimblecombe, A Bonazza, C Grossi Sampedro, I Harris, and P Messina. Mapping climate change and cultural heritage. In M Drdacky, editor, *7th EC Prague Conference on Safeguarded Cultural Heritage - Understanding and Viability for the Enlarged Europe*, pages 119–124. ITAM, Prague, 2007. URL https://ueaeprints.uea.ac.uk/id/eprint/26474/.

A. Sardella, E. Palazzi, J. von Hardenberg, C. Del Grande, P. De Nuntiis, C. Sabbioni, and A. Bonazza. Risk mapping for the sustainable protection of cultural heritage in extreme changing environments. *Atmosphere*, 11(7), 2020. ISSN 2073-4433. doi: 10.3390/atmos11070700. URL https://www.mdpi.com/2073-4433/11/7/700.

O. Sass and H.A. Viles. How wet are these walls? testing a novel technique for measuring moisture in ruined walls. *Journal of Cultural Heritage*, 7(4):257–263, 2006. ISSN 1296-2074. doi: https://doi.org/10.1016/j.culher.2006.08.001. URL https://www.sciencedirect.com/science/article/pii/S1296207406000744.

K. Sato, Y. Tamura, K. Osato, and R. N. Horne. Assessing poroelastic properties of a geothermal reservoir by tidal signal analysis. *Geothermics*, 100:102352, 2022. ISSN 0375-6505. doi: https://doi.org/10.1016/j.geothermics.2022.102352. URL https://www.sciencedirect.com/science/article/pii/S0375650522000062.

S. Save, L. Buffat, C. Batchelor, D. Vannieuwenhuyse, M. Bois, and B. Durand. Fleeing from a little bit of water: A very 'un-roman' response to changing environmental constraints. a case study from monteux, southern france. southern france. volume Special Volume 3, pages 113–117, 06 2012.

A. Savitzky and M. J. E. Golay. Smoothing and differentiation of data by simplified least squares procedures. *Analytical Chemistry*, 36:1627–1639, 1964.

D. H. Schoellhamer. Singular spectrum analysis for time series with missing data. *Geophysical Research Letters*, 28(16):3187–3190, 2001. doi: https://doi.org/10.1029/2000GL012698. URL https://agupubs.onlinelibrary.wiley.com/doi/abs/10.1029/2000GL012698.

D. Schweizer, V. Ried, G.C. Rau, and P. Stoica. Comparing methods and defining practical requirements for extracting harmonic tidal components from groundwater level measurements. *Math Geosci*, 53:1147–1169, 2021. URL https://doi.org/10.1007/s11004-020-09915-9.

E. Sesana, A. S. Gagnon, C. Bertolin, and J. Hughes. Adapting cultural heritage to climate change risks: Perspectives of cultural heritage experts in europe. *Geosciences*, 8(8), 2018. ISSN 2076-3263. doi: 10.3390/geosciences8080305. URL https://www.mdpi.com/2076-3263/8/8/305.

E. Sesana, A. S. Gagnon, C. Ciantelli, J. Cassar, and J. Hughes. Climate change impacts on cultural heritage: A literature review. *WIREs Climate Change*, 12, 05 2021. doi: 10.1002/wcc.710.

W. R. Sill. Self-potential modeling from primary flows. *GEOPHYSICS*, 48(1):76–86, 1983. doi: 10.1190/1.1441409. URL https://doi.org/10.1190/1.1441409.

B. D. Smith and M. A. Zeder. The onset of the anthropocene. *Anthropocene*, 4:8–13, 2013. ISSN 2213-3054. doi: https://doi.org/10.1016/j.ancene.2013.05.001. URL https://www.sciencedirect.com/science/article/pii/S2213305413000052. When Humans Dominated the Earth: Archeological Perspectives on the Anthropocene.

F. A. Spane. Considering barometric pressure in groundwater flow investigations. *Water Resources Research*, 38(6):14–1–14–18, 2002. doi: https://doi.org/10.1029/2001WR000701. URL https://agupubs.onlinelibrary.wiley.com/doi/abs/10.1029/2001WR000701.

A. G. Stephenson. Harmonic analysis of tides using tideharmonics, 2016. URL https//CRAN.R-project.org/package=TideHarmonics.

A. N Strahler. Hypsometric (area-altitude) analysis of erosional topography. *Geological society of America bulletin*, 63(11):1117–1142, 1952.

X. Sun, Y. Xiang, Z. Shi, X. Hu, and H. Zhang. Sensitivity of the response of well-aquifer systems to different periodic loadings: A comparison of two wells in huize, china. *Journal of Hydrology*, 572:121–130, 2019. ISSN 0022-1694. doi: https://doi.org/10.1016/j.jhydrol.2019.02.029. URL https://www.sciencedirect.com/science/article/pii/S0022169419301866.

B. Suski, A. Revil, K. Titov, P. Konosavsky, M. Voltz, C. Dagès, and O. Huttel. Monitoring of an infiltration experiment using the self-potential method. *Water Resources Research*, 42(8), 2006. doi: https://doi.org/10.1029/2005WR004840. URL https://agupubs.onlinelibrary.wiley.com/doi/abs/10.1029/2005WR004840.

P.N. Swarztrauber. *Vectorizing the Fast Fourier Transforms.* Academic Press, Cambridge, 1982.

R. G. Taylor et al. Ground water and climate change. *Nature Climate Change*, 3(4):322–329, April 2013. ISSN 1758-6798. doi: 10.1038/nclimate1744. URL https://doi.org/10.1038/nclimate1744.

W. Tegel, A. Seim, G. Skiadaresis, F. C. Ljungqvist, H.-P. Kahle, A. Land, B. Muigg, K. Nicolussi, and U. Büntgen. Higher groundwater levels in western europe characterize warm periods

in the common era. *Scientific Reports*, 10(16284), 2020. URL https://doi.org/10.1038/s41598-020-73383-8.

W. M. Telford, L. P. Geldart, and R. E. Sheriff. *Applied Geophysics*. Cambridge University Press, second edition, 1992.

M. Temmer, J. Rybák, A. Veronig, and A. Hanslmeier. What causes the 24-day period observed in solar flares? *Astronomy and Astrophysics*, pages 707–712, 2005. doi: DOI:10.1051/0004-6361:20041833. URL http://dx.doi.org/10.1051/0004-6361:20041833.

K. Titov, A. Revil, P. Konosavsky, S. Straface, and S. Troisi. Numerical modelling of self-potential signals associated with a pumping test experiment. *Geophysical Journal International*, 162 (2):641–650, August 2005. ISSN 0956540X, 1365246X. doi: 10.1111/j.1365-246X.2005.02676.x. URL https://academic.oup.com/gji/article-lookup/doi/10.1111/j.1365-246X.2005.02676.x.

K. Titov, P. Konosavsky, and M. Narbut. Pumping test in a layered aquifer: Numerical analysis of self-potential signals. *Journal of Applied Geophysics*, 123:188–193, 2015. ISSN 0926-9851. doi: https://doi.org/10.1016/j.jappgeo.2015.10.006. URL https://www.sciencedirect.com/science/article/pii/S0926985115300409.

N. J. Toll and T. C. Rasmussen. Removal of barometric pressure effects and earth tides from observed water levels. *Groundwater*, 45(1):101–105, 2007. https://doi.org/10.1111/j.1745-6584.2006.00254.x.

A. M. Tomé, D. Malafaia, A. R. Teixeira, and E. W. Lang. On the use of singular spectrum analysis. *arXiv: Signal Processing*, 2018. URL https://api.semanticscholar.org/CorpusID:125627634.

C. Torrence and G. P. Compo. A practical guide to wavelet analysis. *Bulletin of the American Meteorological Society*, 79(1):61 – 78, 1998. doi: https://doi.org/10.1175/1520-0477(1998)079<0061:APGTWA>2.0.CO;2. URL https://journals.ametsoc.org/view/journals/bams/79/1/1520-0477_1998_079_0061_apgtwa_2_0_co_2.xml.

C. Turnadge, R. S. Crosbie, Olga Barron, and Gabriel C. Rau. Comparing methods of barometric efficiency characterization for specific storage estimation. *Groundwater*, 57(6):844–859, 2019.

doi: https://doi.org/10.1111/gwat.12923. URL https://ngwa.onlinelibrary.wiley.com/doi/abs/10.1111/gwat.12923.

UNESCO. Abu simbel: The campaign that revolutionized the international approach to safeguarding heritage, 2023. URL https://en.unesco.org/70years/abu_simbel_safeguarding_heritage. accessed online: 14/12/2023.

M. Van Camp and P. Vauterin. Tsoft: graphical and interactive software for the analysis of time series and Earth tides. *Computers & Geosciences*, 31(5):631–640, June 2005. ISSN 00983004. doi: 10.1016/j.cageo.2004.11.015. URL https://linkinghub.elsevier.com/retrieve/pii/S0098300404002456.

G. Van Der Kamp and J. E. Gale. Theory of earth tide and barometric effects in porous formations with compressible grains. *Water Resources Research*, 19(2):538–544, 1983. doi: https://doi.org/10.1029/WR019i002p00538. URL https://agupubs.onlinelibrary.wiley.com/doi/abs/10.1029/WR019i002p00538.

G. Van Rossum and F. L. Drake. *Python 3 Reference Manual*. CreateSpace, Scotts Valley, CA, 2009. ISBN 1441412697.

R. Vautard, P. Yiou, and M. Ghil. Singular-spectrum analysis: A toolkit for short, noisy chaotic signals. *Physica D: Nonlinear Phenomena*, 58(1):95–126, 1992. ISSN 0167-2789. doi: https://doi.org/10.1016/0167-2789(92)90103-T. URL https://www.sciencedirect.com/science/article/pii/016727899290103T.

D. Vermeersch and M. Chupin. Le complexe religieux de Vaux-de-la-Celle à Genainville (95): Nouvelle proposition de phrasage du sanctuaire d'apre les derniere fouille. en: Etudier les lieux de culte de gaule-romiane. *Edition Monique Mergoil*, 2012. Montagnac.

R. Verner and G. Herbrik. Bond yields and stock returns comparison using wavelet semblance analysis. *Investment Management and Financial Innovations*, 14:281–289, 07 2017. doi: 10.21511/imfi.14(2-1).2017.12.

K. H. C. Vincent, 2007. https://whc.unesco.org/en/documents/132003.

R. R. B. von Frese, M. B. Jones, J. W. Kim, and J.-H.< Kim. Analysis of anomaly correlations.

Geophysics, 62(1):342–351, 02 1997. ISSN 0016-8033. doi: 10.1190/1.1444136. URL https://doi.org/10.1190/1.1444136.

N. Wagner and Z. Michalewicz. An analysis of adaptive windowing for time series forecasting in dynamic environments: Further tests of the dyfor gp model. pages 1657–1664, 07 2008. doi: 10.1145/1389095.1389406.

C. Wang, F. Dai, Y. Liu, Y. Wang, H. Li, and W. Qu. Shallow groundwater responses to rainfall based on correlation and spectral analyses in the heilonggang region, china. *Water*, 15(6), 2023. ISSN 2073-4441. doi: 10.3390/w15061100. URL https://www.mdpi.com/2073-4441/15/6/1100.

C.-Y. Wang and M. Manga. *Response to Tides, Barometric Pressure and Seismic Waves*, pages 83–153. Springer International Publishing, Cham, 2021. ISBN 978-3-030-64308-9. doi: 10.1007/978-3-030-64308-9_5. URL https://doi.org/10.1007/978-3-030-64308-9_5.

Chi-Yuen Wang, Mai-Linh Doan, Lian Xue, and Andrew J. Barbour. Tidal response of groundwater in a leaky aquifer—application to oklahoma. *Water Resources Research*, 54(10):8019–8033, 2018. doi: https://doi.org/10.1029/2018WR022793. URL https://agupubs.onlinelibrary.wiley.com/doi/abs/10.1029/2018WR022793.

Chi-Yuen Wang, Ai-Yu Zhu, Xin Liao, Michael Manga, and Lee-Ping Wang. Capillary effects on groundwater response to earth tides. *Water Resources Research*, 55(8):6886–6895, 2019. doi: https://doi.org/10.1029/2019WR025166. URL https://agupubs.onlinelibrary.wiley.com/doi/abs/10.1029/2019WR025166.

H.F. Wang. Quasi-static poroelastic parameters in rock and their geophysical applications. *PAGEOPH*, 141:269–286, 1993. URL https://doi.org/10.1007/BF00998332.

E. P. Weeks. Barometric fluctuations in wells tapping deep unconfined aquifers. *Water Resources Research*, 15(5):1167 – 1176, 1979.

H.-G. Wenzel. The nanogal software: Earth tide data processing package: Eterna 3.3. *Bulletin d'Informations des Mar´ees Terrestres*, 124:9425–9439, 1996.

W. B. Wilkinson and F. C. Brassington. Rising groundwater levels – an international problem. In R. A. Downing and W. B. Wilkinson, editors, *Applied Groundwater Hydrology*. Oxford Science Publications, Oxford University Press, 1991.

P. Xie, L. Wu, Y. Sang, F. Chan, J. Chen, Z. Wu, and Y. Li. Correlation-aided method for identification and gradation of periodicities in hydrologic time series. *Geoscience Letters*, 8, 12 2021. doi: 10.1186/s40562-021-00183-x.

S.-Y. Yang, H.-D. Yeh, and K.-Y. Li. Modelling transient temperature distribution for injecting hot water through a well to an aquifer thermal energy storage system. *Geophysical Journal International*, 183(1):237–251, 10 2010. ISSN 0956-540X. doi: 10.1111/j.1365-246X.2010.04733.x. URL https://doi.org/10.1111/j.1365-246X.2010.04733.x.

T. Zádorová and V. Pení žek. Formation, morphology and classification of colluvial soils: a review. *European Journal of Soil Science*, 69(4):577–591, 2018. doi: https://doi.org/10.1111/ejss.12673. URL https://bsssjournals.onlinelibrary.wiley.com/doi/abs/10.1111/ejss.12673.

S. Zhang, Z. Shi, G. Wang, Z. Zhang, and H. Guo. The origin of hydrological responses following earthquakes in a confined aquifer: insight from water level, flow rate, and temperature observations. *Hydrology and Earth System Sciences*, 27(2):401–415, 2023. doi: 10.5194/hess-27-401-2023. URL https://hess.copernicus.org/articles/27/401/2023/.

Y. Zhang, F. Huang, and G. Lai. Reaearch on skempton's coefficient b based on the observation of groundwater of changping station. *Earthquake Science*, 22:631–638, 12 2009. doi: 10.1007/s11589-009-0631-z.

A. Zhigljavsky. Singular spectrum analysis for time series: Introduction to this special issue. *Statistics And Its Interface*, 5:255–258, 2010.

Y. Zhu and B. Li. The relocation of general zhang'fei temple. *Journal of Chinese Architecture and Urbanism*, 4, 07 2022. doi: 10.36922/jcau.v4i1.63.

APPENDIX A

Appendix

A.1 History of the site and archaeological studies

Table A.1: Historical and archaeological events at the site

· Period	Event	Description
-500 to -52	Iron Age	Protohistoric necropolis and the development of an initial fountain
1^{st} Century AD	The first (small) *fanum* type temple and a *numphaeum* was built by the Gauls	
2^{nd} Century AD	Construction of the theater, secondary buildings and the double-*cellae*-temple by the Gallo-romans	A unique model of a *fanum* type of temple with double *cellae* that was rare in the romanised Gauls territories
3^{rd} Century AD	The ancient drainage channels were constructed	An indication that flooding was a problem faced by the inhabitants while an attempt was made the masonry and craft men to control, mitigate the situation

Table A.2: Historical and archaeological events at the site (second part)

Period	Event	Description
5^{th} Century AD	Abandonment and pilfering of the site	Many hypothesis have been put forward to account for the abandonment: • The German led invasion at the end of the 3^{rd} Century AD Mitard et al. (1993) • The *Merovingian Sarcoghagi* • Incessant flooding after heavy rainfall
$\cdots$ to around 20^{th} Century AD	Accumulation of more than 2 - 3 m of silts (and waste piled by the locals) and the discovery of the site	Excavations led to the unearthing of the vestiges; reconstruction of the site history
1935 – 1948	Initial excavations led by Architect Pierre Orième	Interrupted by World War II
1960 – 1991	Excavations at the Scared Area	P.H. Mitard and his team are credited with the recovery of the temple walls and restorations works at the paved entrance e.g. Mitard et al. (1993)
From 1989	The Îl-de-France region through it Department of Historic Archaeology was responsible for excavations	Isabelle Daveau led the excavations at the *cavea* of the theatre
In 1993	Excavations: West of the Sacred Area by Laurent Cholet and his team Cholet and Delestre (1992)	Unearthed a residential area

Table A.3: Historical and archaeological events at the site (third part)

· Period	Event	Description
In 1995	Desiltation of the 3^{rd} Basin	Didier Vermeersch carried out the restoration of the basin by desilting it to study it frame, structure and hydraulic characteristics
In 2004	The Archaeology Students Association of the Department of Val-d'Oise at the Univeristy of Cergy-Pontoise (now CY Cergy Paris University)	The students involvement in research and learning with routine archaeological activities at the excavation sites under the supervision of Didier Vermeersch
2004 – 2014	Investigations of the Numphaeum and baths	By Didier Vermeersch
2010	Excavations at the cultural area	A section of a wall discovered
2004 – 2014	Investigations: Facade of the Theater	By Vivien Barrière
2015 – $present$	Investigations: Facade of the amphitheater cultural area: central and communal space	Uncovering of a quadrangular enclosure delimited by a fence wall or a platform
2016	Excavations at the cultural area	The second section of the wall discovered
2019 – 2020		The skeletons of a sheep was unearthed (e.g. Barrière (2021))

B.2 Water level data collection

Table A.4: Typical length of water level data collection as a function of the intended use of the data

Period	Days/weeks	Months	Years	Decades
To determine the hydraulic properties of aquifers (aquifer tests)	✓	✓		
Mapping the altitude of the water table or potentiometer surface	✓	✓		
Monitoring short-term changes in in groundwater recharge and storage	✓	✓	✓	
Monitoring long-term changes in in groundwater recharge and storage			✓	✓
Monitoring the effects of climatic variability			✓	✓
Monitoring regional effects of groundwater development			✓	✓
Statistical analysis of water-level trends			✓	✓
Monitoring changes in groundwater flow directions	✓	✓	✓	✓
Monitoring groundwater and surface water interaction	✓	✓	✓	✓
Numerical (computer) modeling of in groundwater flow or contaminant transport	✓	✓	✓	✓

✓ Most applicable for intended use ✓ Sometimes applicable

for intended use

Source: USGS Circular 1217

C.3 Preprocessing

C.3.1 Access and visualize data

Listing A.1: Assessment and visualization of water levels with Python

```
#import libraries
import numpy as np
import pandas as pd
import matplotlib.pyplot as plt
from matplotlib import dates as mpl_dates
from matplotlib.dates import *

# access data: open the file and copy the section containing the data and the
headers (Date/time, Pression, temperature) into a notepad and save as a CSV file

# read and parse date
dfOct = pd.read_csv("vei_af605_211028094823_AF605.csv'',
engine=‘‘python", index_col=False, sep='\t') # The delimiter may be ';' or ','
# vei_af605_211028094823_AF605.csv is a file containing e.g. datetime,
# water pressure and groundwater temperature data

dfOct['Date/time'] = pd.to_datetime(dfOct[‘Date/time'],
dayfirst=True,format={'%Y%m%d'})
dfOct.head()

#view_data
df_Oct

#edit_columns_if_required
dfOct=dfOct.rename(columns={‘Temp{e}rature[{A}{C}]':‘Temperature[{$^{\circ}$C}]'})
dfOct=dfOct.rename(columns={‘Pression[cm]': ‘Pressure[cm]'})
dfOct
```

```
#visualised_data
plt.style.use('seaborn')
fig, ax = plt.figure(figsize=(15,8))
x=dfOct['Date/time']
y=dfOct['Pressure[cm]']

plt.plot(x, y, color='g')
plt.title('Groundwater Level Fluctuations: September – October,
 2021 \n Borehole Location: West of the Theatre',fontsize=14,fontweight='bold')
plt.ylabel('Water Pressure [cm]',fontsize=14,fontweight='bold')
plt.xlabel('Date/time', fontsize=14, fontweight='bold')
plt.tight_layout()
plt.legend()#if required

#format date if required
date_format = mpl_dates.DateFormatter('%d-%m-%Y')
plt.gca().xaxis.set_major_formatter(date_format)

#save, view plot
plt.savefig('OctData_2021',format=None,edgecolor='w',bbox_inches="tight")
plt.show()
```

C.3.2 Serial date number

The measured water pressure in the *PzTh* was also treated with the SSA to decompose the data into components and for possible extraction of periodic phenomena or signals. Data from February 2022 to June 2023 was preprocessed and the date time part of the data was converted to serial date number as required by the SSA code written in MATLAB programming language. The steps followed in the conversion of the date time to serial number are provided in the Python programming language (appendix C.3).

Listing A.2: Conversion of datetime to serial date number with python

```
# import libraries
import numpy as np
import  pandas as pd
# read data with datetime with pandas
df = pd_read.csv('file')
# display pandas datetime
df['Date/time']


ts_df = (df['Date/time'])


# results in seconds converted to days
ExcelSerialNum =
((ts_df-pd.Timestamp('1899-12-30')) / pd.Timedelta(seconds=1))/(24*60*60)
# substract the number of days since 1970-01-01 and convert days to minutes
ExcelSerialNum = ((ExcelSerialNum - 42736)*24*60)
# round up result to two decimal places
ExcelSerialNum = round(ExcelSerialNum, 2)


print(ExcelSerialNum)


# convert out to DataFrame
df["Time"]= ExcelSerialNum
```

D.4 Electrical resistivity tomography

D.4.1 RES2DINV file format

For the inversion procedure, the RES2DINV program requires the data in an ASCII format in a Windows notepad file. The extension usually ends with a .DAT, e.g. LESVAUX.DAT. The items in the file are arranged following the order shown in the first column of Table A.5. The corresponding description of each item is given in the second column along the same row.

The file is structured into the preamble and the measured data. The preamble consists of the file name, unit electrode spacing, and the array type. It also includes information on the type of data, apparent resistivity, or resistance. It also requires the user to indicate whether *Induced Polarisation* (IP), data is present or not with a designated value. Topographic data can be added below the measured data by indication of the value.

In the measured data section, the values are the number of electrodes, the x- and z- position of C_1 electrode, the x- and z- position of C_2 electrode the x- and z- position of P_1 electrode the x- and z- position of P_2 electrode and lastly, the apparent resistivity values. Table A.6, A.7 and A.8 shows the file used for the inversion of each profile. The input file ends with a few zeros in files without topographic data.

Topographic is added after the measured data section. It would consist of the horizontal and vertical coordinates of a point along the ERT survey line. It begins with a header line written immediately after the measured data section without the zeros (Table A.8). It is followed by a number, usually 2, to indicate the inclusion of topographic data. This is followed by the number of topographic data and the sequence of the data in two columns. The first column is the horizontal coordinate while the second column is the vertical values. The file is closed with 1 and four zeros (Table A.8).

Table A.5: Wenner-Schlumberger array: file format for a profile surveyed

Input File	Comments
Profile N°	Name of survey Line
0.4	Unit electrode spacing
11	Array type, 11 for general array, 7 for Wenner-Schlumberger
	Type of measurement (0 = app. resistivity, 1 = resistance)
0	0 is use here to indicate apparent resistivity values
2808	Number of data points
2	The value 2, here indicate XYZ location format is used
0	no IP data
4 0.4 0.0 ...	number of electrodes, x- and z- position of first current electrode, ... resistivity value
0	
0	
0	
0	

Table A.6: Wenner-Schlumberger array: file format for P_1

File inputs
Profile P1
0.4
7
0
Type of measurements (0 = app. resistivity, 1 = resistance)
0
2808
2
0
⋮ **measured data continued**
0
0
0
0

Table A.7: Wenner-Schlumberger array: file format for P_2

File inputs
Profile P2
1.00
11
7
Type of measurements (0 = app. resistivity, 1 = resistance)
0
2808
2
0
4 1.00 0.00 2.00 0.00 3.00 0.00 53.82
⋮ **measured data continued**
0
0
0
0

Table A.8: Wenner-Schlumberger array: file format for P_3

File inputs
Profile P3
0.4
11
0
Type of measurements (0 = app. resistivity, 1 = resistance)
0
2266
2
0
⋮
⋮ **measured data**
⋮
Topography in separate list
2
56
⋮
⋮ **topo data**
⋮
1
0
0
0
0

E.5 SSA: values of long and short term periods

Table A.9: Eigenvalues and corresponding periods of decomposed long and short term components in the water pressure data of the Sacred Area borehole (PzSa): February 2022 - July 2023

Eigenvalue n°	**Long Periods, LP** ($k = \frac{2}{3}N$)		**Short Periods, SP** ($k = 0.95N$)	
1	96.863	$\pm$ 18.134	7.228	$\pm$ 0.052
2	93.858	$\pm$ 20.030	7.066	$\pm$ 0.057
3	65.400	$\pm$ 4.653	5.800	$\pm$ 0.035
4	66.640	$\pm$ 5.531	5.080	$\pm$ 0.034
5	18.545	$\pm$ 0.440	10.380	$\pm$ 0.184
6	18.536	$\pm$ 0.516	10.377	$\pm$ 0.165
7	213.973	$\pm$ 60.755	15.882	$\pm$ 0.288
8	53.067	$\pm$ 5.697	15.814	$\pm$ 0.296
9	29.541	$\pm$ 1.078	17.402	$\pm$ 0.331
10	29.176	$\pm$ 1.062	34.775	$\pm$ 2.283
11	12.244	$\pm$ 0.328	3.728	$\pm$ 0.013
12	12.234	$\pm$ 0.338	3.978	$\pm$ 0.020
13	14.027	$\pm$ 0.206	4.318	$\pm$ 0.023
14	9.260	$\pm$ 0.159	3.583	$\pm$ 0.013
15	9.270	$\pm$ 0.153	3.393	$\pm$ 0.011
16	9.284	$\pm$ 0.209	2.742	$\pm$ 0.011
17	23.630	$\pm$ 1.430	2.739	$\pm$ 0.011
18	23.819	$\pm$ 1.538	2.953	$\pm$ 0.045
19	526.790	$\pm$ 0.000	2.952	$\pm$ 0.025
20	7.076	$\pm$ 0.053	42.236	$\pm$ 3.544

residual 0.5000 ± 0.0003

Table A.10: Eigenvalues and corresponding periods of decomposed long and short term components in the water pressure data from the borehole at the Store House Frontage (PzShf): March 2022 - July 2023

Eigenvalue n°	**Long Periods, LP** ($k = \frac{2}{3}N$)		**Short Periods, SP** ($k = 0.95N$)	
1	482.770	± 0.000	7.058	± 0.072
2	264.993	± 69.087	7.056	± 0.071
3	102.290	± 18.599	6.191	± 0.079
4	101.429	± 20.479	10.377	± 0.146
5	64.943	± 9.571	11.429	± 0.123
6	62.718	± 9.260	11.443	± 0.128
7	18.490	± 0.607	5.075	± 0.064
8	18.498	± 0.545	16.095	± 0.310
9	52.584	± 5.150	4.650	± 0.044
10	29.330	± 1.198	34.240	± 1.682
11	29.471	± 1.344	3.984	± 0.022
12	12.311	± 0.250	3.982	± 0.021
13	12.305	± 0.259	3.581	± 0.013
14	45.123	± 5.161	3.396	± 0.013
15	9.300	± 0.137	2.743	± 0.012
16	9.307	± 0.141	2.742	± 0.012
17	23.300	± 1.499	2.952	± 0.019
18	24.979	± 1.594	2.953	± 0.017
19	14.020	± 0.257	2.500	± 0.016
20	13.970	± 0.231	41.276	± 2.246

residual 0.49930 ± 0.00031

Table A.11: Singular spectral analysis: West of the Theatre (PzTh) water pressure from 1^{st} February, 2022 - 6^{th} June, 2023

Eigenvalue n°	**Long Periods, LP** ($k = \frac{2}{3}N$)	**Short Periods, SP** ($k = 0.95N$)
1	510.63	510.63
2	268.14	54.41
3	107.02	22.76
4	95.73	14.00
5	64.90	12.33
6	54.29	8.59
7	18.39	8.58
8	18.25	7.05
9	28.86	6.22
10	28.85	5.69
11	12.33	5.05
12	12.31	4.64
13	22.67	4.32
14	22.77	3.78
15	14.09	3.51
16	14.06	3.27
17	24.93	2.74
18	9.24	2.71
19	9.24	3.08
20	8.58	2.97

Residual LP: 10.46 | SP: 0.50

Table A.12: The periods of the long and short term components and their associated eigenvalues for Year 2017, 2018 and 2019 water pressure

Eigenvalue n°	**Long Periods, LP** ($k = \frac{2}{3}N$)	**Short Periods, SP** ($k = 0.95N$)
1	689.40	14.83
2	321.85	14.81
3	70.00	7.90
4	71.16	7.90
5	268.66	18.31
6	59.14	10.45
7	57.52	10.44
8	24.65	6.65
9	24.51	5.88
10	29.04	5.63
11	29.09	4.88
12	45.21	4.88
13	44.51	4.55
14	32.66	4.33
15	21.00	4.17
16	19.82	4.08
17	23.31	3.32
18	32.93	3.28
19	11.00	2.65
20	11.00	2.65

Table A.13: The periods of the long and short term components of groundwater pressure data in Borehole for day 28 - 42 of Year 2018 and associated eigenvalue groups

Eigenvalue n°	**Long Periods, LP** ($k = \frac{2}{3}N$)	**Short Periods, SP** ($k = 0.95N$)
1	6.73	0.50
2	8.64	0.50
3	4.92	0.33
4	2.79	0.33
5	2.39	0.25
6	1.46	0.25
7	1.40	0.18
8	2.24	0.19
9	1.15	0.17
10	0.70	0.15

Table A.14: Extracted periods, inferred harmonic components and associations in groundwater and barometric pressure data (McMillan et al., 2019; Merritt, 2004; Rau et al., 2020)

Data Window Interval (days)	Extracted Period (days)	Frequency (cpd)	Infer Earth tides Constituent (s)	Groundwater	Barometric Pressure	Tidal cycle
01 - 14	1.0910	0.9166	O_1	**YES**	⋯	D
	0.4964	2.0146	⋯	⋯	⋯	⋯
07 - 21	1.2911	0.7745	⋯	⋯	⋯	⋯
	1.2922	0.7737	⋯	⋯	⋯	⋯
	0.4987	2.0052	K_2	**YES**	**YES**	$S-D$
14 - 28	1.3612	0.7346	⋯	⋯	⋯	⋯
	1.1096	0.9012	O_1	**YES**	**YES**	D
	1.1143	0.8974	Q_1	**YES**	**YES**	D
	0.4979	2.0086	S_2	**YES**	**YES**	$S-D$
21 - 35	0.95825	1.0435	K_1	**YES**	**YES**	$S-D$
	0.49976	2.0010	S_2	**YES**	**YES**	$S-D$
28 - 42	1.43710	0.6958				
	0.49957	2.0017	S_2	**YES**	**YES**	$S-D$
35 - 49	1.3206	0.7572	⋯	⋯	⋯	⋯
	0.4618	2.1653	⋯	⋯	⋯	⋯
42 - 56	1.2348	0.8098	⋯	⋯	⋯	⋯
49 - 63	0.97781	1.0227	K_1	**YES**	**YES**	D
	0.50240	1.9904	S_2	**YES**	**YES**	$S-D$
	0.49311	2.0279	S_2	**YES**	**YES**	$S-D$
56 - 70	0.50155	1.9938	S_2	**YES**	**YES**	$S-D$
	0.49964	2.0014	S_2	**YES**	**YES**	$S-D$
63 - 77	0.4994	2.0025	S_2	**YES**	**YES**	$S-D$
	1.2405	0.8061	⋯	⋯	⋯	⋯
	0.4988	2.0050	K_2	**YES**	**YES**	$S-D$
70 - 84	0.5005	1.9998	S_2	**YES**	**YES**	$S-D$
77 - 91	1.26050		⋯			
	0.95964	1.0421	K_1	**YES**	**YES**	D
	0.50161	1.9933	S_2	**YES**	**YES**	$S-D$

• D = Diurnal; S-D = Semi-diurnal; **YES** = harmonic component present

F.6 Tidal strain sensitivity

For each water pressure dataset from the three boreholes designated PzSa, PzShf and PzTh, decomposed into frequency components using DFT (see subsection 5.2.3). The extracted amplitude and the phase of each component are tabulated in tables A.15, A.16 and A.17 while the components from the tidal strain are shown in table A.18.

The ratio of the amplitude of a component in the water A_w to the corresponding amplitude of the same component in tidal areal strain A_t is known as the areal strain sensitivity A_s (equation A.1). In the classic definition, it is the ratio of the amplitude of the water level response dh to earth tides to the amplitude of the areal strain produced by earth tides (Cutillo and Bredehoeft, 2011; Rojstaczer and Agnew, 1989).

Table A.15: Tidal components, frequency, extracted amplitude and phase values for `PzTh`

Tidal component	Frequency (cpd)	Amplitude (kPa)	Phase (°)
M_2	1.932274	0.038	91.470
K_1	1.002738	0.256	32.986
S_2	2.000000	0.316	-144.430

$$A_s = -\frac{dh}{\varepsilon_A} = \frac{A_w}{A_t} \tag{A.1}$$

where, $\varepsilon_A = \varepsilon_{11} + \varepsilon_{22}$ = tidal (areal) strain.

Table A.16: Tidal components, frequency, extracted amplitude and phase values for `PzShf`

Tidal components	Frequency (cpd)	Amplitude (kPa)	Phase (°)
K_1	1.002738	0.175	125.792
S_2	2.000000	0.373	95.263

Table A.17: Tidal components, frequency, extracted amplitude and phase values for `PzSa`

Tidal component	Frequency (cpd)	Amplitude (kPa)	Phase (°)
K_1	1.002738	0.325	125.792
S_2	2.000000	0.450	95.263

Table A.18: Tidal components, frequency, amplitude and phase values for tidal strain at PzSa

Tidal component	Frequency (cpd)	Amplitude ($nstr$)	Phase (°)
M_2	1.932274	7.95	136.970
K_1	1.002738	10.25	-69.384
S_2	2.000000	3.65	-48.940
N_2	1.895982	1.45	105.025
O_1	0.929536	8.05	-67.494

G.7 Phase shift

Table A.19: Strain, tidal sensitivity and phase shift for PzSa

Tidal components		Data	Components: Amplitude: Value	Components: Amplitude: $\frac{A_w}{A_t}$* (kPa)	Components: Phase	Components: Phase shift
K_1	PzSa	Water pressure	0.325	0.0317	125.792	195.356
		Strain	10.25		-69.384	
S_2	PzSa	Water pressure	0.45	0.1233	95.265	144.205
		Strain	3.65		-48.940	

* A_w = amplitude of earth tide component in the water, A_t= amplitude of tidal component in areal strain, A_s = l strain sensitivity

Table A.20: Strain, tidal sensitivity and phase shift for PzTh

Tidal components		Data	Components: Amplitude: Value	Components: Amplitude: $\frac{A_w}{A_t}$* (kPa)	Components: Phase	Components: Phase shift
K_1	PzTh	Water pressure	0.256	0.0250	32.986	102.37
		Strain	10.25		-69.384	
S_2	PzTh	Water pressure	0.316	0.0866	-144.430	-95.49
		Strain	3.65		-48.940	
M_2	PzTh	Water pressure	0.038	0.0048	-91.470	-45.5
		Strain	7.95		-136.970	

* A_w = amplitude of earth tide component in the water, A_t= amplitude of tidal component in tidal areal strain, A_s = strain sensitivity

Table A.21: Strain, tidal sensitivity and phase shift for `PzShf`

Tidal components		Data	Components			
			Amplitude		Phase	Phase shift
			Value	$\frac{A_w}{A_t}$* (kPa)		
K_1	PzShf	Water pressure	0.175	0.01707	125.792	195.356
		Strain	10.25		-69.384	
S_2	PzShf	Water pressure	0.373	0.1022	95.263	144.940
		Strain	3.65		-48.940	

* A_w = amplitude of earth tide component in the water, A_t = amplitude of tidal component in areal strain, A_s = strain sensitivity

H.8 Aquifer evaluation test: submersible pump

Table A.22: Submersible pump specifications

Description	**Parameters**
Power	280 $watt$
Current	2.30 A
Voltage	230 V
Diameter	¾"
Frequency	50 Hz